SOFT-MATTER TRIBOLOGY: UNDERSTANDING THE MICROSTRUCTURE TO PROPERTY RELATIONSHIPS OF HYDROGEL-LIKE MATERIALS

BY

TOOBA SHOAIB

DISSERTATION

Submitted in partial fulfillment of the requirements
for the degree of Doctor of Philosophy in Materials Science and Engineering
in the Graduate College of the
University of Illinois Urbana-Champaign, 2021

Urbana, Illinois

Doctoral Committee:

Professor Rosa M. Espinosa-Marzal, Chair
Professor John R. Abelson
Assistant Professor Qian Chen
Assistant Professor Simon A. Rogers
Assistant Professor Christopher Evans

ABSTRACT

Biological tribosystems are excellent examples of nature leveraging soft matter properties to achieve exceptional lubrication for prolonged periods of activity. In these systems, lubrication is provided by sparsely crosslinked, polymeric surface layers imbibed with an aqueous lubricant. A prominent biological tribosystem is the articular cartilage, an avascular tissue consisting of an extracellular matrix made of collagen fibrils and proteoglycans, with a small number of chondrocyte cells. However, in this tissue, there exists a gradient in the orientation of the collagen fibers and water content as a function of the distance from the bone, which emphasizes the importance of the microstructure in cartilage's functionality, i.e. a load-bearing tissue that maintains low friction and wear. In fact, recent studies have shown that the cartilage's articulating surface comprises of a network of highly hydrated mucins, polysaccharides, glycoproteins, and phospholipids, which play a key role in maintaining low friction in boundary lubrication. This has been evident in studies performed on multiple other biphasic, non-biological hydrogels as well, where a prominent effect of the interfacial microstructure is observed on their mechanical and tribological properties. Yet, not only there is a lack of knowledge but also wide discrepancy about the fundamental underlying mechanisms relating the dynamic and static frictional dissipation to the microstructure of these materials. Conversely, this fundamental gap in knowledge also limits progress in the design of functional replacements, based on hydrogel-like materials.

Our aim was to not only advance the existing knowledge about the frictional dissipation of hydrogels, by precisely correlating the role of microstructure to the tribological performance, but also, to establish design principles that can help combat some of the existing challenges related to their application as tribological biomaterials. In light of this, the doctoral work presented here has achieved the following specific goals:

I. Studied, modeled and quantified influence of the microstructure, crosslinking degree and stiffness of the polymer on the dynamic and static frictional response

II. Scrutinized the relation between friction force and interfacial rheology of hydrogels

III. Elucidated the pathways of network formation in double network hydrogels which lead to enhanced mechanical and frictional response

IV. Scrutinized mechanical and tribological response of biological hydrogels in physiologically relevant conditions

By combining powerful state-of-the-art experimental techniques such as the Dynamic Light Scattering (DLS), Atomic Force Microscopy (AFM) and extended surface forces apparatus (SFA), we have demonstrated that the main mechanisms behind the frictional dissipation of hydrogels arise directly from their biphasic nature – the polymeric network and the imbibing fluid. In the context of dynamic friction, the viscous-adhesive model developed here quantifies the hydrogel's frictional response by considering an interplay of adhesive and viscous dissipation directly arising from the hydrogel's microstructure. The model accounts for confinement effects, poroelastic deformation, and the influence of the polymer on the viscous friction force, and helps reconcile seemingly contradictory models proposed previously. The adhesive contribution was modeled as a combination of reversible, transient adhesive bonds between the hydrogel and the countersurface and the poroelastic deformation of the hydrogel during shear, while the role of viscous dissipation was revealed to be directly related to the rheological performance of the hydrogel's interface. In the latter, the polymer and imbibed fluid, both dictated viscous dissipation. Scrutiny of the rheological behavior of hydrogel thin films in tandem with nanotribology was conducted to show that the effective viscosity measured in rheology agrees with the friction behavior, although it is not sufficient to capture the rich frictional response of hydrogels as a function of sliding velocity.

In the context of static friction, the combined effects of microstructure, interfacial shear stresses, interfacial ageing, and temperature were all tied together into a conceptual phase diagram for the static friction of hydrogels. Feasibility of the models developed for the dynamic and static friction was validated by extending the concepts to other hydrogel systems such as physically crosslinked agarose and cartilage, thereby demonstrating the universality of the proposed mechanisms for biphasic soft materials.

The study was further extended to DN hydrogels and biological hydrogels. Systematic investigations of the DN hydrogels comprising of agarose and polyacrylamide hydrogels as independent, interpenetrating networks revealed the design limitations of achieving high strength and high lubricity, simultaneously. Lastly, the novel experimental study on the gel-like surface of the articular cartilage was conducted as a direct application of this research. The graded response of the cartilage's gel-like articulating surface in elevated calcium concentrations was traced back to changes in the surface and sub-surface microstructure, which was reported to subsequently modulate the mechanical and tribological response of the material.

In summary, through its collective experimental studies and comprehensive models, this doctoral work provides the basic framework to understand lubrication mechanisms of hydrogel-like materials in light of their microstructure. Furthermore, it also helps provide the basic design principles for fabricating hydrogels capable of achieving low friction coefficients and augmented wear resistance through the precise control of their microstructure. Lastly, the novel methodologies and protocols stemming from this dissertation open up previously unexplored research avenues and hence can influence diverse areas of inquiries, not only limited to biolubrication and biomedical applications but soft robotics and microelectromechanical devices.

ACKNOWLEDGMENTS

A long and exciting journey finally culminates. The past few years have been truly transformational, as I grew from a naive undergraduate student with a passion for science into a "viable" researcher. I was given this amazing opportunity by my advisor Prof. Rosa Espinosa-Marzal, who welcomed me in her lab and was not only my research mentor but also my professional guide. You put in an immense effort to groom me professionally. I thank you for having the heart to invest in your students completely. I have learnt an incredible amount from you, I owe all my achievements to you and will forever be grateful. You are an amazing mentor.

I also want to thank my mentor, Prof. John R Abelson. Your presence and guidance have been unwavering for me throughout my time at UIUC. I look up to you as a guide, a mentor and as a father figure. Thank you for always lifting me up and letting me know that I'm capable of great things. I would also like to show gratitude to my committee members Prof. Qian Chen, Prof. Simon Rogers and Prof. Christopher Evans for their constructive and critical advice and insights on my research. Also, Prof. Prathima Nalam for providing me guidance and support in the formative years of my PhD and Prof. Markus Wimmer for giving me an amazing opportunity to collaborate and learn. I would like to acknowledge my home department MatSE, CEE, where I conducted my research, and NSF for providing funding (grant # 17-61696).

How can I forget my family in the room 4224 - Yijue Diao, Mengwei Han, Josue Lopez, Gus Greenwood and Binxin Fu. You guys are the best! It was because of you all that I was able to pull through. I will forever miss your comradeship. I'd also like to mention my family away from home in Urbana-Champaign -"errand" best-friend Varsha, my brothers Dhawal and Shreyas through thick and thin, my roommates Zainab, Kulsoom and Fatima. Sherry the chef, and my boba and gossip buddy, Wajih (sorry- Professor Wajih!). My lovely friend and a gem of a person,

Hareem. Thanks to my undergraduate students Ray, Justin and Paige for giving me the opportunity to be a small part of your journeys. You all are extraordinary and make me immensely proud!

Now my actual family. Abbu, it was your dream and I'm proud to have done it for you. Thank you for all the sacrifices you've given for me to be where I am today. Ammi, I feel ridiculous just thinking about what I'm trying to do - to put into words your contribution. I cannot, ever. Thank you God for giving me a mother like you. Thank you my dear Aapa, for being the source of warmth and support and just being there whenever I needed you. My person, Amina, for never, ever letting me feel alone, even if we were thousands of miles apart.

Finally, I would like to thank my new family, my better half - Mohid, thank you for being a supportive partner. For being considerate, for missing on trips, weddings and weekends with me and not complaining. I hope you have not gotten used to flying solo. Thank you for taking full responsibility of our daughter as I went through the final stretch while managing your own work. It was a struggle for you as much as for me. And lastly, the most important human for me now, Mahnur. You're too little and naive to know this, but you've done a lot for me in these few months. You are the light of my life and the warmth of my heart. I owe you eternity for putting up with my absence and I promise to make it up to you. Hopefully when you grow up, you'll appreciate that it was all for the greater good.

Dedicated to my parents, Shoaib and Iffat Hashmi

TABLE OF CONTENTS

CHAPTER 1: INTRODUCTION

Tribosystems in nature, such as the oral cavity, the corneal epithelium and the articular cartilage provide life-long exceptional lubrication (2). Biological tribosystems exhibit a biphasic composition, i.e. a macromolecular network consisting of mucins(3, 4), polysaccharides(5), phospholipids(6), or glycoproteins(7), and a water-based lubricant(2). Because of their structural semblance to multiple biotribosystems, hydrogels often serve as model systems to understand biolubrication. Hydrogels are biphasic materials composed of a polymer network and large amounts of water, which renders them soft, viscoelastic –reflecting the intrinsic viscoelasticity of the polymer network– and poroelastic –because of the flow of the interstitial fluid. Their biocompatibility makes hydrogels promising biomaterials for targeted medical applications, which has further increased the interest in investigating hydrogel's frictional characteristics(8-11). While substantial efforts have gone into the synthesis and characterization of hydrogels, the link between their microstructure and the corresponding tribological response lacked clarity(12-20).

Research on the tribological properties of single network (SN) hydrogels show varying trends depending on the type of hydrogel(12, 21-25). As a function of sliding velocity, dynamic friction follows a non-monotonic trend in general but it strongly depends on the microstructure of the hydrogel(16, 26-28). At slow velocities, friction is thought to originate from adhesive contribution and can either increase, decrease or remain constant depending on microstructure. For e.g. in adhesive hydrogels, Gong's research describes friction arising from the attachment and detachment of the polymer to the counter surface, hence a function of microstructure(21, 29, 30). The model assumes that a transition from the adhesive to viscous regime occurs with an increase in the sliding speed. Attempts have been made to relate this experimental transition velocity with

that expected from de genes scaling theory but fail in quantitative agreement(28). At high velocities, dynamic friction is thought to originate from viscous dissipation. While the model by Gong, associates it to hydrodynamics, where a water film separates the two surfaces. In contrast, other studies have shown either a non-Newtonian behavior(13, 16, 28), or stick-slip (15, 20) both evidence of the influence of the polymer on friction at high velocities. Still, there is a lack of generality and quantitative experimental agreement across literature regarding interpreting and quantifying hydrogels frictional response. Commonalities do exist, such as the significance of the microstructure in dictating the adhesive frictional response of hydrogels and a transition from adhesive to viscous friction. The clear absence of agreement regarding the origin of the friction response, indicates a gap in the fundamental knowledge about hydrogel lubrication, specifically with regards to the hydrogel microstructure. This gap is even more prominent for hydrogels with more complex microstructure, such as in the case for double network hydrogels, which we believe directly, arises from the lack of fundamental knowledge about their microstructure.

Another important tribological response is the static friction, which is the initial threshold force required to commence sliding. In fact, damage of soft tissues in biological tribosystems is often related to static friction or intermittent stiction, also known as stick slip motion. Despite the relevance of static friction in determining the tribological performance and long term integrity of hydrogel-like materials, only a handful of studies explore the static friction of synthetic or biological hydrogels(31-34), while even here the knowledge is quite limited and not well understood.

Based on the current literature we can identify gaps in the fundamental understanding about the frictional dissipation in hydrogels, and in particular the microstructure to property relationships for these materials. This doctoral work was thus motivated to extend the knowledge about the

relation between the frictional response and the microstructure of hydrogels with single and double networks as well as biological hydrogels as the materials of interest. The output of this work is a thorough framework of dynamic and static friction of a multitude of hydrogel-like materials based on their microstructure. The fundamental knowledge derived from this work provides new understanding about biolubrication and brings guidance for the design of functional gels with potential applications in a multitude of research areas, where the processes occurring at the migrating hydrogel interface are of relevance. Furthermore, the protocols developed during this dissertation period are novel and enable investigation of hydrogel-like materials using powerful tools such as the eSFA.

This dissertation has ten chapters. Chapter 1 briefly introduces the background, motivation and the outcomes of this research. Chapter 2 is the literature review. Chapter 3 describes the methodologies developed for microstructural characterization of hydrogels. Chapter 4 introduces the dynamic friction of SN hydrogels with varying microstructure (25) and Chapter 5 summarizes the quantitative viscous-adhesive model developed for the dynamic friction of SN hydrogels. (26). Chapter 6 is on the static friction of SN hydrogels (35). Studies on the tribology and rheology of hydrogel thin films via an extended surface forces apparatus (eSFA) are described in Chapter 7. Chapter 8 is on the modulation of DN hydrogels composition as a means to modulate friction. Chapter 9 explores a real-life extension of this research by studying the biological hydrogels i.e. the articular surface of the cartilage(36). The dissertation is concluded in Chapter 10 with an outlook followed by references and Appendix A.

CHAPTER 2: LITERATURE REVIEW

This chapter briefly summarizes the current state of the art on the mechanical and tribological behavior of hydrogel-like materials. First, we describe the state of the arts for dynamic and static friction of mainly SN hydrogels. Then, existing gaps in the fundamental knowledge around double network hydrogels, their formation and their frictional dissipation are introduced. Finally, a direct implication of this research, the current understanding of the damage pathways of a biological hydrogel, i.e. cartilage preceding the disease Osteoarthritis (OA) is discussed.

2.1. Dynamic friction as a function of load and sliding velocity

Numerous studies have experimentally explored the load and speed dependence of the frictional response of hydrogels and have showed often a deviation from Amonton's law. The reported effects of the load on friction are disparate, ranging from an increase of friction with load(37), a load-independent friction force(38) and even a decrease in friction with increase in load(39, 40), perhaps as a result of the increase in surface conformity. Regarding the influence of the velocity, friction coefficients of poly(vinyl alcohol) hydrogels against a hard and impermeable counter-surface decreased with the sliding velocity (37, 40, 41), while an opposite trend was observed for poly(N-isopropylacrylamide)(39). The different trends of friction with velocity were attributed to the slow dynamics of the polymer. For instance, for poly(N-isopropylacrylamide) hydrogels, long contact times (slow sliding) enable the polymers to disentangle in response to the applied shear, while with increasing velocities, there is no sufficient time for disentanglement to occur and stretching and rupture of the adhesive bonds across the interface occur, thereby causing an increase in the dissipated energy. The poroelastic response of hydrogels has been also associated to velocity-dependent changes in hydrogel friction more recently(19).

Comprehensive experiments by Gong et al. have helped to reconcile the seemingly contradictory velocity-dependence of the frictional response, since they demonstrated the non-monotonic trend of the friction force, first increasing (i.e. velocity-strengthening) and then decreasing (i.e. velocity-weakening) with sliding velocity(22, 27, 29, 30). Furthermore, it was reported that, after a minimum was achieved at a so-called critical velocity V_c, friction increased with velocity, which was associated to elastohydrodynamic lubrication(27). Below the critical velocity V_c, hydrogel friction was described in the context of Schallamach's model for rubber friction.(42) Here, the adhesive friction is originated by the interplay between formation and rupture of adhesive and reversible molecular bonds across the interface, being both thermally activated processes, yet affected by the shear force. According to this model, friction results from the energy dissipated when these bonds are broken. The fluctuation length (ξ) and relaxation times for polymer attachment and detachment were used to describe the adhesive component of friction(30). The so-called adsorption-desorption model used scaling arguments to define the critical velocity, $V_c = k_B T/\eta\xi^2$, based on the relaxation characteristics of the *free* (unconfined) polymer(12, 27), T being the temperature, k_B the Boltzman constant and η the viscosity of the solvent. This model is powerful in *qualitatively* describing many reported experimental results. For example, friction can be modulated by varying the adhesion to the counter-surface, which can be increased through the collapse of the gels in a poor solvent(39, 43), *via* a greater crosslinking degree(12, 44-46) or through changes of the monomer chemical composition(41). Nevertheless, the *quantitative* comparison of the model to experimental results has been very limited(30), and recent works have emphasized the lack of quantitative agreement, including the deviation from the predicted critical velocity, V_c.(17, 28, 47).

Several studies have attributed the increase in hydrogel friction with sliding velocity (above V_c) to hydrodynamic lubrication, thereby presuming the absence of contact between the counter-surfaces, and thus, assuming that hydrogel lubrication is provided by a thin film of aqueous solution (37, 40, 41, 48, 49). The assumption of fluid-film lubrication has been, however, challenged by others (17, 28, 47). Indeed, as for other viscoelastic materials, like rubbers(50), one should expect that the ability to dissipate shear forces via internal damping should contribute to hydrogel friction. While a few works have recognized the relevance of the viscoelastic contribution to friction(51), the pioneering work by Baumberger is noteworthy(16, 17). Here, the increase in friction with sliding velocity was proposed to result from the shear thinning of a hydrogel layer, and an agreement between experiment and model was observed at small contact stresses. Inspired by the scaling relation between microstructure and viscoelastic behavior of hydrogels, the viscous frictional dissipation was described using scaling arguments of the Gaussian (i.e. unconfined) polymer. This work also confirmed the time-dependence (aging) of the static friction via hold-slide-hold experiments, which was associated to the increase of the adhesive bonding strength with contact time. This observation was consistent with the often-observed velocity-weakening friction in experiments (22, 27, 29, 30) and it was attributed to adhesive friction.

Although appreciable consensus exists behind the peculiar dependencies of hydrogel friction on load and velocity, a prediction of the behavior based on hydrogel microstructure and underlying mechanisms is still not possible, which emphasizes the gap in the fundamental knowledge.

2.2. Static friction and contact ageing

In the context of *dry* friction, experimental studies have shown an increase in static friction with the increase of loading time, commonly called *contact ageing*. Adhesion models (52) give

the static friction as the critical shear strength of the interface at the commencement of motion multiplied by the true contact area. Contact ageing has been majorly related to the increase in the true contact area (A_r) with time due to plastic or viscoelastic creep of multiasperity contacts. Strengthening caused by chemical bonding across the interface, e.g. for polymers (52) and silica/silica tribopairs (53), is considered a concomitant process that contributes to contact ageing through the increase in interfacial shear strength (σ_s). If contact ageing occurs, and despite of its origin, the static friction is observed to increase logarithmically with loading time. This logarithmic relation has been found for rocks (54), ceramics (53) and polymer glasses (52).

Based on a handful of precedent studies (31-33, 55, 56), the same two mechanisms have been proposed to be responsible for hydrogel's static friction as for rocks, polymer glasses and ceramics. For instance, Baumberger *et al.* proposed that the increase in static friction at gelatin/glass interfaces with hold time stems from the reconfiguration of the confined polymer chains, which gradually pin to the glass countersurface (56). However, this could not explain the different ageing rates of the investigated hydrogels. Based on confocal microscopy images, it was proposed later that, when the interfacial water between (agar) hydrogel and a glass surface is squeezed-out under static loading, multiple contact junctions gradually form within the apparent contact area (33). A logarithmic increase of static friction with hold time was reported for poly(N-isopropylacrylamide) hydrogels (55). A more complex picture started to emerge from a study of the effect of temperature on the static friction between like-charged hydrogels (31). Here, the static friction was shown to decrease with temperature, and a maximum, not discussed by the authors, appeared at low temperature. The origin of this behavior was loosely attributed to the influence of temperature on the structure of hydration water. While this argument is difficult to rationalize in

our opinion, their experimental finding suggests that the mechanisms underlying hydrogel's static friction are actually more intricate than originally proposed.

2.3. Double-network hydrogels and their challenges

Often hydrogels are proposed as prime candidates for cartilage replacement owing to their structural semblance to biological tissues, their functionality, and biocompatibility[1,2]. One outstanding challenge is to design hydrogels with excellent biomechanical response along with their inherent advantage to reduce wear and friction. In 2003, Gong proposed a solution by creating double network (DN) hydrogels, where the first network (PAMPS) is tightly cross-linked and comprised of a brittle polyelectrolyte, while the second network (PDMAAm) is loosely crosslinked, soft, ductile and neutral [9-12]. These hydrogels had comparable mechanical strength and toughness to the articular cartilage and industrial rubber[4,13], thereby paving the way for viable replacement biomaterials. Double networks are also conceptually appealing since cartilage and other skeletal tissues intrinsically incorporate double networks into their extracellular matrix in order to achieve ordered and dynamic structures and robust mechanical properties.

Multiple network combinations have had success in achieving improved mechanical properties [8,9,14-18]. For instance, DN hydrogels with a physically crosslinked first network such as agarose [14,15,19], collagen [20,21] or alginate[22,23] can eliminate the damage associated with a covalently crosslinked first network. Nakajima et al demonstrated that two different types of networks are possible: truly independent DN gels (t-DN) hydrogels or connective DN hydrogels (c-DN hydrogels)[25]. DN hydrogels with PAMPS as the first network when crosslinked with methylenebisacrylamide (bisAAm) can result in unreacted double bonds of the crosslinker. These double bonds can then react with the second network's prepolymer, resulting in covalent links between the first and the second network and hence termed as the c-DN hydrogels. By rendering

all the unreacted double bonds inert in the first network, the authors were able to synthesize two independent, interpenetrating networks, and hence a truly independent or t-DN hydrogels. They also found that t-DN were stronger than c-DN hydrogels, provided the second network is loosely crosslinked. Several works have shown that the amount of monomer and crosslinker of the second network significantly influences the resulting microstructure and properties of the hydrogel[8,15,16,24,26-29] and that a fine balance is required to achieve extraordinary property enhancements.

Yet, this discovery came with a caveat; Gong's studies noted that to achieve low frictional coefficients with DN hydrogels, a third component had to be added [30]. For example, the friction coefficient provided by PAMPS/PAAm DN hydrogel ranged from 10^{-2} – 10^{-1}, while high lubricity ($\mu \sim 10^{-5}$) was only achieved if a linear, un-crosslinked polymer was imbibed in the DN hydrogel. The authors attributed the low coefficients of friction to the shear of free and highly mobile linear polymer chains at the hydrogel interface. The high friction of DN hydrogels has been observed in multiple other works [18,30]. For instance, PVA/PAAm hydrogels showed friction coefficients as high as ~0.1 – 0.2 in migrating and stationary contacts [28]. Later studies have revealed lower friction coefficients (μ~10-2-10-3) for DN hydrogels comprising of poly-(2-Acrylamido-2-methylpropane sulfonic acid)/poly-(N,N'-dimetyl acrylamide) (PAMPS/PDMAAm) [16] and alginate/PAAm [22], but the underlying mechanisms and the structure-property relationships for enhanced lubricity are almost non-existent. Recently, Bonyadi et al showed that a charged first network could render superlubricity to PAMPS/poly (N-isopropylacrylamide-co-acrylamide) DN hydrogel at low velocities which was associate with a fluid film preventing the contact between the sliding surfaces [31]. Chemical gradients in DN hydrogels can also influence the frictional response [18]. For example, DN hydrogels composed of alginate and PAMPS showed an alginate

rich skin, which could be easily delaminated, revealing a softer hydrogel surface underneath with a friction coefficient ~10^{-2}. The authors contributed the surface heterogeneity to the oxygen inhibited free-radical polymerization and to the diffusion-controlled crosslinking of alginate within the double network.

Even though the effects of changing the composition of first and second networks on hydrogel properties have been investigated, fundamental insight relating the composition to microstructure and the microstructure to property is lacking, thereby limiting property prediction and design optimization. In particular, studies of the kinetic friction of DN hydrogels are still limited [9,16,28,30,32] and only cursory.

2.4. Wear and degradation of biological hydrogels

First, we describe the structure of the articular surface. Articular cartilage (AC) is a load-bearing avascular tissue in synovial joints that provides low-friction motion between the articulating surfaces. The wear-resistant tissue is composed of an extracellular matrix (ECM) with a well-ordered three-dimensional structure, secreted by a small number of embedded chondrocytes cells, and ~70%-80% in weight of imbibed fluid. Early studies recognized that an amorphous (gel-like) surface layer of several microns in thickness -also known as the *lamina splendens* (57, 58)- covers the cartilage's superficial zone. This surface layer has a distinct structure, high water content and is much softer than the underlying cartilage (59). Its composition, however, is still under debate(60) (61, 62). Independently of its composition, there is agreement that this surface amorphous layer helps to maintain a low friction coefficient during boundary lubrication(60).

One of the unresolved questions concerns the origins of damage of such hydrogel-like materials. In particular, pathways to structural damage and wear under shear, leading to diseases such as osteoarthritis (OA) of soft tissues like the cartilage, have still not been convoluted. A

recent finding is that damage in the case of cartilage, generally occurs within the stick-slip (stiction and subsequent bond rupture) regimes of motion and sliding, and is not directly related to the kinetic friction coefficient(34). Using a Surface Forces Apparatus (SFA), it was found that prolonged exposure of cartilage surfaces to stick-slip sliding resulted in a significant increase of surface roughness, indicative of severe morphological changes (damage) of the cartilage surface. Osteoarthritis (OA), a common diseases of the joints, manifests by a depletion of proteoglycans, followed by break down of Type II collagen, mechanical failure and erosion of the articular cartilage(63). There is some evidence for the prevalence of elevated calcium and phosphate contents in cartilage with progression of OA(64). Specifically, with progress from grade 1 to 3, the calcium content has been seen to increase by a factor of ~5. Recent works have also shown that the increased concentration in calcium-phosphate complexes in articular cartilage of early-stage OA(65) is responsible for cellular dysfunction.(65, 66) A recent review reports that deposition of calcium pyrophosphate and basic calcium phosphate crystals is found in 100% of cartilage samples from patients with OA undergoing joint replacement surgery(67). For crystallization to happen, the interstitial fluid must be supersaturated, thereby also supporting the exposure to elevated calcium and phosphate concentrations. It is also conceivable that because proteoglycans are lost during OA, less calcium can be stored in the tissue and more becomes available at the interface. It is known that calcium can bind to negatively charged carboxylic groups of amino acids in collagen (68) and to the glycosaminoglycans, *e.g.* of aggrecan (69). Furthermore, due to its bivalency, calcium ions can crosslink molecules like collagen(64), aggrecan(69), hyaluronan (70) and cartilage oligomeric matrix protein (71); a phenomenon commonly known as “ionic bridging”. While fluctuations of calcium concentrations have been

associated with structural and mechanical changes of (dehydrated) cartilage(72, 73), the implications of calcium concentration to the hydrated cartilage surface are very limited.

CHAPTER 3: THE MICROSTRUCTURAL CHARACTERIZATION OF HYDROGELS

We introduced briefly the structural hierarchy earlier w.r.t the cartilage in Chapter 1 and 2. Clearly, the specific functionalities such as high lubricity and hydration depends on the microstructure of the surface layer. Hydrogels, essentially polymeric networks imbibed with large amounts of water can be characterized via a mesh size, ξ. According to the scaling theory, in a thermodynamically favorable solvent, the characteristic mesh size of the network scales with the polymer volume fraction ν by an exponent n, where $n = 0.75$ in the semi-dilute regime(74). This characteristic size, also known as the correlation length, or mesh size, ξ defines the distance between crosslinks and hence can serve as a metric to determine a multitude of gel's characteristics, such as the permeability, polymer relaxation times, and the elastic modulus, as listed in Table 3.1. In equilibrium, the relaxation time of the polymer chains in the network can be described by the mesh size, and the imbibing fluid's viscosity as shown here. Furthermore, the osmotic pressure of the hydrogel network is also equal to the elastic plateau modulus of the hydrogels in equilibrium swollen state. Pressures above the osmotic pressure will cause interstitial fluid to flow. Depending on these characteristic properties, the mechanical and tribological response can vary tremendously across hydrogels. Hence, characterization of the microstructure is the first step to understand hydrogel tribology.

Owing to the challenges of visualizing the hydrogel's pristine microstructure through classical microscopy, over the course of this research, different techniques i.e. dynamic light scattering (DLS) and atomic force microscopy (AFM) were employed to understand the microstructure and estimate the mesh size of the hydrogels. The focus of these investigations was to evaluate the feasibility of DLS for the characterization of the mesh size by comparison to our

own SEM results and SAXS results in literature while also investigate the structural hierarchy, if present.

Table 3.1. Characteristic properties of hydrogels: mesh size (ξ), polymer relaxation time (τ_A), osmotic pressure (Π) and poroelastic relaxation time (τ_w).

Property	Equation	Ref.
Mesh Size ($\boldsymbol{\xi}$)	$\xi = \phi^{-\frac{\nu}{3\nu-1}}$ where ϕ is the polymer volume fraction, and in semi-dilute regime, $\nu = 3/5$ (good solvent) ; $\nu = 1/2$ (θ-solvent)	[13]
Polymer relaxation time (τ_A)	$\tau_A \sim \eta_s \xi^3 / k_B T$ where η_s is the solvent viscosity, k_B is the Boltzmann constant, and T the temperature	[13]
Osmotic pressure ($\boldsymbol{\Pi}$)	$\Pi \sim G' \sim k_B T / \xi^3$ where G′ is the shear storage modulus.	[13, 14]
Poroelastic relaxation time (τ_w)	$\tau_w = \frac{6\eta_s \pi a^2}{P\xi^2}$ where a is the contact radius and P the pressure	[15]

3.1. Materials and methods

3.1.1. Materials

Poyl(acrylamide) (PAAm) hydrogels with varying monomer and crosslinking concentrations, which are chemically crosslinked hydrogels. PAAm hydrogels were prepared with 4.4, 6.4 and 12.4 wt% of the acrylamide monomer and an increasing crosslinker concentration, specifically, 0.11, 0.30 and 0.74 wt% of bisacrylamide, following the protocol in ref.80. We refer to these hydrogels as 4%, 6% and 12% PAAm hydrogels, in the following. Physically-crosslinked agarose hydrogels, also with a single network, were synthesized with agarose concentrations ranging between 0.5 and 2 wt.%.

3.1.2. Hydrogel preparation

All experiments were conducted on PAAm hydrogels. Acrylamide 40% w/v solution (monomer), N.N'-methylene bis(acrylamide) (crosslinker), ammonium persulfate (initiator) and tetramethylethylenediamine (TEMED) (accelerator) were purchased from Sigma-Aldrich (USA). Solutions of acrylamide (4.4, 6.4 and 12.4 wt%) and bis-acrylamide (0.11, 0.30 and 0.74 wt%) were prepared in DI water. Each solution was degassed for 15 minutes prior to the addition of 1/100 and 1/1000 of the initiator and the accelerator, respectively. After this, fixed amount of the solution was quickly pipetted onto a hydrophobic glass slide and the droplet was covered with a hydrophilic coverslip. Gelation of the sandwiched solution was allowed to proceed for 30 minutes, after which the coverslip with the hydrogel was removed from the hydrophobic glass slide and rinsed in DI water to remove any excess of solution. The final thickness of the hydrogels was ~2 mm. The hydrogel samples were stored in DI water at 4 ºC for one day prior to any testing.

To render the glass surface hydrophobic, glass slides (25 mm x 75 mm) were first rinsed liberally with dichlorodimethylsilane. The solution was left on the slide for 1 minute, before rinsing copiously with DI water, followed by subsequent drying. Coverslips were made hydrophilic to ensure the grafting of the hydrogels to their surface. Here, the coverslips were cleaned by UV-O3 and then covered with a film of 0.1 M NaOH solution, which was allowed to evaporate evenly from the surface. Next, the coverslips were covered with 200 μL of 3-aminopropyltriethoxysilane (APTES) for 5 minutes, and then rinsed with DI water. Finally, the coverslips were immersed in a 0.5% (v/v) solution of glutaraldehyde in phosphate-buffered saline solution for half an hour with the NaOH and APTES treated surface facing up. Following a final rinse with DI water, the coverslips were ready to be used. All chemicals were obtained from Sigma Aldrich, USA.

To prepare hydrogel samples for Atomic Force Microscopy (AFM) measurements, 40 µl of this solution were quickly pipetted on the hydrophobic glass slide, and then sandwiched between glass slide and the silane-treated coverslip. After 30 minutes, the coverslips (carrying the hydrogels) were removed from the hydrophobic glass slides, rinsed with DI water, and stored in DI water at 4°C for 1 day. To prepare hydrogel samples for Dynamic Light Scattering (DLS), 750 µl of solution were pipetted into a microcuvette and also allowed to gel for 1 day. After gelation for 1 day, all hydrogels were immersed in DI water. For imaging with a Scanning Electron Microscopy (SEM), thicker hydrogels (3-4 mm) were prepared in circular hydrophobic glass molds (diameter = 25 mm). The hydrophobic functionalization of the glass molds was carried out following the procedure described above.

3.1.3. Scanning Electron Microscopy (SEM)

Scanning electron microscope (Hitachi S4700, High resolution SEM, USA) was used to image the hydrogel network after their critical drying. PAAm hydrogels were dehydrated progressively by successive immersions of 1 hour in a series of ethanol aqueous solutions (30%, 50%, 70%, 90% and 100%) and finally they were kept in 100% ethanol for 12 hours. The samples were then dried using a critical point dryer (Tousimis, Autosamdri-931), where the ethanol was exchanged with liquid carbon dioxide; they were held at the supercritical point of CO_2 for 2 minutes, followed by a slow purge. Prior to imaging, the dried hydrogels were coated with Au/Pd for 30 seconds. A voltage of 10 kV and a current of 10 µA were used while the working distance was maintained at ~12 mm.

3.1.4. Dynamic Light Scattering

Dynamic light scattering Zetasizer 3000 (Malvern, USA) was used to conduct dynamic light scattering (DLS) measurements on PAAm SN hydrogels at a fixed wavelength λ of 632 nm

and a scattering angle θ of 90°. Single exponential decay functions were fit to the autocorrelation functions according to $g^2(\tau) - 1 \sim A \cdot \exp(-\Gamma\tau)^2$ to extract the characteristic decay rate **Γ**. Applying Tanaka's model(75), the decay rate was used to estimate the correlation length of the network via:

$$D_c = \frac{\Gamma}{q^2} \quad \text{(Eq 3.1)}$$

$$\xi_c = \frac{k_B T}{6\pi\eta D_c} \quad \text{(Eq 3.2)}$$

where D_c is the cooperative diffusion coefficient, q^2 is the wave vector, ξ_c is the correlation length and η is the solvent viscosity. For ergodic and homogeneous systems (no static scattering), a single correlation length, which typically represents (liquid-like) fluctuations of the polymer, *i.e.*, the distance between crosslinks, is determined. While we do not observe static scattering for the PAAm SN hydrogels, it did occur for DN hydrogels and will be discussed briefly in Chapter 7. Hydrogels with static scattering (e.g. due to inhomogeneities) require elaborated spatial-dependent DLS measurement and analysis,(76-78) which is out of the scope of the present collection of w

3.1.5. Atomic Force Microscopy (AFM)

Indentation experiments were conducted by colloidal probe AFM using a JPK Nanowizard Ultra (JPK Instruments, Berlin, Germany). A silica sphere with a diameter of ~ 10μm (Microspheres-Nanospheres, USA) was attached to the end of a tipless cantilever (nominal spring constant = 0.4 N/m, CSC37-No Al/tipless, Mikromash, USA) using epoxy glue (JB-Weld, Sulphur Springs, TX, USA). The AFM cantilevers were cleaned in an ethanol (Sigma-Aldrich, USA) bath followed by a UV ozone chamber for at least 30 minutes before each experiment.

The Hertz contact model was fit to the approach curves in a "piecewise" manner, as described in detail in refs (35, 79) to extract elastic modulus as a function of indentation depth using the following equation:

$$F = \frac{4}{3} E^* R^{1/2} h^{3/2} \quad \text{(Eq 3.3)}$$

where R is the radius of the colloid, E* is the contact modulus, $1/E^* = (1 - \upsilon_{sample}^2)/E$, E is the elastic modulus of the sample and ν its Poisson's ratio (~ 0.45 for PAAm hydrogels(80)). To determine the elastic modulus of PAAm hydrogels within Hertzian validity, a/R (a is the contact radius, $a = \sqrt{R.d}$) and d/h ratios of ~ 0.35 and 0.005, respectively, were maintained, indicating small deformation and no substrate effects(81), and justifying the use of the Hertz model. The elastic moduli of the hydrogels were determined fitting Equation (3), starting with the smallest indentation. The fit was concluded once deviation from the experimental curve was recorded, after which the next fit started. This process resulted in the measurement of at least two moduli, corresponding to the surface and the bulk of the PAAm hydrogels.

3.2. Results and discussion

3.2.1. Visualizing the pore structure via SEM

Figure 3.1 shows SEM images of PAAm hydrogels with an acrylamide concentration of 4%, 6% and 12% at two different magnifications. A small but visible decrease of the hydrogel volume occurred upon critical drying of all hydrogels, which means that the visualized network structure might differ from that of the water saturated hydrogels. Nevertheless, the images agree well with previous reports(82). Long and entangled polyamide strands between crosslinks are observed in the images of 4%-PAAm hydrogels. Defects (or large pores) in these hydrogels are shown in **Figure** A2. As the acrylamide concentration increases, the mesh size decreases and the length of the polymer strands between crosslinkers becomes smaller. Even though the PAAM-12% hydrogels undergo a more significant collapse upon drying (**Figure** 3.1c, see black arrow), some regions retain the original architecture of the hydrogel and have been used for the determination of the mesh size distribution. While the large pores in PAAm-12% and PAAm-6% hydrogels are of similar size (79.6 and 90 nm, respectively), the smaller pores have a smaller diameter in PAAm-12% hydrogels compared to PAAm-6% hydrogels (32 and 49 nm). The largest

pore size (220 nm) is observed in 4%-PAAm hydrogels, demonstrating the effect of smaller crosslinking degree.

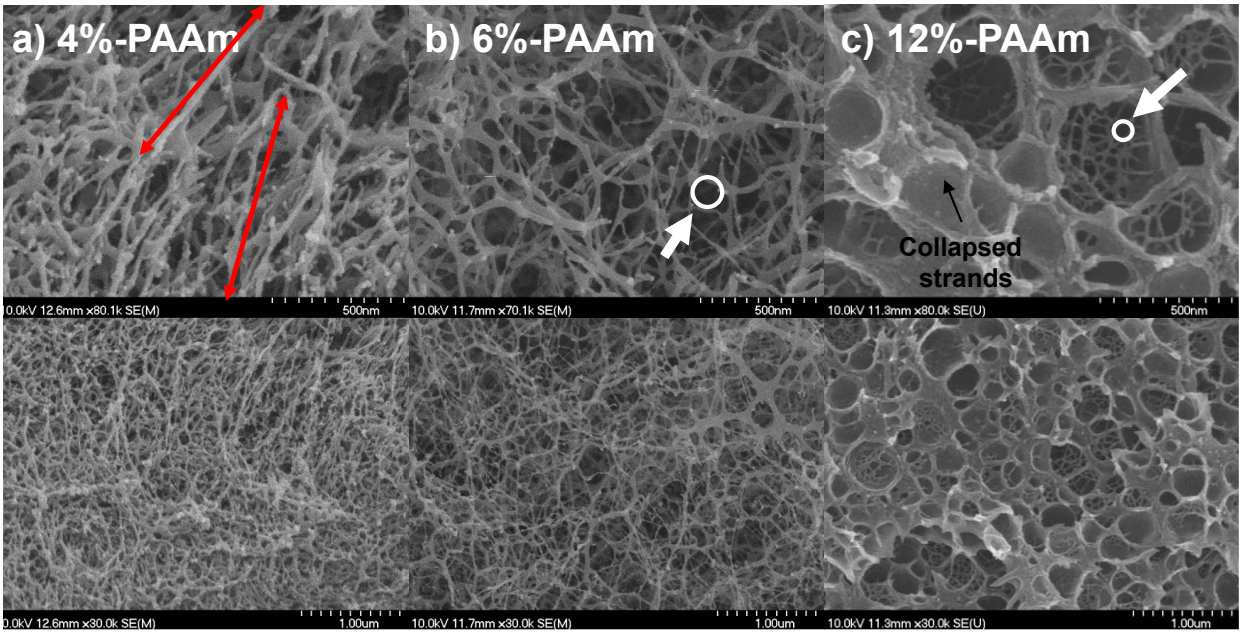

Figure 3.1 SEM Pictures of PAAm-hydrogels with acrylamide concentrations of a) 4 wt%, b) 6 wt% and c) 12 wt% after critical drying. The arrows in a) point to the length of network strands between two crosslinks; the circles in b) and c) show the smallest pore size.

3.2.2. Dynamic Light Scattering

We have dedicated extensive efforts to study different types of hydrogels by DLS. While this Chapter only includes results obtained on the PAAm hydrogels, mesh sizes estimated by DLS are also going to be mentioned in Chapter 7 for the DN hydrogels. Figure 3.2 shows representative DLS results (the autocorrelation function) for the three polyacrylamide hydrogels (4%, 6% and 12% hydrogels). At least six samples were investigated for each polymer concentration. The initial amplitude of the autocorrelation function decreased below 1 with increased with polymer concentrations, which is characteristics of gels, while this value is ~1 for polymer solutions. A single relaxation decay mode is shown for the three polyacrylamide hydrogels. Therefore, the autocorrelation functions were fit to single exponential decay functions [(75)]. The lines in Figure 3.2 shows the fits to the experimental results. As evidenced in the three figures, there is a deviation

of the fits from the experimental results at the longest decay times. It seems that a second plateau is achieved, which could be related to the presence of inhomogeneities in the chemically crosslinked hydrogels. Structural inhomogeneities, resulting either from crosslinking or from molecular associations, are observed in both chemically and physically crosslinked hydrogels, the characteristic size of which is generally much larger than the length scale defining the osmotic properties (83, 84). Although our instrument does not allow us investigating the second (slow) relaxation mode, and providing details about the inhomogeneities, this analysis ensures that the correlation length corresponding to the fast relaxation mode is not influenced by such inhomogeneities, but it is the de Gennes correlation length.

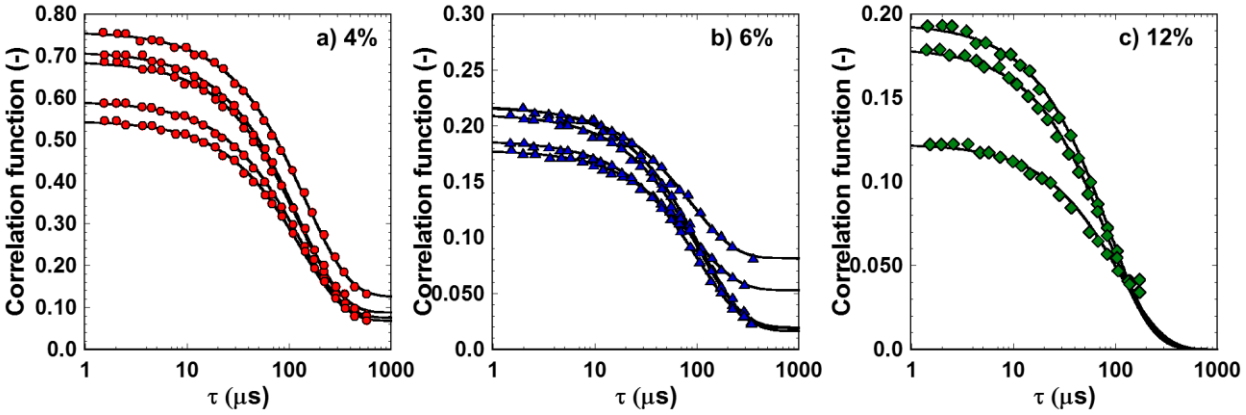

Figure 3.2 Correlation functions obtained from dynamic light scattering measurements for a) 4% PAAm, b) 6% PAAm and c) 12% PAAm hydrogels. The black lines show fits to single exponential decays $\boldsymbol{g^{(2)}(\tau) - 1 \sim A \cdot exp(-\Gamma\tau)}$, where $\boldsymbol{g^{(2)}(\tau)}$ is the correlation function, $\boldsymbol{\Gamma}$ is a decay rate and $\boldsymbol{\tau}$ is the decay time. A cooperative diffusion coefficient ($\boldsymbol{D_c}$) is calculated as $\boldsymbol{D_c = \Gamma/q^2}$, where $\boldsymbol{q}$ is the scattering vector scattering vector $\boldsymbol{q = \left(\frac{4\pi n}{\lambda}\right) \sin\left(\frac{\theta}{2}\right)}$, from which a correlation length, $\boldsymbol{\xi_c = k_B T / 6\pi\eta D_c}$, can be calculated, where $\boldsymbol{k_B}$ is the Boltzman constant, $\boldsymbol{T}$ the temperature, and $\boldsymbol{\eta}$ the solvent viscosity (~1mPa.s)

We obtained ξ_c as 13.8+/-0.5, 10.1+/-0.2 and 7+/-0.4 nm for 4, 6 and 12% hydrogels with this analysis. These values are shown in Figure 3.3 as a function of the monomer concentration for 4%, 6% and 12% hydrogels (4.5, 6.4 and 12.4 wt% acrylamide). There is a deviation from the expected scaling relationship: the exponent is -0.65, while it should be -0.75 for a good solvent. This deviation has been reported previously(85, 86) and is associated to the fact that the osmotic

pressure of the polymer solution is not equal to that of the hydrogel due to hydrogel's finite elasticity(85, 86). Furthermore, a change of the concentration regime due to dehydration during the DLS measurements samples might also explain this deviation.

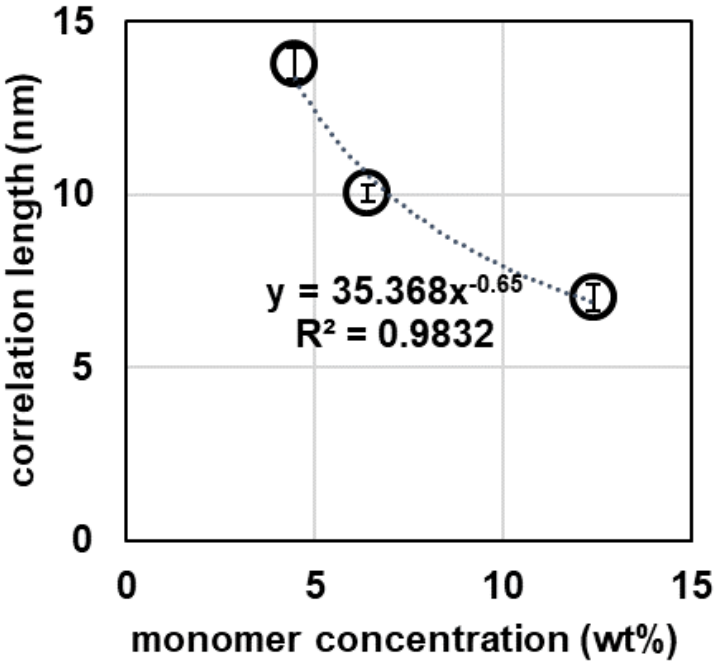

Figure 3.3 The correlation length corresponding to the cooperative diffusion as a function of the monomer concentration. The dotted line shows fit to a power law, where the characteristic exponent is -0.65.

We have also found extensive work that demonstrates the good agreement between SAXS or SANS with DLS (87-89). One such work collected SAXS data for 10 h per sample on a 2D wire detector with 1024 x 1024 pixels. The 2D S(q) scattering spectra were integrated along the azimuthal direction to produce 1D curves for a range of compositions, specifically from 3.75 to 17.5% PAAm. By varying the composition and fitting the spectra with Lorentzian line-shapes of the $form\, S(q) = 1/\,(q\text{^}2 + \Gamma\text{^}2)$, they determined the correlation length from ξ=1/Γ. With increasing polymer content, they observed a broadening shoulder corresponding to an increase in the Lorentzian width, Γ, and a reduction in correlation length from 9.4 nm to 1.3 nm. Their data

also shows that at low q-number there is a deviation from the Lorentzian function (an excess of intensity). This can also be attributed to the presence of large inhomogeneities related to the crosslinking process, which is consistent with our DLS measurements. Furthermore, the concentration of monomer in 4% and 12% PAAm hydrogels is close to two of the investigated hydrogels, but the hydrogels deviate in the crosslinker concentration. Note that DLS gives larger mesh size for the hydrogels compared to SAXS. Nevertheless, the hydrogels were prepared in different labs and with different crosslinker concentrations.

To evaluate its precision in determining the mesh size and we have also conducted DLS studies on other hydrogels such as the physically crosslinked agarose and have found good agreement with literature(90), as well as on more complex microstructures such as the double networks. The latter is discussed in Chapter 8. As this method does not require any drying, we believe it is an accurate way of determining the equilibrium *bulk* microstructure of the hydrogels. We have also investigated the mesh size of 6% and 12% hydrogels as a function of temperature (not shown in this dissertation). Although the influence of the temperature was small, it was reproducibly non-monotonic, and a peak at ~22 °C was observed for both hydrogels. According to literature, the solubility of polyacrylamide in water decreases above 25 °C due to the promoted hydrophobic interaction, and hence, the decrease in the mesh size reflects this decrease in solubility and in swelling. This further validates DLS as a powerful tool to characterize the hydrogels' mesh size.

3.2.3. Atomic Force Microscopy

Representative piecewise Hertzian fits to the approach portion of the force curves obtained on 4, 6 and 12% PAAm hydrogels are shown in Figure 3.4. This yields a surface layer thickness of 640 ± 75, 330 ± 200, and 250 ± 92 nm for 4, 6, and 9% hydrogels, respectively, with an elastic

modulus of only ~335 ± 120, 455 ± 139, and 482 ± 176 Pa. The elastic modulus increases gradually with depth and a modulus equal to 1.05 ± 0.08, 8.7 ± 0.4, and 16.5 ± 3.8 kPa is achieved at depths of 640 ± 75, 620 ± 92, and 467 ± 27 nm for 4, 6, and 9% hydrogels, respectively, which does not vary further with indentation depth.

Hence, with the AFM indentation measurements, a surface comprising of soft, lightly crosslinked brush-like layer ranging from 640 to 330 nm in thickness was identified where the elastic moduli were significantly lower than the bulk moduli.

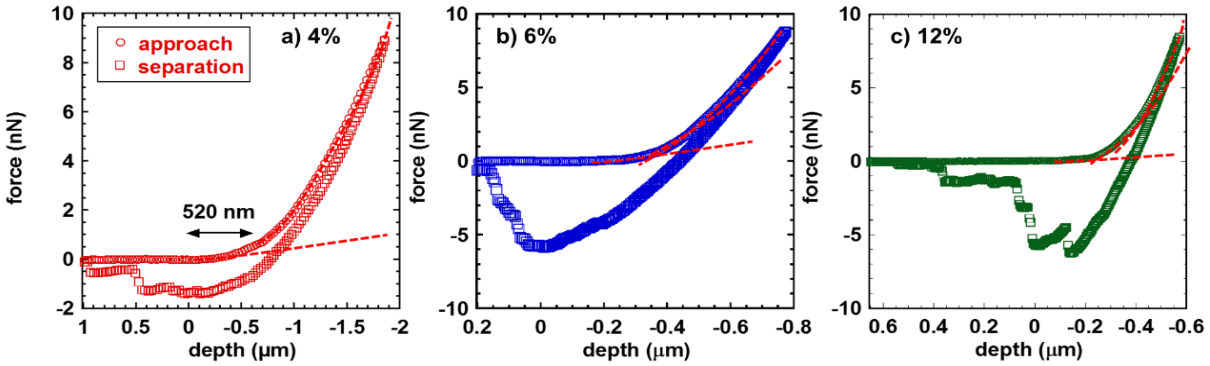

Figure 3.4 Representative force indentation curves obtained on the three hydrogels. Circles show approach and squares show retraction of the colloid tip. Red dashed lines show piecewise fits to the indentation depth according to the Hertz contact model (equation 3).

3.3. Conclusions

Hydrogel's properties rely on the mesh size or mesh size distribution, and hence, we aimed to provide a simple and accurate method for microstructural characterization of hydrogels. Characterization of hydrogels' microstructure via SEM is quite common, however it required the critical drying of the hydrogels and we found that critically drying the hydrogels leads to a significant change of the microstructure. In contrast, we show that scaling laws can be applied to the measurements obtained from dynamic light scattering and the results obtained from this analysis are comparable to measurements done on similar hydrogels with SAXS. Hence, DLS is

an appropriate technique to characterize the bulk mesh size of hydrogels. Moreover, the correlation function may also be used to identify inhomogeneities of the network via static scattering or additional structural (fluctuation) lengths of the polymer network via multiple relaxation modes.

With AFM microindentation, we further saw a gradient in the crosslinking and hence microstructure of the hydrogels. We found that the elastic modulus changed as a function of the indentation depth from 1-8 kPa. This is in agreement with recent publications where a crosslinking gradient exists as a function of the hydrogel's depth when synthesized against a hydrophobic mold (91). Furthermore, this also revealed a brush-like surface on the hydrogels, with brush lengths ranging in 100s of nanometers for the three different crosslinking densities at room temperature. This is an important finding as it helped us to understand and quantify the structural lengths we were probing in tribological measurements.

The work described in this chapter is published as the microstructural characterization sections for Chapters 4 and 5. The techniques mentioned in this chapter are also employed in Chapters 7 and 8 for characterization of double network hydrogels and biological hydrogels, respectively.

CHAPTER 4: UNDERSTANDING THE EFFECT OF MICROSTRUCTURE ON DYNAMIC FRICTION OF SINGLE NETWORK HYDROGELS

In this chapter, we have studied the frictional characteristics of hydrogels with varying acrylamide and crosslinker concentrations by colloidal probe lateral force microscopy as a function of load and speed, while the stick-slip response has been comprehensively analyzed by statistical tools. The results are first discussed in light of available models for hydrogel lubrication, which are then extended to account for the observed phenomena.

4.1. Materials and Methods

PAAm hydrogels were prepared with 4.4, 6.4 and 12.4 wt% of the acrylamide monomer and an increasing crosslinker concentration, specifically, 0.11, 0.30 and 0.74 wt% of bis-acrylamide. These hydrogels are referred to as as 4%, 6% and 12% PAAm hydrogels, in the following chapter. Detailed synthesis is already provided in Chapter 3.

4.1.1. Indentation measurements

Indentation measurements were performed on each hydrogel sample at an approach/retraction velocity of 2 μm/s at room temperature just before the friction measurements. At least ten measurements were carried out per loading condition and sample. The JKR model (92) was fit to the indentation force-depth curves upon retraction to determine the elastic modulus, the contact radius and the interfacial energy. Following equations were used for the fits:

$$h = h_0 + \frac{a^2}{3R} + \frac{F}{2aE^*} \qquad \text{(Eq 4.1)}$$

$$a^3 = \frac{3R}{(4E^*)}\left(F + 3\pi\gamma R + (6\pi\gamma RF + (3\pi\gamma R)^2)^{\frac{1}{2}}\right) \qquad \text{(Eq 4.2)}$$

where F is the indentation force, h the indentation depth, h_o the contact point, R the colloid radius, a the contact radius, γ the surface energy, and E^* the contact modulus defined as $\frac{1}{E^*} = \left(\frac{1-\nu_{gel}^2}{E_{gel}}\right) \Big/ \left(\frac{1-\nu_{sil}^2}{E_{sil}}\right)$; here, E_{gel} is the elastic modulus of the hydrogel, E_{sil} is the elastic modulus of the silica colloid (72.2 GPa (93)), and ν is the Poisson's ratio of the hydrogel ($\nu_{gel} = 0.45$) and silica colloid ($\nu_{sil} = 0.168$), respectively.

Three fitting parameters (h_0, E^* and γ) were determined from the fit of Eqns. 1-2 to the experimental data *via* a least squared curve fitting algorithm built in MATLAB. The retraction curve was fit from the maximum indentation depth to the minimum force, which is defined as the pull-off force (F_{adh}).

4.1.2. Stick-Slip Analysis

To quantify the stick-slip, the lateral force drops Δf during slip were calculated for each applied load and speed by using the statistical software R version 3.4.0 for data ingestion, preprocessing and analytics. A spatial resolution of 512 over a sliding distance of 10 μm was selected and no smoothing was applied. The cutoff for the force drops was determined on lateral force loops measured with the colloid far away from the surface (no contact), which corresponds to the noise of the instrument and is ~0.06 nN. At least ten lateral force loops were analyzed per sliding condition on each single hydrogel. Multimodal Gaussian distributions were fitted to the slip histograms. Mean value, variance and frequency of each mode were compared in bubble diagrams.

4.2. Results

4.2.1. AFM-Indentation

The elastic moduli and adhesion energies of the prepared hydrogels were measured by AFM indentation with a silica colloidal probe. **Figure** A2 shows an increase in the elastic modulus (2.2 ± 0.9, 6.6 ± 2.2 and 30.3 ± 9.7 kPa) with increase in polymer concentration (4%-PAAm, 6%-PAAm and 12%-PAAm hydrogels); we note that the average values of the elastic moduli (for each concentration) were calculated by averaging the mean elastic moduli obtained from each indentation map, while the standard deviation was determined for the mean elastic moduli. The high variability of the hydrogel elastic modulus, especially at high crosslinking degrees, has been reported before for PAAm hydrogels and attributed, among others, to the formation of highly crosslinked clusters, causing the global network to be more inhomogeneous and to soften(94). Further, there is a significant influence of the hydrogel network on the adhesion energy. **Figure** A2 shows that the surface energy (adhesion energy normalized by the JKR contact area) increases with acrylamide concentration, indicating that the main contribution to the adhesion energy is attributed to polymer-colloid interactions.

4.2.2. Load-dependence of friction force

Figure 4.1 shows the friction force as a function of normal load for 4%-PAAm, 6%- PAAm and 12%-PAAm hydrogels, thereby illustrating results for samples with different elastic moduli: 1.1 kPa for 4%-PAAm, 3.8 kPa for 6%-PAAm and 15.5 kPa for 12%-PAAm hydrogels are shown in **Figure** 4.1 a, and 3.5 kPa for 4%-PAAm, 5.8 kPa for 6%-PAAm and 27 kPa for 12%-PAAm hydrogels are depicted in **Figure** 4.1 b. Despite the pronounced changes in elastic moduli, the changes in the load-dependent friction force are thus small, except for the softest hydrogels, where a plateau, and even a decrease in the friction force, was observed above loads ~50 nN in some

occasions; an example is shown in Figure 4.1 a (see arrow). As discussed later, the origin for this behavior is the extensive deformation of 4%-PAAm hydrogels and pile-up effect upon high normal loads, which partially hinders sliding and induces an apparent decrease in the measured friction force. This was never observed in 6%-PAAm and 12%-PAAm hydrogels.

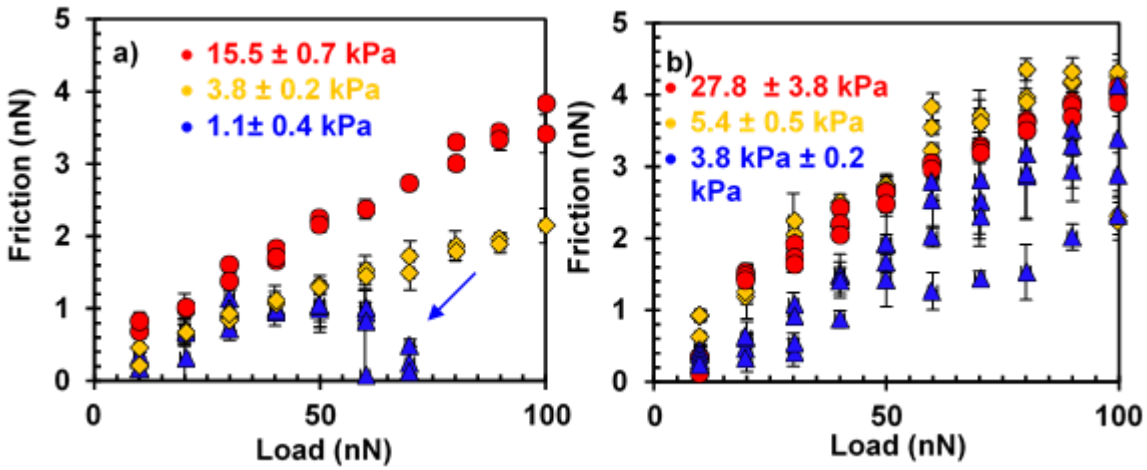

Figure 4.1 Friction vs. normal load for 4%-PAAm (blue triangles), 6%-PAAm (yellow diamonds) and 12%-PAAm (red circles) hydrogels. The diagrams a) and b) demonstrate that the elastic modulus has a small influence on the load-dependent friction force, except for 4%-PAAm hydrogels, where deformation and pile-up effects of very soft hydrogels can cause an apparent decrease in friction (see arrow). Friction force measurements were conducted at a sliding speed of 2 μm/s and a sliding length of 10 μm.

4.2.3. Speed-dependence of friction force

Representative results of the speed-dependent friction force under two selected normal loads (5 and 50 nN) are shown in **Figure** 4.3 for a) 4%-PAAm, b) 6%-PAAm and c) 12%-PAAm hydrogels, respectively. No clear trend of the friction force with polymer concentration was observed. Importantly, an initial decrease in friction was typically observed for all hydrogels at both 5 and 50 nN below a transition speed (labeled as V^*), beyond which friction increased with speed. The transition speed, V^*, was found to augment with increase in polymer concentration, which caused the regime of increasing friction force with speed to be less obvious for the hydrogels

with the highest polymer concentrations under the selected conditions (**Figure** 4.2); in fact, this regime was occasionally not attained by 12%-PAAm hydrogels under an applied load of 50 nN.

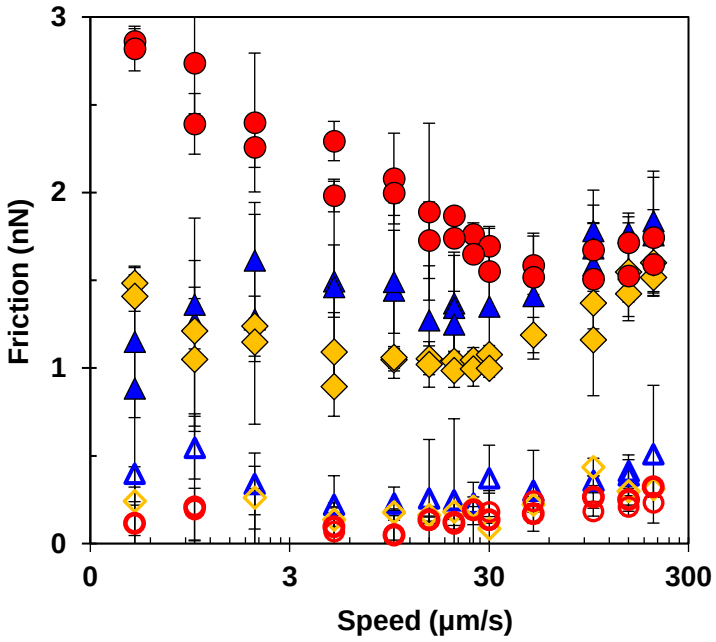

Figure 4.2 Representative speed-dependent friction force for 4%-PAAm (1.84 kPa, triangles), 6%-PAAm (3.8 kPa, diamonds) and 12%-PAAm (15.5 kPa, circles) hydrogels at normal loads of 5 nN (open symbols) and 50 nN (filled symbols). The sliding speeds range from 0.5 µm/s to 200 µm/s and the scan length was fixed at 10 µm.

Figure 4.3 shows representative lateral force loops for the three hydrogels at selected conditions: 5 nN at a) low (1 µm/s, below V*) and b) high (100 µm/s, above V*) speed, and c-d) at 50 nN at the same speeds. These loops are generated when the AFM colloid slides on the hydrogel surface 10 µm to the right (trace) and to the left (retrace). An increase in the width loop clearly occurs when the applied load is augmented (compare c with e), which indicates the increase in friction; note the different scale of the Y-axis selected in each diagram.

The loops measured on 4%-PAAm hydrogels at high loads show occasionally a very pronounced tilt (Figure 4.3 e) that deviates from the theoretical lateral force loop (Figure 4.3 b, full line). In fact, this “tilt” phenomenon was recently investigated in detail for polymer brushes

(95) and it is caused by extensive deformation of soft films: the tip indents the hydrogel and pushes material to the right or to the left (Figure 4.3 a), which causes the hydrogel to pile-up and (partially) hinders sliding. This is important because, as demonstrated in ref. (95), extensive deformation can cause a remarkable underestimation of the friction force. In fact, the plateau that was sometimes observed in the load-dependent friction force curves for 4%-PAAm hydrogels (see arrow in **Figure** 4.1 a) coincides with the occurrence of the tilt of the loops, and hence, it is attributed to partial sliding due to hydrogel deformation and pile-up. **Figure** 4.3 b illustrates the possible types of lateral force loops during partial sliding (dash line) and no sliding (round dot line) due to deformation and pile-up. There are possibilities to avoid this phenomenon, e.g. using a larger colloid to decrease the pressure. However, larger silica colloids are very rough, which dramatically affects our measurements, in particular, the stick-slip described in the following section. Since deformation and pile-up only affected occasionally the friction force measurements conducted on 4%-PAAm hydrogels at the highest loads (>50 nN), these data have been removed from the following analysis to avoid an underestimation of the friction force.

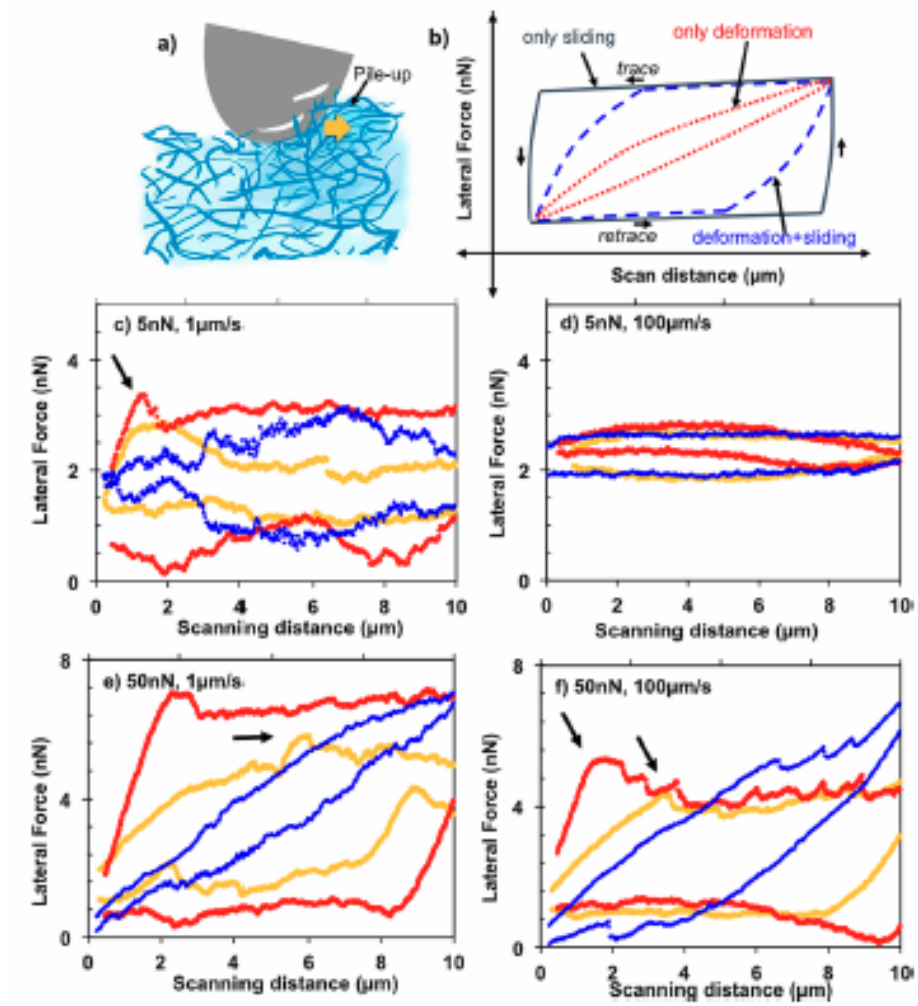

Figure 4.3 Cartoon showing a) deformation of hydrogel and pile-up while pulling the colloid laterally before sliding occurs, and b) characteristic lateral force loops upon sliding (full line), deformation and sliding (dash line) and only deformation with no sliding (round dot line). The friction force is calculated as the half of the loop width during sliding, which in case of extensive deformation can cause a tremendous underestimation of the friction force, Lateral force loops representative for 4%-PAAm (blue), 6%-PAAm (yellow) and 12%-PAAm (red) hydrogels at c) 5 nN and 1μm/s, d) 5 nN and 100 μm/s, e) 50 nN and 1 μm/s and f) 50 nN and 100 μm/s. Their respective Young's moduli are 2.5 ± 0.1, 9.3 ± 0.1 and 39.2 ± 3.5 kPa. Note that the Y-axis has a different scale in each diagram; the arrow in each diagram gives a lateral force of 5 nN. Extensive deformation is only shown in e-f) for 4%-PAAm hydrogels.

4.2.4. Stick-slip analysis

The friction loops reflect the intermittent (sawtooth-like) motion of the colloid, which is reminiscent of an irregular stick-slip (see e.g. **Figures** 4.3 c, 4.3 e, 4.3 f). To quantitatively evaluate the differences in stick-slip at the investigated sliding conditions, the lateral force drops, Δf, during a slip were calculated and bimodal Gaussian distributions were fitted to the. Average and standard deviations of each mode (or peak) and its probability were compared via bubble diagrams (Figure 4.4). We only show the bubble diagrams for the largest peak, for which the major differences were observed. The friction characteristics of the three hydrogels were investigated with colloids of different roughness (RMS ranging from 5 to 10 nm within the area of contact). It is important to note that the roughness enhanced the force drops during slip. Therefore, separate bubble diagrams

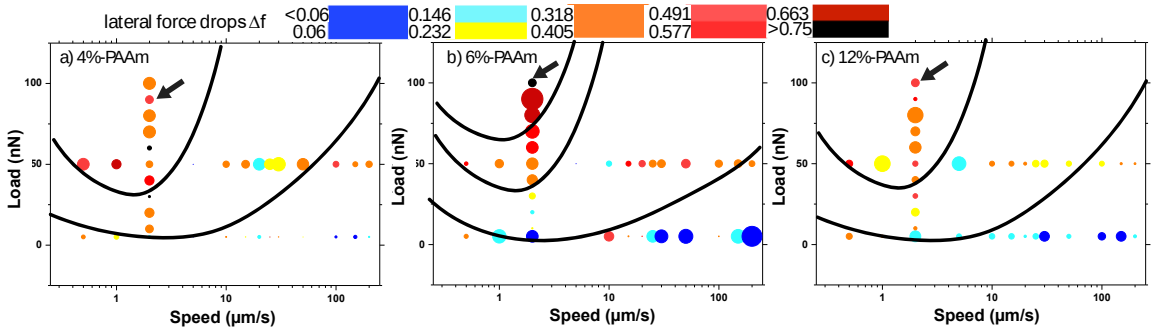

Figure 4.4 Bubble charts for the lateral force drop during slip ($\Delta \boldsymbol{f}$) for 4%-PAAm (a), 6%-PAAm (b) and 12%-PAAm (c) hydrogels as a function of applied load and sliding speed. The color represents the magnitude of the stress drop, while the size of the bubble represents the frequency of occurrence. The lines are boundaries between regions of high (red-orange), medium (yellow) and low (blue) stick-slip events. At the highest normal loads (~100 nN) stick-slip seems to be reduced, especially on 4%-PAAm hydrogels (see arrows), likely due to deformation and pile-up.

Irregular sliding (with associated stress drops larger than 0.06 nN) was observed at most of the conditions on all hydrogels, which reflects the direct interaction between the polymer chains and the colloid surface. Upon an applied load of and above ~20 nN, stick-slip was substantial. Nevertheless, by increasing the speed, the frequency of the stick-slip events and also the magnitude

of the stress drop decreased, but it was still present in most of the lateral force loops. Only at low loads and high speeds, smooth sliding was often observed on 4%-PAAm hydrogels (see the small size of the blue bubbles at 5 nN in Figure 4.4a). At the highest applied load (~100 nN, see arrows), the occurrence of stick-slip events apparently decreased, likely because polymer fluctuations are restricted under high loads.

In the case of gel-like materials, stick-slip happens when the polymer chains are pulled and stretched while they adhere (stick) to the colloid, until the pulling force is stronger than the adhesion force, which yields a slip(96). Stretching of the polymer depends on the degree of entanglement and crosslinking, and hence, it varies across the sliding distance due to the heterogeneous nature of the hydrogel surface, which is consistent with the irregular stick-slip observed in the lateral force loops. The hydrogel microstructure substantially affects the stick-slip frictional response. Across experiments with different colloids, stick-slip was most prominent for 6%-PAAm hydrogels, while 12%-PAAm hydrogels exhibit less pronounced stick-slip than 4%-PAAm hydrogels. This suggests a trade-off between the adhesion energy and the contact area: an increase in polymer concentration and crosslinking enhances adhesive interactions between colloid surface and hydrogel (Figure A1a), however, the larger elastic modulus reduces the contact area and the number of interactions.

4.3. Discussion

The energy dissipation mechanisms underlying the frictional characteristics of hydrogels are intrinsically different from those of hard rough substrates. Although hydrogel-liquid interfaces are rough due to the thermal fluctuations of the polymer chains, the large deformation imposed by the applied load, the long relaxation times of macromolecules and the presence of a liquid phase, i.e. the poroelastic behavior of the hydrogel, lead to intrinsically different energy dissipation

mechanisms that need to be taken into account to predict and explain frictional characteristics of hydrogels and lubrication mechanisms. We use the described experimental results in the previous section to provide insight into these mechanisms.

The friction force gradually increases with load, although deviating from the Amonton's law (**Figure**s 4.1). This is not surprising(97), since, first, adhesion, which increases with applied load(19), is significant, and, second, friction depends on speed. The tenuous increase in the load-dependent friction force with increase in polymer concentration is consistent with the proposed adsorption-desorption model; larger fluctuation amplitudes ($\xi \sim E^{-\frac{1}{3}}$), which are expected for 4%-PAAm hydrogels, imply longer times for re-adsorption (τ_D) to the counter-surface, and hence, smaller friction force compared to more crosslinked hydrogels at the same applied load. While SEM cannot be used to characterize each single hydrogel network, i.e. its mesh size or correlation length, the elastic modulus can be easily measured prior to each friction force measurement on the same sample and area, which is an advantage considering the variability of properties across PAAm hydrogels. We thus propose to use the initial elastic modulus, E, which spans over one order of magnitude in this study (1-40 kPa), to represent the fluctuation characteristics of the near-surface hydrogel region.

The non-monotonic variation of friction with speed (**Figure** 4.2) –first decreasing below a transition value, V^*, at which friction achieves a minimum value, $F_{\min}$, and then increasing above V^*, reveals the action of, at least, two different mechanisms underlying friction at the sliding interface. **Figure** 4.5 a shows that the transition speed V^* depends on the elastic modulus of the hydrogels in a non-linear fashion according to $V^* \sim E^{1/3}$ upon an applied load of 50 nN, which implies that the increase in friction with speed is facilitated at the sliding interface of softer hydrogels. Figure 4.5b shows that the minimum friction force $F_{\min}$ increases with elastic modulus

–approximately as $F_{\min} \sim E^{\frac{1}{5}}$– in qualitative agreement with the adsorption-desorption model(21), as described above. The agreement between this power law and the experimental results is only partial, which might be caused by hydrogel heterogeneities and by the silica colloid, whose properties (e.g. roughness, hydrophilicity) varied across experiments. Upon a load of 5 nN, there is no clear trend for the transition speed as a function of the elastic modulus, however, the precision of the AFM may not be sufficient to distinguish the minimum friction force due to its small magnitude, and hence, this is not further discussed.

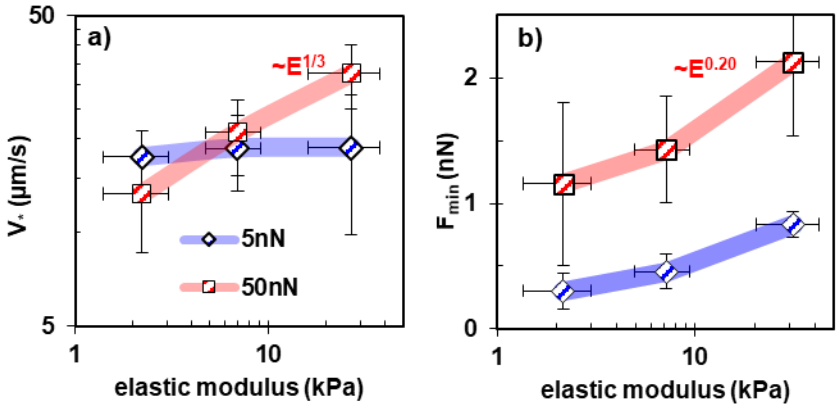

Figure 4.5 a) Transition speed, $\boldsymbol{V^*}$, at which the minimum of the friction force, $\boldsymbol{F_{min}}$, is achieved and b) $\boldsymbol{F_{min}}$ as a function of elastic modulus at the applied normal loads of 5 nN (diamonds) and 50 nN (squares). At 50nN, the transition velocity $\boldsymbol{V^*}$ scales with $\boldsymbol{\sim E^{1/3}}$ and the minimum friction force $\boldsymbol{F_{min}}$ scales with $\boldsymbol{\sim E^{1/5}}$, while the trends are not clear at 5 nN, likely because the measurement precision is not sufficient to clearly identify the minimum friction force.

Like in previous works, we thus assume that the frictional behavior at speeds below V^* results from polymer chains continuously adsorbing to and detaching from the colloidal probe with a fluctuation amplitude that is related to the mesh size characteristics. The relaxation time for re-adsorption is given by $\tau_D = \frac{\xi^3 \eta}{k_B}$, according to the scaling theory(74), which yields a critical speed, $V_c = \frac{\xi}{\tau_D} \sim \frac{k_B T}{\eta \xi^2} \sim \frac{(k_B T)^{\frac{1}{3}} E^{\frac{2}{3}}}{\eta}$, at which the polymer fluctuation time is equal to the interaction time upon sliding $\tau = \tau_D$; note that the constants are missing in this equation. Inspired by ref. (98),

Figure 4.6 shows the normalized friction force F by F_{min} as a function of the dimensionless speed $\frac{V}{V_c}$. We emphasize that we refrain from quantifying friction via a friction coefficient due to the evident deviations from the Amonton's law in our experiments. A satisfactory collapse of the normalized friction force is obtained as a function of the dimensionless velocity $\frac{V}{V_c}$ at speeds smaller than V^*, demonstrating that the normalized friction force scales with $F/F_{min} \sim (E^{-\frac{2}{3}}V)^n$, n ≈-0.1. The collapse demonstrates that the relaxation time τ_D is a good parameter to describe the influence of the hydrogel network on the normalized friction in this regime. A decreasing friction with speed appears if the time allowed for interactions to happen at the sliding interface is too short for the polymer to re-adsorb to the opposing surface after detachment. This yields a decrease in kinetic friction below the static friction, thereby causing stick-slip(96). As a matter of fact, we observe significant stick-slip in our measurements (**Figure** 4.4), which is a clear evidence for the direct contact between the hydrogel and the colloid surface. The stick-slip is irregular and is influenced by the applied load and the sliding speed: higher load and slower sliding enhance squeeze-out of the fluid (drainage)(19), and thereby, polymer dehydration, which increases the adhesive interaction between polyacrylamide and the colloid surface, and thus, promotes stick-slip.

It is important to note that the normalized transition speed V^* by V_c is several orders of magnitude smaller than 1, which cannot be justified by missing scaling factors (expected to be ~1). In contrast to this, the results from a previous work(47) show that the transition at Gemini hydrogel interfaces occurs at $V/V_c \sim 1$. Our effort to validate the calculations in this previous work have failed and for the given parameters by the authors, we found that $V/V_c < 0.001$ in ref. (47)in good agreement with the results presented here. This suggests that an additional mechanism hinders the critical speed to be attained, and a transition happens at V^*.

It is also worth mentioning that previous works have revealed a boundary lubrication regime at even lower speeds, where friction either increased and/or remained constant with rising speed(21). Figure 4.2 shows an example for 4%-PAAm hydrogels, where friction first increases at the lowest speeds, before the decrease of friction with increasing speed was measured. According to Gong's model this happens if the interaction time is sufficient long for re-adsorption of the polymer chains to take place, i.e. at sufficiently slow speeds. Such initial increase of friction with speed was, however, rarely observed in our experiments, and we do not further discuss it here due to the small amount of data.

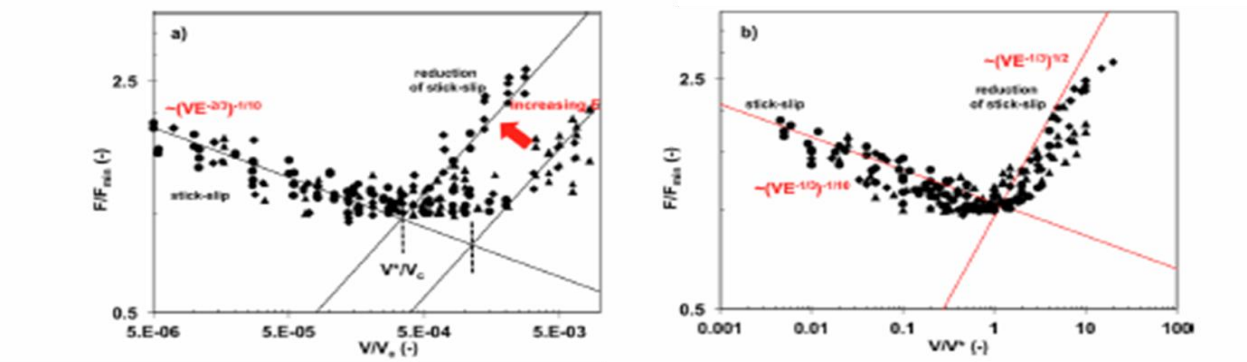

Figure 4.6 Normalized friction force as a function of a) $\frac{V}{V_c}$ under two applied loads, 5 nN and 50 nN and b) force as a function of V/V^*. Two scaling laws $\frac{F}{F_{min}} \sim \left(\frac{V}{V_c}\right)^n$ were determined: n≈-0.1 for V<V* and $n \approx 0.5$ for V>V*. The normalized friction at V>V* on hydrogels of different elastic modulus do not collapse because $\frac{V^*}{V_c} \sim E^{-\frac{1}{3}}$. The symbols correspond to 4%-PAAm (triangles), 6%-PAAm (diamonds) and 12%-PAAm hydrogels (circles).

Figure 4.6a shows a notable spread of the normalized friction force as a function of $\frac{V}{V_c}$ at $V > V^*$, which is attributed to the network influence on the transition speed, $V^* \sim E^{\frac{1}{3}}$, which yields $\frac{V^*}{V_c} = E^{-\frac{1}{3}}$, thereby hindering the collapse of the normalized friction force. Evidently, this deviation indicates that V_c is not a good scaling parameter in this regime. Instead, Figure 4.6b shows the

normalized friction force as a function of V/V^*. Although the scatter of data is large, the distinction with regard to the elastic modulus vanishes, and it provides an approximate scaling law $\frac{F}{F_{\min}} \sim (V/V^*)^{\frac{1}{2}}$ in this regime. The origin for the poor collapse might be related to the surface properties of the colloids, which varied across experiments. Nevertheless, we cannot exclude that the selected scaling parameter, $V^* \sim E^{\frac{1}{3}}$, is not appropriate to describe this scaling law, and instead, one of the modes of the mesh size distribution (i.e. a single correlation length) dictates the change in friction in this regime; this requires further investigation. Furthermore, considering that $F_{\min} \sim E^{1/5}$ and $V^* \sim E^{\frac{1}{3}}$, this suggests that in this regime, the friction force only depends weakly on the elastic modulus, i.e. on the fluctuation length of the hydrogel network. This is confirmed in Figure 4.6, which shows a good overlap of the friction force attained by the three different hydrogels at $V > V^*$.

If elasto-hydrodynamic lubrication would occur in this speed regime, as claimed before(21), the friction force would be expected to be given by $F \sim A\eta V/h$, where h is the lubricant thickness. According to Hamrock&Dowson's model in the elasto-hydrodynamic regime (99), $h \sim E^{-\frac{4}{9}} V^{\frac{2}{3}}$, and assuming $A \sim E^{-\frac{2}{3}}$, the (viscous) friction force F should scale with $\sim (E^{-\frac{2}{3}} V)^{1/3}$, which differs from our experimental results (see **Figure** A3). Deviations from the original model by Hamrock and Dowson, however, are possible, since the hydrogel surface is permeable and hydrogels are poroelastic, properties that are not accounted for in this model. Nevertheless, it is evident that full-fluid film lubrication is not attained in most of our experiments, as evidenced by the stick-slip analysis, which demonstrates the occurrence of direct chain-colloid interactions.

A mechanistic explanation for the observed scaling law $\frac{F}{F_{min}} \sim \left(\frac{V}{V^*}\right)^{\frac{1}{2}}$ is proposed based on the likelihood for re-adsorption: at sufficiently fast sliding ($V > V^*$), when the time allowed for interaction at the sliding interface is reduced below this critical value, $\tau^* = \frac{\xi}{V^*} \sim \frac{E^{-\frac{1}{3}}}{E^{\frac{1}{3}}} = 1$, re-adsorption is not dictated by the time for re-adsorption $\tau_D \sim \xi^2 \sim E^{-\frac{2}{3}}$. Instead, it is dominated by the likelihood of attachment, fairly independent on the fluctuation length of the hydrogel network. The increase in the likelihood of interaction with speed yields an increase in the number of chains that are *effectively* adsorbed at each point of time, thereby causing the friction force F to increase, to some extent, independently of the fluctuation length. Our future work will be dedicated to get more insight into this regime by expanding the range of investigated hydrogel networks.

A similar trend for the friction force as a function of speed was observed for the speed-dependent friction force for PAAm hydrogels against a glass ball (as countersurface) measured with a tribometer(21), and for cartilage-cartilage interfaces, measured with a surface forces apparatus(96). The authors attributed it to a transition from boundary to elastohydrodynamic lubrication. Our results suggest that, although a transition to elasto-hydrodynamic could happen at even higher speeds, under the investigated conditions there is still direct interaction between the hydrogels and the colloid sphere, which is reflected in stick-slip in our measurements. Hydrogel deformation must play a significant role in the onset of hydrodynamic lubrication, but classical models do not account for the permeable and non-linear poroviscoelastic nature of hydrogels, and hence, a prediction of the conditions for the onset of fluid-film lubrication is not possible yet.

A first attempt to connect the poroelastic behavior of hydrogels to the lubrication mechanism has been recently reported, however, only in the regime where friction decreased with increasing

speed(19). The authors showed how short durations of applied pressure and faster sliding speeds do not disrupt interfacial hydration, which maintains low friction, while at low speeds, where interface drainage dominates, an increase in adhesion energy - directly derived from poroelastic relationships- and the osmotic suction work against slip to achieve higher friction. It should be noted that this continuum approach is consistent with the adsorption-desorption model applied here, considering that polymer fluctuations (and low friction) are hindered with hydrogel dehydration or squeezing-out of the liquid phase.

It is interesting to compare our results to a previous study of the frictional behavior of Gemini hydrogel interfaces(98), which showed a transition from velocity-independent to velocity-dependent friction coefficient. The absence of the initial decrease in friction with speed could be related to the more favorable interactions between the polymer chains compared to the interactions between polymer chains and silica surface. We also note that the velocity-dependent friction coefficient above the transition speed showed an excellent collapse for hydrogels with different mesh size, in contrast to our results. We cannot explain this difference yet, but we assume that the dynamics at the Gemini interface might either affect the likelihood of re-attachment of the polymer chains or the range of investigated hydrogel networks was too narrow to reveal this phenomenon. Nevertheless, the coefficient of friction at Gemini hydrogel interfaces also scales with $(V)^{\frac{1}{2}}$ above the transition speed, in excellent agreement with our results.

In summary, we have shown that boundary lubrication at the hydrogel-colloid interface exhibits a non-monotonic change of friction with speed and intermittent sliding. The scaling laws that predict friction above and below the transition speed V^* deviate from those found for Gemini interfaces, which seems reasonable since the fluctuation dynamics that lead to re-adsorption are expected to be different at hydrogel-hydrogel interfaces. It is intriguing that beyond the reported transition

($V > V^*$), the hydrogel network has a small influence on the friction force, and our current work is trying to scrutinize the origin of this result. Further, the thermal fluctuations at the colloid-hydrogel interface manifest as irregular stick-slip. Since stick-slip sliding is commonly at the origin of irreversible transformations of soft surfaces, and hence, wear processes, understanding the mechanisms that yield this intermittent frictional response with different relaxation times, thus below and above V^*, will be also the subject of our future investigations.

4.4. Conclusions

This work has investigated the frictional characteristics of hydrogel-silica interfaces by using colloidal probe AFM. PAAm hydrogels with 4, 6 and 12 wt% acrylamide exhibit a complex microstructure with several correlation lengths and/or mesh sizes, which led us to choose the initial elastic modulus as the material parameter to characterize the hydrogel network. By scrutinizing the speed-dependence of the friction force over three orders of magnitude, two different lubrication mechanisms were discerned, both being explained by the fluctuation dynamics of the polymer chains at the sliding interface. Below a transition speed V^* that scales with $E^{\frac{1}{3}}$, the decrease in friction with speed $\sim \left(VE^{-\frac{2}{3}}\right)^{-\frac{1}{10}}$ supports energy dissipation via continuous attachment to and detachment of the polymer chains to the colloid surface. Friction is governed by the amplitude of such fluctuations (or mesh size), while stick-slip reflects the adhesive interactions between the polymer and the silica counter-surface. According to our results, less crosslinked hydrogels can mediate lower friction forces due to the longer relaxation times of the polymer chains to re-adsorb on the counter-surface; however, the transition into the regime, where friction increases with speed, is favored on less crosslinked hydrogels. Above the transition speed, V^*, the occurrence of stick-slip decreases, yet it does not vanish, while the scaling law for the friction force switches

(approximately) to $\sim(VE^{-\frac{1}{3}})^{\frac{1}{2}}$, both supporting the transition to a different lubrication mechanism. While the stick-slip characteristics of hydrogel-silica interfaces are shown to depend on the hydrogel microstructure and to vary with load and speed, future studies are needed to elucidate the different relaxation mechanisms.

CHAPTER 5: THE VISCOUS-ADHESIVE MODEL FOR HYDROGEL FRICTION

This chapter summarizes the viscous adhesive, quantitative model developed for hydrogel friction. The model accounts for the effects of confinement of the polymer network provided by a solid surface and poroelastic relaxation as well as the (non) Newtonian shear of a complex fluid on the frictional force and quantifies the frictional response of hydrogels-solid interfaces. Finally, the review delineates potential areas of future research based on the current knowledge.

5.1. Materials and methods

PAAm hydrogels with 4, 6 and 12% monomer were utilized throughout the study. Synthesis has been mentioned in Chapter 3. Indentation and friction-force measurements were conducted with an Atomic Force Microscope (Nanowizard Ultra, JPK Instruments, Germany). Silica beads with two diameters, 20 μm (Duke Scientific, Thermo Scientific, CA, USA) and 5 μm (Microspheres-Nanospheres, USA), were attached to the end of tipless cantilevers (nominal spring constant = 0.4 N/m, CSC37-No Al/tipless, Mikromash, USA) using an epoxy glue (JB-Weld, Sulphur Springs, TX, USA). Before attaching the colloids, the normal stiffness of the cantilevers was determined by the thermal noise method and the lateral stiffness was obtained by means of the wall calibration method(100). The AFM cantilevers were cleaned in an ethanol bath followed by UV ozone for 30 minutes just before the AFM experiment. RMS roughness of each silica colloid within the area of contact with the hydrogel was determined *via* reverse imaging using a clean test grating (MikroMasch, Spain) and was smaller than 5 nm.

5.2. Results

A prominent hysteresis was measured between loading and unloading indentation curves with large work of adhesion on unloading (not shown). The elastic modulus and the surface energy

of the hydrogels were obtained by using the JKR model to fit the unloading indentation curves. Figure 5.1a shows results for selected 4%, 6% and 12% hydrogel samples, for which average elastic moduli were found to be 2.3 ± 0.9 kPa, 6.8 ± 0.9 kPa and 18.6 ± 3.1 kPa, respectively. These values are in good agreement with previously reported elastic moduli of polyacrylamide hydrogels with similar composition(101, 102). As shown in Figure 5.1b, the surface energy is largest for the 6%-hydrogels, which indicates that the combination of a higher polymer concentration (compared to the 4%-hydrogels) and a smaller crosslinker concentration (compared to 12%-hydrogels) favors the adhesion to the colloid surface. The latter is expected to enhance the mobility of the polymer network thereby enabling the matrix to conform better to the colloid. Although the trends of both properties were consistent across the synthesized samples with the same polymer concentration, the values varied, and hence, they were determined for each single sample where friction was measured. The corresponding values of the elastic moduli are given in the following diagrams.

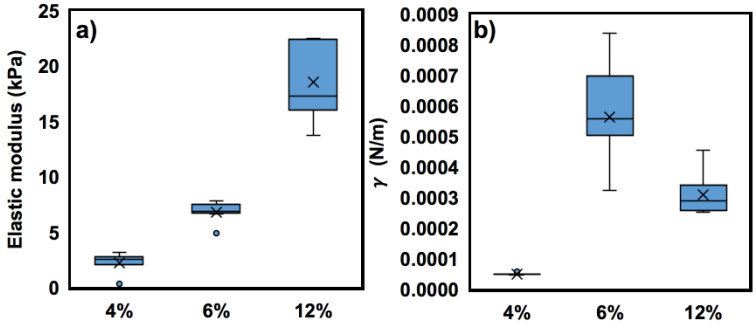

Figure 5.1 a) Elastic modulus and b) surface energy (γ) of representative 4%, 6% and 12% hydrogels obtained by fitting the JKR model to the indentation (unloading) curves. The box diagrams show the mean (middle line), average (cross), 25% and 75% quartiles, outliers if present (circles) and standard deviation of the elastic modulus and the surface energy. The Hertzian contact mechanics model was also fit to the loading force-indentation curves, which led to elastic moduli in good agreement with those obtained using the JKR model. Colloid radius=20 µm. Indentation rate= 2 µm/s. Spring constant=0.5 N/m.

Figures 5.2 a-c show representative friction-force measurements for 4%, 6% and 12% hydrogels as a function of the velocity and at different normal loads (see color legend in Figure 5.2a). A different velocity dependence of the friction force is observed as a function of the polymer concentration. Friction decreases with sliding velocity for 4%-PAAm hydrogels, while it increases with sliding velocity for 12%-hydrogels, thereby exhibiting clear velocity-weakening (i.e. decrease in friction with increasing velocity) and -strengthening frictional responses (i.e. increase in friction with increasing velocity), respectively. In the case of 6%-PAAm hydrogels, a transition from a velocity-weakening to a velocity-strengthening behavior was often observed (Fig. 2b). It is to be noted that the increase of friction with applied normal load is not always obvious (see e.g. Figure 5.2b, under applied loads of 30 nN and 40 nN), which is mainly attributed to the concurrent influence of load and velocity on the friction force.

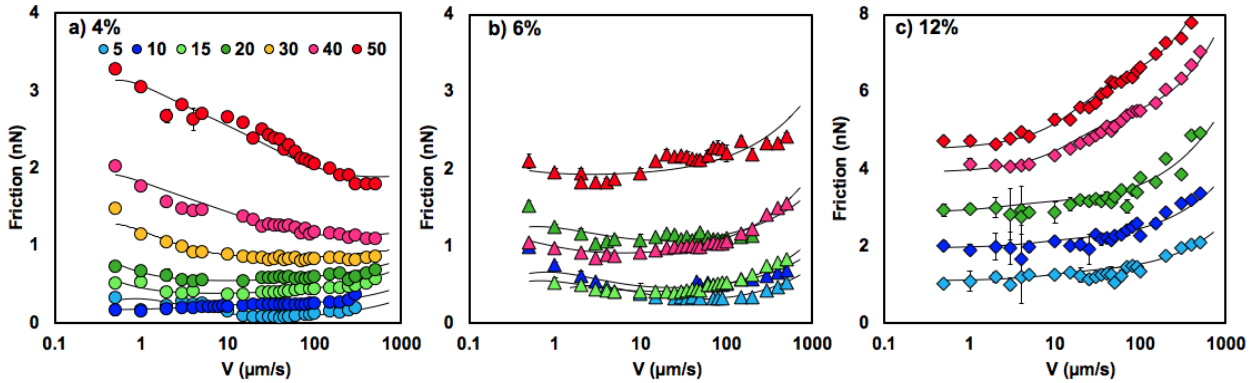

Figure 5.2 Friction force as a function of the sliding velocity for a) 4% (circles), b) 6% (triangles) and c) 12% (diamonds) PAAm hydrogels at following normal loads: 5 (light blue), 10 (dark blue), 15 (light green), 20 (dark green), 30 (yellow), 40 (fuchsia) and 50 (red) nN. The elastic moduli of the three hydrogels are a) 1.8 ± 0.9, b) 9.9 ± 0.2 and c) 12.9 ± 1.3 kPa, respectively. At least 4 loops were used to calculate the friction force. There is a quantitative agreement between consecutive loops, which is reflected in the small error bars (often smaller than the symbol size and therefore not visible), indicating that the hydrogel deformation is reversible, i.e. the hydrogel fully recovers during the measurement of each loop. The black lines give the calculated friction force according to the viscous-adhesive model (Eqs. 2-5). Colloid diameter=20 μm. Spring constant= 0.4 N/m. Note the different scale on the Y-axis of (c).

While 4% and 12% hydrogels show a consistent behavior across samples, the behavior of 6%-hydrogels showed certain variability, *i.e.*, different trends of the friction force were observed

as a function of the velocity. Such variable response of 6% hydrogels is attributed to the transitional nature of their frictional characteristics, reflected in the prominent minimum in friction at an intermediate velocity (Figure 5.2b).

Friction was also measured with 5µm colloids and representative experimental results are shown in Figure 5.3. Here, a minimum in the friction force is reproducibly observed for the three hydrogels, *i.e.* a transition from a velocity weakening to a velocity-strengthening frictional response. Although the loads applied with 5 and 20µm colloids were the same, the use of a smaller colloid results in higher contact stresses at the same applied loads, and thereby, it leads to a more prominent squeeze-out of the interstitial water, as justified later (see calculated contact stresses in Table A1 in the Appendix A).

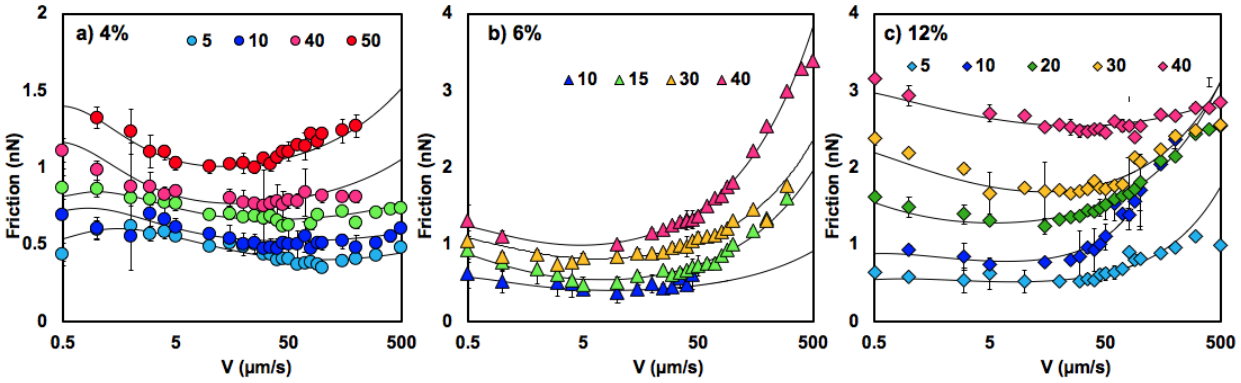

Figure 5.3 Friction force as a function of the sliding velocity for a) 4% (circles), b) 6% (triangles) and c) 12% (diamonds) PAAm hydrogels at following normal loads: 5 (light blue), 10 (dark blue), 15 (light green), 20 (dark green), 30 (yellow), 40 (fuchsia) and 50 (red) nN. The elastic moduli of the three hydrogels are a) 2.34 ± 0.3 b) 14.9 ± 0.9 and c) 17.5 ± 0.5 kPa. At least 4 loops were used to calculate the friction force. The black lines give the calculated friction force according to the viscous-adhesive model (Eqs. 5.2-5.5). Colloid diameter=5 µm. Spring constant= 0.36 N/m.

Figure 5.4 shows representative measurements of the lateral force as a function of the sliding distance. Only 10 µm of the total sliding distance (29 µm) are shown here to illustrate the lateral force at the turning point, when the velocity of the cantilever changes from zero to 1 µm/s

at a constant load of 40 nN. For the three selected hydrogels, there is an initial increase of the lateral force over a distance of ~2 µm, before the force decreases and achieves a plateau. The recorded height of the cantilever demonstrates that this change in the lateral deflection of the cantilever is not originated by the surface topography, which excludes pile-up of the hydrogel. Instead, the increase in the lateral deflection arises from static friction between the hydrogel and the colloid. On applying a tangential force, the near-surface region of the hydrogel deforms more than the bulk (~2 µm), and when the energy stored overcomes the work of adhesion, the colloid starts sliding. Similar results were observed under other conditions, with more or less pronounced increase in lateral force (stick) depending on load and polymer concentration. Since the sliding distance was selected to be much larger than the stick length, and the friction force (i.e. the half loop width) was only calculated during the sliding period, the experimental results in Figures. 5.2 and 5.3 only reflect the steady-state kinetic friction.

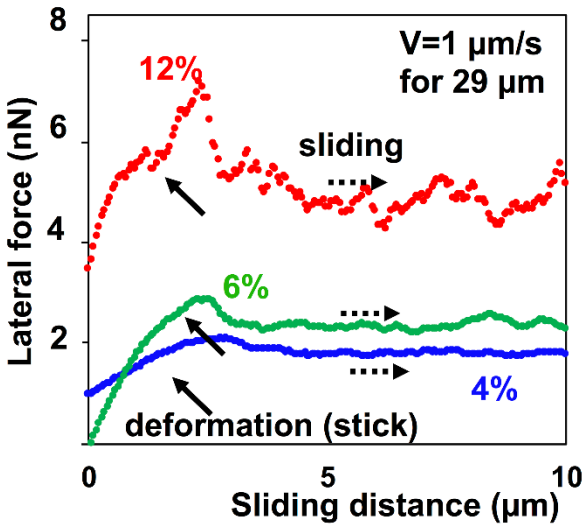

Figure 5.4 Lateral force as a function of the sliding distance for three selected hydrogels with elastic-moduli of 1.8 (0.1) (blue, 4% hydrogel), 4.9 (0.2) (green, 6% hydrogel) and 12.9 (1.3) kPa (red, 12% hydrogel), respectively, at the sliding velocity of 1 µm/s and a load of 40 nN. Only the initial 10 µm of the total stroke length are shown to illustrate the stick period (full arrow) *vs.* sliding (dashed arrow). Colloid diameter: 20 µm.

5.2.1 Model for Viscous and Adhesive Hydrogel Friction

The proposed model to quantify hydrogel friction considers the superposition of an adhesive and a viscous friction force. The adhesive contribution to friction is based on the theory originally developed by Schallamach for rubber friction (50, 103), which can be applied to any adhesive sheared interface bridged together by reversible, adhesive bonds. The present model, however, differs from previous approaches because it considers the effect of load on polymer relaxation; therefore, we refrain from using simplified scaling arguments, which neglect this phenomenon. The viscous contribution to friction originates from the deformation of a near-surface hydrogel region of μm-thickness, which is shown to exhibit shear-thinning behavior.

The colloid interacts with the hydrogel through a number (N) of transient adhesive bonds (so-called bridges or junctions(104)), which determine the adhesive contact area $A_b = N \cdot \Delta$, each junction of area Δ. These junctions form and are stretched in the lateral direction until the polymer detaches from the colloid and relaxes to its equilibrium state, while other junctions form simultaneously in an incoherent manner. Each junction is characterized by thermal activation energies of formation ΔE_f and rupture ΔE_r; detachment occurs either by thermal excitation or by an external shear force. The mean time of bond rupture depends on ΔE_r according to $\tau_0 \sim \tau^* exp(\Delta E_r / kT)$, and it may be reduced by the applied lateral force, $\tau_r = \tau_0 exp(-(\mathrm{f} \cdot \mathrm{l}_a)/kT)$, where f is the lateral force acting on each junction and l_a is a shear-activated length of molecular dimensions(103). The rupture of bonds can also happen when a critical deformation of the junction or yield length (l^*) is reached (104). The transient bonds reform after a characteristic mean time according to $\tau_f \sim \tau^* exp\left(\Delta E_f / kT\right)$. The fluctuation time of the polymer, τ^*, can be increased due to the confinement imposed by the countersurface compared to the unconfined

condition (105) and to large deformations(106), thereby differing from predictions according to Gaussian elasticity, $\tau^{u}\sim\eta\xi^{3}/k_{B}T$. (107)

The adhesive friction force F_{adh} is thus given by the elastic force of each junction f multiplied by the number of junctions in adhesive state N. According to ref. (104), an analytical expression can be derived to describe the adhesive friction in the context of Schallamach's model, if it is assumed that the lateral force does not decrease the energy barrier for bond rupture. As justified in the SI, this approximation ($\tau_r = \tau_0$) is acceptable for hydrogels because the lateral force is small. The simplified expression for the adhesive component of friction (see the derivation in the SI) is given by:

$$F_{adh} = Nf = N\frac{\Delta \mathrm{GVt}}{\mathrm{d}} = \frac{\mathrm{A}_b \mathrm{GVt}}{\mathrm{d}} \sim \frac{A_b G V \tau_0}{\mathrm{d}} \frac{\left(1 - \left(1 + \frac{l^*}{V\tau_0}\right) exp\left(-\frac{l^*}{V\tau_0}\right)\right)}{1 - exp\left(-\frac{l^*}{V\tau_0}\right)}$$

Eq. (5.2)

G being the shear modulus, d the thickness of the junction, Vt/d the strain of the adhesive bridge, and t the time elapsed since the zero-state stress. A_b is estimated as $A_b = A_v\langle t_b\rangle/(\langle t_b\rangle + \tau_f)$, A_V being the contact area during sliding, and $\langle t_b\rangle$ the mean life time of the adhesive junctions, $\langle t_b\rangle$=$\tau_0(1 - \exp(-l^*/V\tau_0))$, which accounts for the probability to stay in an adhesive state. Thus, the adhesive friction force depends on G, d and on microscopic characteristics of the polymer network at the interface, l^*, τ_0 and τ_f. Eq. (2) predicts that friction increases with velocity at low sliding velocities owing to the increasing elongation of each junction with speed (Vt), while the rupture of the adhesive bonds is increasingly promoted with greater velocities but at a lesser rate so that the friction force increases with velocity, approximately in a logarithmic fashion. At high

velocities, as only a few bonds can form simultaneously, friction is mainly dictated by the rate of bond formation, $1/\tau_f$, thereby yielding a velocity-weakening mechanism for the friction force. The competition between bond rupture and formation leads to a peak or a plateau of the friction force over an intermediate velocity range.

The failure of this theory to predict sliding friction of rubbers at very slow velocities was recognized by Schallamach(42). The adhesive friction did not tend to zero by decreasing the velocity (as expected from Eq. (2), but instead, a *quasi* velocity-independent friction value (F_0) was observed in experiments(50), which was associated to static friction (42, 108). Indeed, the hydrogel-glass interfacial strength has been also observed to age (increase) logarithmically with contact time, which was attributed to the slow increasing number of adhesive bonds with time (17). As shown in Figure 5.4, static friction is also present at the hydrogel -colloid interface, which suggests that a (quasi) velocity-independent term (F_0) might be needed to describe hydrogel friction more precisely.

Inspired by previous attempts to describe the friction force of contacts lubricated by polymer melts(109), we propose to model the viscous component of friction as a viscous force assuming a Couette flow of a hydrogel film with an effective viscosity η_{eff}:

$$F_{vis} \sim \frac{16}{5} A_V \eta_{eff} \frac{V}{\delta} \log\left(\frac{2R}{\delta}\right)$$

Eq. (5.3)

where δ is the thickness of the sheared film. Eq.(3) is strictly valid for a sphere-plane geometry with R $\gg \delta$, while the most common relation, $F_{vis} \sim A_V \eta_{eff} V/\delta$ is only valid for plane-

plane geometries. The effective viscosity η_{eff} is described according to $\eta_{eff} \sim \eta_0 \dot{\gamma}^n = \eta_0 (V/\delta)^n$, which accounts for Newtonian ($n = 1$) and non-Newtonian behavior ($n \neq 1$) of the hydrogel film.

At applied pressures smaller than the osmotic pressure of the hydrogel(110) (Π), a time-dependent response arises from the rearrangements of the polymer network(110). If the applied pressure is, however, larger than Π , the solvent is squeezed-out and the poroelastic response of the hydrogel influences the time-dependent contact area (111, 112). The contact stress in our experiments (Table S2) may be larger than the osmotic pressure, as described later, and hence, we cannot exclude that fluid drainage happens. The migrating contact area A_V (the subindex V indicates a sliding contact) thus differs from the static contact area (A_0, where the subindex 0 indicates the contact at a sliding velocity V=0, *i.e.* upon indentation) at the same applied load as a result of the time-dependent deformation. In the limit of small deformations(113, 114), the sliding contact radius a_V can be roughly approximated as:

$$a_V^2 \sim R\delta_V = a_0^2 \frac{\delta_V}{\delta_0} = a_0^2 \frac{\delta'(1 - \exp(-t'_V/\tau_{PV}))}{\delta'(1 - \exp(-t'_0/\tau_{P0}))}$$

τ_P being the relaxation time of the hydrogel (due to fluid drainage and/or to rearrangements of the polymer network) with an effective diffusivity D ($\tau_{PV} \sim a_V^2/D$ and $\tau_{P0} \sim a_0^2/D$, assuming D to be the same for the static and migrating contact areas) and t' the contact time ($t'_0 = \delta_0/\dot{\delta_0}$ and $t'_V = a_V/V$). The indentation depths, δ_V and δ_0, are described according to a Kelvin-Voigt model, which has been shown to be appropriate for polyacrylamide hydrogels(115). The linearization of this expression yields:

$$a_V^2 \sim a_0^2 \frac{t'_V/\tau_{PV}}{t'_0/\tau_{P0}} = a_0^2 \frac{R\dot{\delta_0}}{V a_V}$$

And after rearranging, the velocity-dependent contact radius a_V and area A_V are approximated as:

$$a_V \sim \left(\frac{a_0^2 \dot{\delta}_0 R}{V}\right)^{1/3}$$

$$A_V = \pi(a_V^2 + \delta_V^2)$$

Eq. (5.4)

This analysis resulted in significant change of the contact area as a function of velocity and load. It should be noted that Eq. (5.4) is only valid in the limit of small deformations (R>>δ) and after linearization of the indentation depth (δ_v and δ_0), and hence, deviations of our experimental results from the model are obviously expected. A precise estimation of the sliding contact area would require solving a contact mechanics problem coupled with flow mechanics using appropriate finite element modeling for large deformations and additional consideration of the viscoelasticity of the polymer network, which is out of the scope of this work.

The total friction force results from the addition of the adhesive and viscous contributions and the quasi-velocity independent friction term:

$$F = F_0 + F_{adh} + F_{vis}$$

Eq. (5.5)

5.2.2. Fitting Procedure

The JKR model was used to calculate the static contact radius a_0 and the indentation depth δ_0 as a function of the normal load using the elastic modulus and surface energy of the hydrogels, and Eq. (4) was applied to roughly estimate the sliding contact radius a_V and the contact area A_V,

as a function of the sliding velocity. Eqs. (5.2-5.3) and (5.5) were then fit to the experimental results using l^*, τ_0, F_0, τ_f, η_0 and n as fitting parameters. The fits shown in Figures 5.2-5.3 were accomplished under the assumption that both the thickness of the sheared hydrogel film δ in Eq. (5.3) and of the junction d in Eq. (5.2) are equal to the indentation depth δ_V, and hence, a function of load and sliding velocity. It is noteworthy that the thickness of the sheared hydrogel film δ was assumed to be equal to the mesh size previously (17). However, this assumption did not lead to good results here. The origin for this discrepancy could rely on the greater contact stress and hydrogel deformation in this work, but an accurate comparison to ref. (17) is not possible since the stress at the sliding contact is unknown.

An iterative method using a non-linear solver in MATLAB was used to find the best fitting parameters, which required the assumption of appropriate initial values. The fluctuation time of the unconfined polymer, $\tau^u = \eta\xi^3/k_BT$ (2.3, 1.2 and 0.24 μs for 4%, 6% and 12% hydrogels with ξ equal to 21, 17 and 10 nm, respectively; see SI) gives the lower bound for τ_0 and τ_f, where $\tau_0 \geq \tau_f$. Furthermore, it was found that τ_0 and τ_f influence the increase and the decrease of the adhesive friction with velocity, respectively, while the value of friction at the plateau was strongly sensitive to l^*. The initial guess for the stretched length of the polymer bridges before rupture, l^*, was assumed to be the mesh size of the polymer network, ξ. The fit was facilitated by noting that the onset of the velocity-weakening regime is given by $V_{c2} \sim l^*/\tau_f$. A peak in friction was sometimes observed under small applied loads (Figure 5.3a), which implies $\tau_0 = \tau_f$. The onset velocity V_{c2} and the peak, when measured, helped to determine the appropriate range of relaxation times. The initial guess for the viscosity was 1 mPas and Newtonian behavior (n=0); these parameters only affected friction at the highest sliding velocities. Due to the large number of fitting

parameters, convergence was not always achieved in Matlab and the fits were then facilitated by manually testing some parameters.

The black lines in Figures 5.2a-c and 5.3a-c show the calculated friction force according to our viscous-adhesive friction model. The fits to the model let us recognize that the behavior of the 12% hydrogel is intrinsically different. This is illustrated in Figure 5.5a, which shows representative results for the three hydrogels under an applied load of 40 nN. While 4% and 6% hydrogels exhibit a velocity-weakening adhesive friction (at low sliding velocity), an increase in friction with velocity was reproducibly observed for 12%-hydrogels over the same range of sliding velocities. Such increase in friction with velocity cannot be justified by a viscous force with plausible parameters. Instead, the precise logarithmic dependence of friction on velocity (see yellow line in Figure 5.5a) suggests the adhesive (elastic) origin of friction in this regime(104). It should be noted that the distinct behavior of the 12%-hydrogels vanishes when higher compressive stresses are applied with a smaller colloid (Figure 5.5b). A comparison between osmotic pressure ($\Pi \sim k_B T/\xi^3$, *i.e.* Π ~416, 804 and 3340 Pa for 4%, 6% and 12% hydrogels, respectively) and contact stress supports that fluid drainage might be hindered during the friction-force measurements on 12 % hydrogels with the 20μm colloid, while the much higher compressive stress applied with the 5μm-colloid promotes fluid drainage under all investigated conditions. This comparison supports that poroelastic fluid drainage contributes to the observed velocity-

weakening frictional behavior. However, the simplified model (Eq. (4)) does not allow a precise evaluation of the poroelastic contribution.

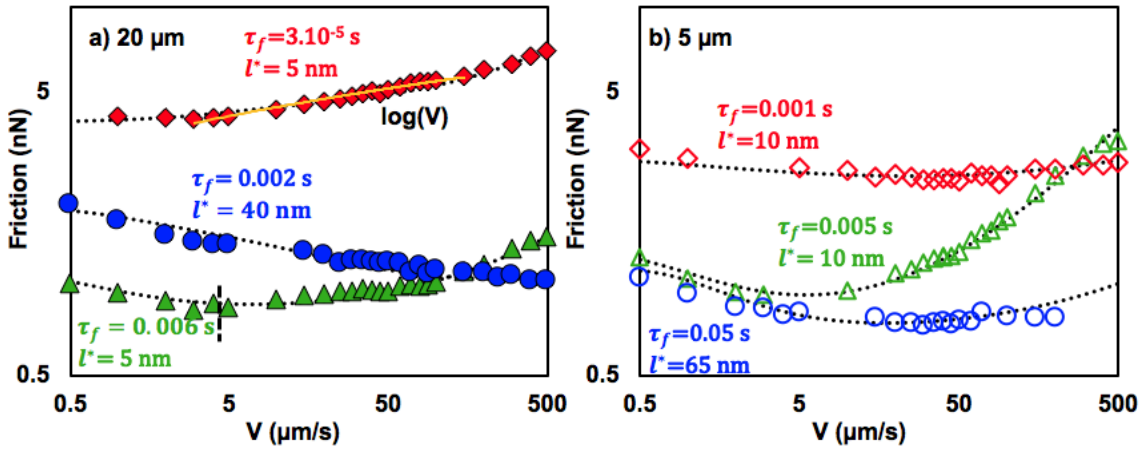

Figure 5.5 Comparison of the measured and calculated friction force as a function of the velocity at a normal load of 40 nN for 4% (blue circles), 6% (green triangles) and 12% (red diamonds) hydrogels. The measurements were conducted with a) the 20µm colloid (full symbols) and b) the 5µm colloid (empty symbols). The time required for polymer attachment to the colloid $\boldsymbol{\tau_f}$ and the yield length of the polymer strands $\boldsymbol{l^*}$ are shown in the diagram. The effective viscosity was modeled according to $\boldsymbol{\eta_{eff} = \eta_0 (V/\delta_V)^{-0.3}}$, with $\boldsymbol{\eta_0}$=0.01, 0.08 and 0.36 Pas/(1/s)$^{-0.3}$ with the 20 µm colloid and $\boldsymbol{\eta_0}$=0.2, 1.8 and 0.4 Pas/(1/s)$^{-0.3}$ with the 5 µm colloid for 4%, 6% and 12% hydrogels, respectively. The dashed lines show the fit of the viscous-adhesive friction model to the experimental results.

5.3. Discussion

5.3.1 Evaluation of the fitting parameters

Figure 5.6a-c show box diagrams with the fitting parameters for experiments conducted with the 20µm-colloid. The characteristic time of polymer attachment to the colloid (τ_f) was reliably determined only for the hydrogels that clearly exhibited a velocity-weakening adhesive friction at slow sliding velocity. Since this behavior was much less prominent for 12% hydrogels, only a few curves were analyzed in this case. The decrease in τ_f (i. e. shorter time for bond re − formation) with increase in polymer concentration is evident in Figure 5.6a, and it indicates that polymer-colloid interactions become more favorable with increase in the polymer concentration. The obtained values for τ_f are at least two orders of magnitude larger than the fluctuation times

of the free polymers ($\tau^u \sim \eta\xi^3/k_BT$). The large variation of τ_f for the 4%-hydrogels is originated by the remarkable effect of the load. Here, it is likely that the more pronounced drainage of the fluid with increasing load favors polymer attachment, which causes τ_f to decrease by two orders of magnitude and to become of the same order of magnitude as that of 6% hydrogels (~2.10^{-2} s). In the limit of high polymer concentration, one could expect τ_f to become so small that the velocity-weakening regime would vanish. This is consistent with the results for 12%-hydrogels. In this case, the time of polymer detachment from the colloid, τ_0, dictates the friction force, thereby yielding a *quasi*-logarithmic dependence of friction on velocity (Fig. 5a). Under these conditions, τ_0 is ~$3(0.8).10^{-4}$ s with a small effect of the load. Under all conditions, it is necessary to consider a velocity-independent term, F_0, to fit the model to the experimental results, which is discussed in detail later.

At the highest velocities (above the minimum in friction), the viscous dissipation dictates the measured friction force. A non-Newtonian shear-thinning behavior reproduces very well the experimental results using an exponent for the effective viscosity n ranging between -0.3 and -0.35 across all experimental conditions. We emphasize that the use of an effective viscosity is a well-established approximation to account for the viscous dissipation of a viscoelastic material under shear loading(109). Friction measurements were also conducted with the same colloid on a glass surface in water, for comparison. Figure A4 shows that the dependence of friction with sliding velocity transitions from logarithmic to linear at ~50μm/s. The linear increase in friction with velocity is attributed to full-fluid film lubrication, where the fluid (water) exhibits a Newtonian behavior, as expected. These reference measurements support that the frictional response at high sliding velocity shown in Figures 5.2 and 5.3 reflects the shear thinning behavior of the hydrogel. As shown in Figure 5.6c, η_0 increases with polymer concentration and with load,

which is consistent with the squeeze-out of the fluid and a more solid-like behavior of the hydrogel under shear loading. Figures 5.6d-f show similar trends of the fitting parameters for the experiments conducted with the 5 μm colloid. However, the viscosity-parameter η_0 is about an order of magnitude higher and τ_f is significantly smaller than in Figures 5.6a and 5.6c, respectively. Both trends may be justified by the larger applied pressures with this colloid, and therefore, more significant fluid drainage and higher polymer concentrations within the contact region.

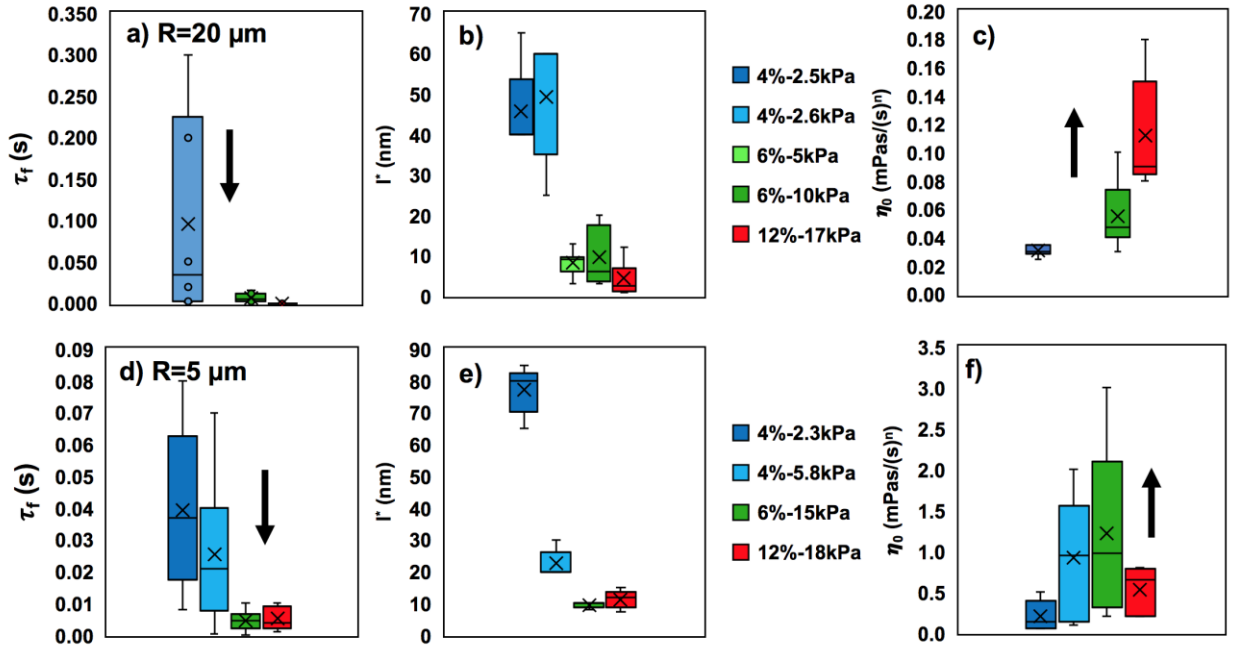

Figure 5.6 Box diagrams for the (a,d) characteristic time for polymer attachment τ_f, (b,e) yield length, l^*, and (c,f) viscosity parameter, η_0, for 4% (blue), 6% (green) and 12% hydrogels (red) with n~-0.3 (shear-thinning behavior), except for 12% hydrogels, where n increased to zero, with (a-c) 20 μm and (d-f) 5 μm colloid. The legend in the center shows the corresponding average elastic moduli of the selected hydrogels. The arrow indicates how the fitting parameter changes with an increase in load. The fitting parameter F_0 is shown in Figures 5.8c-d. Assuming that the fluctuation time of the polymer τ^* is given by the fluctuation time of the unconfined polymer, $\tau^u \sim \eta\xi^3/k_B$, the activation energies for bond formation ΔE_f can be roughly estimated, yielding 4.6(0.5)kT, 3.7(0.3)kT and 2.8(0.2)kT for 4%, 6% and 12% hydrogels, respectively.

Figure 5.6b displays an obvious decrease in the yield length l^* with increase in polymer concentration. The average values (l*~50, 10 and 5 nm for 4%, 6% and 12% hydrogels, respectively) correlate well with the mesh size of the hydrogels. Nevertheless, it is worth mentioning that l^* represents the deformation of a junction with length d (l^*/d ~ strain). Since d was assumed to equal the indentation length, the values of l^* might be influenced by this assumption. Our future work will be dedicated to understand better this relation.

We note that although the adhesion energy does not appear as an explicit parameter in this model, it is accounted for in the values of τ_f and τ_0 (characteristic time for bond formation and bond life times) and in the mesh size. Longer bond life times (longest for 4% hydrogels), and smaller relaxation times for re-attachment and mesh size (smallest for 12% hydrogels) promote adhesion, which is consistent with the maximum in adhesion energy observed for 6% hydrogels (Figure 5.1b).

5.3.2. Collapse of the Friction-Velocity curves into a Master Curve

An inspection of the results in Figures 5.2 and 5.3 shows a transition velocity V^* into a regime where friction is mainly dominated by viscous dissipation. At this transition velocity, a minimum in friction (F_{min}) is achieved under most of the conditions (except for 12 % hydrogels with the 20µm-colloid). Following the practice in our previous work(25), Figure 5.7a represents the normalized friction force as a function of the normalized velocity: the Y-axis gives the ratio between the friction force and the minimum friction value F_{min}; while the X-axis shows the ratio between the sliding velocity and the corresponding transition velocity, V^*. The different colors correspond to the different applied loads with the 20µm-colloid and the different symbols (circles and triangles) are used to distinguish the hydrogel composition (4% and 6% hydrogels). Except for the 12%-hydrogels (not shown), which exhibit a velocity-strengthening adhesive friction at

low velocities (Figure 5.2c), a good collapse of the normalized friction force is observed. In Figure 5.7b, the normalized friction force as a function of the normalized velocity measured with both colloids (with diameters of 5 and 20 μm) are shown together, confirming the good collapse of all the data, also for the 12% hydrogels with the 5μm-colloid. This indicates that the minimum (F_{min} and V^*) encompasses both the effects of the compressive stress, and hydrogel microstructure, if friction is mainly dictated by a (velocity-weakening) adhesive component and the concurrent (velocity-strengthening) viscous dissipation. As illustrated in Figures 5.7a-b, we find $F/F_{min} \sim (V/V^*)^m$ for most experimental conditions. The exponent m depends on the origin of energy dissipation, thereby changing from m ~-0.10 (adhesive friction) to m ~0.3 (viscous friction). These exponents are neither sensitive to the contact stress nor to the hydrogel microstructure. As illustrated in Figure 5.7, there is a deviation from the proposed power-law for some experiments (~5-10 nN, m~0.5), which suggests a different molecular mechanism underlying lubrication. We note that Gemini hydrogel interfaces also yield m ~0.5(28, 116). Since this happens at the lowest loads in our experiments, it might be associated with the lack of confinement of the polymer under small loads, but this still requires further investigation.

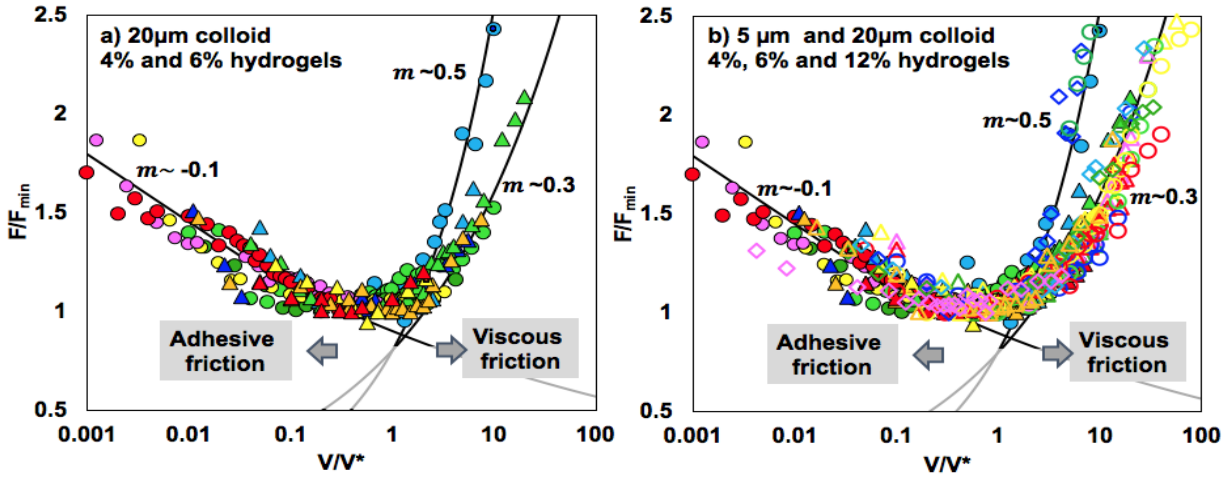

Figure 5.7 Normalized friction force ($\boldsymbol{F/F_{min}}$) as a function of the normalized velocity ($\boldsymbol{V/V^*}$) for 4% (circles), 6% (triangles) and 12% (diamonds)-hydrogels measured a) with a 20 µm colloid and b) with 20 µm (full symbols) and 5 µm (empty symbols) colloids. The black lines give $\boldsymbol{F/F_{min}}\sim(\boldsymbol{V/V^*})^{\boldsymbol{m}}$, with $\boldsymbol{m}$~-0.1 for the velocity-weakening friction regime and $\boldsymbol{m}$~+0.3 to +0.5 for the viscous regime.

5.3.3. Reconciling Previous Models for Hydrogel Friction

In previous works(27, 28, 116), the minimum in friction was related to a critical velocity $V_c \sim \xi/\tau^u \sim k_B T/\eta\xi^2$, at which the fluctuation time of the unconfined polymer τ^u equals the interaction time of the polymer in the sliding contact, reminiscent of the Deborah number(117). Other works on polymer friction have, however, proposed that models focused on the relaxation of free polymer chains are not adequate when the polymer is in a confined state(118), as we expect for the hydrogel-colloid interface to some extent, especially when the fluid is drained. In fact, our previous work(25) demonstrated that the experimentally determined V^* was orders of magnitude smaller than V_c. This is not surprising, since the physical concept of the transition velocity V^* significantly differs from V_c. To demonstrate this, we simplify the viscous-adhesive model assuming a plane-plane geometry and friction only resulting from a velocity-weakening adhesive friction and viscous dissipation, since these two terms are responsible for the observed minimum

in friction in our experiments. Under small deformations ($a_V^2 \sim R\delta_V^2$ and $A_V \sim \pi a_V^2$) and assuming $\tau_f \sim \tau_0$, Eqs.5.2-5.5 can be simplified as follows:

$$\mathrm{F} \sim \frac{G l^*}{2}\frac{A_b}{\delta_V}\left(1+\frac{l^*}{V\tau_f}\right)+\eta_{eff}V\frac{A_V}{\delta_V}+\mathrm{F}_0$$

$$\mathrm{F} \sim \frac{G(l^*)^2}{2V\tau_f}\pi R+\eta_{eff}V\pi R+F_0$$

Eq. (5.6)

where $\eta_{eff} \sim \eta'_0 V^n$ to account for a non-Newtonian behavior; note that the effective viscosity is described here as a function of the velocity and not of the shear strain rate, as in Eq. (5.3), in order to obtain a simple analytical expression for the derivative of the friction force F. This function achieves a minimum ($dF/dV = 0$) at the transition velocity V^*:

$V^* = \left(\frac{G l^{*2}}{2(1+n)\tau_f \eta_0}\right)^{\frac{1}{2+n}}$ for $n \geq 0$, and $V^* = l^*\left(\frac{G}{2\tau_f \eta_0}\right)^{0.5}$ for $n = 0$

Eq. (5.7)

at which the viscous contribution to friction equals the adhesive contribution. Eq. (7) only gives a simplified estimation of V^*, and hence, we refrain to quantitatively compare it to our experimental values. Nevertheless, it proves that the transition velocity V^* encompasses the bulk viscoelastic behavior of the hydrogel by means of G, η_0 and n, as well as the relaxation characteristics of the polymer network that determine the interfacial adhesive bonds (l^* and τ_f). We emphasize that the transition velocity V^* arises from the interplay of adhesive and viscous friction, while the critical velocity $\mathrm{V_c}$ (in previous works) only refers to the relaxation behavior of the polymer network. This suggests that the viscous dissipation hinders $\mathrm{V_c}$ to be experimentally attained.

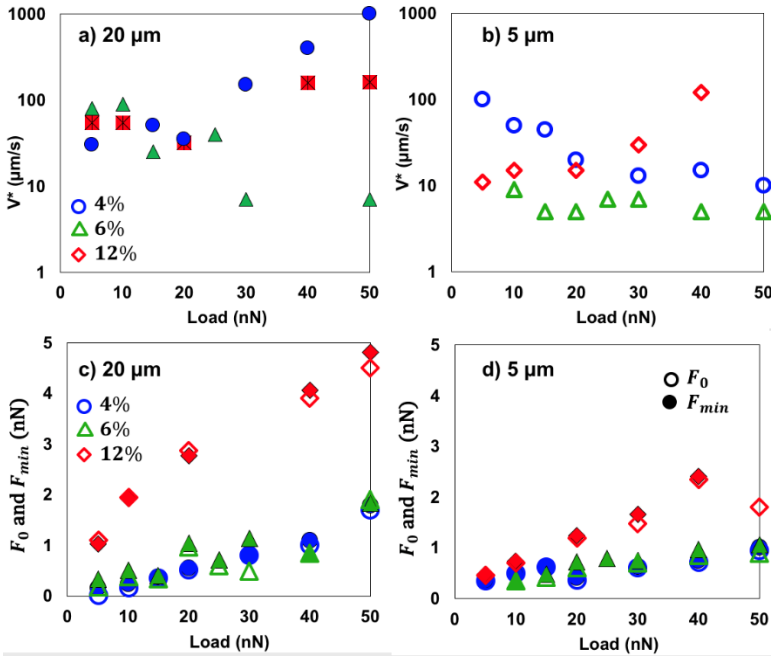

Figure 5.8 (a-b) Transition velocity $\boldsymbol{V^*}$, (c-d) friction minimum $\boldsymbol{F_{min}}$ (full symbols) and static friction $\boldsymbol{F_0}$ (empty symbols) as a function of load for 4%, 6% and 12% hydrogels, measured with the (a-c) 20 µm colloid and (b-d) 5µm colloid for the experiments shown in Figures 5.2 and 5.3. The transition velocity $\boldsymbol{V^*}$ for 12% hydrogels with the 20µm-colloid has been also depicted (red squares with stars in Figure 5.8a), even if a minimum was not attained at $\boldsymbol{V^*}$ in this case. Estimated $\boldsymbol{V_c = k_B T/\eta\xi^2}$ yields 9.3 mm/s, 14 mm/s, 41 mm/s for 4%, 6% and 12% hydrogels with $\boldsymbol{\xi}$ equal to 21, 17 and 10 nm, respectively.

Figures 5.8a-b show the experimentally determined transition velocity V^* for the three hydrogels. Eq. (5.7) can qualitatively explain the convoluted influence of hydrogel viscoelasticity, interfacial properties and stress on V^*: hydrogels with higher polymer concentration and crosslinking degree have both a higher shear modulus and effective viscosity, and shorter relaxation length l^* and time τ_f. As shown in Figure 5.6, the viscosity and relaxation times were found to change with load in an opposite fashion, which is then reflected in the complex variation of V^* with load. When using the 20µm-colloid (Figure 5.8a), the viscosity increase with load seems to predominantly affect 6% hydrogels, thereby causing V^* to decrease with an increase in load; while in 4% hydrogels, the decrease of the relaxation time with load seems more relevant, especially at high loads, and V^*

increases with an increase in load. When using the 5µm-colloid, i.e. at higher contact stresses and more pronounced squeeze-out of water, the change in viscosity with load seems to dictate the variation of V^*, while the effect of the relaxation time appears more prominent for the 12% hydrogels, perhaps because it is so small. Figure 5.8b suggests that, at the highest contact stresses, the transition into viscous dissipation is delayed for hydrogels with higher polymer concentration and crosslinking degree (smaller mesh size), however, at the cost of a higher static friction, as discussed next.

Combining Eqs. 5.6-5.7, the minimum in friction is given by $F_{min} = \mathrm{F}_0 + l^* \pi R \sqrt{G\eta_0/2\tau_f}$ for n=0; a similar expression is obtained for shear thinning that we do not show here for simplicity. A collapse of the normalized friction (F/F_{min}) vs. normalized velocity (V/V*) is only possible if the static friction is given by:

$$F_0 = k l^* \pi R \sqrt{\frac{G\eta_0}{2\tau_f}}$$

Eq. (5.8)

and therefore, $F_{\min} = (\mathrm{k}+1)\mathrm{F}_0$, k being a constant that might depend on the colloid, but this phenomenon still requires more systematic studies. Eq. (5.8) thus implies that F_{min} cannot be smaller than F_0 (velocity-independent friction). This has been obtained in the limit of small deformations, $A_V/\delta_V \sim \pi R$, and assuming $\tau_f \sim \tau_0$, a plane-plane geometry and Newtonian behavior. Although deviations from these expressions are obviously expected for the experimentally investigated hydrogels, Figures 5.8c-d confirm the correlation between F_0 (fitting parameter) and F_{min} (minimum friction force) in experiments, implying that the minimum friction force is limited by F_0. Importantly, F_{min} is similar for 4% and 6% hydrogels, which seems to result from the balance between adhesive and viscous friction -viscous friction is greater for 6% hydrogels than

for 4% hydrogels, while the opposite is observed for the adhesive friction- but F_{min} is much greater for 12% hydrogels. In summary, there is a complex interplay between microstructure and adhesive and viscous frictional dissipation.

5.4. Conclusions

The discussed results indicate that efficient hydrogel lubrication is dictated by the convolution of bulk and interfacial properties and it depends on the loading conditions. Despite the simplicity of the proposed model, it enables to correlate the hydrogel's microstructure to the frictional response through physically-based parameters, and it helps to predict the hydrogel's frictional response under different loading conditions in the absence of wear.

Furthermore, the described model can inspire design strategies that afford control of the velocity-weakening frictional response. For instance, a less crosslinked surface layer supported by a more crosslinked (stiffer) hydrogel appears as a design approach to increase V^* according to Eq. (5.7), and therefore, to shift the viscous dissipation to higher sliding velocities. As a matter of fact, biological systems that are characterized by very low coefficients of friction exhibit graded microstructures. Mucins, which are gel-forming, high molecular weight glycosylated proteins, are present in the inner most layer of the tear film on the surface of the cornea to provide protection, hydration and lubrication during regular eye functions (119, 120). Similarly, glycoproteins with bottle-brush structures adsorb on the surface of (poroelastic) cartilage and help to reduce friction(121, 122). Synthetic approaches have already proved the efficiency of this relation. For instance, the surface functionalization of PDMS(123) and (pHEMA) hydrogels(47) with polymer brushes and entangled polymer networks have shown a decrease in friction coefficient by orders of magnitude while retaining the structural integrity of the system. Along the same lines, contact

lenses exhibit a graded microstructure with surface layers that have a lower elastic modulus and higher water contents compared to the core material(8).

CHAPTER 6: STATIC FRICTION AND CONTACT AGING OF HYDROGEL-LIKE MATERIALS

The effect of contact time, load, sliding velocity and temperature on static friction and adhesion between polyacrylamide (PAAm) hydrogels (with three different microstructures) and a silica colloid is investigated in this chapter. A phase diagram for hydrogels' static friction is inferred from this study and its implications on biological tribosystems and biomaedical applications are discussed.

6.1. Materials and Methods

6.1.1. Materials

All experiments were conducted on 4, 6 and 9% PAAm hydrogels.

6.1.2. Static Friction measurements

Lateral force measurements were conducted with an AFM at various lateral velocities of the piezo, loads and temperatures on all three hydrogels to determine static friction. The experiments were repeated at least on three different samples of each hydrogel type to confirm the reproducibility of the results. At the point of reversal of the piezo (i.e. under zero tangential force), the normal load was maintained constant for a period of time (t_{hold}) that ranged from 5 to 60 seconds; this was repeated three times per loading condition and sample. The lateral velocity of the piezo was varied between 0.2 and 10 μm/s, while the scan length was kept constant at 28 μm. Normal loads between 5 and 50 nN were selected for the static friction-force measurements. A petri dish heater (JPK Instruments, Germany) was used to modulate the temperature in the range of 25 to 60 ºC. At least 4 hours of equilibration time were allowed at each selected temperature to ensure that hydrogels, sample holder, fluid, as well as colloid, were in thermal equilibrium. The

static friction F_s was defined as the maximum lateral force before sliding started and the friction force dropped to the dynamic value (see Figure 6.1b). A GUI developed in MATLAB was used to determine F_s. Both height and lateral deflection of the cantilever were inspected to ensure that pill-up did not happen. Loads higher than 30 nN were not applied in static friction measurements on 4% hydrogels above room temperature.

6.1.3. Indentation measurements

Indentation measurements were performed on each hydrogel sample at an approach/retraction velocity of 2 μm/s at room temperature just before the friction measurements. The colloid was retracted after a hold time varying between 0 and 60 s, and the pull-off force was defined as the minimum value in the retraction curve; at least ten measurements were carried out per loading condition and sample. The adhesion energy was obtained from the integral of the negative portion of the force-indentation depth curve upon retraction (see Figure A1). Pull-off force and adhesion energy correlate very well under all conditions, and hence, we show only the pull-off force. On selected samples (at least two per hydrogel type), the indentation measurements were also carried out at modulated temperature between 25 ºC and 50 ºC. The results shown in Figs. 1-5 and in the SI correspond to the average values and the standard deviation of static friction and pull-off force. Elastic moduli were obtained by fitting the JKR model.

6.2. Results

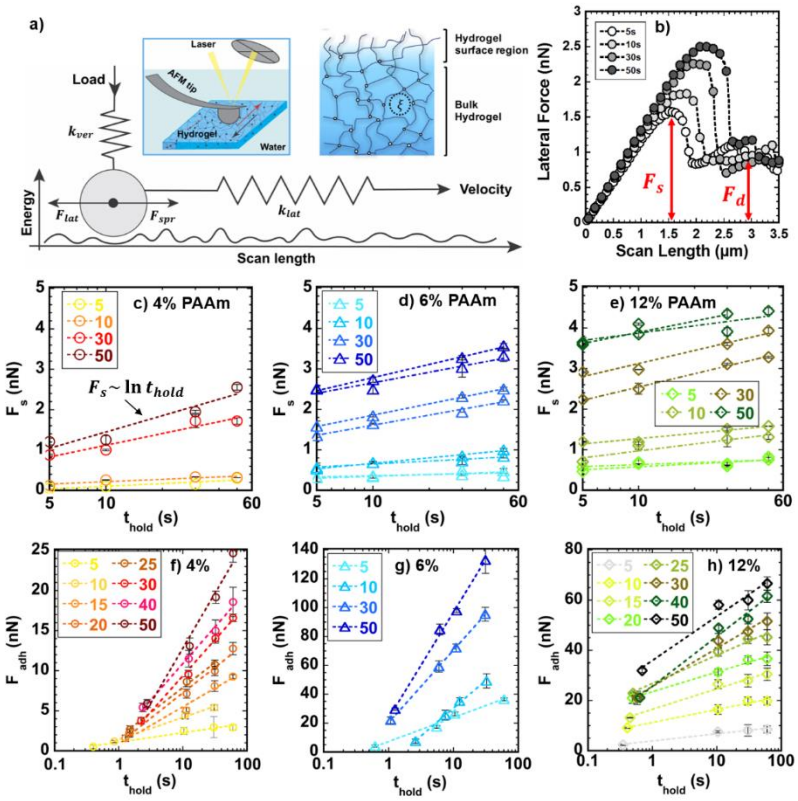

Figure 6.1 Static friction and adhesion at room temperature (25ºC). a) Schematics of lateral force measurements by AFM. When the colloid is laterally pulled, it experiences a lateral force $\boldsymbol{F_{lat}}$, which leads to a torsion of the cantilever, while the applied load ($\boldsymbol{L}$) is maintained constant. The laser reflected by the cantilever quantifies its deflection, and the lateral force is determined with the lateral spring constants ($\boldsymbol{k_{lat}}$). b) Lateral force measured while the cantilever is laterally pulled at a velocity ($\boldsymbol{V}$) of 2 μm/s after loading times ($\boldsymbol{t_{hold}}$) of 5, 10, 30 and 60 s ($\boldsymbol{L}$=50 nN) for a 6 % hydrogel. The diagram shows static friction ($\boldsymbol{F_s}$) and the drop to dynamic friction ($\boldsymbol{F_d}$), once sliding commences; c-e) Static friction *vs.* hold time at normal loads of 5, 10, 30 and 50 nN for c) 4% (circles in red-yellow shades), d) 6% (triangles in blue shades) and e) 12% (diamonds in green shades) hydrogels, at lateral velocities of 5 μm/s (dash-dotted line) and 10 μm/s (dashed line). The lines represent logarithmic fits ($\boldsymbol{F_s \sim \ln t_{hold}}$) with a R^2-value better than 0.85 at loads larger than 5 nN (see Table S1); the fits exhibit occasionally smaller R^2-values under 5 nN. f-h) Pull-off force ($\boldsymbol{F_{adh}}$) *vs.* hold time ($\boldsymbol{t_{hold}}$) at normal loads between 5 and 50 nN (see legend) for f) 4%, g) 6% and h) 12% hydrogels at an approach/separation velocity of 2 μm/s; the hold time includes the contact time during approach and separation of the colloid, which is smaller than 2.5 s in all cases. In all diagrams in this work, the markers give the average of at least 3 and at most 10 measurements and the error bars represent the standard deviation. The error bars are occasionally smaller than the marker size, and therefore, not always visible. Colloid Radius = 10.6 μm. Cantilever stiffness= 0.42 N/m.

PAAm hydrogels were prepared with 4.4, 6.4 and 12.4 wt% of the acrylamide monomer and are referred to as 4%, 6% and 12% hydrogels in the following. The chemically crosslinked hydrogels have characteristic mesh sizes of 21, 17 and 11 nm, respectively (26). AFM lateral force measurements were conducted with a silica colloid glued to the end of a tipless cantilever (Figure 6.1a). A constant normal load (L) was applied on the hydrogel for a period of time (static loading time or hold time, t_{hold}) before the cantilever was pulled laterally at constant velocity (V) by a piezo. Figure 6.1b illustrates the lateral force after selected hold times as a function of the piezo position. The static friction (F_s) is defined as the maximum lateral force before sliding commences, which is characterized by the sudden drop in friction to the value given by the dynamic friction (F_d). Figs. 1c-e show the static friction as a function of hold time at selected normal loads (see legend) for c) 4%, d) 6% and e) 12% hydrogels, respectively. The logarithmic increase of static friction with hold time at room temperature is reminiscent of the contact ageing characteristic of dry interfaces described in the Introduction.

The logarithmic relation between static friction and hold time is maintained in the range of lateral velocities between 0.5 and 10 μm/s, but the static friction becomes larger with an increase in the lateral velocity (V). This is illustrated in Figs. 1d-e for 5 and 10 μm/s (dash-dotted and dashed lines, respectively). Figure 6.2 provides additional evidence for the reproducible increment in static friction with lateral velocity for the three hydrogels which is discussed later. In contrast, the static friction was observed to deviate from the logarithmic increase and to remain constant or even decrease with hold time at the slowest probed velocity (0.2 μm/s). This demonstrates that the time under shear loading before sliding occurs (i.e. while the piezo moves at the selected velocity V and the lateral force increases to F_s in Figure 6.1b) also affects contact ageing. During this period of time, the hydrogel undergoes deformation, thereby dissipating part of the energy stored during

static loading. If there is sufficient time (i.e. at slow velocity), static friction decreases, and contact ageing can be completely lost, which occurs at 0.2 μm/s here.

The adhesion was measured upon retraction of the colloid from the hydrogels after hold times varying between 0 and 50 s (Figure 6.1f-h). The pull-off force (F_{adh}) was defined as the minimum force in the retraction curve (Figure A1). The highest pull-off forces were measured for 6% hydrogels, while the smallest values were obtained for 4% hydrogels (Figure 6.5). This can be explained by the contribution of both the interfacial energy (γ) and the contact area (A_r) to adhesion, as follows. Using the JKR model (114) to analyze indentation force-depth curves upon retraction yields both terms, γ and A (see SI text and Table S2). Although the interfacial energy is highest for 12% hydrogels, likely stemming from their largest polymer concentration, the contact area between 6% hydrogels and the colloid is larger than that of 12% hydrogels, which explains the greater pull-off force of 6% hydrogels. While the contact area between the colloid and 4% hydrogels is the largest, the interfacial energy (γ) is about one order of magnitude smaller, which leads to the smallest values of the pull-off force. Similar to the static friction of the three hydrogels at room temperature, the pull-off force increases with the logarithm of the loading time (Figure 6.1f-h), supporting that the increase in static friction with hold time is associated to the adhesion of the hydrogel to the colloid, which is consistent with the adhesion model (52).

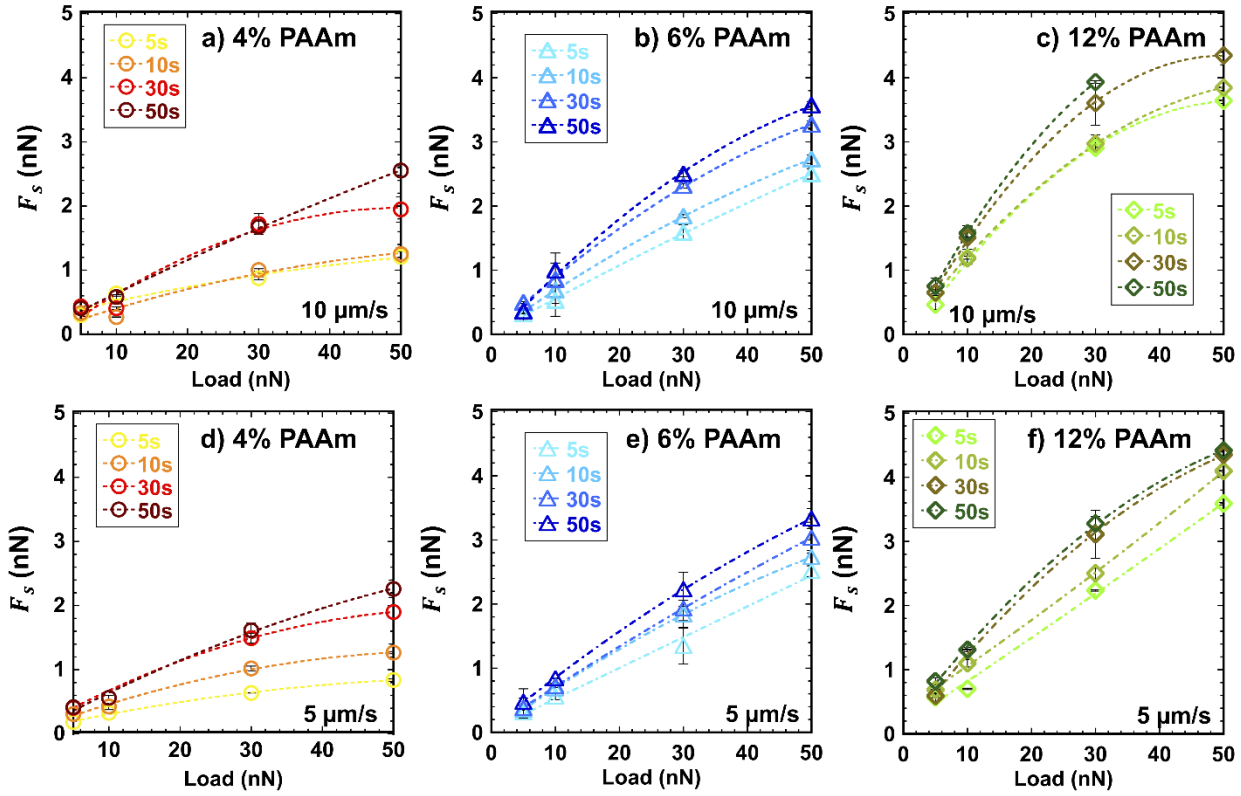

Figure 6.2 Load dependence of static friction at room temperature. Static friction as a function of normal load for a) d) 4% PAAm, b) e) 6% PAAm and c) f) 12% PAAm hydrogels at various hold times (see legend, in seconds) and lateral velocities of (a-c) 10 μm/s and (d-f) 5 μm/s. The static friction significantly increases with normal load, but the relation between friction and normal load is often sublinear. Temperature =25 ºC. Colloid Radius = 10.6 μm. Cantilever stiffness= 0.42 N/m.

Figure 6.2 shows the static friction significantly increases with normal load, as expected however non-linearly (dashed lines) as shown for lateral velocities of 5 and 10 μm/s. This is consistent with the sublinear relation between dynamic friction and normal load reported for the same polyacrylamide hydrogels previously (25). This deviation from Amonton's law (i.e. the linear relation between friction and load) has been attributed to the significant increase in adhesion with applied load (124).

Pull-off and lateral force measurements were also conducted as a function of temperature ranging between 25 and 60 ºC. Representative results of the static friction as a function of hold

time and temperature are shown in Figs. 3 and 4, respectively. The dashed lines in Figure 6.3 represent the fits to a logarithmic function of the hold time. Deviations from this logarithmic trend are generally observed when the temperature increases, but the response is very different for each hydrogel type and load. In the case of 6% hydrogels, for instance, an increase of temperature to 50ºC results in a reversed change of the static friction with hold time at 20 nN (Figure 6.2a), while the logarithmic trend is preserved at 50 nN (Figure 6.2b). In contrast, the static friction of 4% and 12 % hydrogels only increases logarithmically with hold time at 25ºC and 30ºC under similar loading conditions (Figure 6.2c and 6.2d). The most prominent ageing behavior at high temperature is thus observed for 6% hydrogels, which are the hydrogels that exhibit the highest adhesion to the colloid (Figures 6.1 and 6.5).

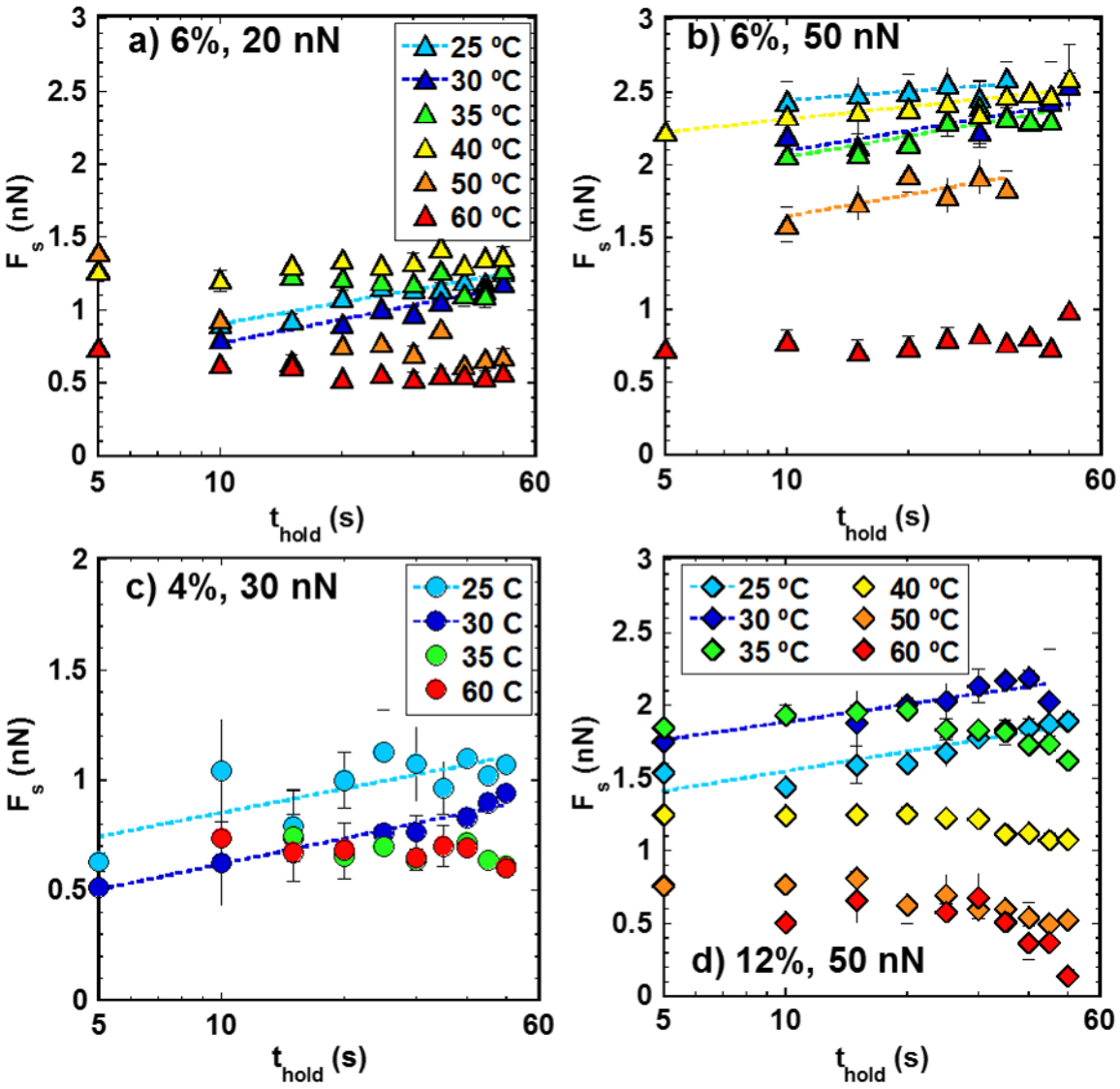

Figure 6.3 Time dependence of static friction in the temperature range 25ºC – 60ºC. Static friction $\boldsymbol{F_s}$ as a function of hold time $\boldsymbol{t_{hold}}$ measured at 25 ºC (light blue), 30 ºC (dark blue), 35 ºC (green), 40 ºC (yellow), 50 ºC (orange) and 60 ºC (red) for 6% hydrogels at (a) 20 and (b) 50 nN (triangles), (c) 4% hydrogels at 30 nN (circles) and (d) 12 % hydrogels at 50 nN (diamonds). The dashed lines represent the logarithmic fit to the data, with a regression coefficient R^2 better than 0.87. The thick semi-transparent lines are to guide the eye. Colloid radius = 10.7 μm. Cantilever stiffness = 0.42 N/m. Lateral velocity: 1 μm/s.

Figs. 4a-f show the prominent variation of the static friction with temperature. This representation reveals a local minimum and either one or two local maxima in the static friction of 6% and 12% hydrogels and are labeled as T_{min}, T_p and T_p^*, respectively. The higher shade intensity represents longer hold times (see legend) before pulling the cantilever laterally. Hence, the increase

in static friction with the color intensity at a particular temperature indicates contact ageing, while the opposite trend is related to the decrease in static friction with hold time. Contact ageing is more remarkable in 6% hydrogels and at lower temperatures, as mentioned earlier. The reverse trend, i.e. that static friction decreases with longer hold times, is more pronounced on 12% hydrogels above 30 – 40 ºC at the three loads (Figs. 4d-f); note that the logarithmic relation persists up to higher temperatures if higher loads are applied. In the case of 4% hydrogels (Figure A5), the static friction decreases with temperature, and it becomes *quasi* independent of temperature and hold time. It is thus evident that the microstructure of the hydrogels plays an important role in dictating the relations between static friction, temperature and hold time.

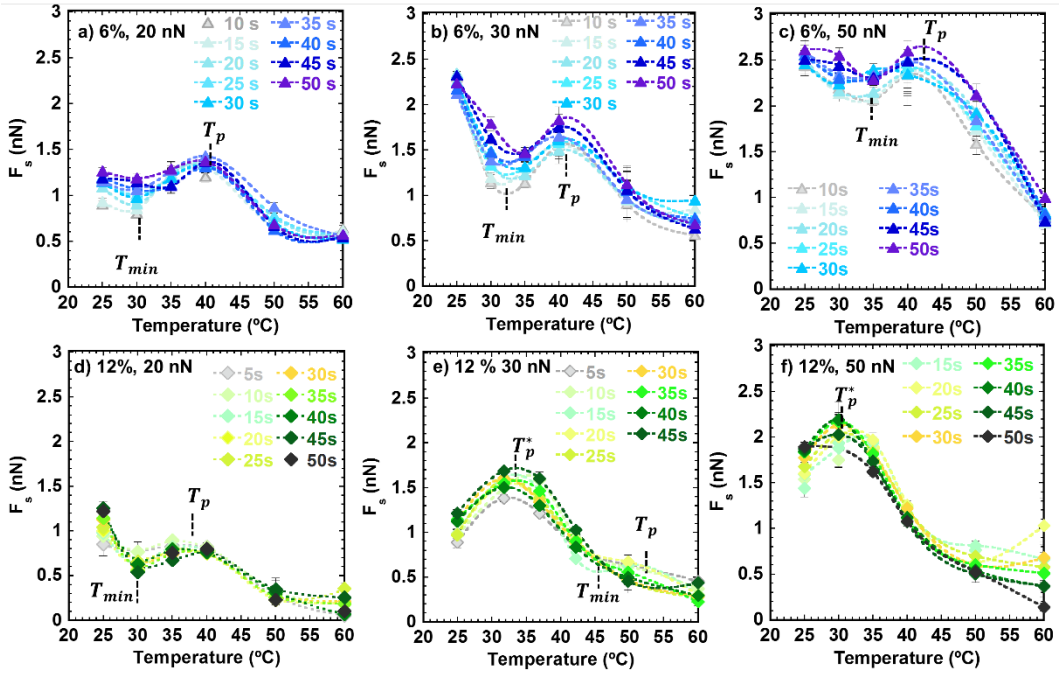

Figure 6.4 Temperature dependence of static friction and of Young's modulus. a-f) Static friction $\boldsymbol{F_s}$ as a function of temperature for different hold times between 5 s and 50 s (see legends) for 6% hydrogels at a) 20, b) 30 and c) 50 nN, for and for 12% hydrogels at d) 20, e) 30 and f) 50 nN. The lines show the fits of the experimental results to spline functions to determine $\boldsymbol{T_p^*}$, $\boldsymbol{T_p}$ and $\boldsymbol{T_{min}}$ at the extrema of the static friction; a collection of the characteristic temperatures is shown in Figure 6.7c. Colloid radius = 10.7 μm. Cantilever stiffness= 0.42 N/m. Lateral velocity for friction-force measurements: 1 μm/s.

Similarly, the change of the pull-off force with temperature is non-monotonic and strongly dependent on hydrogel's microstructure (Figure 6.5). The pull-off force between the silica colloid and 4% hydrogels drops initially with temperature, and then, it plateaus. A prominent decrease in pull-off force with increase in temperature and the highest values in pull-off force are observed for 6% hydrogels; local minima and maxima (θ_{min} and θ_p) are obvious, especially at smaller loads. In the case of 12% hydrogels, the pull-off force also varies non-monotonically with temperature,

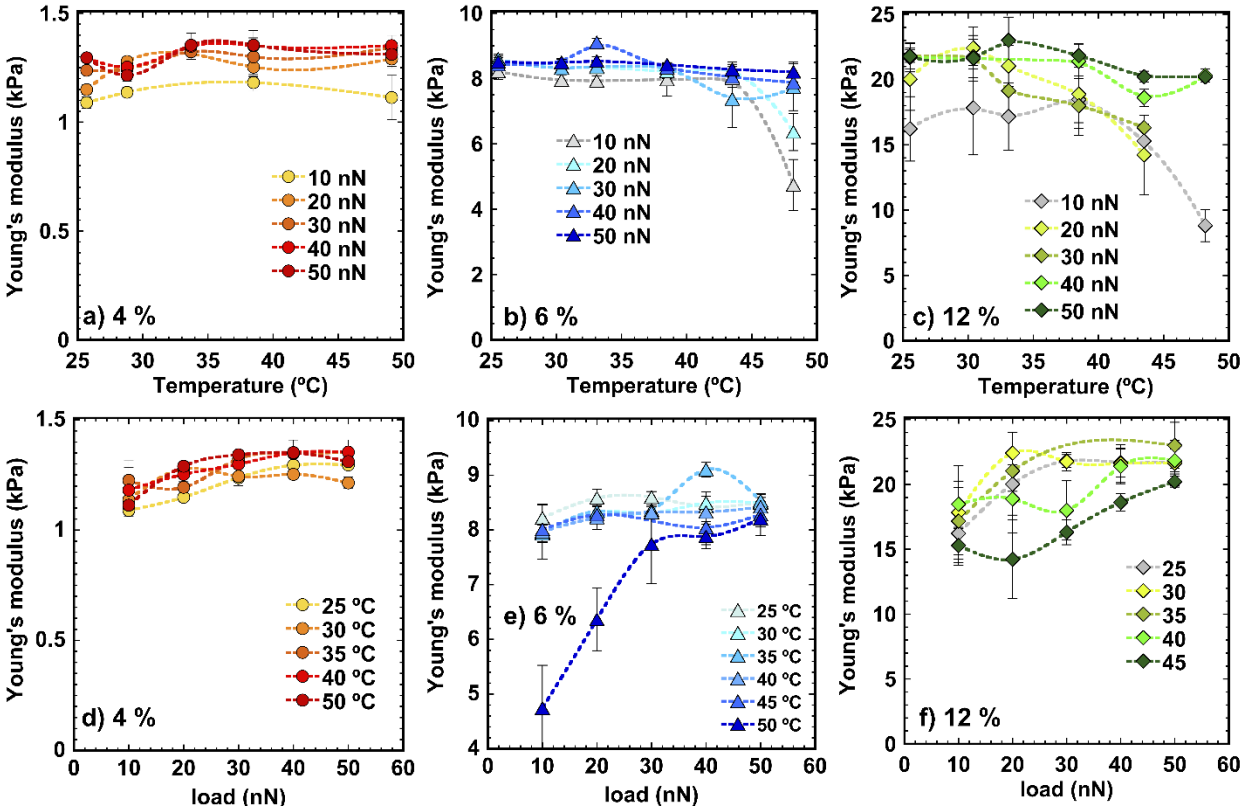

Figure 6.5 Elastic modulus of the hydrogels as a function of the temperature for a) 4% (circles), b) 6% (triangles) and c) 12% (diamonds) hydrogels. The elastic moduli were determined from colloidal probe indentation experiments using the JKR. The applied normal load prior to the retraction of the cantilever was varied in the range 10-50 nN (legend). The same data are shown in d-f) with the load in the X-axis and the temperature in the legend. Colloid radius = 10.7 μm. Cantilever stiffness = 0.42 N/m. Approach and retract speed: 1 μm/s.

with very prominent extrema under all applied loads. While θ_{min} and θ_p differ from T_{min} and T_p (for the static friction), these results support that (non-monotonic) changes in adhesion with temperature may underlie the variation in static friction, which is discussed later.

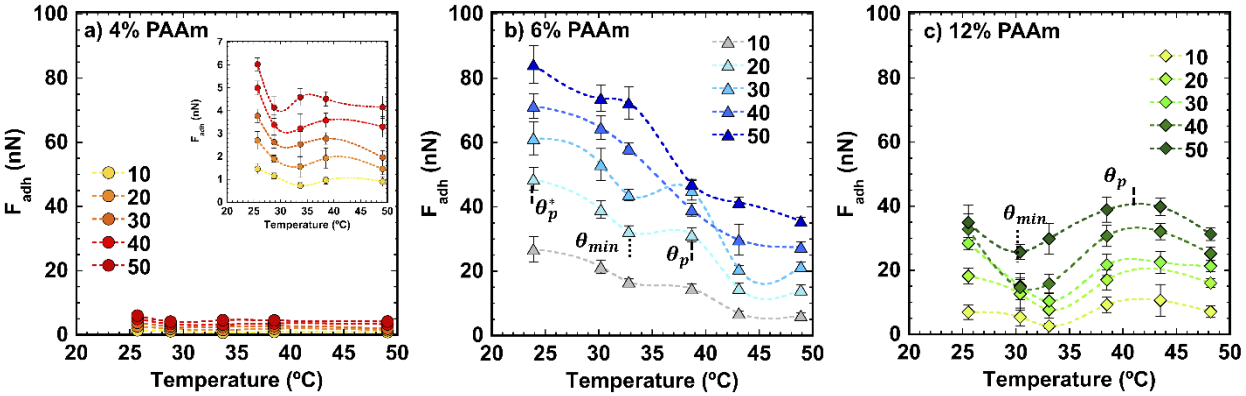

Figure 6.6 Pull-off force ($\boldsymbol{F_{adh}}$) as a function of temperature for a) 4% PAAm, b) 6% PAAm and c) 12% PAAm hydrogels. The applied normal load prior to the retraction of the cantilever was varied in the range 10-50 nN (see legend). The inset in a) shows a magnification of the pull-off force. The contact times range from 0.8, 0.5, and 0.2 s (at the load of 10 nN) to 2.4, 1.2, and 0.8 (at the load of 50 nN) for 4, 6 and 12% PAAm hydrogels, respectively. The lines show the fits of spline functions to the experimental results to determine the characteristic temperatures of the extrema values of the pull-off force. Approach and retraction speed = 1 μm/s. Colloid radius = 10.7 μm. Cantilever stiffness = 0.42 N/m.

Figure 6.6 shows the elastic moduli of 12% hydrogels; a detailed explanation of the method used to determine the elastic moduli is described in materials and methods. The surface region of the hydrogel is softer, as demonstrated by the smaller elastic modulus of the hydrogels measured upon an applied load of 10 nN compared to higher loads. In the case of 12% hydrogels, the elastic modulus decreases by 45% as the temperature increases from 25.4 to 48.2 ºC upon a normal load of 10 nN, while at higher loads (20 – 50 nN) the decrease of the modulus with increase in temperature ranges from 4 to 8 %. Similarly, for 6%, hydrogels, a decrease in modulus is seen when the temperature is increased, especially when the modulus is determined upon an applied normal load of 10 nN. In the case of 4% hydrogels, however, the influence of the temperature on the elastic moduli is less significant, as it also happens to the static friction. If the change in the

pull-off force with temperature would solely result from a change of contact area, an inverse correlation between the elastic modulus (E) and the pull-off force would be expected according to the JKR model ($F_{adh} \sim A_r \sim E^{-2/3}$). Figures 6.5-6.6 provide evidence for the lack of such correlation. Figure 6.6c reveals that (i) the elastic moduli measured under an applied load of 10 nN are significantly smaller than at higher loads for 6% and 12% gels (~40-50% smaller) and slightly smaller for 4% gels (~20% smaller); (ii) at the highest applied loads (40 and 50 nN), the influence of load on the modulus is not statistically significant for all gels; (iii) and the behavior is transitional under applied loads of 20 and 30 nN for 12% gels. We attribute these results to the well-known inhomogeneous polymerization of polyacrylamide hydrogels close to a hydrophobic surface, which leads to reduced crosslinking near the surface (91). The transitional load-dependent behavior of 12% gels indicates higher gelation inhomogeneity compared to the other two gels, perhaps due to the higher polymer concentration and hence significant concentration gradient as a function of distance from the glass surface. The elastic modulus determined upon indentation is associated to the mechanical response of a superficial region with a specific thickness approximately given by the indentation depth. For instance, the indentation depth at an applied load of 10 nN at room temperature is ~ 1.64, 0.49, 0.31 μm for 4%, 6% and 12% hydrogels, respectively, and it increases to 3.45, 0.74, 0.52 μm upon an applied load of 30 nN. Hence, the smaller elastic moduli determined at 10 nN might thus originate from the more significant influence of the hydrogel's surface region with reduced crosslinking. Based on this, we propose this "skin" has a thickness in the range of hundreds of nanometers (in 12% and 6 % hydrogels) to ~1-1.5 μm (in 4% hydrogels). Interestingly, a softening of the surface of 6% and 12% hydrogels (probed at 10 nN) is reproducibly observed at 50 ºC, the highest examined temperature (Figs. 6). We attribute this to the increased mobility of the near-surface uncrosslinked polymer chains at

high temperature. The higher crosslinking of the sub-surface hydrogel (probed at higher loads) makes the elastic modulus less susceptible to changes in temperature.

6.3. Discussion

Contact ageing, that is, the logarithmic increase in static friction with the time of static loading, is a characteristic of the investigated hydrogel-glass interfaces at room temperature. This logarithmic relation is also observed for the pull-off force vs. loading time, supporting that the mechanism underlying contact ageing is related to an increase in adhesion with the duration of static loading. To quantify contact ageing, the empiric expression $F_s = L(\alpha_s^L + \beta_s^L \ln t_{hold})$ was fit to the experimental results exhibiting a logarithmic relationship and the corresponding logarithmic slopes (β_s^L) are shown in Figure 6.7a. The logarithmic slope is of the same order of magnitude for the three hydrogels, which suggests that, despite the differences in the hydrogels' mesh size, the underlying mechanisms are similar. The higher values of β_s^L at 10 μm/s compared to 2 μm/s reflect that the viscoelastic relaxation upon slow shear (before sliding commences), which was shown to reduce the static friction, also attenuates the ageing rate. While β_s^L is of the same order of magnitude than that reported for polymer glasses far from their glass transition (52), our results are intrinsically different. First, β_s^L for polymer glasses increases by a factor of ~3-4 around their glass transition as the polymer mobility increases. In contrast, the logarithmic increase of the static friction with hold time is lost on 4% and 12 % hydrogels above ~30-40ºC. In Figure 6.4a, the decrease in β_s^L with increase in temperature in the case of 6% hydrogels indicates that the ageing rate also becomes less severe at higher temperature. Second, the increase in load leads to a prominent decrease in β_s^L, which indicates that the ageing rate becomes progressively alleviated with an increase in load.

The change of hydrogel's static friction with temperature is non-monotonic (Figure 6.4). Reported relations for adhesion hysteresis, dynamic and static friction of rubbers (125) and thin liquid films (126) also peak at a characteristic temperature, observation time or velocity. This was reconciled by Israelachvili in a phase diagram as a function of the Deborah number, $D_e = \tau/\mathrm{t}$ (τ being a characteristic relaxation time and t the observation time), or of the temperature, based on the time-temperature superposition principle (124). The Deborah number characterizes the material fluidity, i.e. the observation that "given enough time even a solid will flow". If there is enough time for relaxation to happen, the polymer network behaves liquid-like (small D_e values, high temperature). At short observation times (large D_e values, low temperature), there is less time for the polymer to relax, so that it behaves like a solid. The influence of the temperature on adhesion and friction can be described *via* a rate process of polymer attachment to and detachment from the colloid during static loading. Being thermally activated rates, both are promoted by an increase in temperature. If the temperature is high enough, the mobility of the polymer could be sufficient to detach from the colloid and diffuse out of the contact during static loading; this characterizes the liquid-like behavior, and it yields a decrease in adhesion and friction with temperature (126). In contrast, if the interfacial polymer's behavior is solid-like, an increase in temperature would enhance polymer attachment, adhesion and static friction. This behavior would lead to a single peak in the static friction at T^*. Previous studies on dynamic friction of rubbers have related this peak to their glass transition temperature T_g, so that $T^* \sim T_g$ +50 K (125).

As biphasic polymeric materials holding large amounts of water, hydrogels undergo two main stress relaxation mechanisms, viscoelastic and poroelastic; the latter is related to the pressure-induced drainage of the interstitial water (14). The viscoelasticity of flexible polymers like polyacrylamide is characterized by the thermal fluctuation time $\tau_P^0 \sim \eta\xi^3/k_BT$, η being the fluid

viscosity, k_B the Boltzman constant, T the temperature, and ξ, the mesh size. According to de Gennes' scaling theory (127), the osmotic pressure of hydrogels is related to that of semidilute polymer solutions at the overlap concentration, i.e. $\Pi \sim k_B T \xi^{-3}$. In equilibrium, the osmotic pressure equals the elastic contribution $\Pi \sim G$, so that the elastic modulus G can be approximately related to its mesh size. With the elastic modulus of the selected hydrogels measured with a parallel plate rheometer under volume conserving conditions (0.44, 0.80 and 3.1 kPa), a mesh size of ~21, 17 and 11 nm was estimated for 4, 6 and 12% hydrogels, respectively (26). This mesh size yields relaxation times (τ_P^0) in the order of a few µs, *i.e.* much shorter than the loading times in static friction measurements (seconds). However, the confinement provided by the colloid restricts the mobility of the interfacial polymer, and hence, relaxation times at the confined interface (τ_P) are greater than τ_P^0. Nevertheless, an increase of the relaxation time by six orders of magnitude is unlikely, considering that the relaxation time of polymer melts only increases by two orders of magnitude upon confinement (128).

According to this simple estimation, the polymer network should relax in a time scale much shorter than probed in static friction experiments, thereby excluding its effect on contact ageing. However, this does not apply to the polymer network in the near-surface region. Here, the less crosslinked polymer exhibits much longer relaxation times. For instance, assuming the presence of a brush-like superficial layer with a length of ~1 µm, the relaxation time τ_P^0 would be ~1 s and this relaxation time could be further prolonged upon the confinement provided by the colloid ($\tau_P > \tau_P^0$). Therefore, it is possible that the observed increase in static friction (and adhesion) with hold time is related to the relaxation of the less crosslinked and confined polymer in the near-surface region, which forms a higher number of adhesive bonds to the glass surface with prolonged contact time.

The change in hydrogel's static friction with temperature is, however, more intricate, and a local minimum at T_{min} and one or two maxima are reproducibly observed (Figure 6.4), which suggests the action of additional mechanisms. Taking into account that the osmotic modulus of the relaxed hydrogels is close to the elastic modulus determined under volume conserving conditions (129), the applied pressure overcomes the osmotic modulus under most of the loading conditions (Table S2). Pressures above the osmotic modulus cause a redistribution of water and polymer within the stressed region (110). Accordingly, drainage of the interstitial water with a concurrent increase of the contact area with time happens during static loading and contributes to the increase in static friction with hold time, as well. The relevance of this phenomenon in our experiments is supported by the estimated poroelastic relaxation times (τ_W) according to $\tau_W = 6\pi\eta a^2/P\xi^2$, a being the contact radius and P the pressure (14). This expression yields values in the order of a few seconds for the three hydrogels at room temperature (Figure A6), and hence, in the same order of magnitude as the hold time in this work. Admittedly, this is a rough estimation, but a more precise calculation of the fluid drainage would require the numeric solution of coupled mechanical and mass transfer models, which is out of the scope of this work.

It is thus proposed that the superposed poroelastic and polymer relaxation associated to the biphasic nature of hydrogels (τ_P and τ_W) leads to two characteristic peaks (T_p^* and T_p) and a local minimum (T_{min}) in the static friction, which is generalized in a phase diagram in Figure 6.7b (black line). At temperatures below T_p^*, the static friction increases with an increase of temperature, which is associated with the solid-like response of the hydrogel; here, polymer attachment to the colloid is enhanced with temperature, yielding an increase in the shear strength of the interface (σ_s). The peak at lower temperature (T_p^*) is, however, only obvious in the case of 12% hydrogels (Figure 6.4e-f), which suggests that the investigated temperatures are too high to probe this behavior in 4

and 6 % hydrogels with looser polymer networks. Interestingly, the glass transition of polyacrylamide is ~-10 ºC (130), and T_p^* for 12% hydrogels is ~30 ºC, which is 40 K above T_g, in qualitative agreement with the relation reported for T^* of rubbers (125).

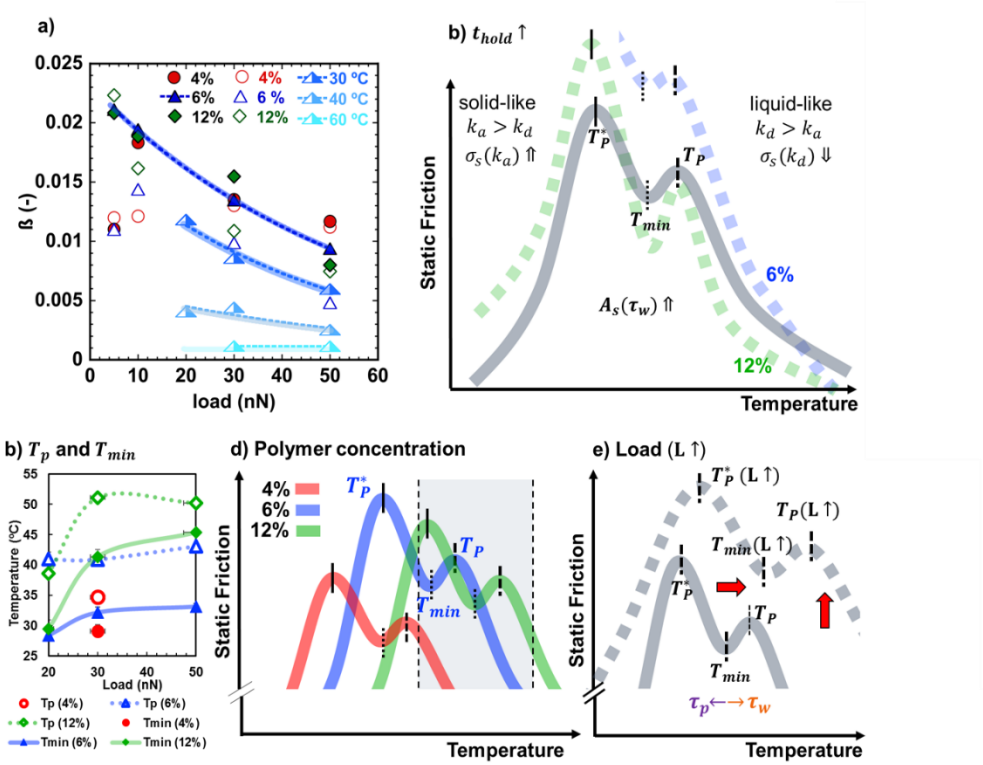

Figure 6.7 Logarithmic slope and phase diagram of hydrogel's static friction, including the effects of hold time, mesh size and load. a) Logarithmic slope $\boldsymbol{\beta_s^L}$ at selected velocities of 10 µm/s (full markers) and 2 µm/s (empty markers) at 25ºC for the three hydrogels and at higher temperatures (30ºC, 40ºC, 60ºC, split triangles) only for 6% hydrogels. b) Phase diagram of hydrogels' static friction and effect of increase in hold time (blue dashed line for 6% hydrogels and green dotted line for 12% hydrogels); effects of d) hydrogel's microstructure (i.e. mesh size) and e) load. The characteristic temperatures $\boldsymbol{T_{min}}$ and $\boldsymbol{T_p}$ shift to higher values with decrease in mesh size (~21, 17 and 11 nm for 4%, 6% and 12% hydrogels, respectively) and are shown in c) as average and standard deviation in the range of investigated hold times. $\boldsymbol{T_{min}}$ and $\boldsymbol{T_p}$ for 12% hydrogels at 30 and 50 nN correspond only to $\boldsymbol{t_{hold} < 20}$ s, because they vanish at longer loading times.

In the range of examined temperatures, the decrease in static friction with temperature is prominent. This reflects the liquid-like behavior of the polymer above T_p^*. Here, polymer diffusion and detachment are enhanced, which causes a decrease in shear strength σ_s with temperature, and

thus, friction. Drainage of water concurrently happens during static loading. The liquid drainage is yet enhanced with temperature due to the reduction of water viscosity (from 0.89 mPa.s at 25ºC to 0.47 mPa.s at 60ºC), thereby leading to greater contact areas A_r with increasing temperature.

This may partially compensate the decrease in shear strength due to the liquid-like behavior of the polymer network. These two competing mechanisms are at the root of the (more or less pronounced) extrema at T_p and T_{min}. Above T_p, the liquid-like behavior of the interfacial polymer dictates the decrease of both the interfacial strength and the static friction with temperature.

Hydrogels' mesh size ξ determines poroelastic and polymer relaxation times, and thereby, the temperatures at which local minimum (T_{min}) and maxima (T_P and T_P^*) are achieved. T_{min} and T_P were obtained by fitting a spline function to the results in Figs. 4a-f and the values are depicted in Figure 6.7c. In the case for 4% hydrogels, T_P is below room temperature, and therefore, not measured. Hence, maxima and minima shift to higher temperatures with a decrease in mesh size (~21, 17 and 11 nm for 4%, 6% and 12% hydrogels, respectively). Note that the range of selected temperatures only probes a small region of the phase diagram of the investigated hydrogels (Figure 6.7d). This could explain that T_p^* can be only examined for 12% hydrogels. The behavior of 4% hydrogels seems to achieve the so-called "bulk thermodynamic limit" or liquid behavior (dashed line), where the influence of the temperature vanishes (124).Considering that both relaxation times are of relevance under the investigated conditions, it is proposed that hydrogel's contact ageing results from the superposed effects of polymer relaxation at the confined interface and fluid drainage; the former affects the time-dependent interfacial strength $\sigma_s(t_{hold})$ and the latter influences the true contact area $A_r(t_{hold})$. This let us reconcile our results with the adhesion model for rubber's ageing, which gives the static friction as $F_s(t_{hold}) = A_r(t_{hold}) \cdot \sigma_s(t_{hold})$ and $F_s \sim \ln(t_{hold})$, as observed in experiments (52). The key difference is that, while drainage of the

interstitial water leads to a monotonic increase of A_r with hold time, the change of σ_s with time is non-monotonic. The result is an intricate evolution of hydrogel's static friction with hold time (Figure 6.7b, dashed lines). According to our conceptual model, contact ageing happens at $T < T_p^*$ due to both the poroelastic and the polymer relaxation. Above T_p^*, the liquid-like behavior of the polymer increasingly hinders contact ageing due to the promoted polymer diffusion and detachment from the colloid. Here, the increase of static friction with hold time is dictated by the fluid drainage and the corresponding increase in contact area. Beyond T_p, the polymer detachment/diffusion gradually dominates, and contact ageing vanishes eventually. For instance, the prominent decrease of the static friction of 12 % hydrogels with hold time and the vanishing minimum (Figs. 4e and 4f) are the signature of the increasingly dominating liquid-like behavior of this interface. It is evident that the liquid-like behavior of 6% hydrogels is only achieved at temperatures close to 60ºC, and hence, contact ageing of this interface is more prominent, as is its adhesion (Figure 6.5).

Importantly, when higher loads are applied, opposite trends are expected for both contributions: τ_P should increase due to the enhanced interfacial confinement, thereby slowing down the rate of interfacial polymer bonding and diffusion, while τ_W should decrease with load, leading to a faster growth of the contact area. The prominent decrease in β_s^L with load suggests that the viscoelastic relaxation is responsible for the slowdown of the ageing rate with increase in load (Figure 6.7a). Finally, the longer polymer relaxation times can explain why T_p shift to higher temperatures when the load increases from 20 to 30 nN (Figure 6.7c), which also justifies the increase in T_{min}. The influence of the load on the phase diagram of hydrogel's static friction is thus schematically shown in Figure 6.7e.

The pull-off force follows a non-monotonic trend as a function of temperature similar to that observed for the static friction (Figure 6.4a-f). The concomitant effects of poroelastic and polymer relaxation -characteristic of hydrogels- give rise to two peaks (θ_p and θ_p^*) and a local minimum (θ_{min}) analogous to T_{min}, T_p and T_p^* for the static friction. The estimation of poroelastic and polymer relaxation times demonstrate that both types of relaxation are also important in indentation measurements. Due to the experimental limitations of our AFM, only temperatures between 25 and 60 ºC can be examined, and hence, θ_p, θ_{min} and θ_p^* are not always detected.

Considering the large error bars in the results of 4% hydrogels and the small adhesion energy (note the different scale of the Y-axis in Figure 6.5a, b and c), we believe that θ_p is smaller than room temperature for 4 % hydrogels, and a state close to the bulk thermodynamic limit is probed in this case. In contrast, θ_p and θ_{min} of 6% and 12 % hydrogels are prominent. An increase in temperature above θ_p^* leads first to a decrease in the adhesion energy, which is associated with the more significant liquid-like behavior of the hydrogel; here, polymer diffusion is promoted, which weakens the shear strength of the adhesive contact (σ_s). The increase in temperature simultaneously promotes fluid drainage from the stressed region, mainly due to the decrease in the viscosity of water with temperature. This leads to an increase in the contact area. The increase in contact area partially compensates the reduction of shear strength, and it leads to the appearance of a minimum at θ_{min} and a maximum at θ_p. At temperatures above θ_p (~37ºC for 6% hydrogels and ~40-43ºC for 12% hydrogels), the liquid-like behavior of the hydrogels explains the decrease in adhesion with temperature.

A prominent difference between static friction and adhesion phase diagrams is that θ_p^* is close to 25ºC for 6% hydrogels, while θ_p^* is not measured for 12% hydrogels, which indicates that

it is below room temperature. Another difference is that θ_{min} shifts to lower temperatures with an increase in load (see Figure 6.5c). As discussed previously, when higher loads are applied, opposite trends are expected for polymer and poroelastic contributions: τ_P should increase with load due to the enhanced interfacial confinement, thereby slowing down the rate of interfacial polymer bonding and of diffusion/detachment, while τ_W should decrease with load, leading to a faster growth of the contact area. As a consequence of longer polymer relaxation times, T_p should shift to higher temperatures with load, which is observed for the static friction in a narrow load range. The shift of θ_{min} to lower temperatures with increase in load for the adhesion energy suggests that the pull-off force is more influenced by the poroelastic relaxation. This might be partially originated by the much shorter hold (loading) times applied in our pull-off force experiments (<2.5 s in Figs. 5 and S6) compared to static friction measurements (5-50 s). Furthermore, we cannot exclude that the different results partially originate from the distinct loading conditions in adhesion and static friction force measurements; during retraction of the colloid microcontacts rupture progressively, while microcontacts have to rupture more dramatically when laterally pulling the colloid.

Note that an adhesion hysteresis phase diagram has been proposed before for dry interfaces (124). Adhesion hysteresis is the difference between the work needed to separate two surfaces and that originally gained on bringing them together. In the case of the hydrogels, there is no attraction to the colloid upon approach. Instead, there is a weak hydration-polymer mediated repulsion that is negligible compared to the significant adhesion to the colloid upon separation, and hence, adhesion hysteresis and adhesion are believed to be roughly analogous for this system.

6.4. Conclusion

Damage of soft biological tribosystems has been related to the static friction that prevents interfacial motion. Despite the enormous amounts of water held in hydrogels, adhesion is responsible for the logarithmic increase in static friction with loading time, a phenomenon called ageing, which is observed to depend on hydrogel's microstructure and to vanish at sufficiently high temperature. This work reveals two main mechanisms underlying contact ageing, namely the polymer viscoelasticity at the confined interface and the poroelastic relaxation due to fluid drainage. The experimental results demonstrate the intricate role of the hydrogel's microstructure (i.e. mesh size) in dictating the static friction and how it can be modulated by varying the temperature, the duration of the static loading and the load. Hence, the proposed phase diagram provides a new understanding of static friction, which should be universal for hydrogel-like materials, like those ubiquitous in biological tribosystems. Moreover, the findings of this work help understand the role of stratified microstructures of biological tribosystems with gel-like surface layers holding large amounts of water, and thus, less susceptible to contact ageing. Our measurements on surface of bovine cartilage exhibits static frictional characteristics similar to 12% PAAm hydrogels. The knowledge emerging from this work can inspire customized design of hydrogels for targeted applications, not only for replacement and regeneration of biological tissues but also for soft robotics and soft micro-electromechanical devices, among others.

CHAPTER 7: RHEOLOGY AND TRIBOLOGY OF HYDROGELS WITH AN EXTENDED SURFACE FORCES APPARATUS (eSFA)

As described in Chapter 2, current assumptions for the viscous dissipation range from hydrodynamic lubrication mediated by the Newtonian behavior of the solvent to non-Newtonian shear of the hydrogel interfacial region and a polymer-relaxation lubrication mechanism. While all of these assumptions are consistent with experimental observations, measurements dedicated to examining the interfacial rheology of adhesive and repulsive contacts with hydrogels are still needed to provide fundamental insight into the interfacial behavior. Rheological models that specifically account for the time-dependent variation of friction in static contacts have been already considered(131, 132). The Surface Forces Apparatus (SFA) is a well-known method for precisely determining the thickness of (sub)nanometer fluid films, normal surface forces and friction. One advantage of this method is that the measurements of the film thickness are also possible during shear loading, so that it can determine the change in thickness with sliding velocity. The surface forces apparatus was extended (eSFA) to perform nanorheological and tribological studies of thin polymer films previously(109, 128, 133, 134). In this chapter, we aimed to understand the interfacial rheology of hydrogel thin films under tribological conditions in order to gain mechanistic insight into the viscous contribution to friction.

7.1 Methods

7.1.1. Sample preparation

The protocol for preparing mica surfaces and the operation of the SFA has been described in detail previously [127-130]. Briefly, mica (Optical grade # 1, S&J Trading, NY) was manually cleaved in pairs with thicknesses in the range of 2-8 μm. The freshly cleaved mica was back-coated

with 40 nm silver using an e-beam evaporator. Mica sheets of equal thickness were glued onto two curved glass discs (radius ~ 2 cm), by spin coating a film of epoxy glue (Epon 1004 F).

For fixing synthetic hydrogels such as the poly(acrylamide) (PAAm) hydrogels to mica, 3-Aminopropyltriethoxy silane (APTES) functionalization of mica assisted via N,N – diisopropylethylamine (DIPEA) was conducted. Use of DIPEA with APTES has been reported to enhance monolayer deposition on mica in an earlier study(135). Hydrogel thin films were polymerized directly on the functionalized mica surfaces by sandwiching the pre-polymer solution (15 μL) with a hydrophobically modified mica counter surface. The protocol was in part adapted from Degen et al(136). This method resulted in PAAm hydrogel thin films with thickness in the range of microns, covalently attached to mica, hence suitable for performing thin film interferometric measurements. For the measurements in this chapter, we primarily chose the concentration of 6% PAAm hydrogels as described in Chapter 3, however, we also discuss measurements conducted on 4% PAAm hydrogel briefly.

7.1.2. Methodology

The eSFA setup was successfully extended to perform nanorheology and nanotribology on hydrogel thin films to scrutinize the relationship between friction and interfacial rheology of hydrogel networks. Figure 1 shows the eSFA set up, where the normal force is measured as the difference between the piezo motion and the spring deflection (D) multiplied by the normal spring constant (K_n). This normal spring was calibrated by measuring the deflection of the spring due to a known weight, yielding K_n = 1000 N/m.

Upon the shear of the sandwiched medium, in this case the hydrogel, the lateral force, was measured by four strain gauges (FLK-1-11-3LJCT, Texas Measurements, College Station, TX) attached to the lateral springs and assembled in a Wheatstone bridge configuration. The conversion

for voltage to spring deflection was obtained by connecting the disc holders with a rigid metal rod and measuring the voltage reading when the piezo driver was moved by a known distance. This resulted in a conversion factor $K_2 = 7.1\ 10^{-5}$ m/mV. The constant of the lateral spring was determined by applying a known force on the spring assembly and recording the resulting voltage and deflection. The lateral spring constants for the experiments in this chapter are $K_x = 356$ N/m and $K_x = 501$ N/m.

Using the set-up shown in Figure 1, the motion in the lateral direction was possible at a constant velocity (for friction measurements) as well as in a sinusoidal fashion (for rheological measurements). For rheological measurements, a cosine displacement input was applied through the lateral piezoelectric actuator (P754, Physik Instrumente, Germany). The piezo controller (E-754, Physik Instrumente, Germany) was synchronized with a data acquisition system (Pacific Instruments, Concord, CA) so that the piezo motion triggered a time zeroing of the recorded data. The resolution in time was measured as 0.1 ms.

After determining the thickness of the mica pair in air, one of the discs was disassembled and the hydrogel thin film was grafted on the mica, as described earlier. The disc was replaced in the eSFA after gelation and the SFA cuvette was filled with DI water. After this, using motors in the x and y direction to scan the contact, the point of closest approach (PCA) was identified. Treating the system in the interferometer as a "symmetric" mica-mica contact, the gap distance between the two mica surfaces and its refractive index were constantly measured. This allowed us to measure the change of the refractive index and of the thickness of the hydrogel film confined between the two mica surfaces in real time; e.g. variations in compression of the hydrogel could yield a variation of the refractive index due to the change of the water content. The refractive index

measurements are most accurate at surface separations smaller than 1 μm, and hence, the precision of this measurement for the hydrogel films was low.

Slow compression and decompression of the hydrogels at constant rate of 1 nm/s and/or 5 nm/s were performed at least three times prior to and after the rheological and tribological tests to determine the resistive force to compression (labelled as force isotherm). The thickness of the hydrogel thin films was estimated via the onset of the repulsion upon each approach. Rheological and tribological tests were performed at multiple compressions i.e. $(1 - \mathrm{D/H}) * 100$, ranging from c~7% (in the linear regime) to 70%, where H is the hydrogel thickness in the uncompressed state and D is the gap distance and hydrogel thickness in compressed state.

In frequency-sweep tests, the amplitude of the piezo motion, A_0, was set so that the strain was 2% - 5%, while the frequency, ν, was varied from 0.051 Hz to 20 Hz. The noise in our data close to the resonance frequency ~40 Hz was high, which limited the confidence in data obtained at frequencies higher than ~10 Hz. Amplitude sweeps were conducted at a selected frequency of 1 Hz with A_0 of 0.5% to 50% strain at each compression. The strain applied deviates from the piezo motion (A_0), due to the deflection of the spring, which is accounted for in our analysis.

For tribological tests, the sliding distance of $15\ \mu m$ was selected while sliding speeds were varied from 0.3 to 300 $\mu m/s$. This corresponds to strains in the range ~136 to 833% Tribological tests at high compressions did not lead to sliding, and hence, we limit our discussion to low to medium compression. Reliable data at higher speeds was often limited as sliding was often not observed.

7.1.3. Analysis

While our setup was inspired by Luengo *et al.*,(109) there are subtle differences between the two eSFAs thereby requiring a separate derivation of the equation of motion. In our system, only one surface is subjected to a motion while the other is stationary. The equation of motion for the surface connected to the piezo results from the balance between the spring force and the friction force:

$$K_x \cdot \delta - \eta \cdot \Omega \cdot V = 0$$

where η is the viscosity of the medium between the two mica surfaces, Ω a geometric factor based on Reynold's lubrication theory; for parallel plates, $\Omega = S/D$, S being the contact area between the parallel planes geometry, D the separation at the PCA and for a sphere-plane geometry, $\Omega = 16/5\ \pi R\ log\ (2R/D)$, R is the radius of the sphere, and V the relative velocity between the two mica surfaces. The surface displacement x is given as:

$$x = z - \delta$$

Where the displacement of the piezo is z, and the deflection of the spring is δ. The relative velocity between the two surfaces is given by:

$$V = \dot{x} - \dot{y}$$

Since the counter surface is stationary, we can assume that the corresponding friction term is negligible. This yields:

$$V = \dot{x} - \dot{y} = \dot{x} = \dot{z} - \dot{\delta}$$

$$K_x \cdot \delta - \eta \cdot \Omega \cdot (\dot{z} - \dot{\delta}) = 0$$

This expression gives the viscosity of the sandwiched medium as $\eta = \frac{K_x \delta}{(\dot{z} - \dot{\delta})\Omega}$.

For a purely linear viscoelastic behavior, it is informative to determine loss and elastic components of the viscosity. Given a cosine input displacement, $z = A_0 \cos(\omega t)$, the deflection of the cantilever is given as $\delta = A_1 \cos(\omega t + \phi)$, where ω is the angular frequency ($\omega = 2\pi\nu$), ν the frequency, and ϕ the phase difference. The parameters A_1 and ϕ are measured during the experiments and can be used to describe the real and imaginary components of the complex viscosity, $\eta = \eta' - i\eta''$:

$$\eta'' = \frac{K_x}{\omega\Omega} \frac{f\cos(\phi) - 1}{f^2 + 1 - 2f\cos(\phi)}$$

$$\eta' = \frac{K_x}{\omega\Omega} \frac{f\sin(\phi)}{f^2 + 1 - 2f\cos(\phi)}$$

Eq. (7.1)

where η' is the real component (loss) and η'' is the imaginary component (elastic), $f = \frac{A_0}{A_1}$, and D the thickness of the confined hydrogel thin film. The effective viscosity of the medium (gel) is hence obtained from:

$$\eta_{eff} = \sqrt{\eta'_{gel}{}^2 + \eta''_{gel}{}^2} = \frac{K_x}{\omega\Omega\left(f^2 + 1 - 2f\cos(\phi)\right)^{1/2}}$$

Eq. (7.2)

Storage and loss moduli are determined from the complex viscosity as:

$$G'_{gel} = \omega\eta''$$

$$G''_{gel} = \omega\eta'$$

Eq. (7.3)

The strain rate is given as

$$\dot{\gamma} = \frac{V}{D} = iw\frac{A_0 - A_1\, exp\,(i\phi)}{D}\, exp\,(iwt)$$

Where the maximum strain rate is:

$$\dot{\gamma}_0 = \frac{\omega\sqrt{(A_1 sin\phi)^2 + (A_0 - A_1 cos\phi)^2}}{D}$$

Eq. (7.4)

The maximum shear stress is thus determined as $\sigma_0 = \eta_{eff}\dot{\gamma}_0$.

Rheological data processing was done using a code developed in MATLAB.

Raw data from tribological tests was analyzed as follows. The raw signal from the spring deflection was plotted as a function of time as shown in Figure 7.1 c. This signal corresponds to the spring deflection (in mV) in the forward and reverse direction as is evident from the reversal of the deflection in the raw data (blue and red arrows, Figure 7.1 c). Using a MATLAB script, the signal was cut into trace and retrace, the retrace profile was flipped in the x-axis and both data sets were plotted as a function of the scanning distance as shown in Figure 1d. This is what we define as a friction loop and friction was calculated by taking the half of the difference between the trace and the retrace, multiplied by the lateral spring constant. At least three loops were considered when calculating the average friction and standard deviation at slow sliding velocities, while the first

loop was discarded at each condition. Note that there was an inherent tilt in the loops, even far away from the hydrogel surface, likely associated with a small misalignment between the two surfaces. Despite this artifact, we could observe a static friction threshold as well as friction sliding in most of our measurements. From the measured friction force, an effective viscosity was also estimated using $\eta_{eff} \sim \frac{F_L}{\frac{16}{5}\pi \cdot R \cdot V log\left(\frac{2R}{D}\right)} = \frac{F_L \Omega^S}{V}$. Here, we have assumed $\Omega = \frac{16}{5}\pi R log\ \frac{2R}{D}$ for $R >> D$, considering a sphere-plane geometry.

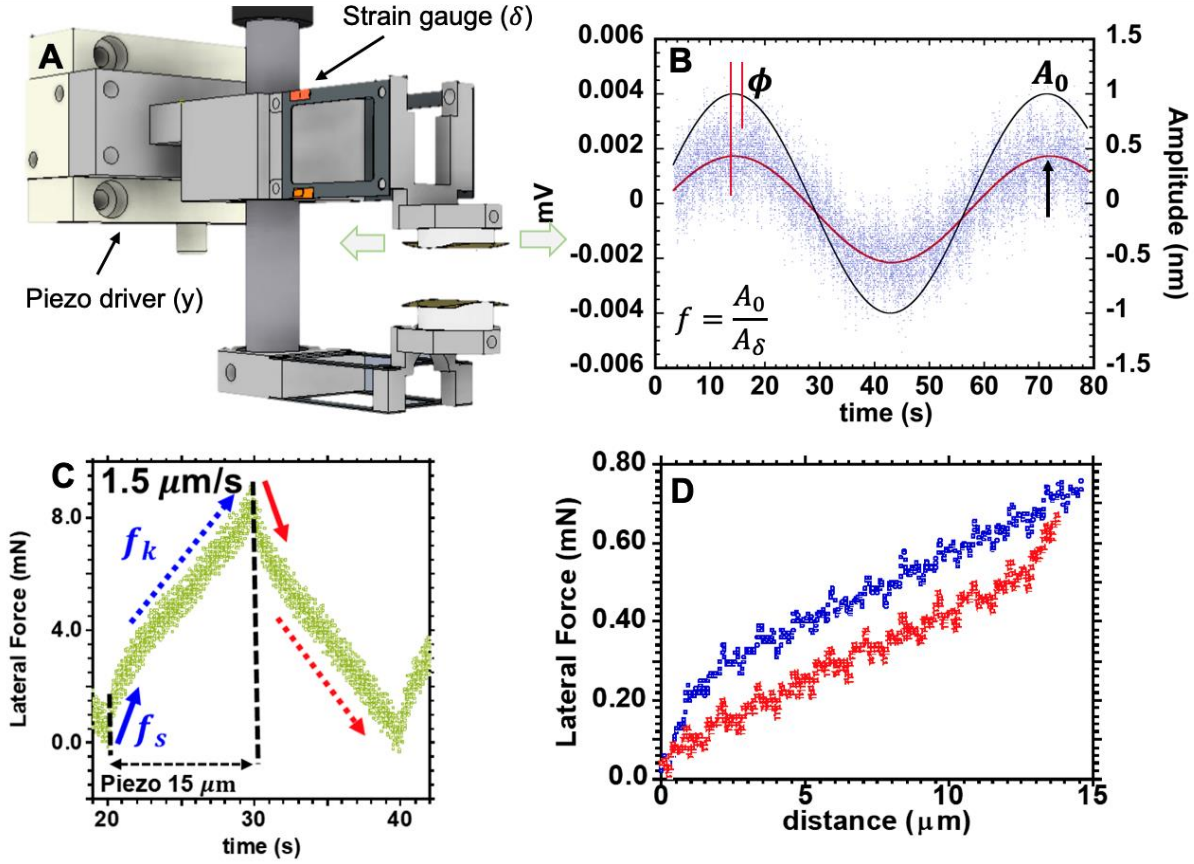

Figure 7.1 a) eSFA sample holders with normal and lateral spring assemblies. b) input (arbitrary amplitude) and output signals c) Raw signal measured during tribology, f_s is the static friction, while f_k is the kinetic or sliding friction d) Friction loop at $V = 1.5\ \mu m/s, D = 1.8\ \mu m$ for a 6% PAAm hydrogel. Lateral spring constant $K_x = 356$ N/m and normal spring constant K_n= 500 N/m.

7.2. Results

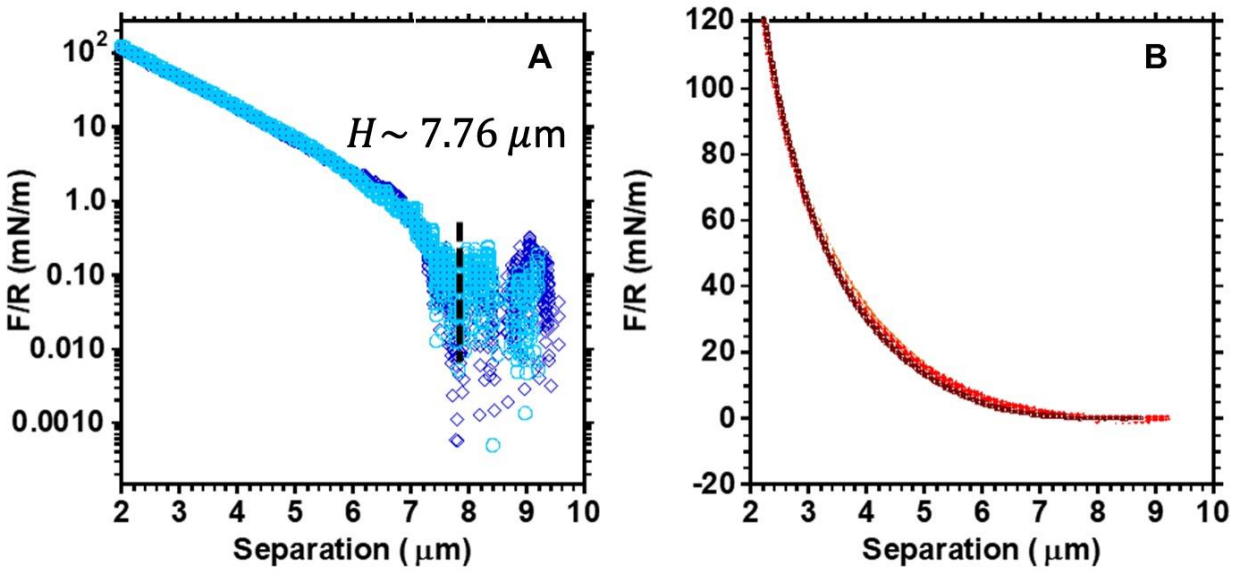

Figure 7.2 A) Approach (first approach – light blue, second approach – dark blue) and B) retract segments (first retract orange, second retract red, third retract brown) on the 6% PAAm hydrogel which is discussed in figures 7.3 and 7.4. The thickness of the hydrogel is indicated as H, with the dashed line. Here, a deviation from the baseline was noticeable. Compression was done at 2 nm/s at 25 ℃. $K_n = 500\ N/m$. Radius = 22.6 mm.

7.2.1. Force isotherms

Figure 7.2 A shows the compression isotherms of a 6% PAAm hydrogel film performed at a compression rate of 1 nm/s. The initial film thickness is measured as the point where a repulsion is first observed and is indicated with the dashed line as H in the figure. The force is divided by the radius of the mica surface, as common in this type of representation. The compression also shows that there is a small change in thickness, i.e. a viscoelastic response upon consecutive compressions. This is expected for a hydrogel-like material, owing to its viscoelasticity, and in fact, it was observed in a eSFA recent study on cartilage thin films, as well(36). Nevertheless, the slow relaxation is surprising considering that the hydrogel was allowed to relax for 2.5 hours between consecutive compressions. Besides this small change, the hydrogel seems to have a robust

response to compression, which exceeds 70% of the hydrogel thicknesses. Importantly, performing these measurements during rheological and tribological measurements let us conclude if a change of microstructure or other irreversible process has occurred during the measurement. Importantly, except the thinnest films (H~4 μm), 6% PAAm hydrogel films were able to preserve their initial thickness.

Representative decompression curves are shown in Figure 7.2 B. It is also worth mentioning that we did not detect noticeable adhesion between the hydrogel and mica, except for the 6% PAAm hydrogels shown in Figures 7.7 J-L, indicating that this was mostly a repulsive contact initially. Minor adhesion was only sometimes observed upon the 2nd or 3rd decompression which we attribute to the increase in adhesion associated with poroelastic drainage(19, 35). However, we observed that, if given enough time, the hydrogel rehydrated and the interface was rendered repulsive again. Only the compression isotherms after the rheological tests on the hydrogel thin films with film thickness < 4 µm showed an irreversible change, indicating material damage during the test. Hence, we will limit our discussion of results to the experiments performed with thicker films ($H > 4\ \mu$m).

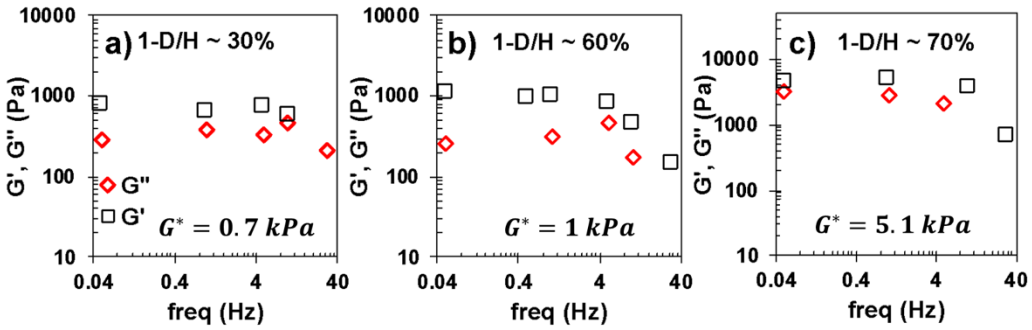

Figure 7.3 *G'* and *G''* as a function of frequency for a 6% PAAm hydrogel at a) 30%, b) 60% and c) 70% compression. The complex shear modulus is given in the plots as G^*. The drop in the storage and loss moduli at high frequencies is likely associated with the instrumental limitation at higher frequencies. Hydrogel thickness (no compression applied) $H = 7.753$ µm. $K_x = 356$ N/m.

7.2.2. Influence of compression on rheological response

Figure 7.3 shows the rheology measurements of a hydrogel film with thickness H~7.753 μm. The hydrogel films always exhibit characteristics of the rubbery plateau region; they are viscoelastic solids with G'>G'' (tan-delta ~0.09-0.9). Frequency sweeps at multiple compressions of the hydrogel films show that, at low compressions, the gel is soft ($G^* = 0.7$ kPa, compression = 30%) and with increased compression, the complex modulus increases. The increase is at first small, where the complex modulus increased only from 0.7 kPa to only 1 kPa as the compression increased from 30 to 60%, which is a remarkable compression. In fact, these values are of the order of magnitude of the bulk modulus of this hydrogel as measured via macro-rheology G^*= 275 $\pm$30Pa. However, the modulus jumps to 5 kPa when the compression goes up to 70%. Based on this, we can infer that the hydrogel can sustain large compressions (and despite the decrease in water content) before the modulus substantially increases. This suggests that the robust hydration of the hydrogel thin film plays a key role in lubrication, and that perhaps the most bound (hydration) water plays a more important role in providing high lubricity at the interface compared to less bound water, which is more easily lost upon compression. Stress-strain curves obtained from the amplitude sweeps conducted at a frequency of 1 Hz are shown in Figure 7.4 on the same hydrogel. Importantly, the stress-strain plot resembles the characteristic relation for a ductile polymeric material undergoing yield. The decrease in stress with strain could indicate damage of the network with an increase in strain or alternatively, a structural change of the network e.g. an alignment of the polymer strands. Note that this trend is not associated with the decrease in G' and G'' due to an increase in the noise close to the device resonance (Fig. 7.3). We also note that increasing the compression shifts the yield point to a higher strain while the gel becomes stiffer,

likely due to the significant decrease in water content, as observed in the previous frequency sweeps as well.

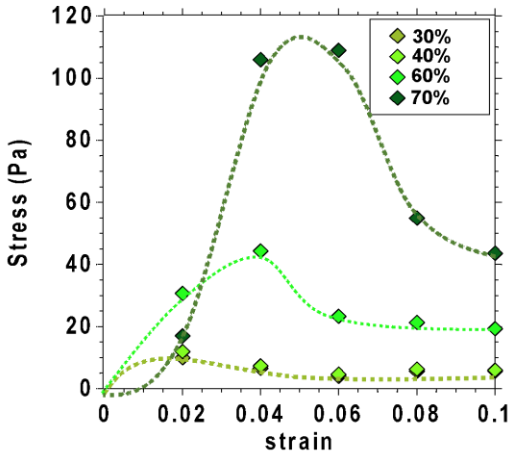

Figure 7.4 Representative stress vs strain curves for 6% PAAm hydrogel upon increasing compressions from 30% to 70%. The dashed lines are added to guide the eye.

7.2.3. Effective viscosity as a function of the crosslinking density

The main objective of this chapter was to elucidate the viscous contribution to friction. More specifically, we wanted to gain insight into the viscous friction force beyond empirical relations. It is well known that the interfacial structure differs from the bulk microstructure of PAAm hydrogels. Hence, to achieve this, the rheological measurements were carried out on films of several microns in thickness to enhance the effect of the interfacial structure, compared to the bulk behavior that we probe in macro-rheology. Furthermore, we emphasize our analysis of the effective viscosity η_{eff}, instead of the storage and loss moduli, to correlate the rheological behavior of the hydrogels to viscous dissipation and the velocity dependent friction in a more straightforward manner.

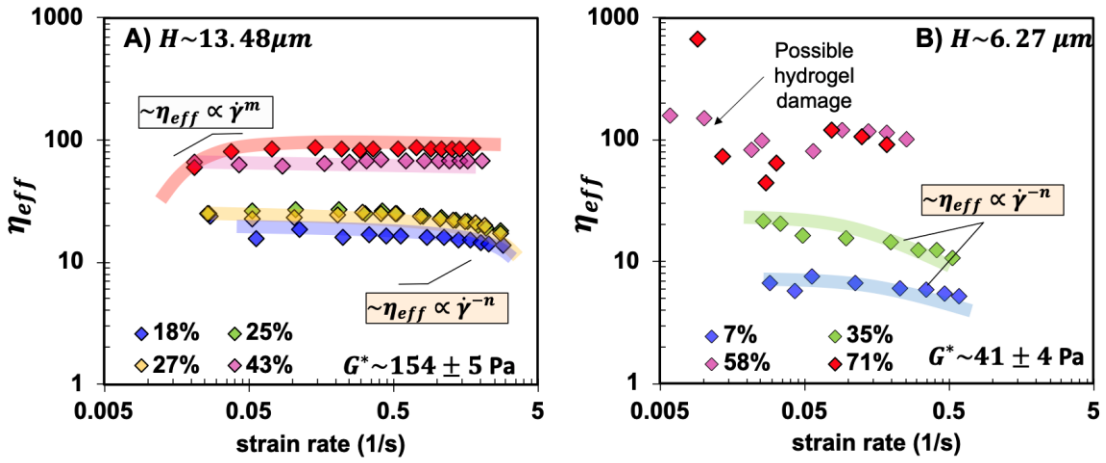

Figure 7.5 Effective viscosity vs. strain rate calculated from the amplitude sweeps as a function of the applied compression (legend) for a) 6% PAAm hydrogel and b) 4% PAAm hydrogel. The translucent lines have been added as a guide. $K_x = 356$ N/m. $G^*$of the hydrogel films in A) and B) were 154 $\pm$ 5 Pa and 41.6 $\pm$ 4.8 Pa at the lowest compressions and 162 $\pm$6 Pa, and ~ 1kPa at the highest compressions for the 6% and 4% PAAm hydrogels respectively. We mention an estimate for the 4% PAAm at high compressions since a plateau in G^*could not be achieved. G^*measured by macro-rheological measurements for the 6% and 4% PAAm hydrogels were 275 $\pm$ 30 Pa and 143 $\pm$ 10 Pa, respectively. The measurements were conducted at a frequency of 1 Hz while the applied strains were changed from 0.5% to 50%. The loads corresponding to the compressions shown in the legend were: 73 μN, 176 μN, 224 μN, 615 μN, 1213 μN and 3 μN, 87 μN, 618 μN, 3179 μN for the 6% and 4% PAAm hydrogels, respectively, in the order of increasing compression.

Figure 7.5 shows the effective viscosity calculated from amplitude sweeps, for two types of PAAm hydrogels, (a) with a high crosslinking degree -6% PAAm, and (b) with a lower degree of crosslinking -4% PAAm. We note that the effective viscosity of 4% PAAm under low compression (~7%) is ~40% (6 Pa.s) that of 6% PAAm (16 Pa.s). The corresponding storage and loss moduli are 40 $\pm$5 Pa and 8.4 $\pm$ 3 Pa for the 4% and 161 $\pm$ 6 Pa and 20.2 $\pm$ 9.5 Pa for the 6% PAAm. This is expected as the latter should have a higher polymer content and crosslinking density. For the 6% PAAm hydrogels, a long Newtonian viscosity plateau as a function of strain rate is measured followed by a small, but noticeable decrease in viscosity as a function of strain rate for compressions of 18%, 25%, and 27%. The plateau viscosity (η_o) is determined to be 16.1 $\pm$ 0.3, 25.1 $\pm$ 0.9, 24$\pm$ 0.7, 67 $\pm$ 0.9 and 84 $\pm$ 1.4 Pas for compressions of 18%, 25%, 27%, 43%,

and 51% for 6% PAAm hydrogels. Importantly, the onset of shear-thinning occurs at a lower strain rate for compressions of 25% and 27% (~0.5 s^{-1}) compared to 18% (~0.8 s^{-1}). In contrast, the shear thinning behavior vanishes above 27%, and instead, a small increase in viscosity at low strain rates is observed at the highest compression (51%, see red curve), i.e., shear strengthening. The plateau effective viscosity also exhibits a sudden jump, when the compression increases from 27% to 43%, indicative of a non-linear increase in viscosity as a function of compression. Note that the viscosities can be clustered into high and low compression regimes, further pointing toward the hydrogel's graded response. Hence, this abrupt change of behavior suggests a graded (non-linear) response of the hydrogel as a function of compression.

For the low crosslinked, 4% PAAm hydrogels also show a similar non-linear change in effective viscosity as a function of compression. Here, the effective viscosities are similar at ~58% and 71% compressions (~100 Pa.s), and interestingly, similar in magnitude to those measured for 6% PAAm hydrogels at similarly high compressions. Comparison of the isotherms of both hydrogels under compression show that 4% PAAm is stiffer than the 6% PAAm thin film. This deviates from the response we have observed in the AFM measurements. Again, this might be related to the different preparation methods in the three types of measurements. Importantly, $G^*4\% < G^*6\%$ at the lowest compressions which is more comparable to macrorheology and in qualitative agreement with our previous results. The effective viscosity as a function of strain rate shows a slightly decreasing trend with strain rate (up to 47%) i.e. shear thinning, while the trend becomes less clear at high compressions. Although, at compressions of 58%, a decreasing viscosity as a function of strain rate is still detected over the whole range of strain rates, the behavior at 71% at low strain rates is unexpected. We believe that under such high compressions, there is a possibility

of hydrogel damage. In fact, isothermal compressions after the lateral tests on this hydrogel revealed that the hydrogel had partially detached from the surface.

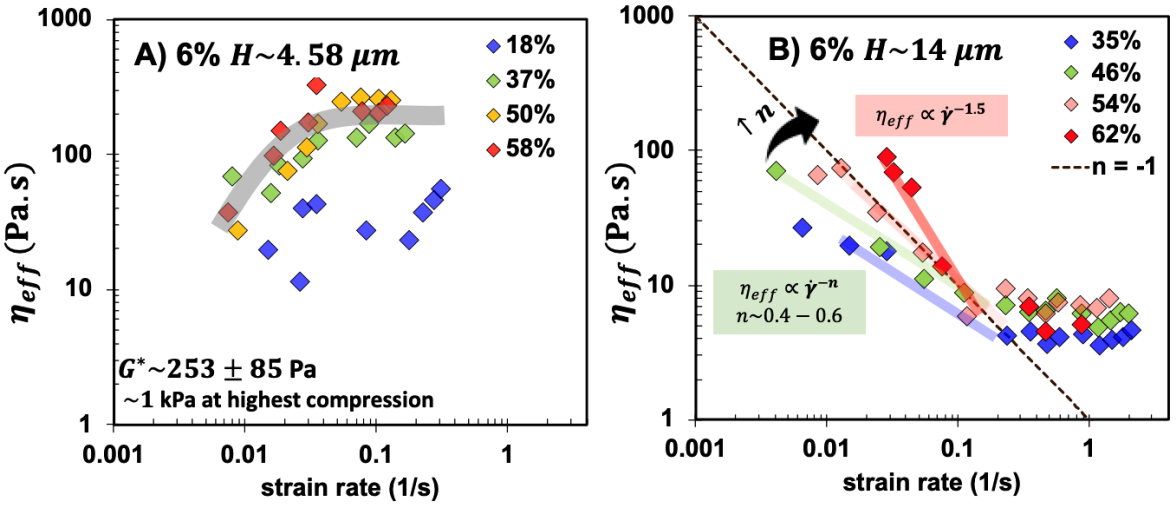

Figure 7.6 Effective viscosity obtained in amplitude sweeps as a function of strain rate and the applied compressions for 6% PAAm hydrogel films with thicknesses of A) 4.58 μm and B) 14 μm. The dashed black line in B corresponds to a power law fit with an exponent of -1. The power law fits to the data in B resulted in the shear thinning exponent n which ranged from -0.45 to -1.5 while the dashed black line is for $n = 1$. The range of loads corresponding to the compressions (legend) are listed in table A4.

The amplitude sweeps for the two hydrogels, i.e. low and high crosslinking densities highlight two hey conclusions: first, decreasing the crosslinking density leads to a more noticeable shear thinning behavior and second, the rheological behavior of the hydrogel films changes as a function of compression, and is not simply due to the gradual decrease in water content. The latter can be rationalized by considering a brushy layer on the surface of the hydrogel, which has a lower crosslinking than the bulk hydrogel, while richer in water. In fact, our previous AFM studies have demonstrated that this brushy layer existed for the 4% and 6% PAAm hydrogels, ranging from ~300 nm to 600 nm thereby in agreement with the results shown here. Certainly, the microstructure of the hydrogel films could deviate from that of the macroscopic hydrogels investigated previously, but a) the *qualitative* good agreement between their elastic modulus at low

compressions and b) the graded response upon compression supports that the main characteristics of the hydrogels are retained in the thin films. Nevertheless, the influence of the top layer is more significant in the SFA experiments with thin films.

The effective viscosity described earlier (Figure 7.5 A) differs from the viscosity measured for the same composition hydrogels with a much smaller thickness (Figure 7.6 A). An increasing viscosity with a strain rate is observed for the thinner hydrogel film. It is important to point out one similarity here; the increase in viscosity is also observed for the 13.48 μm hydrogel at the highest compression of 51% in Figure 7.5 A. This is, however, followed by the plateau viscosity, which is much less prominent for the thinner hydrogels. The discrepancy as a function of the film thickness is however not surprising and we attribute it to the different microstructure and the response to compression of the two films. A three-fold jump in η_{eff} upon compression is observed as the compression increases from 18% to 37%. This is also important to point out as previous works on confined polymer melts have denoted this sudden increase to a liquid to solid transition(126, 133). The non-linear increase in viscosity at a lower compression in comparison to the hydrogel in Figure 7.6 A, indicates that a brushy-layer on the hydrogel is more compressible than the one on the thicker hydrogel.

Figure 7.6 B displays results for a 6% PAAm hydrogel with a thickness of 14 μm. For this case, a power law behavior before the viscosity plateau is observed. This power law behavior - $\eta_{eff} \sim \dot{\gamma}^{n}$, is generally seen for polymer melts. Additionally, transitions of this relation as a function of the strain rate have been reported for polymer melts as a function of confinement(137), which we observe here as well, but as a function of compression. Fits of the relation $\eta_{eff} \sim \dot{\gamma}^{-n}$ to the data reveal that n is 0.6 at 35% and 42%, 0.4 at 46%, 1 at 53%, and 1.5 at 61% compression, respectively. The exponent of $n = 1$ is associated to a plateau in the shear modulus and represents

a solid-like behavior ($G' > G''$). The value $n = 0.6$ is also a significant result as experiments s have shown a similar ($n = 0.667$) exponent for confined liquids, such as small ring silicones(138) and for short n-alkanes (dodecane) under high pressures (139) as well as in MD simulations under constant pressure (140). Importantly, the increase in the exponent as a function of compression is evident and heralds the existence of a transition between a viscoelastic into an elastic behavior.

Commonalities do exist in Figures 7.5 and 7.6. yet with subtle differences. We attribute this likely to the inherent variations in the hydrogels originating during the synthesis; however, we have not been able to control this behavior yet. Importantly, Figures A11 show G' and G'' of the two hydrogels in Figures 7.5 A and 7.6 B, which reveal that the hydrogel film in 7.6 B is quite soft, and dissipative, perhaps related to a much lower crosslinking. The comparison is also tabulated in Table A4. It is also important to mention that in addition to this hydrogel displaying small adhesion during the approach (~ -4.6 mN/m) compressions after the lateral tests revealed that a change in thickness occurred from 14μm to ~ 10 μm.

7.2.4. Frequency modulation rheology

These rheological tests were performed in conjunction with the tribological tests to compare the effective viscosity in both models. The left column in Figure 7.7 shows the effective viscosity obtained from frequency sweeps as a function of the strain rate (Figures 7.7 A, D, G, J). Multiple compressions are shown for each hydrogel. For the 6% PAAm hydrogels increasing the compression shifted the viscosity curve upwards, thereby indicating an increase in viscosity at a given strain rate. This effect was not well observed for the 4% PAAm. Furthermore, the effective viscosity in these tests decreases as a function of the strain rate for all hydrogels. This decrease could be fit by a power law, where $n \sim 0.8 - 1.5$ at low and high strain rates, respectively as shown

with black dashed lines. A clear change of slope is also observed at higher strain rates, where $n > 1$. At very low strain rates (~1E-2) a slight decrease in the exponent is expected, evident from the change of slope, thereby indicating shear thinning. Additionally, even though the accuracy at high frequencies is low in our measurements, we believe the viscosity sometimes achieves the Newtonian plateau, as seen in Figure 7.7 D.

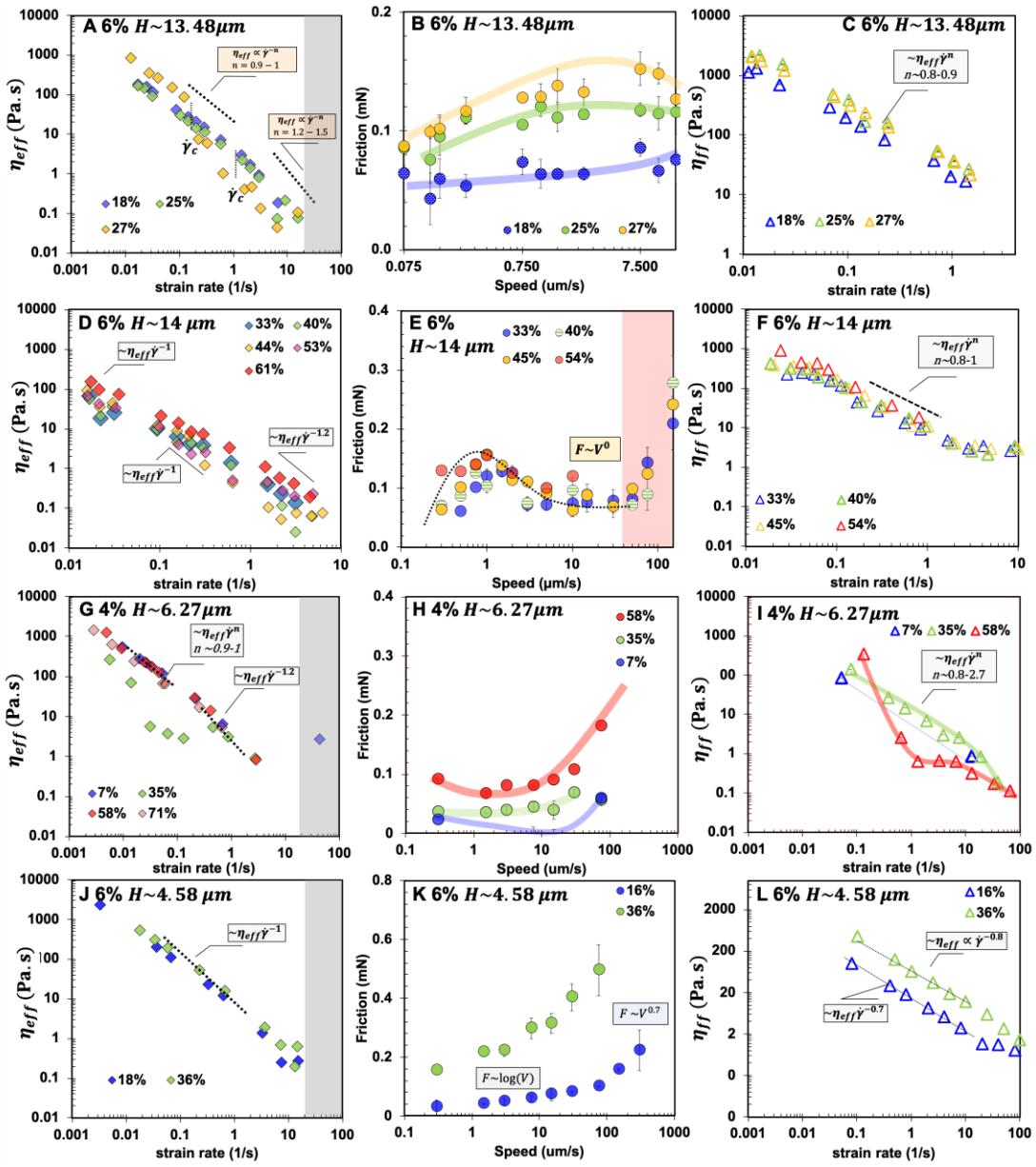

Figure 7.7 Effective viscosity (η_{eff}) calculated with G' and G'', obtained in frequency sweep tests, as a function of strain rate (first column), friction force as a function of sliding velocity (middle column) and an effective viscosity ($\eta_{ff} = F_{vis}/\Omega V$, where F_{vis} is the friction force) with the estimated strain rates applied in tribological measurements (right column). Multiple compressions are shown for each figure (see legend). A-F and J-L are 6% hydrogels with thicknesses of 13.8 μm, 14 μm, and 4.58 μm respectively. G-I are results for the lower crosslinked, 4% PAAm hydrogel thin film with a thickness of 6.27 μm. The translucent lines are added as a guide. The red area in E represents no sliding conditions. Grey shaded areas in the left column highlight the instrumental limit in frequency sweeps. The dashed represent power law fits. Note that the range of strain rates differed in the rheological and tribological measurements, and hence, an absolute comparison is not possible. The range of loads corresponding to the compressions (legend) are listed in table A4.

7.2.5. Tribological tests: effect of film thickness, compression, and crosslinking density

Results from tribological measurements are shown in Figure 7.7 (second and third column). The second column in Figure 7.7 shows friction vs speed measured in the tribological tests conducted at similar compressions as in the rheology measurements. The long sliding range helped to achieve sliding. Resembling rheology, the trends vary as a function of the film thickness, compression and the type of hydrogel and hence we will describe each figure in detail. The η_{ff} obtained from tribological measurements also showed different trends, dependent on the film thickness, applied compressions and strain rates, as well.

At higher compressions, we see either a plateau (25%) or a peak (27%) following the increase, in agreement with our own viscous adhesive model developed for hydrogels(26). Comparison to η_{eff}(7.7 A) reveals that friction should be independent of the velocity when $n = 1$, which is observed for the 25% compressions (plateau) however, it occurs at higher strain rates than those observed in the frequency sweeps. Additionally, the change of slope, where the exponent $n > 1$, corresponds to a friction force decreasing with velocity, which is only observed at the highest speeds at 27% compression. The amplitude sweeps also cannot fully justify the observed trends in friction force. Hence, at higher compressions, only the rheological properties are insufficient to describe the friction curve. Nevertheless, friction increases more steeply at higher compressions which agrees with the increase in viscosity upon compression of the thin film.

The friction behavior observed for the hydrogel with the $H \sim 14$ μm (7.7 E) extends the results in 7.7 B; in addition to the peak in friction, a *quasi-independent* plateau as a function of speed is also observed. Although a transition to viscous dissipation at high velocities is expected, we cannot distinguish between the inherent tilt and the sliding in the friction loops at high sliding

velocities, and thereby associate a large error with the data enclosed in the red bar. The friction behavior observed here is reminiscent of the v-strengthening and the v-weakening discussed in Chapters 4 and 5. For confined liquids, Granick et al proposed that in order to achieve a maximum in the friction force, the effective viscosity has to decrease faster than n = 1 as a function of the strain rate(133). Additionally, decrease in friction following the peak was also related to stick-slip behavior. While stick-slip was not observed in the raw friction loops, we note that the change of slope at $\dot{\gamma}_c$ corresponds to a time τ_c, which is dependent on the compression. For instance, at 27% compression, τ_c ~ 0.31 s, where $\tau_c = \frac{1}{2\pi v}, v \sim 0.5\ Hz$, while at lower compressions, τ_c~0.07 s. Comparison to the friction force, the peak at 27% correlates back to a relaxation time τ_p~1.3 s, hence 4 times longer than that measured in rheology. Note that the small number of data points does not yield an accurate value for $\dot{\gamma}_c$.

It is also noteworthy that in the AFM (Chapter 5), we measured a transitional behavior for the 6% PAAm hydrogel, where the v-weakening followed by viscous dissipation was observed. Here, we can probe the low velocity behavior as well and observe the v-strengthening which precedes the weakening. Even though the effect of load on the magnitude of the friction force is not significant perhaps, also tied to the absence of the jump in strain sweeps η_{eff} at high compressions, we note that for the highest compression, the complete v-strengthening regime is not observed and only part of the peak followed by the decrease in friction is captured. $\eta_{ff}$when plotted as a function of the strain rate shows a shear thinning behavior with n < 1 at the lowest strain rates, which is directly observed as in the $F \sim log\ (V)$ in the friction force. The behavior changes to $n = 1$ within the range of $\dot{\gamma}$ ~ 0.1 -2 1/s which is reflected well with the plateau observed in the friction force at medium velocities. A plateau at high strain rates starts to appear in η_{ff}, because friction starts to increase with the velocity again at high velocities. At low strain

rates, η_{ff} appears to asymptotically achieve a plateau as well, indicating the presence of a second plateau in viscosity where $\frac{\eta_{eff}}{\eta_o} \gg 1$. While the high shear plateau is not clearly observed in the rheological measurements, we believe that the 44% data might be approaching this behavior.

The friction behavior of 4% PAAm hydrogels can be discussed next (Figure 7.7 G-I). At low to medium compressions, a slight dependence of V on the friction force is observed. More specifically, the friction scales with $log\ (V)$ at 47%. This changes when the compression is increased to 66%, the friction behavior changes into "transitional" i.e. we observe a *weak* v-weakening followed by the viscous behavior. Here, the adhesive regime has changed and resembles the case when the Deborah Number (De) > 1, meaning the two surfaces do not have sufficient time to form bonds. This is important, as it shows that the elastic component of the network is *visibly* relevant. The corresponding variation in η_{ff} is also informative. We see an initial elastic response, followed by a plateau in viscosity and shear thinning, which reflects the described changes in friction. It is also important to point out that the strain rates probed in rheological measurements were lower than those applied in the friction tests, and thereby we are only able to see the elastic regime in η_{eff} from rheology.

The effect of the hydrogel thickness is evident when comparing Figures 7.7 B and 7.7 E to 7.7 K. Here for the thinnest hydrogel film, in Figure 7.7 K, friction increases with the log of sliding velocity at low speeds, followed by a viscous dissipation where $F \sim V^{0.7}$. At higher compressions, the log behavior either disappears or is not measurable and a monotonic, although non-linear increase in friction with increasing velocity is observed. The log behavior is mirrored in η_{ff} also, where n = 0.7 and n = 0.8 are measured. The disappearance of log at high velocities and high compression is however intriguing. Since the surface separation (D) is measured simultaneously

during the lateral measurements, we are able to measure the change in surface separation ΔD, at these conditions. Figure 7.8 shows the ΔD or "normal lift" as a function of the sliding speed for the lateral tests in Figure 7.7 K at the two compressions.

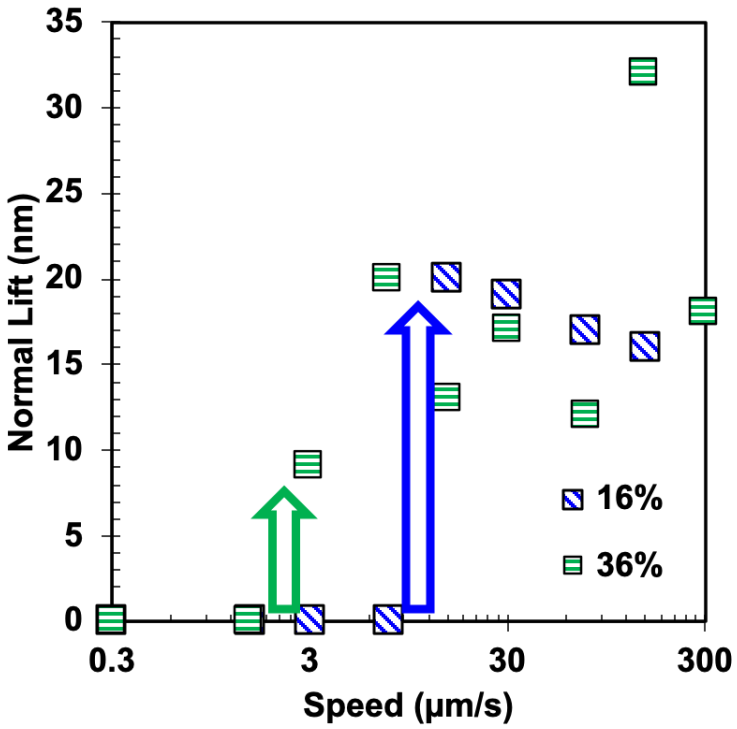

Figure 7.8 Normal lift measured during sliding at each speed for 6% PAAm, H = 4.58 μmat two different compressions/ loads. The arrows point to the change in D from zero to a measurable ΔD . $K_n = 500\ N/m$.

For 16%, no lift is measured up to 7.5 μm/s. After that, a normal lift of 20 nm is measured which decreases as a function of the sliding speed slightly (16 nm at 150 μm/s). At 36% compression, a normal lift is measured at a slower speed of 3 μm/s. These results are in agreement with the deviation of the log behavior in friction as a function of velocity and a plateau in η_{ff} as a function of strain rate, which starts to develop at the highest strain rates.

The results here demonstrate that the rheology of the thin film plays an important role in its frictional response. However, the rich behavior of friction as a function of sliding velocity arises from the combination of the viscous and the elastic/adhesive component.

7.3. Discussion

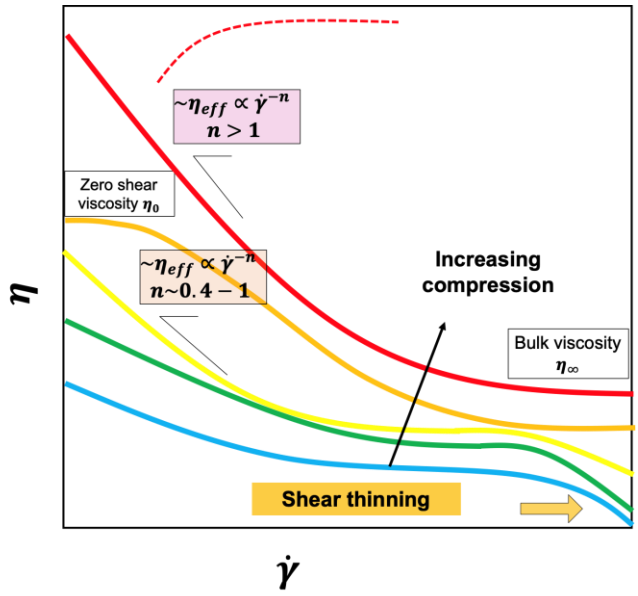

Figure 7.9 A comprehensive map of effective viscosity as a function of shear rate, measured in rheological tests for PAAm hydrogels. Different colors correspond to different compressions. Compression increases progressively from yellow to red, as shown by the arrow. Translucent boxes give the estimates of power-law fits of the exponents. The dashed red line corresponds to data ay very high compressions.

7.3.1. Effective viscosity Map

The observed trends of effective viscosity as a function of strain rate are shown in Figure 7.9. First, the clear, compression dependent shear thinning behavior in amplitude and frequency sweeps is worth discussing. Shear thinning behavior has been observed often for a multitude of materials such as polymer melts and brushes, surfactants, granular media and even hydrogels(141-145). The concept of shear thinning for polymers in solution or melts is based on the disentanglements of polymer chains upon shearing, where the polymer chains become progressively oriented in the direction of shear, hence the resistance to shear and the viscosity

decreases(146). Rabin proposed the "shear blob" model for shear thinning of dilute polymer solutions based on de Gennes scaling laws(147). The shear blobs are coiled segments of polymer chains, so that the characteristic relaxation time of each blob is the inverse shear rate. For shorter times, or the Weissenberg number , $W_e = \dot{\gamma}\tau < 1$, internal polymer dynamics are not much affected by the shear and there is dissipation of energy by small-scale intra-polymer motion where the entropic elasticity and the Brownian motion dominates over shear assisted flow. For longer times, $W_e > 1$, there is no dissipation or relaxation and the polymer segments are deformed in the direction of the shearing motion. He further utilized this model to show that the effective viscosity dependent on the shear rate is similar to the frequency dependent intrinsic viscosity, thereby unifying the idea with the empirical Cox-Merz rule(148, 149). For $W_e \geq 1$, the scaling leads to the characteristic power law behavior for shear thinning. We note that though the Cox-Merz rule is widely utilized, it often breaks in the case of branched polymers(150, 151) and polymeric networks(152, 153). While we observe similarities between the effective viscosity from rheology (or complex viscosity) and the steady state viscosity, many differences exist and hence a superposition is not possible.

For the polymeric networks like hydrogels, shear thinning can also be rationalized by considering intermolecular bonding, such as hydrogen bonding between polymeric chains and the polymer and water as well, which is disturbed upon shear. In fact a decrease in intermolecular interactions upon shear was proposed for the shear thinning behavior of Poly(Gx-co-NIPAM-co-AAc) hydrogels before(154) while the role of hydrogen bonding in the shear thinning behavior of polymer solutions hydrogels has also been reported(155, 156). Considering this mechanism is reversible, one would expect the hydrogel to show time dependent rheological behavior as well. In fact, evidence of thixotropy in PAAm hydrogels was previously proposed by Kim et al (132)

and more recently by Cuccia et al(131). Therefore, the observed shear thinning behavior for PAAm hydrogel thin films is not unexpected.

Now, the increase in compression lead to either an increase in the exponent or a discontinuous jump in the viscosity plateau viscosity. The former is expected for systems in which a transition from a liquid-like to a solid-like behavior takes place upon compression(109, 134). Here, the rationale can be extended to hydrogel thin films where a transition from a visco-elastic to an elastic behavior can occur upon increased compression. The polymer chains at high compressions can be in a "frozen" state with relaxation times much longer than those expected under zero confinement. In fact, our results in Chapters 4 and 5 comprehensively investigate this phenomenon for hydrogels, where under confinement, the relaxation times were orders of magnitude longer than equilibrium, bulk relaxation times. Furthermore, an earlier onset of shear thinning behavior as a function of strain rate upon an increase in compression has also been reported before for confined liquids (133) attributed to the shear assisted alignment of the molecules, in the context of Eyring's theory. Urbakh et al developed scaling relationships for the shear thinning exponent and the applied confinement for confined liquids, by considering distinct velocity profiles for varying levels of confinement{Urbakh, 1995 #210}. In line with Rabin's theory, shear thinning was observed where shear rates were greater than the relaxation times of the confined liquids. An order parameter, which could be representative of the liquid density, polarization or molecular orientation as well as a surface interaction term were considered when defining the liquid flow and the molecular relaxations. Confinement induced changes in the order parameter were shown to result in confined liquid viscosities much higher than their bulk viscosities. A linear velocity profile, where stick occurred at the boundary wall, pertaining to liquid-wall interactions was assumed for low confinement or "thick" films, while for highly

confined films, a step-wise distribution of velocity was assumed where with velocity (v) = V or v = 0, thereby simulating the velocity profiles in thin, solid-like liquid films. For low and high confinements in the former case, shear thinning exponents of $n > 1$ and $n < 1$ were obtained, respectively, which is in good agreement with our own results. Interestingly, in the limiting case of extreme confinement, where a step-wise velocity is considered, the shear-thinning exponent was 3/2, and was independent of the structure parameter or conversely, the confinement. While it is possible to rationalize for liquid thin films, as done by Yoshizawa in the past as well (126), we do not observe this behavior for the hydrogels, where although a change of slope in the effective viscosity vs the shear rate occurs, the exponent is still compression dependent. This is plausible as the level of confinement employed in this study is at least two orders of magnitude larger than the characteristic mesh size of the polymer networks characterized in Chapters 2-5 and a complete "jamming" of the hydrogel film is not expected. Nevertheless, the good qualitative agreement with the low confinement case is encouraging and validates the treatment of the hydrogel thin films as a complex fluid.

On the other hand, the increase in viscosity at low strain rates is observed for systems in which secondary bonding can take place upon confinement or compression(137). This trend is observed for either the thinnest hydrogel films or at high compressions, hence it is possible that hydrogen bonding within the hydrogel could be enhanced when less water is present. Lastly, at the lowest shear rates, a plateau in viscosity η_0, is not observed clearly in our measurements, however the footprint is present in the frequency sweeps for the 6% PAAm hydrogel, where $H \sim 14\mu$m. In the amplitude sweeps, the plateau at higher compressions, where the viscosity undergoes a discontinuous jump could also be the plateau of η_0 instead of the η_∞, however, further

investigations are needed to conclude this. Nevertheless, the striking resemblance of the hydrogel thin film rheology to that of a polymer melt or solution is very intriguing.

7.3.2. Reconciling tribology with rheology

Figure 7.10 summarizes the results for tribology and rheology as a function of speed and the strain rate, respectively. It is important to mention beforehand, the trends were not always observed at the same strain rates in rheology and tribology simultaneously, hence this is not an exact comparison. At low speeds, agreement with the characteristic Eyring's theory(157) which was employed by Schallamach for rubber friction(42, 103) is observed. We extended this to the viscous adhesive friction model in Chapter 5 for hydrogel friction in the *adhesive* regime, where only for the hydrogels with the highest monomer content, a precise logarithmic increase in friction with sliding speed was observe in the AFM. Importantly, even though we observe a weak footprint of shear thinning in rheology, the data mostly follows the power-law with an exponent of 1, corresponding to a constant G' and thereby to a behavior characteristic of a viscoelastic solid. In a currently unpublished work from our lab, Eyring's model was fit to the nanorheological measurements of ionic liquids and the characteristic exponents for the respective data was found to be ~0.4 or lower. We do not observe this exponent, except for only one condition ($H = 14\ \mu$m; 46% compression). Therefore at the lowest sliding speeds, where the interactions between the surface polymer and the countersurface are perhaps most relevant, the effective viscosity is insufficient to capture the rich behavior. This worsens upon compression, which expected due to a further increase in the adhesive/ elastic contribution to friction. Even though the observed shear thinning is weak, the results are important, showing that even at the slowest speeds viscous contributions are there, in contrast to what previous hydrogel friction models have assumed. In fact, in Chapter 5 we consider a speed-independent term, F_o when describing the total friction force

for a PAAm hydrogel in contact with a silica colloid. Modeling the measurements on a repulsive contact (agarose hydrogels and a silica colloid) also required consideration of the term F_o,(158) indicating that it could be arising from the viscous contribution at the slowest velocities.

A peak followed by the decrease in friction corresponds to the conditions where the Deborah number is equal to or greater than 1. A Deborah number of 1 means that the polymer relaxation time and the experimental observation time are equal, polymer to countersurface bonding is enhanced and friction achieves a maximum. This is important, as it shows that the elastic component of the network is *visibly* relevant. After this point, only a few bonds can form between the hydrogel and the countersurface and friction is mainly dictated by the rate of bond formation yielding a v-weakening regime. Here, the effective viscosity should decrease faster than an exponent of 1. As mentioned in the results section, a clear change in the slope of the effective viscosity is observed at higher strain rates, where $n > 1$. This is encouraging, along with the fact that the transition occurs at strain rates, which are at least, the same order of magnitude in both measurements. The lack of resolution owing to small number of data points keep us from determining the exact strain rates at which these transitions occur.

At higher speeds, the plateau in friction indicates that here we should see an exponent of 1. This is the common trend observed in frequency sweeps, especially at higher compressions however, the agreement of corresponding strain rates from friction and rheology is poor. Note that only at low compressions, sometimes the v-strengthening followed by the v-weakening regime is observed in rheology *continuously*. In fact, at high velocities where friction starts to increase with speed again, a progression from power-law to the plateau viscosity and the bulk shear thinning is only continuously observed in amplitude sweeps (shown in the green box).

Nevertheless, our results here demonstrate that the rheology of the thin film plays an important role in its frictional response. However, the rich behavior of friction as a function of sliding velocity arises from the combination of the viscous and the elastic/adhesive component leading to the observed deviations.

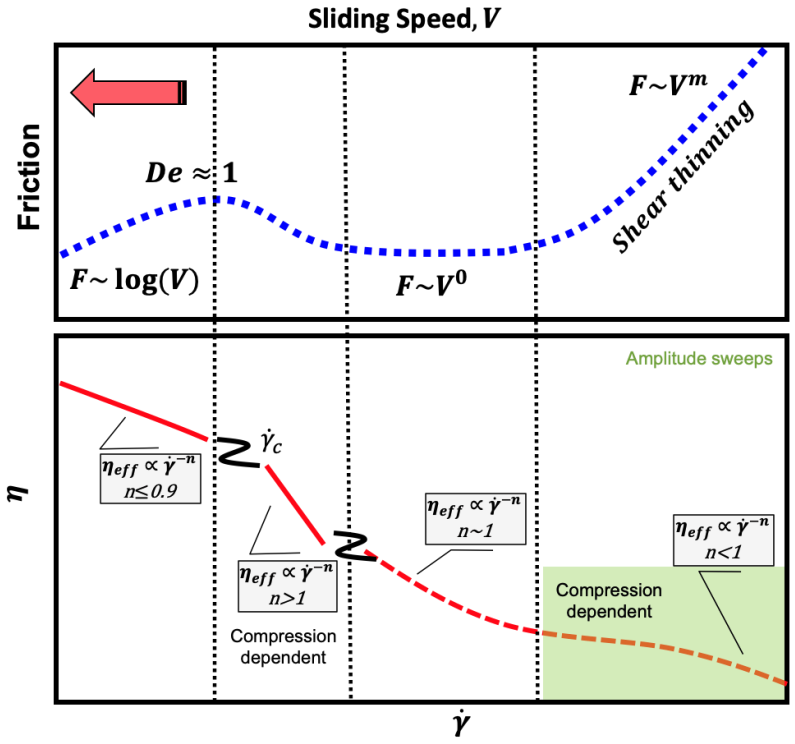

Figure 7.10 The measured friction vs sliding speed (top) and the effective viscosity as a function of strain rates (bottom) are combined to reconcile oscillatory rheological and tribological measurements. The dashed black lines outline various regimes on the friction map. The green box points to trends, which are observed in amplitude sweeps while the red dashed line corresponds to trends that are seen at isolated conditions and not in continuity with the previous regime. The red arrow points to the direction towards which the friction master curve shifts upon an increased compression.

7.4. Conclusions

Simultaneous rheological and tribological measurements of hydrogel thin films were successfully performed in an eSFA. The novel results reveal a graded response of the hydrogel thin films, where a non-linear change in the complex modulus and the effective viscosity is observed

as a function of compression. By performing oscillatory shear (rheology) and shear at a constant velocity (tribology) at different compressions, a spectrum of trends are unraveled. By treating the hydrogel as a complex fluid, agreement of the effective viscosity obtained from rheological and tribological measurements is critically analyzed. The intricate influence of the compression on the effective viscosity and the friction force, and the relevance of viscous contribution at *all* sliding speeds is also highlighted. Future experiments focused on the exploring the low compressions, low strain rates and linear rheological response of the hydrogels could further our understanding of the correlation between rheology and tribology and hydrogels. Furthermore, modification of the surfaces to render them adhesive could also help in expanding the experimental limits, perhaps by truly achieving a "jammed" hydrogel thin film, where the laws governing dynamics of a confined, structured liquid become applicable.

CHAPTER 8: COMPOSITIONAL TUNING OF DN HYDROGELS TO ACHIEVE HIGH LUBRICITY AND HIGH STIFFNESS

In this chapter we report a thorough study of DN hydrogels composed of agarose as the first (physically crosslinked) network and PAAm as the second (chemically crosslinked) network. We systematically modified the second network's composition (PAAm), studied the resulting DN microstructure, elucidated the double network formation pathway and measured the frictional response. This work provides insight into the compositional limitations of the second network to form a viable DN hydrogel with enhanced mechanical and tribological properties.

8.1. Experimental Methods

8.1.1. Hydrogel preparation

All chemicals were purchased from Sigma-Aldrich, USA unless otherwise noted. Agarose-polyacrylamide double network hydrogels were prepared by solutions of agarose powder (1st network prepolymer), acrylamide (2nd network monomer), bisacrylamide (2nd network crosslinker), $\boldsymbol{\alpha}$-Ketoglutaric acid (2nd network's UV initiator), and tetramethylethylenediamine (TEMED) (2nd network's accelerator). The synthesis method was developed based on the protocol reported in ref. (159) with the following modification. Agarose powder was added to *pre-heated DI water to 80 °*$\boldsymbol{C}$ under constant stirring. After 10 minutes of stirring, when the solution became clear (indicative of agarose dissolution), it was allowed to cool down. To prepare the DN hydrogels, a solution of 20mL with acrylamide monomer (AAm) and bisacrylamide crosslinker (bis-AAm) was added to the agarose solution, followed by the initiator and accelerator. Table 1 shows the corresponding concentrations. After stirring for 10 seconds, 2 ml werepipetted into a polycarbonate petri dish. Agarose gelation was allowed to occur for 30 minutes, after which the samples were put under UV light for 4 hours for the second network to form. Four different DN

hydrogels were prepared with different compositions as shown in Table 1. Note that the main difference between 1Ag6PAAm-0.5x and 1Ag6PAAm hydrogels is the crosslinker concentration (0.15 vs. 0.3 wt%). A subset of hydrogels were prepared only with agarose (1wt%). Samples were then equilibrated either in DI or in mixtures of DI and dimethyl sulfoxide (DMSO) for one day prior to testing. For investigating the effect of DMSO, DN hydrogel samples were equilibrated either in DI or in mixtures of DI and DMSO for one day prior to testing. We compare the results in this work with those reported for PAAm SN hydrogels in our previous works(1, 35).

For dynamic light scattering measurements, rectangular slabs were cut from hydrogel samples and inserted in a small volume, plastic cuvette. The cuvette was then filled with DI or mixtures of DI and DMSO to prevent hydrogel drying. For rheological measurements, samples with a diameter of 8 mm were punched from the hydrogel samples. For indentation and friction-force measurements, the hydrogels were used as prepared in the petri dish. For infrared spectroscopy, hydrogel samples were prepared in the petri-dishes, as described above, and the top and bottom surfaces were placed on the ATR-IR crystal as is.

Table 8.1. Composition of the synthesized DN hydrogels. For all hydrogels, the amount of the UV initiator was 1 mol% of the AAm monomer while the amount of the accelerator was 0.1 vol% of the total solution volume. All hydrogel solutions were made up to a total volume of 20 mL. The weight percentages mentioned are calculated with respect to the individual solutions of agarose and PAAm.

Hydrogel name	Agarose wt %	AAm wt %	bis-Aam wt %	AAm:bisAAm mass ratio	AAm:bisAAm mole ratio
1Ag4PAAm	1	4.0	0.10	40.0	87.1
1Ag6PAAm-0.5x	1	5.0	0.15	33.3	72.6
1Ag6PAAm	1	5.0	0.30	16.7	36.3
1Ag9PAAm	1	8.0	0.48	16.7	36.3

8.1.2. Attenuated total reflection infrared spectroscopy

Attenuated Total Reflectance Infrared Spectroscopy (ATR-IR) (PerkinElmer, Frontier, and Pike Technologies, GladiATR with a diamond crystal) was used to determine the chemical footprint of the DN hydrogels. The sample absorbance was collected in the range of 500-4000 cm^{-1}. The baseline correction was done with DI water as background to enhance the polymer footprint. Top and bottom surfaces of the hydrogel samples (~2 mm in thickness) were investigated to evaluate the presence of chemical gradients. Because the penetration depth of the infrared ranges between 1.1 and 2.2 μm, this is a viable method to distinguish between the chemical composition of top and bottom surfaces (36). A dead weight of ~100 g was placed on top of the hydrogels to enhance the hydrogel-crystal contact for each run.

8.1.3. Dynamic Mechanical Analysis

The rheological behavior of the hydrogels was investigated using a Dynamic Mechanical Analysis (DMA, Perkin Elmer, DMA 8000). Frequency and amplitude sweeps using the single cantilever mode were performed in the range of 0.1-20 Hz at constant strain of 2% and as a function of strain from 0.1 to 1% at a constant frequency of 1 Hz. Hydrogels samples (2 mm in thickness and 8 mm in diameter) were loaded into the cell. Storage ($\boldsymbol{G'}$) and loss moduli ($\boldsymbol{G''}$) were measured as a function of frequency and amplitude. For each measurement, the temperature was maintained constant at 25ºC using a water bath.

8.1.4. Colloidal Probe Atomic Force Microscopy

Indentation and friction-force measurements were conducted with an atomic force microscope (AFM, Nanowizard Ultra, JPK Instruments, Germany) using silica colloids (Duke Scientific, Thermo Scientific, CA, USA) with nominal diameters of 20 μm. Detailed methodology is describedearlier in Chapters 4 and 5.

8.1.5. Quantitative Imaging AFM

The surface of DN and SN agarose hydrogel surfaces was imaged by Atomic Force Microscopy (Nano Wizard, JPK Instruments, Ge many) using the quantitative imaging mode (QI) with a sharp tip (HQ:CSC37, No Al, 0.3–0.9 N m−1, Nanoandmore, USA). In QI mode, cross-sections (30 x 30 μm and 5 x 5 μm) were divided into a grid of 256 x 256 pixels and force–distance curves are measured at each pixel at an approach speed of ∼60 μm s−1 and a very small load of ∼1.5-2 nN. From here, the height, adhesion and slope profiles are obtained.

8.1.6. Swelling tests

After the gelation of the agarose SN and agarose-PAAm DN hydrogels in petri dishes, circular discs 2 mm in thickness and 8 mm in diameter were pinched out and immersed in the

solvent (either DI water or water:DMSO mixture). Samples were weighed at 0, 4, 8, 12, 24 and 48 hour intervals. 48 hours were long enough to achieve equilibrium swelling in these systems. The dry mass of the polymer in each sample was also measured by drying the hydrogel discs in air for 48 hours. The swelling ratio was calculated as: $swelling\ \% = \left(\frac{m_w}{m_o}\right) * 100$, where m_w is the mass of the fully swollen hydrogel and m_o is the dry mass.

8.2. Results

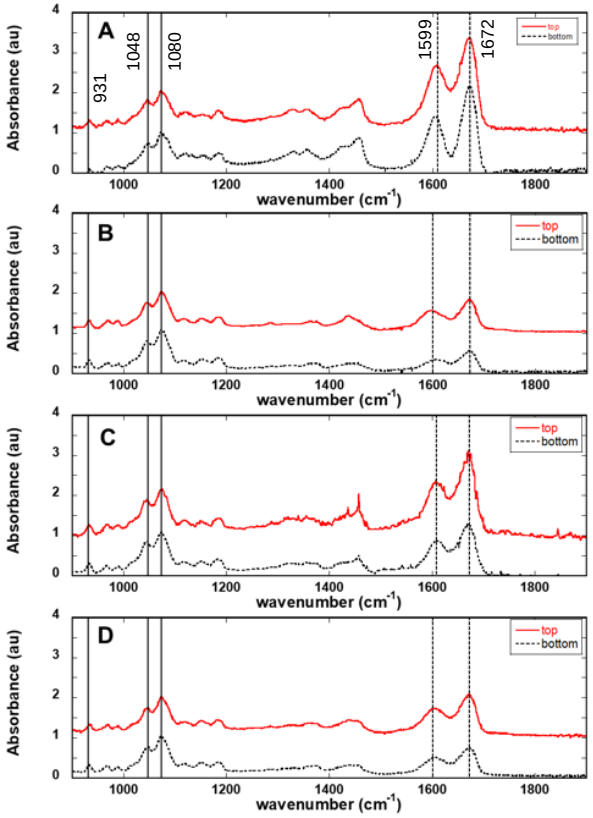

Figure 8.1 ATR-IR absorbance spectra for A) 1Ag4PAAm, B) 1Ag6PAAm, C) 1Ag6PAAm-0.5x and D) 1Ag9PAAm DN hydrogels. The IR bands associated with PAAm and agarose are identified as the dashed and full lines, respectively. The chemical heterogeneity as a function of sample depth is also illustrated here in the form of a comparison between the top (red curves) and bottom (black curves) surfaces of the DN hydrogels.

8.2.1. IR spectroscopy confirms the successful formation of the DN hydrogels and the formation of chemical gradients

1Ag4PAAm, 1Ag6PAAm-0.5x, 1Ag6PAAm and 1Ag9PAAm hydrogels were prepared as indicated in the Materials and Methods section. The chemical composition of bottom and top surfaces of the hydrogels was determined using ATR-IR spectroscopy. Figure 8.1 shows representative IR spectra for the four hydrogels.

The successful polymerization of acrylamide in 1Ag4Paam hydrogels (Figure 8.1a) is confirmed by the detection of strong absorption bands at 1672 cm-1 and 1599 cm-1 (dotted lines), -characteristic of amide I and amide II- on both top and bottom surfaces. Additionally, the presence of the agarose network is confirmed via the vibration bands at 1080 cm-1 for C-H bending in sugars, 1048 cm-1 for C-O, 1371 cm-1 for C-C bending, and 931 cm-1 ascribed to the 3,6-anhydrogalactose(160, 161). Interestingly, broadened peaks at 1440 cm-1 and 1462 cm-1 are also observed in all IR spectra, which can indicate bands corresponding to asymmetric stretching from COO-. This can be due to the hydrolysis of AAm, expected to occur above 40 °C (162). It is most prominent in the top and bottom surfaces of 1Ag4PAAm hydrogels.

The careful analysis of peak shifts corresponding to amide and C-O bands respectively revealed two important findings. First, compared to the 1608 cm-1 amide II band for pure PAAm hydrogels, 1Ag9PAAm showed a shift to lower wavenumbers, i.e. 1599 cm-1 and 1600 cm-1 for the top and bottom surfaces, respectively, while 1Ag6PAAm showed a shift to 1600 cm-1 only for the top surface. A shift to lower wavenumbers for these bands is commonly attributed to hydrogen bonding (163, 164). For 1Ag4PAAm and 1Ag6PAAm-0.5x, a shift to higher wavenumbers (1613 cm-1 and 1610 cm-1, respectively) was observed for both top and bottom surfaces. This indicates that the intermolecular interactions between agarose and PAAm are weakened, and a looser double

network forms. Interestingly, the C-O peak in pure agarose hydrogels at 1046 cm^{-1} shifts to higher wavenumbers in the DN hydrogels. This further supports that the second network, here PAAm, inhibits hydrogen bonding in agarose. This kind of cooperative hydrogen bonding is crucial to form the thick fibrous network of agarose (165).

We also note that the agarose and PAAm footprint, although visible on the top and the bottom surfaces of the four DN hydrogels varies in intensity, pointing towards a chemical gradient as a function of the hydrogel's depth (Figures 8.1b-d). To evaluate the compositional gradients in the four DN hydrogels, Figure 8.2 compares the ratios between the absorbance peaks at 1080 cm^{-1} (C-O) and 1672 cm^{-1} (amide I). As inferred from the different ratios for top and bottom surfaces, the gradient is smallest for 1Ag4PAAm and largest for 1Ag6PAAm hydrogels. A decreasing ratio thus indicates an increasing in PAAm concentration; and hence, there is an enrichment of PAAm on the top compared to the bottom surface. Interestingly, increasing the acrylamide concentration does not lead to a relative increase in PAAm with respect to agarose in the DN hydrogels, as evidenced by the increase in the agarose:PAAm ratios, but quite the opposite, and more so on the bottom surface. This suggests that the agarose hydrogels have a maximum capacity of incorporating AAm, and that increasing the acrylamide monomer concentration in solution does not yield an increase of PAAm in the DN hydrogel.

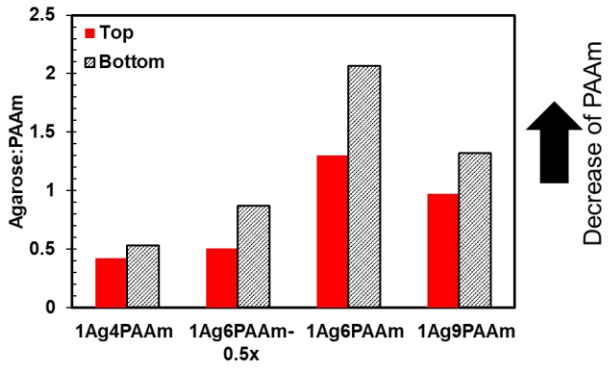

Figure 8.2 Absorbance ratios at 1080 cm^{-1} (agarose peak) and 1672 cm^{-1} (amide I peak) for top (blue) and bottom (red) surfaces of the four DN hydrogel compositions.

8.2.2. Composition-dependent strengthening of DN hydrogels

The autocorrelation functions of 1Ag6PAAm hydrogels exhibited prominent static scattering. This is expected for hydrogel networks with structural inhomogeneities resulting from either inhomogeneous crosslinking or molecular interactions(83) and it could indicate inadequate double network formation. Hydrogels with static scattering (e.g., due to inhomogeneities) require elaborated spatial-dependent DLS measurement and analysis,(76-78) which is outside the scope of this work. The other hydrogels do not exhibit static scattering. For ergodic and homogeneous systems (no static scattering), a single correlation length (ξ), which typically represents (liquid-like) fluctuations of the polymer, *i.e.*, the distance between crosslinks, can be determined by fitting a single exponential decay (Eq. 1-2) to the autocorrelation function based on Tanaka's model(75). Note that we applied this analysis to 1Ag6PAAm hydrogels, and hence, the results for this hydrogel must be considered with caution.

Figure 8.3A shows a non-monotonic change in correlation length as a function of increasing AAm monomer concentration: $\mathbf{60.2 \pm 6.2}$ nm, $\mathbf{6.6 \pm 0.12}$ nm, $\mathbf{4.5 \pm 1.7}$ nm, and $\mathbf{126 \pm 38}$ nm for 1Ag4PAAm, 1Ag6PAAm-0.5x, 1Ag6PAAm, and 1Ag9PAAm DN hydrogels.

In comparison, the correlation lengths for single network 1wt% agarose was $\mathbf{70.2 \pm 30}$ nm. A prominent decrease in mesh size occurs by the addition of acrylamide (from 4% to 6% AAm), but additional increase in monomer concentration (9% AAm) leads to an expansion of the correlation length beyond that of SN agarose hydrogel, indicating a prominent rearrangement of the agarose network. This variation reflects an intricate modulation of the double network via the second network. DLS might be unable to identify two different mesh sizes, and hence, it is unclear whether the correlation length is an indicator of a uniform homogenous network characterized by a single mesh size or it is representing only one of the two networks, though (166). Since SEM studies have reported formation of a uniform, homogenous network for agarose-PAAm DN hydrogels(163), the single correlation length could be good representative of the double network. Importantly, the increase in crosslinker:monomer ratio by a factor of 2 leads to the appearance of heterogeneities (static scattering).

Figure 8.3A shows storage and loss moduli of the DN hydrogels, as determined from strain sweeps at 1 Hz. $G' > G''$ and tan-$\delta < 0.1$, and hence, the hydrogels exhibit a prominent elastic behavior. The lowest and highest tan-$\boldsymbol{\delta}$ values (0.02 and 0.09) are measured for 1Ag6PAAm-0.5x hydrogel and 1Ag9PAAm hydrogels, respectively. The storage moduli are recorded as $\mathbf{17.1 \pm 0.6}$ kPa, $\mathbf{109.4 \pm 16.3}$ kPa, $\mathbf{13.7 \pm 1.1}$ kPa, $\mathbf{9.7 \pm 1}$ kPa for 1Ag4PAAm, 1Ag6PAAm-0.5x, 1Ag6PAAm and 1Ag9PAAm hydrogels, respectively. In comparison, 1 wt% agarose hydrogels have a storage modulus of 20.8 $\pm \mathbf{7.4}$ kPa, while the PAAm hydrogels with 4%, 6% and 9% PAAm have much smaller storage moduli (0.143 $\pm \mathbf{0.01}$ kPa, 0.275 $\pm \mathbf{0.03}$ kPa, 1.14 $\pm \mathbf{0.150}$ kPa, respectively (1)). Rheology measurements on SN 6%-0.5x PAAm hydrogels failed because the hydrogels were very soft.

The comparison between DN and SN hydrogels reveals that only the double network formed in the case of 1Ag6PAAm-0.5x provides significant strengthening: G' of 1Ag6PAAm-0.5x hydrogels is about two and three orders of magnitude larger than that of the reference agarose and PAAm hydrogels with similar monomer concentrations(1), respectively. The results suggest that the strengthening of the double network only happens at a specific composition of the second network, and it concurs with a prominent decrease in the correlation length. Increasing the crosslinking by a factor of 2 weakens the hydrogel significantly, as G' decreases by about one order of magnitude, perhaps as a result of the heterogeneities observed by DLS. Note that these heterogeneities make the value of the correlation length derived from the DLS measurements questionable, and hence, we do not discuss it further.

The elastic modulus and the adhesion energy were also obtained by fitting the JKR model to the indentation force-depth curves upon retraction for the top surface of DN hydrogels, and reference single network hydrogels. In agreement with the rheological results, the highest modulus is obtained for 1Ag6PAAm-0.5x hydrogels (80.5 ± 6.1 kPa), while very similar moduli (19.9 ± 1.3 kPa, 10.8 ± 1.5 kPa and 13.9 ± 0.9 kPa) are obtained for 1Ag4PAAm, 1Ag6PAAm, and 1Ag12PAAm DN hydrogels, respectively.

Swelling measurements in water reveal the highest swelling ratio for 1Ag4PAAm hydrogels followed by 1Ag9PAAm, and then by 1Ag6PAAm hydrogels with both crosslinking ratios. Note that they have also the smallest correlation lengths, but only 1Ag6PAAm-0.5x become stronger than the reference agarose hydrogels. Importantly, IR spectroscopy hints towards the presence of charge, especially in the 1Ag4PAAm hydrogel, where distinct bands corresponding to COO- stretching are observed, which could justify the highest swelling of this hydrogel. Similarly, the absence of this band in 1Ag9PAAm hydrogel is in agreement with a lower swelling hydrogel.

Some studies have reported a dramatic reduction in the macroscopic swelling of DN hydrogels (167), which they attribute to hydrogen bonding between the two networks. Both 1Ag6PAAm-

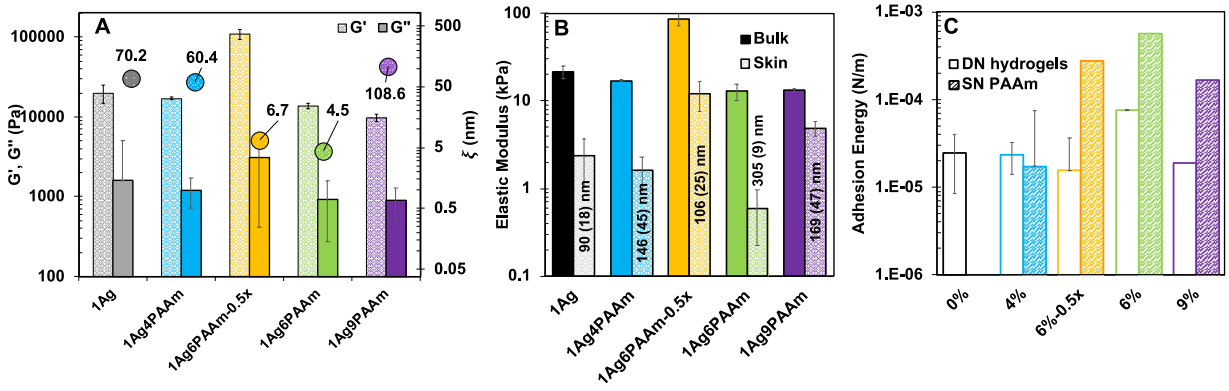

Figure 8.3 A) Correlation lengths (circles), storage modulus (G', patterned bars) and loss modulus (full bars) for 1Ag (grey), 1Ag4PAAm (blue), 1Ag6PAAm (green), 1Ag6PAAm-1.5x (yellow), and 1Ag9PAAm (purple) hydrogels from strain sweeps. B) Elastic modulus obtained from Hertzian fits of bulk and of the surface along with the surface or "skin" layer as a function of DN hydrogel composition. Elastic modulus of the bulk: 19.9 ± 1.3 kPa, 80.5 ± 6.1 kPa, 10.8 ± 1.5 kPa and 13.9 ± 0.9 kPa for the 1Ag4PAAm, 1Ag6PAAm-0.5x, 1Ag6PAAm and 1Ag9PAAm hydrogels, respectively. B) Adhesion energy of DN hydrogels (blue, orange, green and purple striped) and SN hydrogels of 1 wt% agarose and 4%, 6%-0.5x, 6% and 9% PAAm hydrogels (open bars) as reference; the single network agarose hydrogel corresponds to 0% PAAm. Adhesion energy values for the 4%, 6% and 9% PAAm hydrogels have been taken from ref. (1) with permission. Additionally, swelling measurements reveal highest swelling for 1Ag4PAAm (2673%), followed by SN 1Ag (1171%), 1Ag9PAAm (916%), 1Ag6PAAm-0.5x (793%) and 1Ag6pAAm (757%). Colloid radius: 10 µm. Cantilever Stiffness: 0.42 N/m.

0.5x and 1Ag6PAAm hydrogels exhibit a reduced swelling, however, there is no evidence of hydrogen bonding. It is thus possible that the formation of the 2nd network imposes a tension on the agarose network, leading to the dramatic reduction in swelling and mesh size, as revealed by DLS.

8.2.3. Low adhesion energy of DN hydrogels

The work of adhesion of 1wt% agarose hydrogels is small (0.024±.012 mN/m) and reflects the negligible affinity of the hydrogel to the silica colloid (90), while single network 6% and 9% PAAm hydrogels exhibit the largest values (Figure 8.3C). The origin for the high adhesion of 6%

and 9% PAAm hydrogels to the silica colloid has been associated with the formation of hydrogen bonds between the polymer and the silanol groups(1). The highest adhesion energy of 6% PAAm hydrogels results from the combined effects of higher acrylamide concentration than in 4% PAAm hydrogels and larger contact area than in 6%-1.5x and 9% PAAm hydrogels. Figure 8.3C shows that incorporating the PAAm network in the agarose hydrogel reduces the work of adhesion significantly, except in the case of 1Ag4PAAm hydrogels. This is not surprising as both 1% agarose and 4% PAAm hydrogels exhibit similar adhesion energies (~0.023-0.024 mN/m); in addition, the swelling ratio of 1Ag4PAAm hydrogels is larger than that of the other hydrogels. The presence of agarose in the interfacial region, and thereby, the decrease in acrylamide concentration in the other DN hydrogels, results in a decrease in adhesion energy. This decrease is most significant for 1Ag6PAAm-0.5x hydrogels. In this case, FTIR suggests the presence of acrylamide on the top surface, and hence the decrease in adhesion energy is most likely associated with the significant strengthening of the hydrogel, and thereby, the decrease in contact area. The high adhesion energy of 1Ag6PAAm hydrogels could in part be due to the much larger contact area (see the smaller elastic modulus), despite the relative decrease in acrylamide concentration. Moreover, an increase (decrease) in hydrophilicity of PAAm hydrogels with an increase in the crosslinker (monomer) has been reported.–This behavior is consistent with the higher adhesion energy obtained for 1 Ag6PAAm compared to the 1Ag9PAAm (higher AAm concentration) and 1Ag6PAAm-0.5x (lower bis-AAm concentration). In summary, the role of both the high swelling (in the case of 1Ag4PAAm hydrogels) and the depletion of PAAm toward the surface (in 1Ag9PAAm hydrogels) in lowering adhesion is thus evident. This is in agreement with other studies in which alginate-rich surfaces were found for alginate-PAAm DN hydrogels confirming

that a chemical gradient of the two networks exists(168). The role of PAAm in the double network is less understood.

The piecewise fits of the Hertz model to the indentation curves upon approach revealed a near-surface region (labeled as “skin”) with a small modulus underneath a stronger hydrogel (labeled as “bulk”); see Figure 8.3B. The elastic modulus of the hydrogel underneath the skin was consistent with that obtained using the JKR model to fit the retraction curves. The presence of a soft skin has been reported for single network PAAm hydrogels previously (35). The soft “skin” has a thickness of $\mathbf{146 \pm 45}$ nm, $\mathbf{106 \pm 25}$ nm, $\mathbf{305 \pm 8.9}$ nm and $\mathbf{169 \pm 47}$ nm on the top surface of 1Ag4PAAm, 1Ag6PAAm-0.5x, 1Ag6PAAm and 1Ag9PAAm hydrogels, respectively, and the corresponding moduli were found to be 1.6 ± 0.7 kPa, 12 ± 4.5 kPa, 0.6 ± 0.4 kPa, and 4.8 ± 0.9 kPa, respectively. The strongest hydrogel, 1Ag6PAAm-0.5x, has the thinnest skin layer, indicating a more uniform crosslinking across the depth. The results for 1Ag6PAAm hydrogels are intricate. The skin is 2-3 times thicker than that of the other DN hydrogels (and also much softer), while the adhesion energy is higher, which supports an enrichment of PAAm in this case. This is, however, in contradiction to FTIR, where a depletion of PAAm toward the surface was observed. It is possible that the network heterogeneity is responsible for these inconclusive results.

Comparison of tan delta from DMA measurements of SN agarose, SN PAAm and DN hydrogels, we find that the SN agarose hydrogel is less dissipative (lower tan delta) than SN PAAm. Among the DN hydrogels, 1Ag4PAAm, 1Ag6PAAm have tan delta values similar to SN PAAm hydrogels while only 1Ag6PAAm-0.5x show similar values as those seen on SN agarose. This is in agreement with the swelling experiments as well. In contrast, highest tan-delta for 1Ag9PAAm hydrogels and hence the highest dissipation is attributed to the disturbed and hence

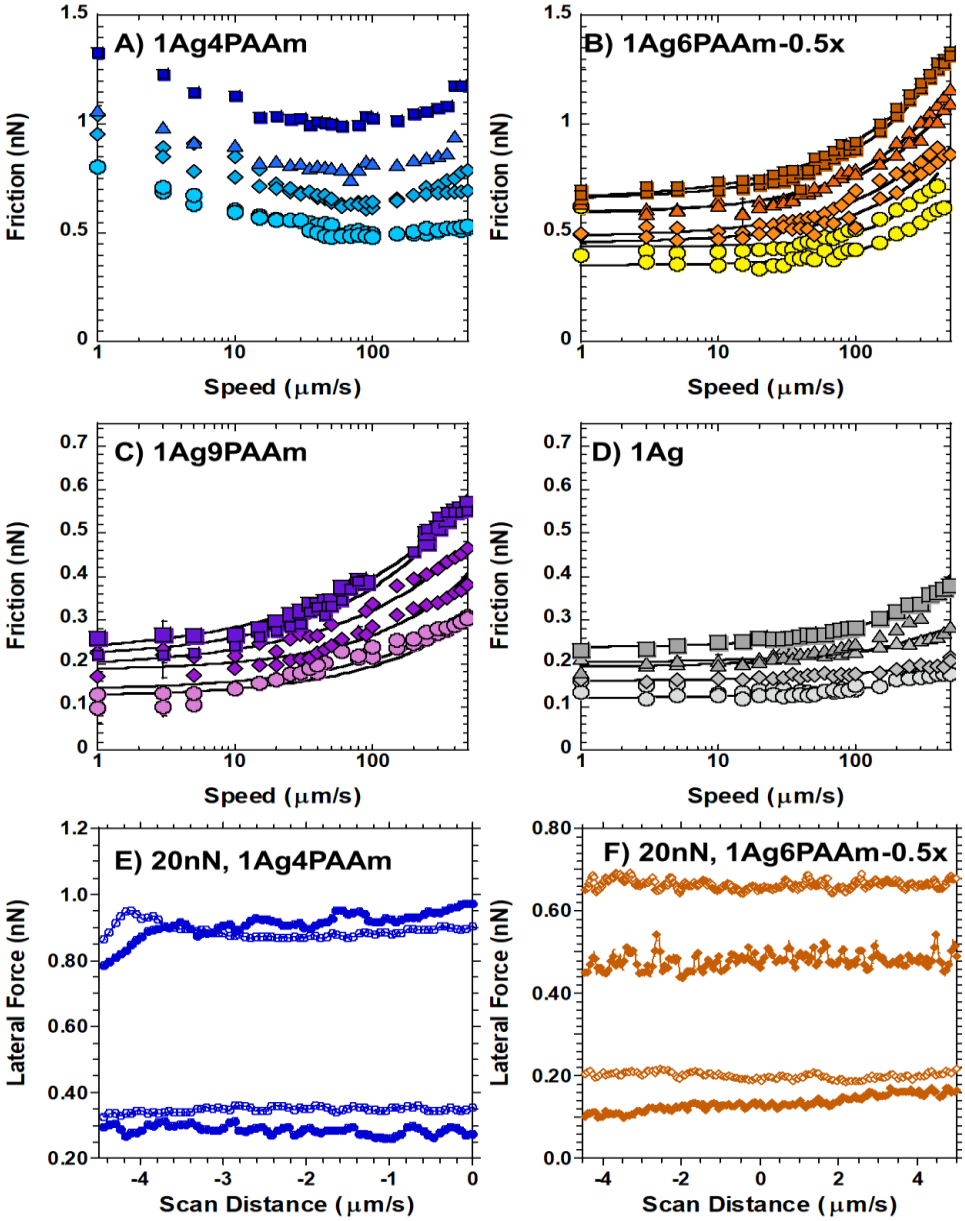

Figure 8.4 A-D) Friction force vs. speed for 1Ag4PAAm (blue), 1Ag6PAAm-0.5x (yellow to orange), 1Ag9PAAm (purple) and SN 1Ag (grey) at normal loads of 20 nN (circles), 30 nN (diamonds), 40 nN (triangles) and 50 nN (squares). The solid black lines in B-D are fits to equation 7. E-F) Friction loops at a selected load of 20 nN and speeds of 1 μm/s (filled symbols) and 100 μm/s (open symbols) for 1Ag4PAAm (blue circles) and 1Ag6PAAm-0.5x (orange diamonds). Speed dependent, poroelastic deformation prior to sliding is observed for the 1Ag4PAAm hydrogels at both speeds, more so at slower speeds, as expected. Multiple stick-slip events and intermittent sliding is observed on the 1Ag6PAAm-0.5x DN hydrogel, more so at slow sliding speeds. Colloid radius: 10 μm. Cantilever Stiffness: 0.42 N/m.

heterogeneous network of this gel. From here, it is expected that the influence of PAAm is seen more in the bulk of the hydrogel than in the surface.

8.2.4. Influence of the chemical makeup on DN hydrogel friction

The dynamic friction between DN and agarose (as reference) hydrogels and a silica colloid as a function of load and velocity are shown in Figure 8.4A-D. Note that the best lubrication is provided by agarose hydrogels under the investigated conditions (Figure 8.5D). The measurements with 1Ag6PAAm hydrogels were noisy and irreproducible, which we attribute to the presence of heterogeneities, and hence, they are not further discussed. The general trend is that friction increases with load (see the increasing friction with color intensity), while the velocity dependence of friction is significantly dependent on the hydrogel composition. Our previous investigations of the frictional dissipation by PAAm hydrogels revealed the existence of adhesive and viscous contributions to friction leading to a prominent velocity-weakening friction at low sliding velocities and an increase in friction with velocity (velocity-strengthening friction) at high velocities, respectively. Both, poroelastic drainage of the brushy interface and its hydrogen bonding to the silica colloid led to a noticeable adhesive contribution and velocity-weakening friction. The viscous regime showed a shear thinning behavior (1, 25). In contrast, a prominent velocity independent plateau at low velocities followed by an increase in friction with velocity at higher velocities was observed for agarose hydrogels (Figure 8.4D).

The friction behavior of 1Ag4PAAm hydrogels (Figure 4A) can be best described as transitional, where the decreasing friction with velocity precedes the increase in friction with further increase in velocity. It is worth mentioning that the frictional response of 1Ag4PAAm hydrogels resembles that of 4%PAAm SN hydrogels(1). The friction loops exhibit a tilt before sliding commences, which becomes more prominent at slow velocities, and it is indicative of a time-dependent deformation before sliding (Figure 4E). This was associated to the poroelastic deformation of the surface-near region (1, 19, 23). Furthermore, the characteristic stick-slip can be

associated with the interaction of PAAm with the silica colloid upon the drainage of water (Chapter 4).

In contrast, the frictional dissipation of 1Ag6PAAm-0.5x and 1Ag9PAAm resembles the behavior of agarose hydrogels more closely. Both 1Ag6PAAm-0.5x and 1Ag9PAAm hydrogels show a *quasi*-speed-independent plateau followed by viscous dissipation, with the transition occurring around ~10 μm/s and 3-10 μm/s (increasing with increasing load), respectively. We propose a tentative correlation between the elastic modulus and the length of the plateau, where a higher modulus leads to a longer plateau or a quasi-speed-independent behavior. The absence of the velocity-weakening regime indicates that the poroelastic deformation is less significant than for 1Ag6PAAm-0.5x hydrogels due to the much higher elastic modulus. Furthermore, significant stick-slip was observed during sliding (**Figure** 8.4F), hence indicating chemical interactions between the surface polymer and the colloid. Note that the swelling ratio of this hydrogel is more than three times smaller than that of 1Ag4PAAm hydrogels, which is consistent with the stronger interactions with the colloid. 1Ag9PAAm hydrogels, exhibit a lower amount of PAAm on the surface compared to 1Ag4PAAm and 1Ag6PAAm-0.5x hydrogels along with a very tight distribution of surface energies across its surface. This suggests that the friction behavior may be dominated by agarose in this case. In fact, 1Ag9PAAm shows smooth sliding similar to that observed for agarose.

Lastly, friction coefficients in DI water of the DN hydrogels ranged from 10^{-2} to 10^{-3}, where the lowest and highest friction coefficients were recorded on the 1Ag9PAAm and 1Ag6PAAm-0.5x DN hydrogels, already indicating a better lubrication than those observed for some of the DN hydrogel systems(169, 170).

8.2.5. Modulation of friction of DN hydrogels via the imbibed fluid

To examine the influence of the imbibed fluid on friction and swelling ratio of agarose and 1Ag6PAAm-0.5x hydrogels were carried out with DMSO-water mixtures. The swelling ratio shows the response of the hydrogels to the solvent composition (Figure 8.5A). The collapse of agarose with increase in DMSO% is significant, while the decrease in swelling ratio of the 1Ag6PAAm-0.5x hydrogels is moderate. DMSO is also a bad solvent for polyacrylamide(171), and hence, a significant collapse of the hydrogel upon an increase in DMSO concentration is expected. However, the results indicate that the double network prevents such collapse from happening. Figure 8.6 A-D show friction measurements in 50% DMSO and 100% DMSO; *cf.* with the results in DI water shown in Figures 8.4B and 8.5D. An increase in DMSO concentration to 50% provides better lubrication than water in the case of 1Ag6PAAm-0.5x hydrogels (Figure 8.4B), whereas a further increase to 100% leads to an overall increase in friction, but still, hydrogel lubrication is improved compared to water. Friction increases in comparison to DI for the SN agarose hydrogel with addition of DMSO, with highest friction measured in the case of 100% DMSO (Figure 8.6D). The long, speed independent plateau of agarose hydrogel is shortened in 50%water DMSO mixture and the viscous regime appears more prominent in the presence of DMSO in comparison to DI. Note that the difference in the frictional response of agarose and 1Ag6PAAm-0.5x hydrogels at 50% DMSO appears to be subtle, but the agarose hydrogels provide better lubrication than the 1Ag6PAAm-0.5x hydrogels in 100% DMSO, as it also happened in water.

Intuitively, one would expect that friction increases with DMSO concentration for 1Ag6PAAm-0.5x hydrogels due to the observed collapse and decrease in water content, which contradicts the experimental results. Note that this correlation presumes that the swelling behavior

of the hydrogel -a bulk property- determines the frictional characteristics, which should depend on the surface properties. QI imaging of the DN hydrogel's surface when equilibrated in 50% DMSO (Figure 8.5) show patches or "domains" (stiffer and less adhesive, hence less hydrated), ranging in size from ~4.5 to 5.7 μm in the water:DMSO mixture, which are not in DI water (Figure 8.6 B, D, respectively) . The depths of these cavities ranged from 300 to 500 nanometers, but there is no information about their presence in the bulk.The effect of a solvent-polymer phase separation is seen more clearly when the second polymerization was done in 50% DMSO (Figure A9), revealing circular domains of a porous structure across the DN hydrogel's surface. Because the frictional response is related to the microstructure of the near-surface region, we believe that the observed decrease in friction in this case is related to this surface microstructure. We note that 1:1 water DMSO mixtures are used in the synthesis of macroporous PAAm hydrogels where reaction induced phase separation causes a porous network to form(171, 172) due to the high affinity of water and DMSO(173, 174). Hence, these domains, observed in the solvent exchange before (Figure A9) or after polymerization of the second network (Figure 8.6C), might result from the non-uniform collapse/swelling of the hydrogel due to inhomogeneities in composition, perhaps,

revealing regions enriched with either one of the reference polymers. The increased stiffness and reduced adhesion also supports collapse of the hydrogel within these features..

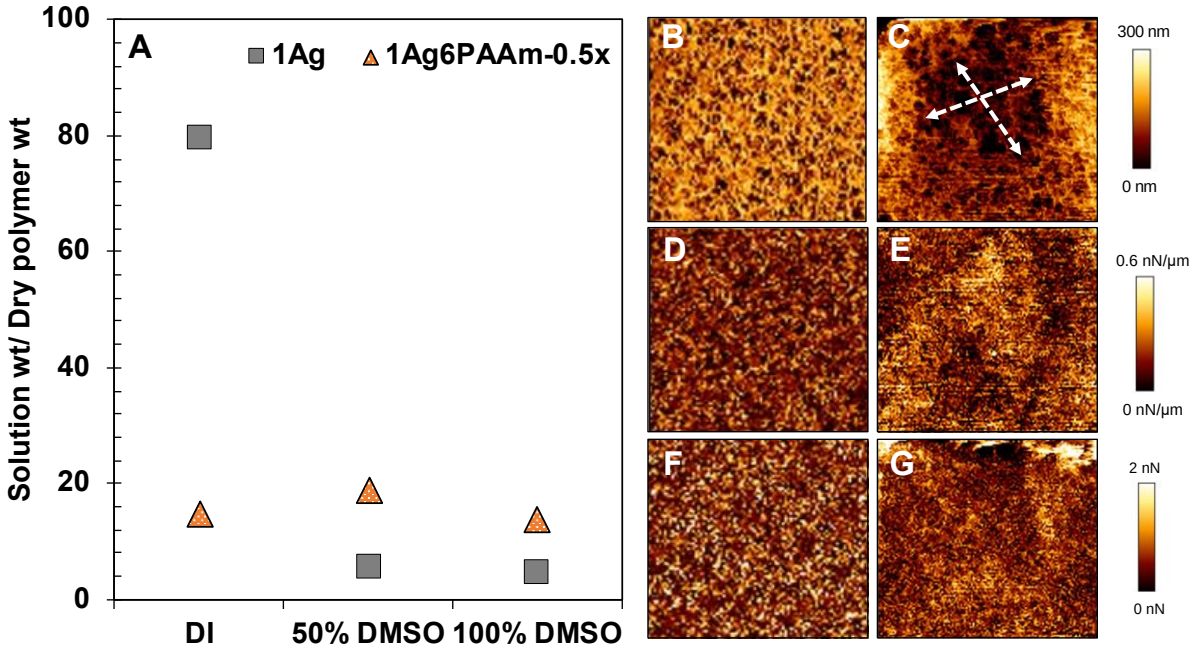

Figure 8.5 A) Swelling behavior of SN agarose and DN 1Ag6PAAM-0.5x hydrogels as a function of the solvent.4 x 4 μm height images of the DN hydrogels obtained via QI method in B) DI and C) 50% DMSO. A darker area points to an area with a relative lower height. Corresponding stiffness and adhesion profiles of the spots are also shown in D, F) in DI and E, G) 50% DMSO, respectively. Increase in the color intensity points to an increase in stiffness or adhesion. The roughly circular region in 50% DMSO observed throughout the sample, vary in size, with sizes ranging from 4.5 μm for the smallest and 5.7 μm for the largest observed feature. Tip: Silica sharp-tip, Stiffness: 0.37 N/m.

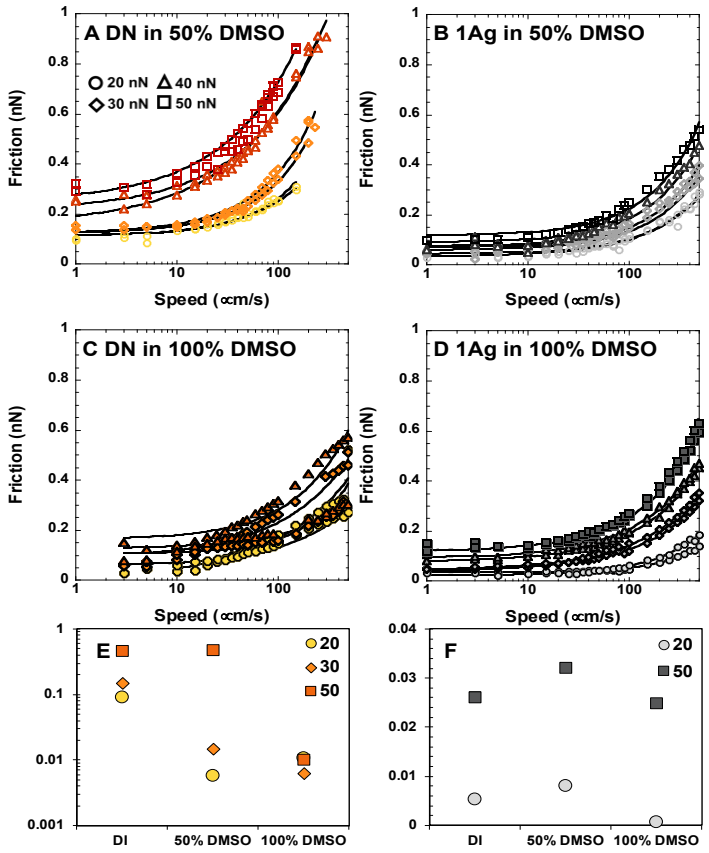

Figure 8.6 Friction force measurements as a function of sliding speeds at different normal loads for a) and c) 1Ag6PAAm-0.5x hydrogel (yellow-orange) and b) and d) for SN agarose hydrogel (greys) in 50:50 Water:DMSO mixture (open symbols) and in DMSO (full symbols), respectively. The colors increase in intensity as the load increases. The elastic moduli for the hydrogels shown in a-d) are 62.7 ±3.58 and 52.2 ±9.2 for 1Ag6PAAm-0.5x in 50% and 100% DMSO in water, and 9.8 ± 2.73 and 5.44 ± 0.5 kPa for agarose hydrogels in 50% and 100% DMSO, respectively. Colloid diameter: 10μm. Cantilever Stiffness: 0.42 N/m.

DN hydrogels thus broadly show frictional behaviors reminiscent of either the 1st or the 2nd network while the surface microstructure also plays an intricate role. The depletion of PAAm toward the surface as well as an increase in swelling ratio promote low adhesion to the colloid. The speed independent regime and low friction observed on agarose hydrogels in the low to medium speed range points towards a hydrodynamic lubrication owing to the repulsive contact between the agarose network and the colloid as well as the brushy layer measured in indentation. This layer is able to incorporate large amounts of fluid and hence can mediate low friction and

speed independent plateau observed at low velocities. In fact, Fits of equation 8.7, with the shear thinning exponent as a fitting parameter (not shown) showed the increasing shear thinning character with an increase in normal load. This occurs due to fluid exudation in the near surface region as the load increases leading to an increase in the polymer concentration within the sheared region. Here, the polymer and the fluid both can mediate lubrication.

8.3. Discussion

8.3.1. Lubrication mechanisms of AgPAAm DN hydrogels

Based on the adhesive-friction model for hydrogel lubrication(35), the viscous component of friction was modeled considering the Couette flow of a hydrogel film:

$$F_{vis} = F_o + \eta_{eff} V.\Omega \qquad (8.7)$$

Where $\boldsymbol{F_o}$ is assumed as a constant here, $\boldsymbol{\Omega = \frac{16\pi}{5} R \log\left(\frac{2R}{h}\right)}$, R = colloid radius, $\boldsymbol{\eta_{eff} \sim \eta_0 (V/h)^n}$ with $\boldsymbol{n}$ < 0 (for shear-thinning behavior) and h is the thickness of the sheared film, which is assumed here to be equal to $\boldsymbol{\xi_s}$, the hydrogel's mesh size in the near surface region(16). This is a simplification, since $\boldsymbol{h}$ can depend on load and velocity. Our model(1) accounts for the influence of the microstructure on the adhesive contribution to friction, but an analysis of this response is out of the scope of this work. The lines in Figure 8.4B-D and Figure 8.6 show the fits of Eq. 7 to the experimental results.

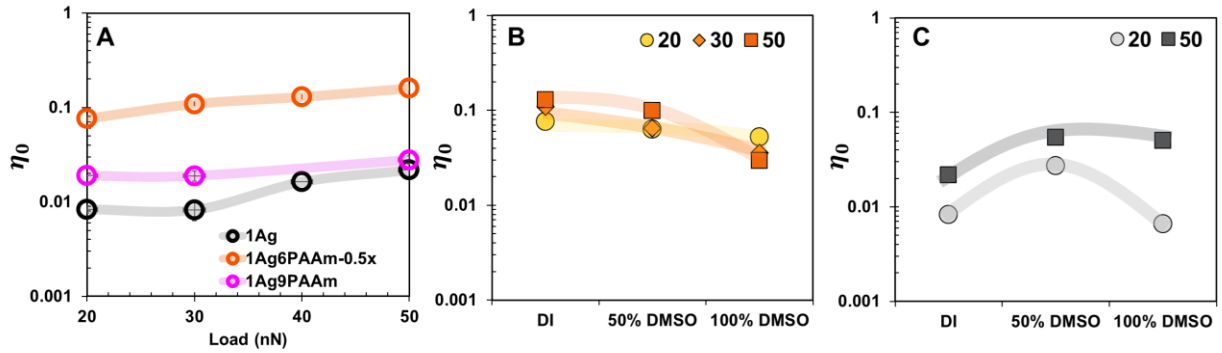

Figure 8.7 Fitting parameters $\boldsymbol{\eta_0}$ for a) the 1Ag (black symbols), 1Ag6PAAm-0.5x (orange symbols) and 1Ag9PAAm (magenta symbols) hydrogels in DI water and for b) 1Ag6PAAm-0.5x and c) 1Ag in water-DMSO mixtures. Translucent lines have been added to guide the eye. In all calculations for the viscosity parameter, a shear thinning exponent of $\boldsymbol{n = -0.3}$ was assumed as a constant.

Figure 8.7A shows the viscosity parameter $\boldsymbol{\eta_0}$ as a function of normal load. We have conducted the fits of equation 7 with a constant shear thinning exponent n, where $n = -0.3$. In agreement with our prior work on single network hydrogels, the increasing $\boldsymbol{\eta_0}$ with load (between 20 and 50 nN) is evident for the three hydrogels and reflects the influence of the polymer network on the viscous dissipation. The increase also starts to level out at high loads (~50 nN, prominent for 1Ag6PAAm-0.5x and 1Ag) possibly because of the interface saturation with the polymer or the polymer brushy layer reaching its compressive limit. Keeping the shear thinning exponent constant we can compare the viscosity parameter of the three hydrogels. The highest viscosity parameter (0.08 to 0.16) are observed for 1Ag6PAam-0.5x hydrogels, which show an enrichment of PAAm at its surface (**Figure** 8.2), while the lowest viscosity parameter (0.008 to 0.02) for the SN agarose hydrogels. As noted earlier, both $\boldsymbol{\eta_0}$ and n must be associated with the properties of the skin layer. Comparing 1Ag with 1Ag6PAAm-0.5x and 1Ag9PAAm hydrogels, we note that the high viscosity footprint for the latter hydrogels may arise due to the enrichment of PAAm at the surface and a thicker skin layer, respectively. We note that 1Ag9PAAm hydrogels have a thick and soft skin layer, possibly arising from the disturbed crosslinking of agarose, which results in a

loose network, as also observed by DLS. This can cause an increase in the viscosity of the interfacial fluid, which consists of both the solvent and the polymer.

Figure 8.7B-C shows how the viscosity parameter changes in water:DMSO solvent mixtures. The value of η_0 for agarose hydrogels exhibits a maximum at 50% DMSO. This maximum reproduces the maximum of the viscosity of water-DMSO mixtures; viscosity of 50% v/v DMSO-water mixture: 2.83 cP, and 100% DMSO: 1.99 cP(175). Given the repulsive nature of the agarose-colloid interface, this supports that friction and lubrication is mainly dictated by the shear of a fluid film between the two surfaces, i.e. fluid-film lubrication. Agarose's ability to crosslink and form a network in DMSO decreases (176). Furthermore, inhibition of crystalline junctions in polysaccharide gels has been observed in DMSO as well, while their formation is promoted in water (176). The result is that the presence of DMSO leads to softer, lower moduli hydrogels with higher polymer concentration and hence a collapsed network. Additionally, water and DMSO are known to preferentially interact with each when together which promotes polymer-polymer interaction over polymer-solvent, leading to a low adhesion of the polymer to the countersurface, in this case silica. Therefore, the collapse of the polymer in DMSO and the enhancement of polymer-polymer interaction causes the fluid film lubrication to dominate, even at the highest loads. This is also evident from the shortening of the speed independent plateau observed for agarose hydrogels in DMSO mixtures in comparison to DI.

For 1Ag6PAAm-0.5x, a decreasing viscosity parameter with increasing DMSO concentration is observed at all loads. A decreasing solvent quality for PAAm with increasing DMSO content (177) should promote the collapse of PAAm close to the surface, where the double network is looser and softer, as inferred from the "skin" studies. The decrease in η_0 with DMSO concentration for the double network suggests that the collapse of the skin, polymer depletion from

the interface which subsequently leading to a solvent rich interfacial layer, dictates the decrease in viscous dissipation. Furthermore, the porous nature of the surface layer, which subsequently decreases the concentration of the polymer on the surface is also expected to influence the viscosity parameter is observed at 50% DMSO. The further decrease of viscosity in 100% DMSO and shortening of the speed independent plateau is attributed to the poor solvent quality for the PAAm brush. Hence, the response seems to be binary, where the solvent viscosity as well as the response of the brushy surface modulates the friction.

8.3.2. About the formation of the double network

Combined results from spectroscopy, correlation lengths and shear modulus for the DN hydrogels confirm formation of the double network for the four compositions. The quality of the double network is evidenced by the correlation function; here, we conclude that a heterogeneous network forms in the DN hydrogels synthesized with 6% Aam and 0.3% bis-Aam, which do not strengthen the material. Interestingly, the heterogeneity is lost upon decreasing the crosslinker content (6%PAAm-0.5x), while the mechanical response of the hydrogel is enhanced 100 folds, compared to the reference agarose SN hydrogel (**Figure** 8.3B, 4A). Because a loose network and no strengthening are observed for 1Ag9PAAm hydrogels, which has the same monomer:crosslinking density as 1Ag6PAAm hydrogels, we propose that a phase separation occurs when a critical monomer concentration is exceeded; perhaps 1Ag6PAAm hydrogel represent the transitional behavior to such phase separated DN hydrogel. It is well-known that two polymers can phase separate due to incompatibility (178). It is also possible that during the gelation of the second network, the swelling capacity of the PAAm is restricted compared to the gelation in solution. The latter may occur if the first network induces confinement-related concentration gradients. The former is also expected to happen due to the different affinity of agarose and PAAm

to water.–Additionally, the crosslinker bis-Aam has been reported to induce phase separation during polymerization of acrylamide(179). Hence, a high crosslinking ratio may enhance phase separation between the two non-interacting polymers. Furthermore, FTIR measurements further supports the weak intermolecular interactions between acrylamide and agarose, further making phase separation likely. This is in contrast with previous studies on DN hydrogels of agarose and PAAm, where a shift to lower wavenumbers was reported and was attributed to the hydrogen bonding between the two polymers(163). Pioneering work by Gong on unraveling the structure of the DN hydrogels had actually shown that the strongest DN hydrogels were obtained for "truly independent" double networks, i.e. where no interaction or crosslinking between the two participating networks existed(180), therefore in our case, absence of inter-network interactions may promote strengthening. The effect of modulating the crosslinking density is intriguing. Figure 8.8B shows that a high strength DN hydrogel forms when the crosslinker mol% is 0.02, and why G' decreases with a further increase. The formation of a strong (t-DN) hydrogel has been shown to depend on the crosslinker concentration before (180). An increase in crosslinker concentration promotes the crosslinking rate and thereby inhibits polymer diffusion through the first network. Additionally, entanglements in the second network also play an important role in the development of high strength and toughness of DN hydrogels. On the other hand, increasing the crosslinking density may restrict the entanglements between PAAm chains(181), thereby limiting the strengthening provided by the second network.

De Genes addressed the problem of two chemically different and hence weakly compatible polymers A and B when crosslinked together(182). When the two polymers are crosslinked below the coexistence curve and then the Flory-Huggins interaction parameter χ is increased, pushing the polymers to segregate, the crosslinking between A and B counteracts this urge. Higher

crosslinking increases the region of compatibility and, depending on a critical value of χ, microphase separation can occur. An analogy can be drawn for the present system here. Initially, the prepolymer solution (AAM and bis-AAM) is added to the dissolved agarose solution at high temperature (~80 °C) and hence the two polymers are miscible, and no precipitation is observed. As the solution cools down, the miscibility of the polymers decreases, while physical crosslinking of the agarose is simultaneously occurring as well. This may result in a heterogenous network with regions rich in agarose and PAAm.

The proposed pathway for the double network formation is thus represented schematically in Figure 8.8A. The gelation of agarose proceeds by liquid phase separation between helical agarose fibers and the linear polymer(183), which leads to in situ formation of pockets with linear agarose, where acrylamide is also confined. During polymerization of the 2nd network, different morphologies appear depending on the composition. In the case of 1AgPAAm6 hydrogels, due to a high number of bisAAm per Aam monomer (16:1), we believe that tightly crosslinked blobs of PAAm form within these pockets and the polymerization occurs rapidly. This hinders diffusion of the monomer to other areas of the agarose network, resulting in spatially isolated PAAm within the agarose network. By decreasing the crosslinker amount (1Ag6PAAm-0.5x), the polymerization can propagate and penetrate *across* the first network resulting in a loosely crosslinked 2nd network (one of the requirements of an effective DN gel). This results in entangled first and second networks, resulting in the enhanced mechanical properties. A similar mechanism was proposed for PAMPS/PAAm DN hydrogels (166). When the monomer concentration is further increased to 9% Aam, it is possible that the two polymers become immiscible with each other, based on the previous discussion. This is further confirmed by a considerable loss of PAAm footprint in FTIR measurement of these hydrogels (**Figure** 8.1D). As the agarose is physically

crosslinked and its gelation still proceeds during gelation of acrylamide, the increasing need for the polymers to segregate upon cooling could also influence the agarose network. It is also possible that competition between spinodal decomposition of Aam and simultaneous crosslinking results in a system containing microphases (**Figure** 8.5 C). However, a further study of the microphase separation is out of the scope of this work.

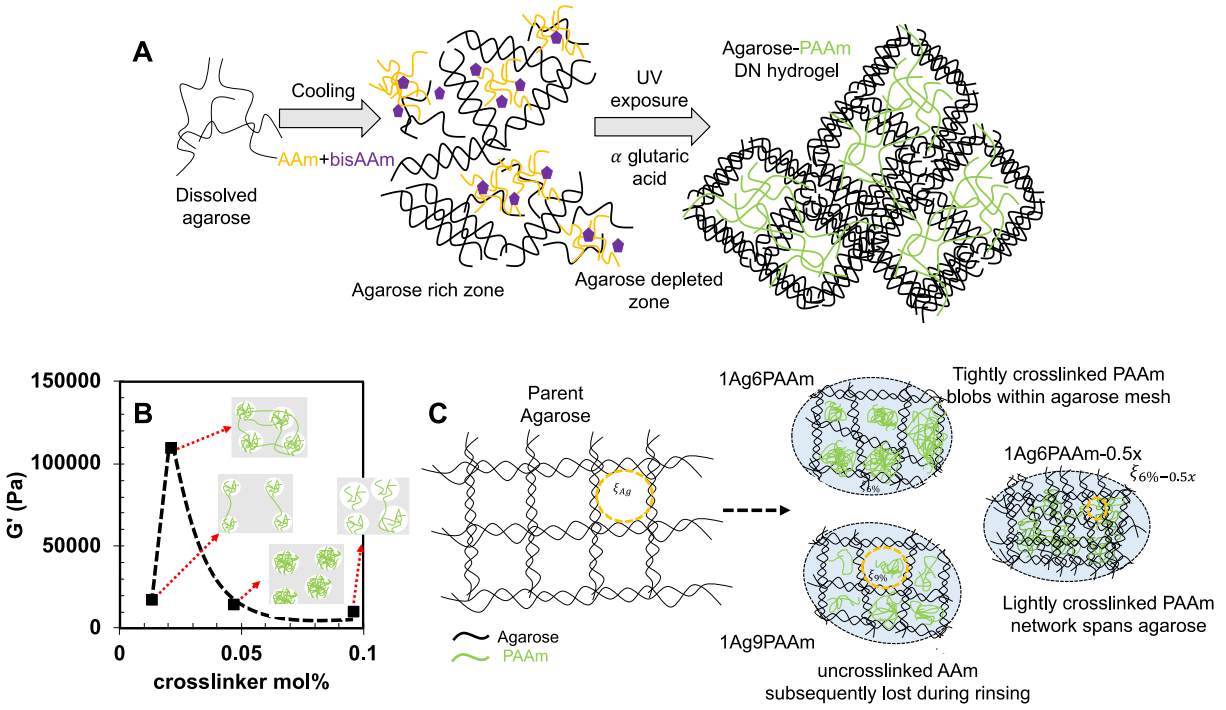

Figure 8.8 A) Double network hydrogel formation, starting with the agarose polymer, addition of Aam and bis-Aam and subsequent UV exposure, resulting in an agarose network with an interpenetrating PAAm network. The agarose fibers undergo a coil to helix transformation and the helices further aggregate into thicker fibers which build the agarose hydrogel's network(165). B) Storage modulus obtained from rheological measurements as a function of the crosslinker mol% in the second network. The dashed lines provide a guide to the eye. The different morphologies expected for the four DN hydrogel compositions are also shown. C) Schematic map describing the various double networks which can form depending on the Aam and bis-Aam concentration. The agarose fibers (black) form helices upon cooling which further aggregate to form a thick fibrous network. The monomer:crosslinker ratio is 16, 32 and 16 for the 1Ag6PAAm, 1Ag6PAAm-1.5x and 1Ag9PAAm gels respectively. The mesh sizes $\boldsymbol{\xi}$ scale with the correlation lengths resolved in DLS.

8.4. Conclusions

In summary, we propose that the combined effect of phase separation and the degree of crosslinking of the second network leads to the different microstructural and mechanical response. For the lowest monomer and crosslinker concentration, a homogenous double network without any phase separation is expected, where the PAAm network is formed very loosely around the agarose network. This hydrogel does not provide a significant enhancement over the reference SN agarose hydrogel, likely due to the small amount of both monomer and crosslinker, creating a second network with a large mesh size and low number of entanglements in the second network. However, an increase in the monomer can cause phase separation in the agarose network of the second network's prepolymer into Aam rich and Aam depleted regions which are subsequently crosslinked, leading to a heterogeneous double network. This heterogeneity counteracts the strengthening provided by the 2nd network. Now, a reduction of crosslinking at the same monomer concentration results in a highly elastic and strong hydrogel. This is attributed to the phase separated regions lightly crosslinked and interconnected to the other Aam rich region as well, perhaps due to a slower kinetics of gelation due a lower amount of crosslinker. A similar trend was observed for truly independent DN hydrogels, where a specific molar ratio was required to achieve strengthening. Increase in monomer concentration while keeping the crosslinker to monomer ratio the same leads to uncrosslinked, yet polymerized Aam, which might be rinsed out. Yet, due to higher monomer concentration, the "pockets" are expected to be either bigger or higher in number, which will in turn modify the agarose network as well, *prior* to the PAAm being rinsed out. As the correlation length is comparable to the parent agarose network, we believe the former is true in this case. Hence, synergistic effects of the polymer phase separation and crosslinking degree can

explain the differences between the four DN hydrogels. Furthermore, the chemical gradient in DN hydrogels influences the tribological properties and friction is responsive to the imbibed fluid. In water, friction follows trends observed for one of the surface enriched polymers. Additionally, except for the 1Ag4PAAm hydrogel, a prominent suppression of the v-weakening (and hence adhesive) regime is observed for the DN hydrogels where a speed independent plateau is observed for the 1Ag6PAAm-0.5x and 1Ag9PAAm DN hydrogels. The length of the plateau is directly proportional to the strength of the hydrogel. Furthermore, a transition from polymer brush like lubrication to a viscous dissipation occurs when DMSO substitutes water.

CHAPTER 9: WEAR OF NATURAL HYDROGELS IN ENHANCED CALCIUM ENVIRONMENTS

This chapter describes results on the microstructural and hence mechanical and tribological changes of a biological hydrogel in enhanced calcium cincentrations. The motivation of this study is osteoarthritis (OA), a degenerative joint disease and a leading cause of disability globally. By combining atomic force microscopy, spectroscopy and an extended surface forces apparatus the change of structural, mechanical and frictional characteristics of the articulating surface of healthy bovine cartilage induced by elevated calcium concentrations was investigated.

9.1. Experimental Section

9.1.1. Cartilage sample preparation

Bovine stifle joints (age 6-8 months) were obtained from a local abattoir and opened to reveal the trochlear groove. Cartilage integrity was assessed, and joints that had cartilage that exhibited exposure to blood and/or bruising were excluded. Using a 3-mm biopsy punch, cylindrical cartilage plugs were removed from the joint. The plugs were then placed into optimal cutting temperature (OCT) compound, with the surface-side of the cartilage plug as the sectioning plane, and frozen at -20°C overnight. The following day, 8-12 μm sections from the cartilage surface of each plug were obtained with a cryostat. Phosphate-buffered saline solution (1× PBS) was prepared by diluting 10× PBS (no calcium, no magnesium, 14200075, ThermoFisher). After each section was cut, it was placed in 2 mL of 1× PBS. The surface was deemed captured when a cartilage section became apparent after gentle rinsing in the saline solution. These samples were then kept in 1× PBS solution at 4°C until the day of testing. Although the sections underwent 1 freeze-thaw cycle, several studies have found that cartilage mechanical properties do not change after a single freeze-thaw cycle (184, 185).

9.1.2. Medium

Solutions of 1× PBS with 0 mM, 1.8 mM $CaCl_2$ and 10 mM calcium chloride ($CaCl_2$) were prepared with $CaCl_2$ from Sigma Aldrich. Before use, all solutions were filtered using a 0.22 µm polyamide filter. . The concentrations of 1.8 and 10 mM represent the calcium concentration in healthy synovial fluid and during progress of OA. Tables S1 and S2 show the saturation index with respect to the calcium phosphate minerals that can precipitate under the selected conditions. At the selected concentrations, the solution was supersaturated with respect to various calcium phosphate minerals as shown by their saturation index calculated with the software Visual MINTEQ v. 3.1. AFM imaging showed that the cartilage's surface remained free of crystals during the duration of the experiments. Note that calcium binding to aggrecan has been reported to prevent mineralization in cartilage (186).

9.1.3. Attenuated Total Reflectance Infrared Spectroscopy

Attenuated Total Reflectance Infrared Spectroscopy (ATR-IR) (PerkinElmer, Frontier, and Pike Technologies, GladiATR with a diamond crystal) was used to determine the chemical footprint of the cartilage samples. Cartilage samples, equilibrated in 1× PBS were placed on the ATR crystal and a light pressure was applied with the help of the sample press knob to enhance the signal. At least two IR spectra were taken for each sample orientation, *i.e.* with the surface of the cartilage section in contact with the ATR crystal (labelled as "top" interface), and with the bottom surface in contact with the ATR crystal (labelled as "bottom" interface).

9.1.4. AFM imaging

Cartilage surfaces were imaged by Atomic Force Microscopy (Nano Wizard, JPK Instruments, Germany) using quantitative imaging mode (QI) with a sharp tip (HQ:CSC37, No Al, 0.3-0.9 N/m, Nanoandmore, USA). In QI mode, cross-sections (30 x 30 µm and 5 x 5 µm) are divided into a grid of 256 x 256 pixels and force-distance curves are measured at each pixel at an approach speed of ~ 60 µm/s and a very small load of ~1 nN. The force curves are converted into a topographic image of the surface. Note that QI is not an indentation measurement but an imaging technique, where the tip applies a very small force on the surface for a very short period of time. This feature is especially useful for imaging soft materials as it prevents application of lateral force, and hence, artifacts due to drag. The raw images were post-processed using JPK software by subtracting a polynomial fit from the surface and replacing empty pixels by interpolation.

9.1.5. Extended Surface Forces Apparatus (eSFA)

Compression and decompression isotherms were obtained using an eSFA, a modified version of the Mk III SFA (Surforce, Santa Barbara, CA),(187) with attachments to improve the accuracy, resolution, mechanical drift, thermal stability, imaging, and essential automation of the instrument; these modifications are described in detail in the literature (188, 189). The transmitted interference spectrum consists of fringes of equal chromatic order that are analyzed by fast-spectral-correlation interferometry to evaluate the surface separation (D) and the refractive index (n) simultaneously. Uniformly thick mica sheets with a thickness between 2 and 5 µm were prepared by manually cleaving ruby mica of optical quality (grade 1; S&J Trading, New York, NY) in a class-100 laminar-flow cabinet. The mica sheets were cut to a size of 1 cm x 1 cm using surgical scissors to avoid

possible contamination with nanoparticles. A silver film of 40 nm thickness was thermally evaporated onto mica sheets in vacuum (2.10^{-6} mbar). The silver-coated mica sheets were glued onto cylindrical lenses with a resin glue (EPON 1004F). The samples were then immediately inserted into the sealed eSFA, the fluid cell was purged with dry nitrogen, and the mica thickness was determined by means of thin-film interferometry in mica-mica contact. Immediately after this measurement, only one of the glass discs was disassembled to graft the cartilage section on mica, while the countersurface was kept as bare mica in the experiments.

Solutions of 10 wt% albumin in 1× PBS and 5 vol% glutaraldehyde in 1× PBS were mixed in a 1:1 ratio and the resulting solution was used to glue the cartilage section onto the mica. 500 µL of the glue solution was pipetted onto the mica surface and a tissue (Kimwipe, Kimberly-Clark Kimtech Science) was used to absorb excess solution so that only a thin layer of the glue solution remained on the surface. This mixture has been used extensively as a tissue adhesive (190). The thickness of this glue layer was determined to be less than 90 nm by multiple-beam interferometry (191). Immediately after this, the cartilage sections were transferred onto the mica surface with the help of blunted-tip tweezers. The glass disc with the cartilage was kept in a closed clean petri dish inside the laminar flow cabinet for a minimum of four hours to allow the binding of cartilage to the mica surface. After the initial 30 minutes, a droplet of 1× PBS was placed on the surface of the cartilage section to avoid dehydration. After four hours, the disc with the cartilage grafted on mica was placed back into the eSFA and the fluid cell was filled with 1× PBS for equilibration. Then, the point of closest approach (PCA) was readjusted with a precision of $\pm$1µm in the lateral direction. The accuracy of the measurement of surface separation

(D) at the PCA is typically $\pm$30 pm, but it is $\pm$5 Å here due to the large thickness of the cartilage samples (~10 μm). The precision of the refractive index measurement was determined to be ~0.03.

Slow compression and decompression of the cartilage sections at constant rate (V) of 1 nm/s were performed at least three times per solution at constant temperature (298 $\pm$0.1 K). First, 1×PBS solution was injected into the fluid cell until complete immersion of the two surfaces (mica vs. cartilage). The experiments with each cartilage section started with 1× PBS, and then, the concentration of $CaCl_2$ was increased stepwise from 0 to 1.8 mM, and then, to 10 mM. Reference measurements were carried out in DI water. To ensure a thorough solution exchange, the two surfaces were first separated to D>50 μm and then the liquid in the fluid cell was depleted and refilled 3 times with the new solution to ensure exchange. Drying of the cartilage did not happen during the exchange of the solution as a drop of solution was maintained between the two surfaces. The compression started after re-equilibration for at least 12 hours. The refractive index (n) and the separation between the two mica surfaces at the PCA (D) were measured in real-time with an acquisition rate of at least 1 Hz. The spring force can be obtained from $F = k_n(D - D_0 + Vt)$, where D_0 is the initial separation at which the net force is zero and t the point of time. Since the Debye length of the selected solutions is smaller than 1 nm (124), the electrical D layer force is of short range and can be ignored. Hence, the thickness of the cartilage was determined from the onset of the increase in repulsion (H) and the measured force is attributed to the resistance to the compression of the cartilage. A spring constant of 2340 $\pm$60 N/m was used in this work.

9.1.6. Colloidal probe AFM for nanoindentation and friction force measurements

An AFM (Nano Wizard, JPK Instruments, Germany) was used for colloidal probe indentation and friction-force measurements. All measurements were conducted with silica colloids of nominal radius equal to 10 μm (Duke Scientific, Thermo Scientific, USA). The colloids were attached to the end of tipless cantilevers (CSC37-No Al/tipless, Mikromash, nominal spring constant = 0.4 N/m) with an epoxy glue (JB-Weld, Sulphur Springs, TX, USA). Using a clean test grating (MikroMasch, Spain) reverse imaging of the attached colloids was conducted to determine the RMS roughness within the contact area and it was found to be less than 6.4 nm. Before starting the experiments, the tips were rinsed in an ethanol bath and cleaned by UV-O_3 (Bioforce Nanoscience, Chicago, IL) for half an hour. The normal stiffness of the cantilevers was determined by the thermal noise and the lateral calibration was performed following the modified Sader's method (100).

Microscale indentation was performed with the colloid on the cartilage sections at an approach/retraction velocity of 0.8 μm/s at room temperature. Force maps were carried out on three different regions of the cartilage. Each force map consisted of 64 curves over an area of 10 x 10 μm. The Hertz model (192) was fit to the indentation curves upon extension of the colloid to the hydrogel in a piecewise manner and the Poisson's ratio of the cartilage was taken as $\nu_c = 0.45$(193). As recently reported for hydrogels (194), this method estimates the change of the elastic modulus as a function of indentation depth, and thereby, allows the characterization of the graded microstructure of the cartilage sections from the top to the bottom.

Lateral force measurements were conducted at a lateral velocity of the piezo of 1 μm/s at a constant scan length of 28 μm, and at three loads, 20, 30 and 50 nN at room

temperature. The experiments were repeated at least on two different regions of the cartilage sections to confirm the reproducibility of the results. At the point of reversal of the piezo (i.e. under zero tangential force), the normal load was maintained constant for a period of time (t_{hold}) that ranged from 5 to 60 seconds; this was repeated three times per loading time. Both height and lateral deflection of the cantilever were inspected to ensure that pile-up did not happen (194).

The combination of experimental techniques, AFM imaging, nanoindentation and eSFA, provides complementary information of the structure of the cartilage's superficial zone at different length scales (Table S3). The sharp tip in QI imaging can resolve the microstructure of the cartilage with sub-micron resolution. Indentation depths smaller than 1 μm are achieved by AFM indentation with contact radius of less than 3.4 μm, whereas the contact radius probed by eSFA goes up to ~400 μm. For a poroelastic and viscoelastic material like cartilage, the time-dependent response to mechanical loading is also relevant: nanoindentation involves time scales smaller than 1.2 seconds, while the unconfined compression in eSFA experiments prolongs over several hours. Therefore, each experimental method probes significantly different length and time scales.

9.2. Results

9.2.1. Structural and mechanical properties

Two compression isotherms of the articular cartilage's surface with an initial thickness of H_0~12.4 μm in 1× PBS are shown in Figure 9.1a (red represents approach and green is used for separation); the cartilage remained unstressed for 7 hr before the next compression started. Both the hysteresis between approach and separation and the decrease of the onset of repulsion during subsequent compressions reveal a change of the cartilage's

surface structure upon compression. It cannot be ruled out that longer equilibration times under unstressed conditions could yield a full recovery of the microstructure (195). However, the observation time in other mechanical tests is typically much smaller. The decrease in the onset of the repulsion of ~1 μm implies the decrease in cartilage thickness to H~11 μm. Upon consecutive compressions in 1.8 mM $CaCl_2$, the change in the cartilage's thickness (Figure 9.1b, H~11.3 μm) and the hysteresis is less prominent, *i.e.* the behavior becomes more elastic. Reference measurements in DI water confirmed the irreversibility of the initial compression, while the variation between compression isotherms in subsequent measurements (in water in Figure A11 or in 1× PBS in Figure 9.1a) leads to a more stable microstructure and subsequent variations are mitigated. Despite this, when the cartilage is equilibrated in 1× PBS with 10 mM $CaCl_2$, the onset of the repulsion remarkably increases in consecutive compression isotherms and the hysteresis becomes more prominent (Figure 9.1c, H~13.8 μm). This points again at a remarkable structural change of the cartilage's surface.

The compressive modulus (B) can be roughly estimated from the compression isotherms assuming an elastic behavior (196), according to:

$$\frac{F}{R} = \frac{\pi B(D-H)^2}{H} \qquad \text{Eq. (1)}$$

The fit of Eq. (1) to the experimental results is possible for the initial compression of ~ 1 μm (see Figure A12 in the SI) and it provides the value of B, which decreases from 7.1±0.6 kPa to 6.2±1.5 kPa upon addition of 1.8 mM $CaCl_2$ to 1× PBS and to 5.9±0.8 kPa with 10 mM $CaCl_2$. Note that these values are of the same order of magnitude compared to reported elastic moduli of the hydrated cartilage's articulating surface (59).

The cartilage's surface was imaged by AFM in the selected solutions. Figure 9.2a-h shows representative images of the cartilage's surface immersed in 1× PBS with different concentrations of $CaCl_2$ at two different magnifications. The surface microstructure is distinct from the subsurface (*cf.* Figure 9.2). The images reveal a coarse and branched network in 1× PBS (Figure 9.2a) with a diameter of d~ 317±84 nm (n=30), *i.e.* much larger than that of the collagen fibers in the subsurface (d~23.8±7 nm, n=94). Higher magnification images reveal a granular microstructure in 1× PBS (Figure 9.2e), which agrees qualitatively with reported AFM images of the cartilage's surface (59, 61, 197). IR spectroscopy reproducibly confirms the presence of proteoglycans in the cartilage's sections and their smaller concentration toward the surface; see a detailed explanation of the results in the SI (Figure 9.2). Furthermore, although the infrared absorption spectra of collagen and elastin are quite similar, IR measurements support the presence of elastin, and hence, the coarser network could be also composed of elastin fibers, which have been reported to have diameters of up to ~1 μm (198).

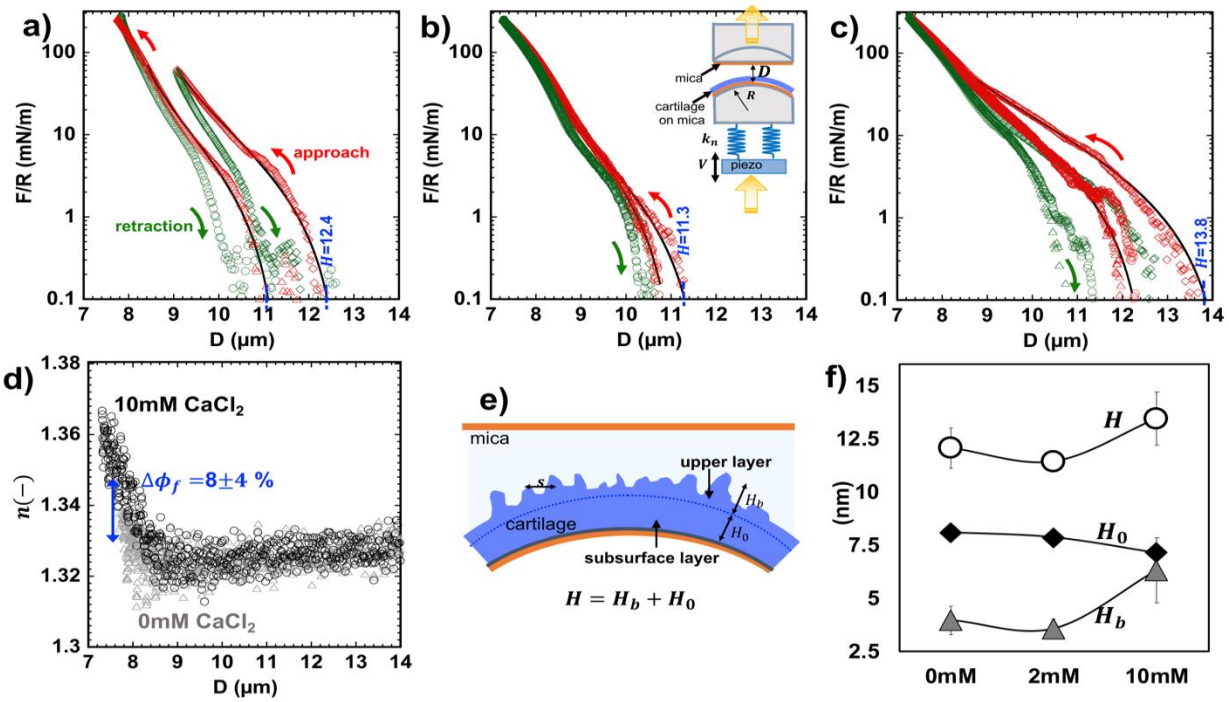

Figure 9.1 Compression isotherms as a function of varying ionic strength. Compression isotherms as a function of the separation between mica surfaces (D) (approach in red and retraction in green) in 1× PBS with a) 0mM, b) 1.8 mM and c) 10 mM CaCl2. The inset in b) shows the schematics of the eSFA for the cartilage experiments (cartilage in blue, mica with silver mirror on the back side in brown). The lines show the fits of Eq. (3) to the experimental results. d) Representative measurements of the refractive index of the confined film between mica surfaces upon compression of the cartilage in 1× PBS with 0 (grey triangles), and 10 mM CaCl2 (black circles). An increase in refractive index reflects the decrease in water content upon compression. e) Cartoon of the articulating surface investigated by eSFA, showing the soft surface layer of thickness H_g and a less compressible layer underneath of thickness H_0. The fitting parameters of Eq. (3) are shown in f). The error bars are sometimes smaller than the markers size, and therefore, not always visible.

Upon equilibration in 1.8 mM $CaCl_2$, the diameter of the network appears thicker (roughly d~415±95 nm, n=21). This is much more prominent in 10 mM $CaCl_2$ (d ~1624±846, n=18) and it demonstrates the significant aggregation of the macromolecular network with a simultaneous increase in RMS roughness and in void size ξ (see caption in Figure 9.2). This is concurrent with the swelling and softening inferred from SFA experiments at this concentration. Overnight re-equilibration in 1× PBS (0 mM $CaCl_2$) does not induce a complete recovery of the surface structure (Figure 9.2d;h), which indicates

that the influence of $CaCl_2$ on the properties of the cartilage's surface is irreversible within the duration of these experiments. The trends are reproducible on different regions of the articular cartilage's surface. Although mineral precipitation is possible (Table S1-S2), AFM imaging showed that the cartilage's surface remained free of crystals. Macromolecules can affect nucleation; they can both inhibit and promote it. For instance, calcium binding to aggrecan has been reported to prevent mineralization in cartilage(199). Nevertheless, the nanosized precipitate might be difficult to image within the complex matrix structure, or it could precipitate underneath the surface, and hence, we do not have evidence to fully support or rule out precipitation.

Images were also taken at different dilutions of PBS, *i.e.* 0.1× PBS, 1× PBS and 3× PBS, in the absence of calcium (Figure 9.2i-k). Increasing the ionic strength to 3× PBS does not lead to aggregation of the solid matrix. Instead, the surface roughness increases from 149±10.0 nm to 194.9±56.7 nm with the decrease in dilution from 0.1×PBS to 3×PBS, which suggests that a partial dehydration of the cartilage might have taken place. In fact, an increase of the ionic strength in the cartilage's external environment (*i.e.* from 0.1× to 3× PBS) is expected to cause a loss of extrafibrillar water in the cartilage to balance the osmotic pressure gradient (200). This dehydration can also happen in the cartilage's surface layer, as glycoproteins (*e.g.* lubricin) and proteoglycans (hyaluronan) are highly negatively charged. In contrast, the changes illustrated in Figs. 2 and 3 when calcium is added cannot be attributed to osmotic pressure effects.

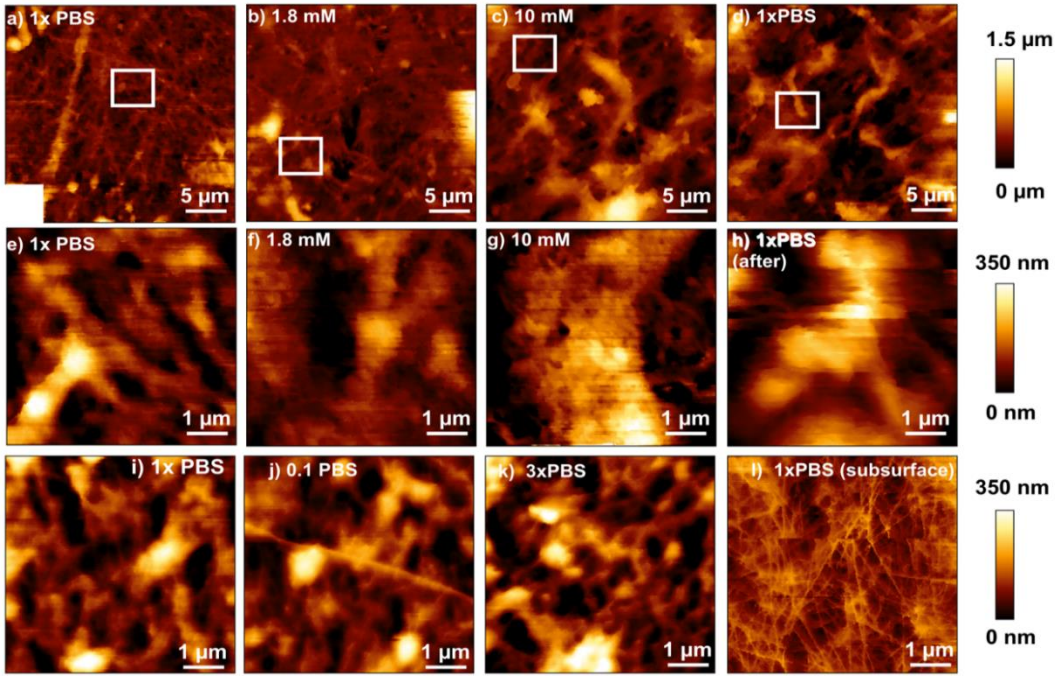

Figure 9.2 Images of cartilage's articulating surface as a function of calcium concentration. QI images of the cartilage surface equilibrated for 5 hr in a;e) 1× PBS, b;f) 1× PBS and 1.8mM CaCl2, c;g) 1× PBS and 10mM CaCl2 and d;h) re-equilibration in 1× PBS (denoted "after"), respectively. First row at low magnification (30 µm x 30 µm) and second row at higher magnification (5 µm x 5 µm). RMS roughness: (a) 278±34 nm, (b) 182±38 nm, (c) 243±50 nm, (d) 267±35 nm while (e) 97±39 nm, (f) 49±10 nm, (g) 133±28 nm and (h) 137±22 nm. Aggregate thicknesses: (a;e) 298±68.3 nm, (b;f) 415±95.16, (c;g) 1624±846 and (d;h) 1865±533 nm. Void size (ξ): (a;e) 819±175 nm, (b;f) 1388±371, (c;g) 1485±410, (d;h) 1611±321 nm. QI images of the cartilage surface equilibrated for 5 hr in i) 1× PBS, j) 0.1× PBS and k) 3× PBS, as reference. l) Image of the cartilage subsurface; the average collagen diameter is 26±6 nm obtained from n=25 fibers per image in 4 images.e

Representative SFA measurements of the refractive index (n) are shown in Figure 9.2d. The refractive index is a measure of the density of the film (201) and it can be roughly modeled according to:

$$n(D) = n_c - \phi_f(n_c - n_f) \quad \text{Eq. (2)}$$

where $n(D)$ is the refractive index as a function of surface separation, n_c is the refractive index of the solid matrix (n_c=1.53, for collagen), n_f=1.337 is the refractive index of water, and ϕ_f is its volume fraction. When the cartilage is compressed to less than ~9 µm, the refractive index notably increases at all solution conditions. Hence, the increase in

refractive index is due to the remarkable loss of water in the cartilage upon compression. The fit of Eq. (2) to the measured refractive index gives a reduction of the water content in cartilage of ~8 $\pm$ 4 vol% with an increase in $CaCl_2$ concentration from 0 to 10 mM. A loss of water with increase in ionic strength is expected to balance the osmotic pressure between the extrafibrillar water and the external environment of the cartilage, and hence, these results are reasonable. However, the compression from 14 to 9 μm does not cause any variation of the refractive index, which remains very close to that of water under the investigated conditions. This implies that the *top* surface layer has a very high water content (>95%), like a gel or brush. Note that the refractive index of the cartilage's superficial zone has been reported to be 1.361$\pm$0.032 (202), and hence, in reasonable agreement with our results considering the precision of the refractive index measurements.

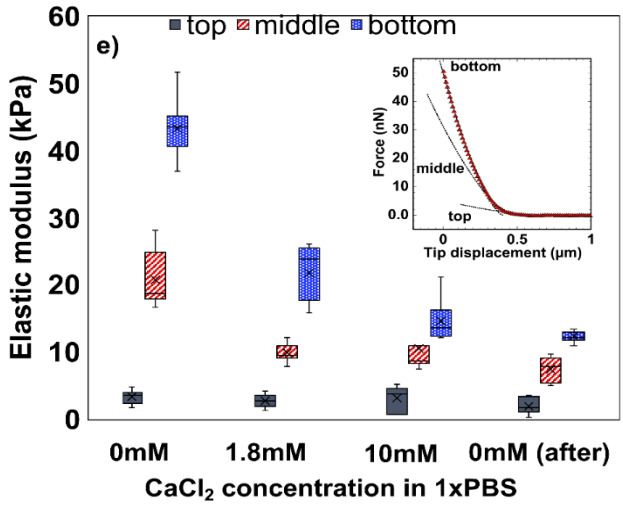

Figure 9.3 Elastic modulus of the cartilage's surface and subsurface as a function of calcium concentration. Elastic modulus according to the Hertz model as a function of CaCl2 in 1× PBS. The Hertz model was applied "piecewise" to determine top, middle and bottom moduli. The inset shows the definition of the elastic modulus as a function of depth. The decrease of the elastic modulus with calcium concentration is more prominent in middle and bottom regions; this was not seen when comparing 1× PBS and 3× PBS in reference measurements. Cantilever stiffness=0.4 N/m. Radius of colloid= 10 μm.

Although the Alexander-de Gennes model (203) is only strictly valid to describe the compression of long neutral polymer brushes, it has been shown to describe well the behavior of charged macromolecules like lubricin and hyaluronan grafted via fibronectin to a substrate in aqueous environment (204). In our case, satisfactory fits to the compression of the cartilage's articulating surface are only achieved *via* a modified model that assumes the presence of a compressible, thermally mobile, well-hydrated surface layer and a much less deformable region underneath (see schematics in Figure 9.1e). This model gives the resistive force to compression (F) normalized by the radius (R):

$$\frac{F}{R} = \frac{8\pi k_B T \cdot H_g}{35\Gamma^{3/2}}\left(7\left(\frac{H_g}{D-H_0}\right)^{5/4} + 5\left(\frac{D-H_0}{H_g}\right)^{7/4} - 12\right) \quad \text{Eq. (3)}$$

H_g being the thickness of the soft surface layer with a solid surface density Γ, H_0 the thickness of the less compressible layer underneath (subsurface), and hence, $H = H_g + H_0$

is the cartilage's section thickness, *i.e.* the onset of the repulsion. The black lines in Figs. 2a-c demonstrate the good agreement between the experimental results and the model.

The fits to the experimental results provide H_0 and H_g. The soft surface layer slightly collapses from H_g=4.0±0.5 μm to 3.5±0.5 μm upon addition of 1.8 mM $CaCl_2$, but it notably expands in 10 mM $CaCl_2$ to H_g=6.2±1 μm. In contrast, with increase in calcium concentration, the subsurface layer gradually collapses from H_0 ~8 to ~7 μm, which is consistent with the increase in osmotic pressure with increase in concentration. Figure 9.1f suggests that the observed increase in refractive index with $CaCl_2$ concentration may be associated with the contraction of the subsurface layer, since the surface layer swells, and hence, it becomes more hydrated in 10 mM $CaCl_2$. The eSFA experiments thus reveal the graded response of the cartilage's surface, *i.e. of the surface (~5 μm in thickness) and subsurface layers* and their different responses to calcium concentration. The graded structure of the cartilage's surface amorphous layer – composed of a gel-like layer on top of a granular stiffer layer – was first proposed by Crockett et al. based on AFM images (59).

Indentation measurements were carried out by AFM to examine the influence of calcium concentration on the mechanical response of the cartilage's articulating surface (see Figure 9.3). In contrast to SFA, indentation maps were measured on pristine cartilage, and hence, the influence of multiple compressions was not investigated by AFM. The indentation depth (d) is smaller than 1 μm, and therefore, only the topmost surface layer is probed here. A deviation of the experimental data from the model was systematically observed close to the surface. Inspired by recent work on hydrogels (194), the Hertz model was fit to the experimental results "piecewise" (see lines in inset of Figure 9.3). This

practice led typically to three elastic moduli on each indentation curve, which is indicative of the nonlinear elastic behavior of the cartilage's surface (Figure 9.3). For example, the elastic moduli are 3.3±1 kPa, 20.7±3.9 kPa and 43.5±4.6 kPa in 1× PBS with an increase in indentation depth. Addition of calcium leads to a gradual decrease in the elastic moduli and there is no recovery upon re-equilibration in 1× PBS, which let us denote this weakening as "irreversible".

In the presence of calcium, jumps happen upon indentation, making it difficult to fit the model to the experimental results. These jumps reflect sudden ionic bridging between the colloid and the negatively charged macromolecules. Importantly, after re-equilibration in 1× PBS, the small jumps in the indentation curves remain, which demonstrates that the calcium is still present in the cartilage. Note that a quantitative comparison between the moduli obtained by eSFA and nanoindentation is not possible due to various reasons. First, eSFA experiments are carried out in *quasi* equilibrium, which mitigates poroelastic effects(205) on the resistance to compression, in contrast to AFM indentation. Second, the contact radius is as large as 400 μm in eSFA while it is less than 3.4 μm in AFM, and hence, the length scales are also very different; the indentation depth in AFM is less than 1 μm compared to more than 4 μm in SFA experiments. Despite these differences, a weakening of the cartilage's surface is inferred from both AFM and SFA with an increase in calcium concentration.

9.2.2. Tribological behavior of the articulating surface

To evaluate the tribological implications of these results, friction-force measurements were carried out in 1× PBS with 0 and 10 mM $CaCl_2$ with a silica colloid as the countersurface. The static loading time before the silica colloid was laterally pulled at

1 μm/s was varied between 5 s and 50 s. Figure 9.4a shows the lateral force as a function of the position of the cantilever at various loading times in 1× PBS under a normal load of 50 nN. The prominent peak corresponds to the static friction or stiction, *i.e.* the friction force at the commencement of sliding, after which friction decreases to the dynamic value.

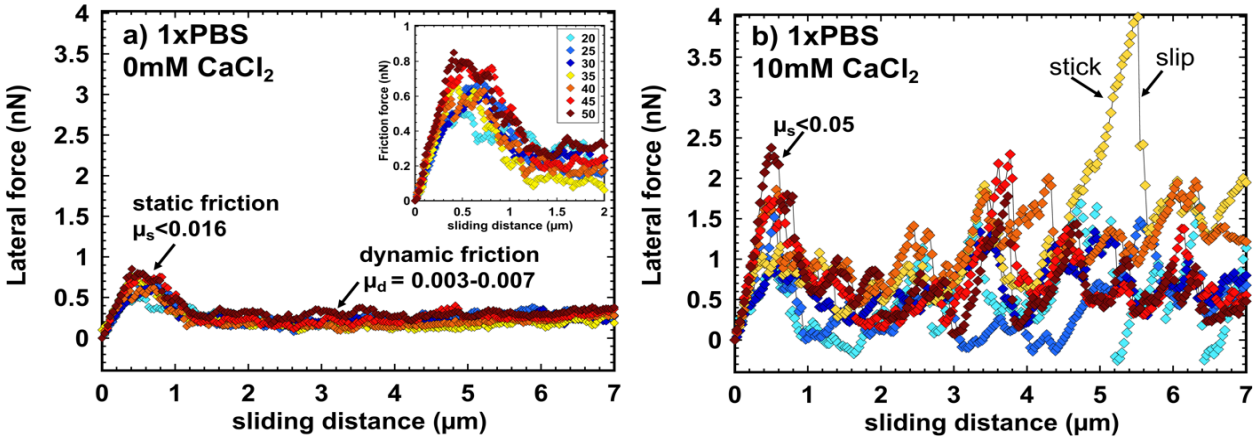

Figure 9.4 Lateral force vs. sliding distance between a silica colloid and articulating surface of cartilage. The lateral force was measured upon a constant load of 50 nN at selected hold times between 20 and 50 s, in a) 1× PBS and b) 1× PBS with 10 mM CaCl2. The arrows in b) help visualize a stick and slip event. The colour legend in both diagrams is shown in the inset of a). Sliding velocity= 1 μm/s. Cantilever stiffness=0.45 N/m. Radius of colloid= 10 μm. The coefficients of friction were determined at loads between 20 and 50 nN.

The inset in Figure 9.4a reveals that the static friction increases with the increase in the hold time in 1× PBS. In contrast, short loading times (≤5 s) lead to negligible stiction to the silica surface. The static friction coefficient (μ_s) is almost one order of magnitude larger than the dynamic coefficient of friction, μ_d (μ_s goes up to 0.016 *vs.* μ_d~0.003). The relative constant dynamic friction coefficient over the sliding distance reflects the smooth motion of the colloid, while its small variation is likely due to the heterogeneity of the cartilage's surface. Importantly, the dynamic friction coefficient of the cartilage's subsurface (Figure 9.2) is μ_d~0.02, i.e. one order of magnitude larger, which reflects the lubricious properties of the articulating surface.

Figure 9.4b shows the measured lateral force while the colloid slides along the cartilage's surface in 1× PBS with 10 mM $CaCl_2$. The sudden jumps of the lateral force indicate that the colloid does not slide smoothly, but instead, it moves intermittently; this is also called stick-slip motion (206). Here, the colloid sticks to the cartilage due to the high adhesion, and when the lateral force is large enough, the colloid detaches from the cartilage, then it slides until it sticks again. The initial stiction peaks are of greater magnitude in the presence of calcium; μ_s is about three times larger than in Figure 9.4a. Furthermore, the stick-slip becomes notorious at all investigated loading times. Such stick-slip may be directly related to the ionic bridging between the silanol groups and the molecules in the cartilage's articulating surface mediated by calcium, as silica is negatively charged at neutral pH (207) and binds to calcium (208). In addition to this, the effect of the loading time is less clear than in 0mM $CaCl_2$, suggesting that calcium bridging between cartilage and silica mitigates the influence of the static loading time.

9.3. Discussion

This experimental study supports the presence of a surface layer in the articulating surface of bovine cartilage with a thickness of ~5 μm, a very high water content and higher compressibility than the layer underneath. According to nanoindentation, the elastic modulus of the cartilage's articulating surface increases with depth by roughly one order of magnitude from 3.3 to 43 kPa. AFM images of the cartilage's surface in 1× PBS reveal a granular microstructure within a coarse fibrous network, with fiber diameters much larger than that of the collagen fibers in the subsurface region. This may be due to the deposition of proteoglycans onto collagen fibrils, as reported for mice articular cartilage (197); and/or to the presence of a network of coarse elastin-rich fibers(61). Although the presence of

collagen is not obvious in these images, it cannot be excluded that both elastin and collagen fibers are part of the hydrated and swollen matrix, together with proteoglycans and glycoproteins, based on IR spectroscopy.

The origin for the hysteresis and lack of recovery upon slow and unconfined *initial* compression in eSFA experiments is intriguing. One possible explanation is that the content of proteoglycans is low, as they are mainly responsible for the re-swelling of cartilage (200); this is supported by the graded composition revealed by IR spectroscopy. In addition to this, the prominent squeeze-out of fluid could promote intermolecular interactions. This is reminiscent of the self-adhesion between aggrecan molecules when subjected to static compression for sufficient long periods of time (209). Note that this happens despite the strong electrostatic repulsion between the highly negatively charged glycosaminoglycan. Hydrogen bonding, hydrophobic interactions between the methyl groups and carbon rings as well as physical entanglements between the glycosaminoglycan side chains are proposed as relevant factors contributing to aggrecan self-adhesion. Similar intermolecular bonding upon removal of water has been proposed for other carbohydrate-rich macromolecules and proteins (210) and between hyaluronan and lipids (211, 212).

The increase in static friction with static loading time supports that time-dependent interactions (here, between cartilage's surface and silica) are relevant. A recent study of hydrogel's static friction has revealed that two main phenomena explain the increase of static friction (194). First, the contact area increases with time due to the gradual drainage of the imbibed fluid. Second, the interfacial shear strength increases with loading time owing to the gradual adsorption of the polymer network to the silica colloid (*e.g.* via hydrogen bonding), which is promoted by water exudation. Since cartilage is a biphasic

material composed of an interstitial fluid and bio-macromolecules, the same mechanisms are expected to be relevant. In fact, various studies have showed that prolonged static (non-sliding) loading leads to the squeeze-out of the fluid from cartilage's superficial zone (213, 214), and thereby to an increase in adhesion and friction (214).

Given the significant aggregation of the solid matrix shown in the AFM images, it is possible that calcium mediates crosslinks between negatively charged molecules present in the surface amorphous layer. Interestingly, the self-adhesion between aggrecan molecules was also found to significantly increase with calcium concentration due to ion bridging of the glycosaminoglycans under static loading (209). A similar behavior could be also expected for small proteoglycans, like decorin, which could bridge between collagen fibrils under static loading. Such enhanced interactions between macromolecules under compression can thus qualitatively explain the hysteresis between compression and decompression and that hysteresis becomes less prominent in subsequent compressions.

Collagen contains positively, negatively charged and polar but uncharged amino acids. The positive charge carried by arginine and lysine is believed to play an important role in the electrostatic interactions between collagen molecules, and thereby, in the self-assembly and stability of the collagen fibrils (215). Calcium ions can bind to the carboxylic groups, and thereby, bridge adjacent collagen molecules and alter collagen self-assembly (68). This is consistent with the reported thickening of collagen fibrils in the presence of calcium(64), although the reported diameter is much smaller than in our AFM images. On the other hand, elastic fibers consist mainly of an elastin core and fibrillar glycoproteins, like fibrillin. While it is not clear yet how calcium binds to elastin and how it affects its properties, fibrillin has multiple calcium binding domains, and its structure and mechanical

properties depend strongly on calcium concentration (216). The lateral packing of fibrillin monomers is calcium dependent; fibrillin adopts a more curved conformation and its stiffness increases with calcium concentration (217) Although the incubation with EDTA results in significant disruption of microfibril morphology, the change is reversible on providing calcium at even much higher concentrations than in the present study, indicating that changes of calcium do not compromise microfibrillar integrity (217). While this behavior alone cannot explain our results, it demonstrates the binding capability of calcium to elastic fibers and the possibility to crosslink adjacent proteoglycans like decorin.

Lubricin, a mucin-like glycoprotein with lubricating properties, is also present on the *lamina splendens* of articular cartilage and in synovial fluid (218, 219). The end-protein domains of lubricin stick to many molecules, including hyaluronan and collagen, while the highly glycosylated mucin domains remain strongly hydrated. A recent study has shown that a calcium concentration above 5 mM causes structural and mechanical changes of lubricin brush layers adsorbed on silicon oxide substrates (220). Calcium thus binds to carboxylate, which leads to a partial brush dehydration and densification, as well as to a partial collapse of the glycans, while both protein-end domains remain firmly stuck to the substrate. This results in certain aggregation and in an increase in brush roughness. Furthermore, while the elastic modulus of the mucin domains increases with calcium concentration (from 0.2 to 0.8 kPa), the end-domains become softer (from 22-34 kPa to 20-26 kPa). This has been associated with the denaturation and unfolding of the end-protein groups. Interestingly, this behavior agrees qualitatively with the observed softening of the cartilage's surface observed in our experiments. In contrast, hyaluronan remains strongly hydrated and without appreciable conformational changes even at calcium concentrations

20-fold larger than in our study (221). It appears that the hyaluronan molecules preserve extended linear regions, implying that coiling and entanglement are hindered, and thereby, relaxation and compressibility behavior stay unchanged. The response of hyaluronan to calcium is essentially of osmotic origin due to electrostatic screening, and hence, this alone cannot explain the observed behavior of the cartilage's surface.

It is, however, challenging to extrapolate the calcium-induced response of single molecules to tissue micromechanics. From a microstructure perspective, the aggregation of the solid matrix upon addition of calcium reveals an increase in the void size ξ, which is concurrent with the increase of the compressibility of the top surface layer and its swelling. Hydrogels are biphasic materials composed of a macromolecular network and large amounts of water, and hence, their structure has some similarity to that of cartilage. In the context of hydrogels' scaling theory (222), the elastic modulus scales as ξ^{-3}, ξ being the mesh size, and its swelling ratio, $Q \sim \xi^3$. Thus, an increase in mesh size yields both softening and swelling of hydrogels. Accordingly, the observed rearrangement of the solid matrix upon addition of calcium could also physically explain the observed softening and swelling of the surface layer.

The tribological implications are also worth discussing. The stick-slip motion in the presence of calcium suggests that the macromolecules in the surface layer stick to silica and are stretched and pulled, as the colloid slides. This should equally happen on cartilage-cartilage tribopairs, although the strength of the adhesive forces will be obviously different. Note that this happens at contact times ($t_V = a/2V \sim 1$ s) that are smaller than the static loading times that yield stiction in the absence of calcium ($t_s > 5$ s). As discussed above, high calcium concentrations also lead to the softening of the surface layer. This suggests

that the synergy between the weakened cartilage's surface and the adhesion to negatively charged counterfaces, both promoted by calcium, might be a mechanism that promotes wear and damage of the cartilage surface as a result of elevated calcium content in cartilage. In fact, several studies have loosely related high adhesion and friction of articular cartilage to joint fatigue and wear of the cartilage's surface (96, 214, 223).

9.4. Conclusions

In these experiments, we used a simple system with calcium and phosphate buffers and the devitalized cartilage surface to exclude the complication of chondrocyte metabolism. Previous to the loss of the structural integrity of the cartilage at the onset of OA, a softening of the cartilage surface (in equilibrium with PBS) has been observed at the nanoscale (197). This works shows that an elevated calcium concentration in the cartilage's surface could justify a softening of the surface amorphous layer. It is also worth noting, that our work does not support the previously proposed relation between elevated calcium concentration in human AC with nanoscale stiffening (64) that was observed at the onset of OA (224). We believe that the reason for this discrepancy as well as the much higher moduli in that work (~1 GPa) rely in the different hydration state of the cartilage, since that previous work carried out nanoindentation on dehydrated cartilage.

CHAPTER 10: CONCLUSIONS AND FUTURE OUTLOOK

Despite their relevance in understanding biolubrication and their significance as functional replacement materials, fundamental understanding of the frictional dissipation pathways of these soft, highly hydrate, biphasic materials lacks absoluteness. Although the existing models provided physical insights into the lubrication mechanisms, the existing knowledge is only partial and qualitative. Furthermore, core, quantitative relationships between the microstructure of these polymeric networks and their frictional dissipation are lacking. Based on the existing knowledge, the work described in this thesis systematically investigated the relation between the microstructure and tribological performance of hydrogel-like materials using state-of-the-art experimental techniques including, but not limited to, dynamic light scattering (DLS), colloidal probe lateral microscopy (AFM) and the surface forces apparatus (SFA).

First, the dynamic frictional characteristics of poly(acrylamide) hydrogels with varying composition were studied over a wide range of sliding velocities and normal loads by colloidal probe lateral force microscopy. We demonstrate that the friction force between the hydrogel and the colloid increased with velocity at sliding velocities above a transition value V^*, while the friction force at slower sliding velocities depended on the composition, and it can either increase or decrease with velocity. Our study revealed two different boundary lubrication mechanisms characterized by distinct scaling laws. Importantly, this work emphasized that the polymer physics scaling laws break down when there are large deformations, confinement and multiple relaxation modes associated with the biphasic nature of the hydrogels. We further modeled the dynamic friction as the combination of viscous dissipation and the energy dissipated through the rupture of the transient adhesive bridges across the interface. We showed that the model parameters were dependent on the relaxation characteristics of the confined polymer network at the interface and

on the (bulk) viscoelastic behavior of the hydrogel and were sensitive to the compressive stress. We also observed a collapse of the experimental data in a non-monotonic *master curve* with a minimum friction force at the transition velocity. Finally, a simple relation for the transition velocity was derived from theory, thereby demonstrating the competing effect of both the adhesive and the viscous contributions to friction, which helps to reconcile discrepancies between previous studies of hydrogel friction.

The above-mentioned model highlighted significance of the viscous contribution to hydrogel's dynamic friction. By extending the state-of-the-art SFA to perform nanorheological and tribological measurements, we were able to scrutinize the relation between the friction force and interfacial rheology of hydrogel thin films. Using hydrogel thin films of a few microns, we enhanced the effect of the interface. The novel experiments revealed a rich response of the hydrogel as a function of the compression (applied load) in both rheological and tribological measurements. (to be added)

Second, to improve and advance our understanding of static friction of hydrogels, we investigated poly(acrylamide) hydrogels with modulated microstructure over a wide range of loading conditions by colloidal probe lateral force microscopy. We showed that static friction stemmed from the adhesion of the polymer to the colloid and from the drainage-induced increase in contact area, and it strongly depended on the hydrogel's microstructure. The temperature dependence of the static friction revealed two peaks originating from the hydrogel's biphasic nature, while contact ageing vanished at high temperature, where friction decreased with contact time. This enabled us to build an unprecedented phase diagram for static friction of hydrogel-like materials, which explains contact ageing *via* the polymer relaxation, a subtle transition between solid-like to liquid-like interfacial behavior, and the poroelastic relaxation. This conceptual

framework for contact ageing will foster new understanding of wear of hydrogels, like those present in biological tribosystems. More broadly, these results have implications in diverse areas of inquiry, in not only biolubrication, but also soft robotics, soft micro-electromechanical devices and translational medicine, where the processes occurring at the moving hydrogel interface are of relevance.

Third, mechanical and tribological properties of DN hydrogels were investigated and the effect of their composition on the resulting hydrogel's microstructure and the mechanical and tribological performance was carefully studied. Here, DN hydrogels composed of physically crosslinked agarose (as the first network) and chemically crosslinked poly(acrylamide) (PAAm) (as the second network) were studied by combining spectroscopy, DLS, AFM and rheology. Our studies showed that for the low acrylamide concentrations, a viable double network forms, where a lightly crosslinked PAAm network reinforces the agarose network. An increase in the monomer concentration lead to phase separation between AAm-rich and AAm-depleted regions, which were subsequently crosslinked within the agarose network, leading to a heterogeneous DN hydrogel. This heterogeneity counteracted the strengthening targeted by the second network. Reduction in the crosslinking degree slowed down gelation and resulted in the interconnection between AAm-rich and depleted regions via *loose* crosslinking. Lastly, increase in the monomer concentration while keeping the crosslinker to monomer ratio constant, lead to an increased immiscibility of the two polymers, hindering the formation of an effective double network. Further, a highly concentration-dependent chemical and structural gradient of the DN hydrogels was revealed, which resulted in a frictional response dominated by either the first or the second network. Based on these results, it was proposed that the subtle balance between phase separation and crosslinking degree of the second network determined the DN microstructure, and its tribological response. The

results not only provided a fundamental insight into the formation and microstructure of agarose-polyacryl(amide) DN hydrogels but also demonstrated the tunability of the DN hydrogel's surface properties.

To conclude, this research significantly advances our understanding of lubrication by soft matter, and in particular of biphasic hydrogel-like materials. It demonstrates how friction of hydrogels can be modulated through the precise control of hydrogel's microstructure, which is key in the design of gel-like systems for aqueous lubrication. An extension of this PhD work is detailed in Chapter 9, where the knowledge and techniques were applied to study the mechanical and tribological response of a biological hydrogel – the articulating surface of cartilage.

10.1. Outlook and Future Direction

While the effects of chemical make-up and charge of hydrogel surfaces was not the focus of this dissertation, precedent works by Gong(225) and Sokoloff(14) have developed models for charged hydrogel friction. Between similarly charged surfaces, a fluid film can be expected, which can collapse under high applied pressures(14). Interestingly, it has been shown that friction can be controlled by adjusting the local molecular conformation of a polyelectrolyte brush via an alternating electric field (226). The intensity of the applied field can regulate the stretching of the polymer chain while sliding, and thereby, the degree of interpenetration between opposite polymer brushes at the interface. The dynamics of the response is controlled by the relaxation times of the polyelectrolyte. While the molecular-level response to an electric field is relatively quick, less is known about the response dynamics of charged hydrogels. Electrotunable behavior offers opportunities for applications in soft robotics, among others, and hence, it is not only fundamentally interesting but also important for these applications. Furthermore, varying the fluid film properties through the modulation of an applied electric field or of the charge density of the

hydrogel can also be a new avenue to elucidate the mechanism of viscous and electroviscous dissipation.

The complexity of the lubrication mechanisms mediated by hydrogels also relies on other factors, including contact roughness and wear which. Surface roughness can significantly affect the frictional characteristics. On the one hand, hydrogels have an inherent surface roughness owing to polymer dynamics at the interface. On the other one, hydrogels with modulated surface topology can be prepared. Hence, it seems imperative to elucidate the influence of surface roughness on the lubrication mechanisms and friction models. Similarly, the relation between frictional dissipation and wear is still not well understood. While several works have examined the tribologically-induced wear of hydrogels that can serve as biological replacement materials (227-230), the understanding of the mechanisms underlying tribologically promoted wear is not only lacking, but even more, the correlation is debated. Therefore, the opportunities of research on hydrogel systems for understanding and designing their tribological response are plenty. In fact, chapters 8 and 9 highlight one of these key factors: the effect of solvent composition on the hydrogel's microstructure and the resulting frictional response. Taking cue from this, here, we would like to highlight one outlook, i.e., the effect of solvent quality on the microstructure, rheological and tribological response of a physically crosslinked agarose hydrogel.

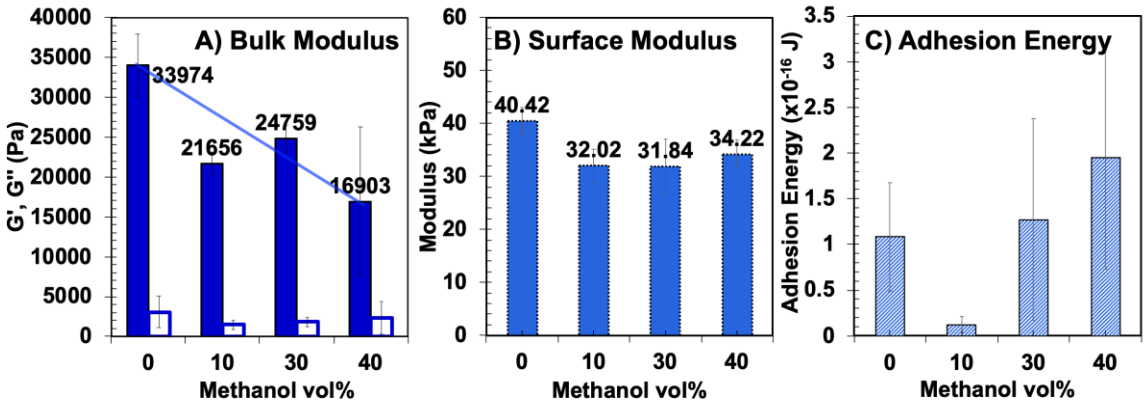

Figure 10.1 Bulk moduli from macrorheology (G' solid bars, G'' empty bars), b) Surface moduli and adhesion energies (area under the retract curve) from nanoindentation measurements via colloidal probe microscopy (AFM) for 1 wt% agarose hydrogels in DI water and water-methanol mixtures.

Figure 10.1 a shows the storage and loss moduli of agarose hydrogels in solvent mixtures of water and methanol. All hydrogels are viscoelastic solids with a predominantly elastic behavior (G'>>G''). A softening of agarose hydrogels is observed with increasing methanol content where the storage modulus changes from 33.9 to 16.9 kPa and loss modulus decreases to 3.06 and 2.93 kPa; while the more prominent collapse at 10% deviating from a quasi-linear relationship. Swelling experiments for these systems (Figure A15) show that agarose undergoes a great collapse in 10% methanol (the swelling ratio decreases from 95% to 70%). Further increase in the collapse is observed with the addition of 40% methanol where the swelling ratio decreases to ~63%. Methanol is a bad solvent for agarose(231), and hence the increasing collapse of the agarose network with increasing methanol content is expected. Importantly, the swelling ratio does not decrease linearly with the methanol volume fraction, but there is a deviation at 10 vol%, with a larger collapse than expected. This can be explained by considering that provided the linear collapse with increase in methanol% at 0, 30 and 40%, it is reasonable that at 10% methanol (in the bulk) more methanol is already present in the agarose hydrogel than in the solvent environment

or there is a significantly different microstructure of this hydrogel. Since agarose is physically crosslinked, some crosslinks could rearrange in the solvent mixture to minimize energy. According to the scaling theory(107) in a good solvent $G' \sim Q^{-2/3}$, where Q is the swelling ratio. Hence, the counterintuitive behavior based on scaling theory further suggests that agarose hydrogels might modify their microstructure, as the hydrogen bonding between agarose provided by water might be altered by the presence of methanol.

The elastic modulus of agarose hydrogels changes slightly with increasing methanol content (40.4 kPa in DI to 34.2 kPa in 40% MeOH) in a non monotonic fashion, slightly different from the bulk moduli (G', G''), perhaps due to the different concentration of methanol at the hydrogel-liquid interface. The adhesion energy obtained from nanoindenation follows a non-monotonic trend with increasing methanol content, where a remarkable decrease is observed for the 10% methanol mixture. At higher concentrations the adhesion energy increases. The trend is similar to the elastic modulus of the near-surface region, and hence, it cannot be explained simply to result from the change of the contact area; note also that the change of adhesion/pull off force is much larger (in %) than that of the elastic modulus. Hence, we believe that chemical interactions between colloid/agarose/solvent are more heavily involved. This is plausible, since the optical properties of the solvent mixture change, the Hamaker constant will also be modified and thereby the interactions.

Figure 10.2 reveals that surface structure. A uniform network exists for the agarose hydrogels in DI water as well as a homogenous slope (stiffness) and adhesion profile, indicating a single phase material. The network comprises of fine fibers, aggregated and interconnected to each other with small pores spanning the image. Note that in 10% MeOH, the image becomes blurry. Furthermore, the decrease in the number of pores is evident along with the vanishing of the

smallest sized pores indicating the aggregation of the agarose fibers and a restructuring of the surface in 10% MeOH. The surface in 30% and 40% methanol looks quite different from 10%, where higher number of pores is visible, however, the aggregation of the network fibers is still prominent. Comparison of the adhesion profile is also telling; first, with increasing methanol content, the interaction between agarose and the tip is reduced and second, the agarose surface responds nonuniformly to the change in solvent quality. This is most obvious in the comparison between Figures 10.2e, g and h where a homogeneously adhesive surface in DI water, forms patches of low and high adhesion in 30% MeOH and subsequently achieves a uniform, low adhesion surface in 40% MeOH. It suggests that the surface evolves and a transition starting at 10% proceeds up to 40% where the surface is homogenous again, perhaps when the methanol content is sufficient to bring about a complete restructuring of the network. The stiffness also reflects the more heterogeneous surface at 10% compared to water, the increasing heterogeneity at 30% and a more homogeneous profile at 40%, perhaps when the transition is complete. One way to confirm a different network an quality of the agarose fibers could be to perform thermogravimetric analysis (90) on these hydrogels.

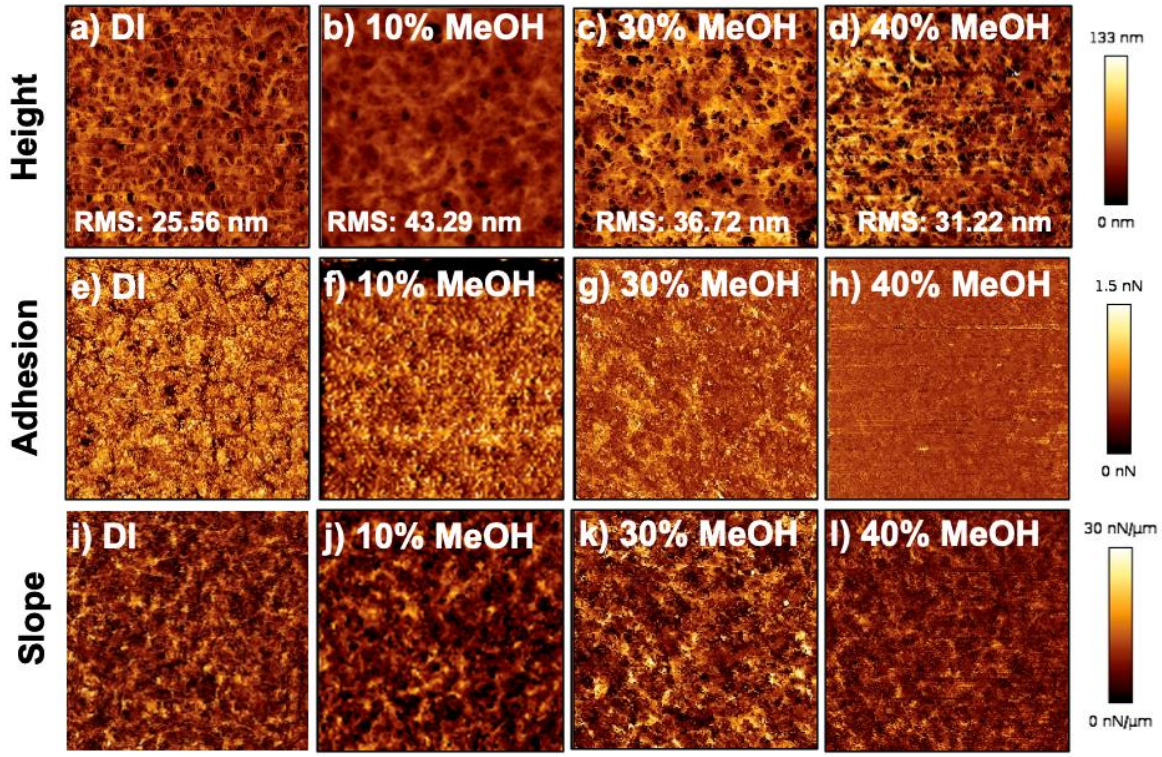

Figure 10.2 QI images of 1 wt% agarose hydrogels in DI water, 10% MeOH, 30% MeOH and 40% MeOH solutions. The top row shows the height profiles while the middle and the bottom rows show adhesion and stiffness profiles, respectively. Each image is 4 x 4 $\boldsymbol{\mu}$m. Tip: Silicon sharptip, $\boldsymbol{K_n = 0.3}$ N/m.

Previous experiments with polymer brushes explained the response to solvent mixtures simply as a result of the solvent quality and leading to swelling or collapse(232). Nonlinear trends were also observed and attributed to preferential solvation among others(233). In the current case, the deviations from the linear relation in agarose hydrogels arise from a change of microstructure. It is noteworthy that this change also extends to DN hydrogels comprising of agarose as the first network (Figure A14). The results here serve as a stepping-stone to model the microstructure to property relationships of hydrogels beyond the framework of the scaling theory by accounting for characteristic microstructural changes upon changing the solvent. In the context of tribology, such modification in microstructure could in theory be modeled as a function of the change in mesh size, and in the bond formation and rupture times by accounting for modified Hamaker constants,

perhaps in a more straightforward manner. Additionally, in the case of solvent mixtures, such as water and methanol, solvent-solvent interactions become important as well. For instance, recent neutron diffraction data (234, 235) and molecular dynamics simulation demonstrated that an extended micro-structure comprising of bi-percolating networks for both water and methanol within a limited range of methanol concentrations formed. Hence, mixtures such as water-methanol, which can form microscopic structures and resulting from the bifunctional nature of methanol and competitive hydrogen bonding can significantly influence the bulk and surface microstructure of the hydrogels and thereby the resulting mechanical and tribological response. Although this calls for incorporating complexity into the existing friction force models on one hand, on the other, it promises a step forward in the direction of soft robotics and switchable tribological response. This outlook thus concludes the dissertation.

This PhD work has significantly expanded the knowledge surrounding tribological response of soft, biphasic hydrogel-like materials by developing comprehensive frameworks to predict the behavior in the context of the material's structure. Also noteworthy are the experimental protocols and analysis methodologies coming out of this research, which will help overcome current challenges in studying soft materials for instance, by expanding them to investigate the lubrication mechanisms mediated by other polymer films, biological tissues, and in other solvents, thereby providing a plethora of exciting and impactful future research prospectives.

REFERENCES

1. Shoaib T & Espinosa-Marzal RM (2018) Insight into the Viscous and Adhesive Contributions to Hydrogel Friction. *Tribol. Lett.* 66(3):96.
2. Dowson D (2012) Bio-tribology. *Faraday Discuss* 156(1):9-30; discussion 87-103.
3. Mantelli F & Argueso P (2008) Functions of ocular surface mucins in health and disease. *Curr Opin Allergy Clin Immunol* 8(5):477-483.
4. Sterner O*, et al.* (2017) Reducing Friction in the Eye: A Comparative Study of Lubrication by Surface-Anchored Synthetic and Natural Ocular Mucin Analogues. *ACS Appl. Mater. Interfaces* 9(23):20150-20160.
5. Swann DA*, et al.* (1974) Role of hyaluronic acid in joint lubrication. *Ann. Rheum. Dis.* 33(4):318-326.
6. Schmidt TA, Gastelum NS, Nguyen QT, Schumacher BL, & Sah RL (2007) Boundary lubrication of articular cartilage: role of synovial fluid constituents. *Arthritis Rheum* 56(3):882-891.
7. Bongaerts JHH, Rossetti D, & Stokes JR (2007) The Lubricating Properties of Human Whole Saliva. *Tribol. Lett.* 27(3):277-287.
8. Dunn AC, Urueña JM, Puig E, Perez VL, & Sawyer WG (2012) Friction Coefficient Measurement of an In Vivo Murine Cornea. *Tribol Lett* 49(1):145-149.
9. Pult H*, et al.* (2015) Spontaneous Blinking from a Tribological Viewpoint. *Ocul Surf* 13(3):236-249.
10. Samsom M*, et al.* (2015) In vitro friction testing of contact lenses and human ocular tissues: Effect of proteoglycan 4 (PRG4). *Tribol Int* 89:27-33.
11. Dunn AC*, et al.* (2008) Friction Coefficient Measurement of Hydrogel Materials on Living Epithelial Cells. *Tribol Lett* 30(1):13-19.
12. Gong JP (2006) Friction and lubrication of hydrogels—its richness and complexity. *Soft matter* 2(7):544-552.
13. Pitenis AA*, et al.* (2014) Polymer fluctuation lubrication in hydrogel gemini interfaces. *Soft Matter* 10(44):8955-8962.
14. Sokoloff JB (2010) Theory of hydrostatic lubrication for two like-charge polymer hydrogel coated surfaces. *Soft Matter* 6(16):3856-3862.
15. Dunn AC*, et al.* (2013) Lubricity of surface hydrogel layers. *Tribol Lett* 49(2):371-378.
16. Baumberger T, Caroli C, & Ronsin O (2002) Self-Healing Slip Pulses along a Gel/Glass Interface. *Physical Review Letters* 88(7):075509.
17. Baumberger T, Caroli C, & Ronsin O (2003) Self-healing slip pulses and the friction of gelatin gels. *The European Physical Journal E* 11(1):85-93.
18. Oogaki S*, et al.* (2009) Friction between like-charged hydrogels—combined mechanisms of boundary, hydrated and elastohydrodynamic lubrication. *Soft Matter* 5(9):1879-1887.
19. Reale ER & Dunn AC (2017) Poroelasticity-driven lubrication in hydrogel interfaces. *Soft Matter* 13(2):428-435.
20. Shoaib T*, et al.* (2017) Stick–slip friction reveals hydrogel lubrication mechanisms. *Langmuir* 34(3):756-765.
21. Kurokawa T*, et al.* (2005) Elastic− Hydrodynamic Transition of Gel Friction. *Langmuir* 21(19):8643-8648.
22. Ohsedo Y, Takashina R, Gong JP, & Osada Y (2004) Surface friction of hydrogels with well-defined polyelectrolyte brushes. *Langmuir* 20(16):6549-6555.
23. Delavoipiere J*, et al.* (2018) Friction of Poroelastic Contacts with Thin Hydrogel Films. *Langmuir* 34(33):9617-9626.
24. Dunn AC*, et al.* (2012) Lubricity of Surface Hydrogel Layers. *Tribol Lett* 49(2):371-378.
25. Shoaib T*, et al.* (2018) Stick-Slip Friction Reveals Hydrogel Lubrication Mechanisms. *Langmuir* 34(3):756-765.
26. Shoaib T & Espinosa-Marzal RM (2018) Insight into the Viscous and Adhesive Contributions to Hydrogel Friction. *Tribol Lett* 66(3):96.
27. Kurokawa T*, et al.* (2005) Elastic-hydrodynamic transition of gel friction. *Langmuir* 21(19):8643-8648.

28. Urueña JM*, et al.* (2015) Mesh Size Control of Polymer Fluctuation Lubrication in Gemini Hydrogels. *Biotribology* 1-2:24-29.
29. Kagata G, Gong JP, & Osada Y (2002) Friction of Gels. 6. Effects of Sliding Velocity and Viscoelastic Responses of the Network. *The Journal of Physical Chemistry B* 106(18):4596-4601.
30. Gong J & Osada Y (1998) Gel friction: A model based on surface repulsion and adsorption. *J Chem Phys* 109(18):8062-8068.
31. Kagata G, Gong JP, & Osada Y (2003) Friction of Gels. 7. Observation of Static Friction between Like-Charged Gels. *The Journal of Physical Chemistry B* 107(37):10221-10225.
32. Juvekar VA & Singh AK (2016) Rate and Aging Time Dependent Static Friction of a Soft and Hard Solid Interface.
33. Nitta T, Kato H, Haga H, Nemoto K, & Kawabata K (2005) Static Friction of Agar Gels: Formation of Contact Junctions at Frictional Interface. *J Phys Soc Jpn* 74(11):2875-2879.
34. Lee DW, Banquy X, & Israelachvili JN (2013) Stick-slip friction and wear of articular joints. *Proceedings of the National Academy of Sciences* 110(7):E567-E574.
35. Shoaib T & Espinosa-Marzal RM (2019) Influence of Loading Conditions and Temperature on Static Friction and Contact Aging of Hydrogels with Modulated Microstructures. *ACS Appl. Mater. Interfaces* 11(45):42722-42733.
36. Shoaib T, Yuh C, Wimmer MA, Schmid TM, & Espinosa-Marzal RM (2020) Nanoscale insight into the degradation mechanisms of the cartilage articulating surface preceding OA. *Biomater Sci-Uk* 8(14):3944-3955.
37. Pan Y & Xiong D (2009) Friction properties of nano-hydroxyapatite reinforced poly(vinyl alcohol) gel composites as an articular cartilage. *Wear* 266(7):699-703.
38. Gong J, Iwasaki Y, Osada Y, Kurihara K, & Hamai Y (1999) Friction of Gels. 3. Friction on Solid Surfaces. *The Journal of Physical Chemistry B* 103(29):6001-6006.
39. Chang DP, Dolbow JE, & Zauscher S (2007) Switchable friction of stimulus-responsive hydrogels. *Langmuir* 23(1):250-257.
40. Pan Y-S, Xiong D-S, & Ma R-Y (2007) A study on the friction properties of poly(vinyl alcohol) hydrogel as articular cartilage against titanium alloy. *Wear* 262(7):1021-1025.
41. Kim SH, Opdahl A, Marmo C, & Somorjai GA (2002) AFM and SFG studies of pHEMA-based hydrogel contact lens surfaces in saline solution: adhesion, friction, and the presence of non-crosslinked polymer chains at the surface. *Biomaterials* 23(7):1657-1666.
42. Schallamach A (1963) A theory of dynamic rubber friction. *Wear* 6(5):375-382.
43. Li A, Ramakrishna SN, Kooij ES, Espinosa-Marzal RM, & Spencer ND (2012) Poly(acrylamide) films at the solvent-induced glass transition: adhesion, tribology, and the influence of crosslinking. *Soft Matter* 8(35):9092-9100.
44. Kim SH, Marmo C, & Somorjai GA (2001) Friction studies of hydrogel contact lenses using AFM: non-crosslinked polymers of low friction at the surface. *Biomaterials* 22(24):3285-3294.
45. Li A*, et al.* (2011) Surface-Grafted, Covalently Cross-Linked Hydrogel Brushes with Tunable Interfacial and Bulk Properties. *Macromolecules* 44(13):5344-5351.
46. Gong JP*, et al.* (2001) Synthesis of hydrogels with extremely low surface friction. *Journal of the American Chemical Society* 123(23):5582-5583.
47. Pitenis AA*, et al.* (2016) Lubricity from Entangled Polymer Networks on Hydrogels. *J Tribol-T Asme* 138(4):042102.
48. Sokoloff JB (2010) Theory of hydrostatic lubrication for two like-charge polymer hydrogel coated surfaces. *Soft Matter* 6(16).
49. Gong JP, Kagata G, & Osada Y (1999) Friction of gels. 4. Friction on charged gels. *The Journal of Physical Chemistry B* 103(29):6007-6014.
50. Grosch KA (1963) The Relation between the Friction and Visco-Elastic Properties of Rubber. *Proceedings of the Royal Society A: Mathematical, Physical and Engineering Sciences* 274(1356):21-39.
51. Rennie AC, Dickrell PL, & Sawyer WG (2005) Friction coefficient of soft contact lenses: measurements and modeling. *Tribol Lett* 18(4):499-504.
52. Berthoud P, Baumberger T, G'Sell C, & Hiver JM (1999) Physical analysis of the state- and rate-dependent friction law: Static friction. *Phys Rev B* 59(22):14313-14327.

53. Li Q, Tullis TE, Goldsby D, & Carpick RW (2011) Frictional ageing from interfacial bonding and the origins of rate and state friction. *Nature* 480(7376):233-236.
54. Dieterich JH (1972) Time-dependent friction in rocks. *Journal of Geophysical Research* 77(20):3690-3697.
55. Suzuki A, Ishii R, Yamakami Y, & Nakano K (2011) *Surface friction of thermoresponsive poly(N-isopropylacrylamide) gels in water* pp 561-568.
56. Baumberger T, Caroli C, & Ronsin O (2003) Self-healing slip pulses and the friction of gelatin gels. *Eur Phys J E Soft Matter* 11(1):85-93.
57. Kobayashi S, Yonekubo S, & Kurogouchi Y (1996) Cryoscanning electron microscopy of loaded articular cartilage with special reference to the surface amorphous layer. *J Anat* 188 (Pt 2):311-322.
58. Teshima R, Otsuka T, Takasu N, Yamagata N, & Yamamoto K (1995) Structure of the Most Superficial Layer of Articular-Cartilage. *J Bone Joint Surg Br* 77b(3):460-464.
59. Crockett R*, et al.* (2005) Imaging of the Surface of Human and Bovine Articular Cartilage with ESEM and AFM. *Tribol Lett* 19(4):311-317.
60. Jahn S, Seror J, & Klein J (2016) Lubrication of Articular Cartilage. *Annu Rev Biomed Eng* 18:235-258.
61. Boyanich R*, et al.* (2019) Application of confocal, SHG and atomic force microscopy for characterizing the structure of the most superficial layer of articular cartilage. *J Microsc-Oxford* 275(3):159-171.
62. Yu J & Urban JP (2010) The elastic network of articular cartilage: an immunohistochemical study of elastin fibres and microfibrils. *J Anat* 216(4):533-541.
63. Buckwalter JA, Mankin HJ, & Grodzinsky AJ (2005) Articular cartilage and osteoarthritis. *Instr Course Lect* 54:465-480.
64. Shao J, Lin L, Tang B, & Du C (2014) Structure and nanomechanics of collagen fibrils in articular cartilage at different stages of osteoarthritis. *Rsc Adv* 4(93):51165-51170.
65. Jung YK*, et al.* (2018) Calcium-phosphate complex increased during subchondral bone remodeling affects earlystage osteoarthritis. *Sci Rep-Uk* 8.
66. Mobasheri A*, et al.* (2019) The chondrocyte channelome: a narrative review. *Joint Bone Spine* 86(1):29-35.
67. McCarthy GM & Dunne A (2018) Calcium crystal deposition diseases - beyond gout. *Nat Rev Rheumatol* 14(10):592-602.
68. Rhee SH, Lee JD, & Tanaka J (2000) Nucleation of hydroxyapatite crystal through chemical interaction with collagen. *Journal of the American Ceramic Society* 83(11):2890-2892.
69. Harder A, Walhorn V, Dierks T, Fernandez-Busquets X, & Anselmetti D (2010) Single-molecule force spectroscopy of cartilage aggrecan self-adhesion. *Biophys J* 99(10):3498-3504.
70. Winter WT & Arnott S (1977) Hyaluronic acid: the role of divalent cations in conformation and packing. *J Mol Biol* 117(3):761-784.
71. Chen H, Deere M, Hecht JT, & Lawler J (2000) Cartilage oligomeric matrix protein is a calcium-binding protein, and a mutation in its type 3 repeats causes conformational changes. *J Biol Chem* 275(34):26538-26544.
72. Pang X, Sun P, Tan Z, Lin L, & Tang B (2016) Effect of calcium ions on the nanostiffness of articular cartilage. *Materials Letters* 180:332-335.
73. Cui F-Z, Li Y, & Ge J (2007) Self-assembly of mineralized collagen composites. *Materials Science and Engineering: R: Reports* 57(1-6):1-27.
74. De Gennes PG (1991) *Scaling Concepts in Polymer Physics* (Cornell University Press, New York).
75. Tanaka T, Hocker LO, & Benedek GB (1973) Spectrum of light scattered from a viscoelastic gel. *J Chem Phys* 59(9):5151-5159.
76. Joosten JGH, Mccarthy JL, & Pusey PN (1991) Dynamic and Static Light-Scattering by Aqueous Polyacrylamide Gels. *Macromolecules* 24(25):6690-6699.
77. Barretta P, Bordi F, Rinaldi C, & Paradossi G (2000) A dynamic light scattering study of hydrogels based on telechelic poly(vinyl alcohol). *J Phys Chem B* 104(47):11019-11026.
78. Shibayama M, Fujikawa Y, & Nomura S (1996) Dynamic light scattering study of poly(N-isopropylacrylamide-co-acrylic acid) gels. *Macromolecules* 29(20):6535-6540.

79. Gombert Y*, et al.* (2019) Structuring Hydrogel Surfaces for Tribology. *Adv Mater Interfaces* 6(22):1901320.
80. Boudou T, Ohayon J, Picart C, Pettigrew RI, & Tracqui P (2009) Nonlinear elastic properties of polyacrylamide gels: implications for quantification of cellular forces. *Biorheology* 46(3):191-205.
81. Nalam PC, Gosvami NN, Caporizzo MA, Composto RJ, & Carpick RW (2015) Nano-rheology of hydrogels using direct drive force modulation atomic force microscopy. *Soft Matter* 11(41):8165-8178.
82. Zhou CJ, Wu QL, Yue YY, & Zhang QG (2011) Application of rod-shaped cellulose nanocrystals in polyacrylamide hydrogels. *J Colloid Interf Sci* 353(1):116-123.
83. Shibayama M & Norisuye T (2002) Gel Formation Analyses by Dynamic Light Scattering. *Bulletin of the Chemical Society of Japan* 75(4):641-659.
84. Rochas C & Geissler E (2014) Measurement of dynamic light scattering intensity in gels. *Macromolecules* 47(22):8012-8017.
85. Horkay F, Burchard W, Hecht AM, & Geissler E (1993) Poly (vinyl alcohol-vinyl acetate) copolymer hydrogels: scattering and osmotic observations. *Macromolecules* 26(13):3375-3380.
86. Horkay F, Hecht A-M, Grillo I, Basser PJ, & Geissler E (2002) Experimental evidence for two thermodynamic length scales in neutralized polyacrylate gels. *J Chem Phys* 117(20):9103-9106.
87. Pradal C, Jack KS, Grøndahl L, & Cooper-White JJ (2013) Gelation kinetics and viscoelastic properties of Pluronic and α-cyclodextrin-based pseudopolyrotaxane hydrogels. *Biomacromolecules* 14(10):3780-3792.
88. Nie J, Du B, & Oppermann W (2006) Dynamic Fluctuations and Spatial Inhomogeneities in Poly(N-isopropylacrylamide)/Clay Nanocomposite Hydrogels Studied by Dynamic Light Scattering. *The Journal of Physical Chemistry B* 110(23):11167-11175.
89. Shibayama M*, et al.* (2004) Structure and Dynamics of Poly(N-isopropylacrylamide)−Clay Nanocomposite Gels. *Macromolecules* 37(25):9606-9612.
90. Shoaib T*, et al.* (2017) Self-adaptive hydrogels to mineralization. *Soft Matter* 13(32):5469-5480.
91. Kii A, Xu J, Gong JP, Osada Y, & Zhang X (2001) Heterogeneous Polymerization of Hydrogels on Hydrophobic Substrate. *The Journal of Physical Chemistry B* 105(20):4565-4571.
92. Johnson KL, Kendall K, & Roberts A (1971) Surface energy and the contact of elastic solids. *Proceedings of the royal society of London. A. mathematical and physical sciences* 324(1558):301-313.
93. Pabst W & Gregorová EVA (2013) Elastic properties of silica polymorphs—a review. *Ceramics-Silikaty* 57(3):167-184.
94. Denisin AK & Pruitt BL (2016) Tuning the Range of Polyacrylamide Gel Stiffness for Mechanobiology Applications. *ACS Applied Materials & Interfaces* 8(34):21893-21902.
95. Ramakrishna SN, Cirelli M, Divandari M, & Benetti EM (2017) Effects of Lateral Deformation by Thermoresponsive Polymer Brushes on the Measured Friction Forces. *Langmuir* 33(17):4164-4171.
96. Lee DW, Banquy X, & Israelachvili JN (2013) Stick-slip friction and wear of articular joints. *Proc Natl Acad Sci U S A* 110(7):E567-574.
97. Israelachvili JN (2011) *Intermolecular and Surface Forces, 3rd Edition* (Elsevier, Amsterdam).
98. Urueña JM*, et al.* (2015) Mesh Size Control of Polymer Fluctuation Lubrication in Gemini Hydrogels. *Biotribology* 1–2:24-29.
99. Stachowiak GW & Batchelor AW (2006) 7 - Elastohydrodynamic Lubrication. *Engineering Tribology (Third Edition)*, (Butterworth-Heinemann, Burlington), pp 287-362.
100. Cannara RJ, Eglin M, & Carpick RW (2006) Lateral force calibration in atomic force microscopy: A new lateral force calibration method and general guidelines for optimization. *Review of Scientific Instruments* 77(5):053701.
101. Gautreau Z, Griffin J, Peterson T, & Thongpradit P (2006) Characterizing viscoelastic properties of polyacrylamide gels. *Worcester, Massachusetts: Worcester Polytechnic Institute*.
102. Resnikoff JIN (2012) The role of extracellular matrix composition and mechanical properties in driving cardiac differentiation of mesenchymal stem cells.
103. Schallamach A (1971) How does rubber slide? *Wear* 17(4):301-312.

104. Drummond C, Israelachvili J, & Richetti P (2003) Friction between two weakly adhering boundary lubricated surfaces in water. *Phys Rev E* 67(6 Pt 2):066110.
105. Dhinojwala A, Cai L, & Granick S (1996) Critique of the friction coefficient concept for wet (lubricated) sliding. *Langmuir* 12(19):4537-4542.
106. Demirci U & Khademhosseini A (2016) *Gels handbook: Fundamentals, properties and applications (in 3 volumes)* (World scientific).
107. Rubinstein M & Colby RH (2003) *Polymer Physics* (OUP Oxford).
108. Savkoor AR (1965) On the friction of rubber. *Wear* 8(3):222-237.
109. Luengo G, Schmitt F-J, Hill R, & Israelachvili J (1997) Thin Film Rheology and Tribology of Confined Polymer Melts: Contrasts with Bulk Properties. *Macromolecules* 30(8):2482-2494.
110. Schulze KD*, et al.* (2017) Polymer Osmotic Pressure in Hydrogel Contact Mechanics. *Biotribology* 11:3-7.
111. Mow VC, Kuei SC, Lai WM, & Armstrong CG (1980) Biphasic creep and stress relaxation of articular cartilage in compression? Theory and experiments. *Journal of Biomechanical Engineering* 102(1):73-84.
112. Strange DGT*, et al.* (2013) Separating poroviscoelastic deformation mechanisms in hydrogels. *Applied Physics Letters* 102(3):031913.
113. Espinosa-Marzal RM, Bielecki RM, & Spencer ND (2013) Understanding the role of viscous solvent confinement in the tribological behavior of polymer brushes: a bioinspired approach. *Soft Matter* 9(44):10572-10585.
114. Johnson KL, Kendall K, & Roberts AD (Surface energy and the contact of elastic solids. *Proc. R. Soc. Lond. A* 324:301-313.
115. Suriano R, Griffini G, Chiari M, Levi M, & Turri S (2014) Rheological and mechanical behavior of polyacrylamide hydrogels chemically crosslinked with allyl agarose for two-dimensional gel electrophoresis. *J Mech Behav Biomed Mater* 30:339-346.
116. Pitenis AA*, et al.* (2014) Polymer fluctuation lubrication in hydrogel gemini interfaces. *Soft Matter* 10(44):8955-8962.
117. Reiner M (1964) The Deborah Number. *Physics today* 17(1):62.
118. Persson BN & Volokitin AI (2006) Rubber friction on smooth surfaces. *The European Physical Journal E* 21(1):69-80.
119. Hodges RR & Dartt DA (2013) Tear film mucins: front line defenders of the ocular surface; comparison with airway and gastrointestinal tract mucins. *Experimental Eye Research* 117:62-78.
120. Bansil R & Turner BS (2006) Mucin structure, aggregation, physiological functions and biomedical applications. *Current Opinion in Colloid & Interface Science* 11(2-3):164-170.
121. Jay GD & Waller KA (2014) The biology of lubricin: near frictionless joint motion. *Matrix Biology* 39:17-24.
122. Swann DA, Slayter HS, & Silver FH (1981) The molecular structure of lubricating glycoprotein-I, the boundary lubricant for articular cartilage. *Journal of biological chemistry* 256(11):5921-5925.
123. Chawla K*, et al.* (2009) A novel low-friction surface for biomedical applications: modification of poly(dimethylsiloxane) (PDMS) with polyethylene glycol(PEG)-DOPA-lysine. *Journal of Biomedical Materials Research A* 90(3):742-749.
124. Israelachvili JN (2011) *Intermolecular and surface forces* (Academic press) 3rd Ed.
125. Grosch KA (1963) The relation between the friction and visco-elastic properties of rubber. *Proceedings of the Royal Society of London. Series A. Mathematical and Physical Sciences* 274(1356):21-39.
126. Yoshizawa H & Israelachvili J (1993) Fundamental mechanisms of interfacial friction. 2. Stick-slip friction of spherical and chain molecules. *J Phys Chem-Us* 97(43):11300-11313.
127. De Gennes PG (1979) *Scaling concepts in polymer physics* (Cornell university press).
128. Peanasky J, Cai LL, Granick S, & Kessel CR (1994) Nanorheology of Confined Polymer Melts. 3. Weakly Adsorbing Surfaces. *Langmuir* 10(10):3874-3879.
129. Horkay F, Magda J, Alcoutlabi M, Atzet S, & Zarembinski T (2010) Structural, mechanical and osmotic properties of injectable hyaluronan-based composite hydrogels. *Polymer* 51(19):4424-4430.

130. Maurer JJ, Schulz DN, Siano DB, & Bock J (1984) Thermal Analysis of Acrylamide-Based Polymers. *Analytical Calorimetry*, eds Johnson JF & Gill PS (Springer US, Boston, MA), pp 43-55.
131. Cuccia NL, Pothineni S, Wu B, Harper JM, & Burton JC (2020) Pore-size dependence and slow relaxation of hydrogel friction on smooth surfaces. *Proceedings of the National Academy of Sciences* 117(21):11247-11256.
132. Kim J & Dunn AC (2018) Thixotropic Mechanics in Soft Hydrated Sliding Interfaces. *Tribol Lett* 66(3):102.
133. Luengo G, Israelachvili J, & Granick S (1996) Generalized effects in confined fluids: new friction map for boundary lubrication. *Wear* 200(1-2):328-335.
134. Granick S & Hu H-W (1994) Nanorheology of Confined Polymer Melts. 1. Linear Shear Response at Strongly Adsorbing Surfaces. *Langmuir* 10(10):3857-3866.
135. Crampton N, Bonass WA, Kirkham J, & Thomson NH (2005) Formation of aminosilane-functionalized mica for atomic force microscopy imaging of DNA. *Langmuir* 21(17):7884-7891.
136. Degen GD, Chen Y-T, Chau AL, Månsson LK, & Pitenis AA (2020) Poroelasticity of highly confined hydrogel films measured with a surface forces apparatus. *Soft Matter* 16(35):8096-8100.
137. Ali I & Shah LA (2021) Rheological investigation of the viscoelastic thixotropic behavior of synthesized polyethylene glycol-modified polyacrylamide hydrogels using different accelerators. *Polymer Bulletin* 78(3):1275-1291.
138. Hu H-W, Carson GA, & Granick S (1991) Relaxation time of confined liquids under shear. *Physical review letters* 66(21):2758.
139. Carson G, Hu H-W, & Granick S (1992) Molecular tribology of fluid lubrication: shear thinning. *Tribology Transactions* 35(3):405-410.
140. Cui ST, McCabe C, Cummings PT, & Cochran HD (2003) Molecular dynamics study of the nano-rheology of n-dodecane confined between planar surfaces. *J Chem Phys* 118(19):8941-8944.
141. Kreer T (2016) Polymer-brush lubrication: a review of recent theoretical advances. *Soft Matter* 12(15):3479-3501.
142. Malhotra S & Sharma MM (2012) Settling of spherical particles in unbounded and confined surfactant-based shear thinning viscoelastic fluids: An experimental study. *Chemical Engineering Science* 84:646-655.
143. Lootens D, Hébraud P, Lécolier E, & Van Damme H (2004) Gelation, shear-thinning and shear-thickening in cement slurries. *Oil & gas science and technology* 59(1):31-40.
144. Ryder JF & Yeomans JM (2006) Shear thinning in dilute polymer solutions. *J Chem Phys* 125(19):194906.
145. Guvendiren M, Lu HD, & Burdick JA (2012) Shear-thinning hydrogels for biomedical applications. *Soft Matter* 8(2):260-272.
146. Mezger TG (2006) The rheology handbook: For users of rotational and oscillatory rheometers. *Vincentz network GmbH & Co. KG, Hannover, Germany*.
147. Rabin Y & Öttinger HC (1990) Dilute polymer solutions: internal viscosity, dynamic scaling, shear thinning and frequency-dependent viscosity. *EPL (Europhysics Letters)* 13(5):423.
148. Cox WP & Merz EH (1958) Correlation of dynamic and steady flow viscosities. *Journal of Polymer Science* 28(118):619-622.
149. Cox W & Merz E (Rheology of polymer melts—A correlation of dynamic and steady flow measurements. (ASTM International).
150. Snijkers F & Vlassopoulos D (2014) Appraisal of the Cox-Merz rule for well-characterized entangled linear and branched polymers. *Rheologica Acta* 53(12):935-946.
151. Hendricks J (2019) Supramolecular Polymeric Solutions in Shear and Extensional Flows.
152. Annable T, Buscall R, Ettelaie R, & Whittlestone D (1993) The rheology of solutions of associating polymers: Comparison of experimental behavior with transient network theory. *Journal of Rheology* 37(4):695-726.
153. Tanaka F & Edwards SF (1992) Viscoelastic properties of physically crosslinked networks: Part 2. Dynamic mechanical moduli. *Journal of non-newtonian fluid mechanics* 43(2-3):273-288.
154. Irfan M*, et al.* (2021) Synthesis and Rheological Survey of Xanthan Gum Based Terpolymeric Hydrogels. *Zeitschrift für Physikalische Chemie* 235(5):609-628.

155. Uman S, Dhand A, & Burdick JA (2020) Recent advances in shear-thinning and self-healing hydrogels for biomedical applications. *Journal of Applied Polymer Science* 137(25):48668.
156. Gao HW, Yang RJ, He JY, & Yang L (2010) Rheological behaviors of PVA/H2O solutions of high-polymer concentration. *Journal of applied polymer science* 116(3):1459-1466.
157. Ree F, Ree T, & Eyring H (1958) Relaxation theory of transport problems in condensed systems. *Industrial & Engineering Chemistry* 50(7):1036-1040.
158. Shoaib T & Espinosa-Marzal RM (2020) Advances in Understanding Hydrogel Lubrication. *Colloids and Interfaces* 4(4):54.
159. Lin T*, et al.* (2018) One-step radiation synthesis of agarose/polyacrylamide double-network hydrogel with extremely excellent mechanical properties. *Carbohydrate polymers* 200:72-81.
160. Priya MV, Kumar RA, Sivashanmugam A, Nair SV, & Jayakumar R (Injectable Amorphous Chitin-Agarose Composite Hydrogels for Biomedical Applications. (2079-4983 (Print)).
161. Hu Z, Hong P-Z, Li S-D, Yang L, & Xie J-Y (2012) Study on the preparation of quaternized chitosan/agarose microspheres for berbamine delivery. *Journal of Polymer Materials* 29(3):361.
162. Godwin Uranta K, Rezaei-Gomari S, Russell P, & Hamad F (2018) Studying the effectiveness of polyacrylamide (PAM) application in hydrocarbon reservoirs at different operational conditions. *Energies* 11(9):2201.
163. Cho MK, Singu BS, Na YH, & Yoon KR (2016) Fabrication and characterization of double-network agarose/polyacrylamide nanofibers by electrospinning. *Journal of Applied Polymer Science* 133(4).
164. Wang FC, Feve M, Lam TM, & Pascault JP (1994) FTIR analysis of hydrogen bonding in amorphous linear aromatic polyurethanes. I. Influence of temperature. *Journal of Polymer Science Part B: Polymer Physics* 32(8):1305-1313.
165. Dai B & Matsukawa S (2013) Elucidation of gelation mechanism and molecular interactions of agarose in solution by 1H NMR. *Carbohydrate Research* 365:38-45.
166. Nakajima T, Furukawa H, Tanaka Y, Kurokawa T, & Gong JP (2011) Effect of void structure on the toughness of double network hydrogels. *Journal of Polymer Science Part B: Polymer Physics* 49(17):1246-1254.
167. Chen H*, et al.* (2016) A comparative study of the mechanical properties of hybrid double-network hydrogels in swollen and as-prepared states. *Journal of Materials Chemistry B* 4(35):5814-5824.
168. Zhang K, Simic R, Yan W, & Spencer ND (2019) Creating an Interface: Rendering a Double-Network Hydrogel Lubricious via Spontaneous Delamination. *ACS Applied Materials & Interfaces* 11(28):25427-25435.
169. Kaneko D, Tada T, Kurokawa T, Gong JP, & Osada Y (2005) Mechanically strong hydrogels with ultra-low frictional coefficients. *Advanced Materials* 17(5):535-538.
170. Shi Y, Li J, Xiong D, Li L, & Liu Q (2021) Mechanical and tribological behaviors of PVA/PAAm double network hydrogels under varied strains as cartilage replacement. *Journal of Applied Polymer Science* 138(16):50226.
171. Murat Ozmen M & Okay O (2008) Formation of macroporous poly(acrylamide) hydrogels in DMSO/water mixture: Transition from cryogelation to phase separation copolymerization. *Reactive and Functional Polymers* 68(10):1467-1475.
172. Ozmen M, Dinu M, & Okay O (2008) Preparation of macroporous poly(acrylamide) hydrogels in DMSO/water mixture at subzero temperatures. *Polymer Bulletin - POLYM BULL* 60:169-180.
173. Brayton CF (1986) Dimethyl sulfoxide (DMSO): a review. *The Cornell Veterinarian* 76(1):61-90.
174. Kirchner B & Reiher M (2002) The Secret of Dimethyl Sulfoxide−Water Mixtures. A Quantum Chemical Study of 1DMSO−nWater Clusters. *Journal of the American Chemical Society* 124(21):6206-6215.
175. LeBel RG & Goring DAI (1962) Density, Viscosity, Refractive Index, and Hygroscopicity of Mixtures of Water and Dimethyl Sulfoxide. *Journal of Chemical & Engineering Data* 7(1):100-101.
176. Watase M & Nishinari K (1988) Thermal and Rheological Properties of Agarose-Dimethyl Sulfoxide-Water Gels. *Polymer Journal* 20(12):1125-1133.
177. Zhuravleva IL, Zav'yalova YN, Bogachev YS, & Gromov VF (1986) The radical polymerization of acrylamide in dimethyl sulfoxide-water mixtures. *Polymer Science U.S.S.R.* 28(4):976-981.
178. Krause S (1972) Polymer compatibility. *Journal of Macromolecular Science—Reviews in Macromolecular Chemistry* 7(2):251-314.

179. Durmaz S & Okay O (2000) Phase separation during the formation of poly(acrylamide) hydrogels. *Polymer* 41(15):5729-5735.
180. Nakajima T*, et al.* (2009) True Chemical Structure of Double Network Hydrogels. *Macromolecules* 42(6):2184-2189.
181. Tsukeshiba H*, et al.* (2005) Effect of polymer entanglement on the toughening of double network hydrogels. *The Journal of Physical Chemistry B* 109(34):16304-16309.
182. de Gennes P-G (1979) Effect of cross-links on a mixture of polymers. *Journal de Physique Lettres* 40(4):69-72.
183. Hayashi A & Kanzaki T (1987) Swelling of agarose gel and its related changes. *Food Hydrocolloids* 1(4):317-325.
184. Moore AC & Burris DL (2015) Tribological and material properties for cartilage of and throughout the bovine stifle: support for the altered joint kinematics hypothesis of osteoarthritis. *Osteoarthritis Cartilage* 23(1):161-169.
185. Peters AE, Comerford EJ, Macaulay S, Bates KT, & Akhtar R (2017) Micromechanical properties of canine femoral articular cartilage following multiple freeze-thaw cycles. *J Mech Behav Biomed Mater* 71:114-121.
186. Eanes ED, Hailer AW, Midura RJ, & Hascall VC (1992) Proteoglycan inhibition of calcium phosphate precipitation in liposomal suspensions. *Glycobiology* 2(6):571-578.
187. Israelachvili JN & Tabor D (1972) The Measurement of Van Der Waals Dispersion Forces in the Range 1.5 to 130 nm. *Proceedings of the Royal Society A: Mathematical, Physical and Engineering Sciences* 331(1584):19-38.
188. Heuberger M (2001) The extended surface forces apparatus. Part I. Fast spectral correlation interferometry. *Review of Scientific Instruments* 72(3):1700-1707.
189. Heuberger M, Vanicek J, & Zäch M (2001) The extended surface forces apparatus. II. Precision temperature control. *Review of Scientific Instruments* 72(9):3556-3560.
190. Chao HH & Torchiana DF (2003) BioGlue: albumin/glutaraldehyde sealant in cardiac surgery. *Journal of cardiac surgery* 18(6):500-503.
191. Heuberger M & Balmer TE (2007) The transmission interferometric adsorption sensor. *Journal of Physics D: Applied Physics* 40(23):7245.
192. Hertz H (1881) Über die Berührung fester elastischer Körper. *Reine Angewandte Mathematik* 92:156-171.
193. Thambyah A, Nather A, & Goh J (2006) Mechanical properties of articular cartilage covered by the meniscus. *Osteoarthritis Cartilage* 14(6):580-588.
194. Shoaib T & Espinosa-Marzal RM (2019) Influence of Loading Conditions and Temperature on Static Friction and Contact Aging of Hydrogels with Modulated Microstructures. *ACS Appl Mater Interfaces* 11(45):42722-42733.
195. Mansour JM (2003) Biomechanics of cartilage. *Kinesiology: the mechanics and pathomechanics of human movement* 2:66-79.
196. Zappone B, Patil NJ, Lombardo M, & Lombardo G (2018) Transient viscous response of the human cornea probed with the Surface Force Apparatus. *PLoS One* 13(5):e0197779.
197. Stolz M*, et al.* (2009) Early detection of aging cartilage and osteoarthritis in mice and patient samples using atomic force microscopy. *Nat Nanotechnol* 4(3):186-192.
198. Mansfield J*, et al.* (2009) The elastin network: its relationship with collagen and cells in articular cartilage as visualized by multiphoton microscopy. *Journal of anatomy* 215(6):682-691.
199. Chen C-C, Boskey AL, & Rosenberg LC (1984) The inhibitory effect of cartilage proteoglycans on hydroxyapatite growth. *Calcified tissue international* 36(1):285-290.
200. Maroudas A, Mizrahi J, Benaim E, Schneiderman R, & Grushko G (1992) Swelling pressure of cartilage: roles played by proteoglycans and collagen. *Mechanics of Swelling*, (Springer), pp 487-512.
201. Raviv U*, et al.* (2002) Properties and Interactions of Physigrafted End-Functionalized Poly(ethylene glycol) Layers. *Langmuir* 18(20):7482-7495.
202. Wang SZ, Huang YP, Wang Q, Zheng YP, & He YH (2010) Assessment of depth and degeneration dependences of articular cartilage refractive index using optical coherence tomography in vitro. *Connect Tissue Res* 51(1):36-47.

203. de Gennes PG (1987) Polymers at an interface; a simplified view. *Advances in Colloid and Interface Science* 27(3-4):189-209.
204. Andresen Eguiluz RC*, et al.* (2015) Fibronectin mediates enhanced wear protection of lubricin during shear. *Biomacromolecules* 16(9):2884-2894.
205. Li LP, Soulhat J, Buschmann MD, & Shirazi-Adl A (1999) Nonlinear analysis of cartilage in unconfined ramp compression using a fibril reinforced poroelastic model. *Clinical Biomechanics* 14(9):673-682.
206. Yoshizawa H & Israelachvili J (1993) Fundamental mechanisms of interfacial friction. 2. Stick-slip friction of spherical and chain molecules. *J Phys Chem-Us* 97(43):11300-11313.
207. Iler RK (1979) The Chemistry of Silica John Wiley & Sons. *New York*:30-62.
208. Iler RK (1975) Coagulation of colloidal silica by calcium ions, mechanism, and effect of particle size. *J Colloid Interf Sci* 53(3):476-488.
209. Han L, Dean D, Daher LA, Grodzinsky AJ, & Ortiz C (2008) Cartilage aggrecan can undergo self-adhesion. *Biophys J* 95(10):4862-4870.
210. Allison SD, Chang B, Randolph TW, & Carpenter JF (1999) Hydrogen bonding between sugar and protein is responsible for inhibition of dehydration-induced protein unfolding. *Archives of Biochemistry and Biophysics* 365(2):289-298.
211. Crockett R*, et al.* (2007) Biochemical composition of the superficial layer of articular cartilage. *J Biomed Mater Res A* 82(4):958-964.
212. Peer D, Florentin A, & Margalit R (2003) Hyaluronan is a key component in cryoprotection and formulation of targeted unilamellar liposomes. *Biochimica et Biophysica Acta (BBA)-Biomembranes* 1612(1):76-82.
213. Bell CJ, Ingham E, & Fisher J (2006) Influence of hyaluronic acid on the time-dependent friction response of articular cartilage under different conditions. *Proc Inst Mech Eng H* 220(1):23-31.
214. Forster H & Fisher J (1996) The influence of loading time and lubricant on the friction of articular cartilage. *Proc Inst Mech Eng H* 210(2):109-119.
215. Maroudas A (1968) Physicochemical properties of cartilage in the light of ion exchange theory. *Biophys J* 8(5):575-595.
216. Bussiere CT, Wright GM, & DeMont ME (2006) The mechanical function and structure of aortic microfibrils in the lobster Homarus americanus. *Comp Biochem Physiol A Mol Integr Physiol* 143(4):417-428.
217. Kielty CM & Shuttleworth CA (1993) The role of calcium in the organization of fibrillin microfibrils. *FEBS Lett* 336(2):323-326.
218. Schmid TM*, et al.* (2002) Superficial zone protein (SZP) is an abundant glycoprotein in human synovial fluid with lubricating properties. *The Many Faces of Osteoarthritis*), pp 159-161.
219. Schumacher BL, Block JA, Schmid TM, Aydelotte MB, & Kuettner KE (1994) A novel proteoglycan synthesized and secreted by chondrocytes of the superficial zone of articular cartilage. *Arch Biochem Biophys* 311(1):144-152.
220. Greene GW*, et al.* (2017) Structure and Property Changes in Self-Assembled Lubricin Layers Induced by Calcium Ion Interactions. *Langmuir* 33(10):2559-2570.
221. Horkay F, Basser PJ, Londono DJ, Hecht AM, & Geissler E (2009) Ions in hyaluronic acid solutions. *J Chem Phys* 131(18):184902.
222. De Gennes P-G & Gennes P-G (1979) *Scaling concepts in polymer physics* (Cornell university press).
223. Nitzan DW (2003) 'Friction and adhesive forces'--possible underlying causes for temporomandibular joint internal derangement. *Cells Tissues Organs* 174(1-2):6-16.
224. Wen CY*, et al.* (2012) Collagen fibril stiffening in osteoarthritic cartilage of human beings revealed by atomic force microscopy. *Osteoarthr Cartilage* 20(8):916-922.
225. Gong JP, Kagata G, & Osada Y (1999) Friction of gels. 4. Friction on charged gels. *J Phys Chem B* 103(29):6007-6014.
226. Drummond C (2012) Electric-field-induced friction reduction and control. *Phys. Rev. Lett.* 109(15):154302.
227. Pan YS, Xiong DS, & Ma RY (2007) A study on the friction properties of poly(vinyl alcohol) hydrogel as articular cartilage against titanium alloy. *Wear* 262(7-8):1021-1025.

228. Pan Y-s & Xiong D-s (2006) Recent development on biotribology of poly (vinyl alcohol) hydrogel. *TRIBOLOGY-BEIJING*- 26(2):188.
229. Katta JK, Marcolongo M, Lowman A, & Mansmann KA (2007) Friction and wear behavior of poly (vinyl alcohol)/poly (vinyl pyrrolidone) hydrogels for articular cartilage replacement. *J. Biomed. Mater. Res. A* 83(2):471-479.
230. Freeman ME, Furey MJ, Love BJ, & Hampton JM (2000) Friction, wear, and lubrication of hydrogels as synthetic articular cartilage. *Wear* 241(2):129-135.
231. Morita T, Narita T, Mukai S-a, Yanagisawa M, & Tokita M (2013) Phase behaviors of agarose gel. *AIP Advances* 3(4):452.
232. Espinosa-Marzal RM, Nalam PC, Bolisetty S, & Spencer ND (2013) Impact of solvation on equilibrium conformation of polymer brushes in solvent mixtures. *Soft Matter* 9(15):4045-4057.
233. Nalam PC*, et al.* (2013) Two-Fluid Model for the Interpretation of Quartz Crystal Microbalance Response: Tuning Properties of Polymer Brushes with Solvent Mixtures. *The Journal of Physical Chemistry C* 117(9):4533-4543.
234. Dixit S, Crain J, Poon WCK, Finney JL, & Soper AK (2002) Molecular segregation observed in a concentrated alcohol–water solution. *Nature* 416(6883):829-832.
235. Dougan L*, et al.* (2004) Methanol-water solutions: A bi-percolating liquid mixture. *J Chem Phys* 121(13):6456-6462.

APPENDIX A: SUPPLEMENTARY INFORMATION

Colloidal probe indentation and JKR model for Chapters 4, 5, 6 and 8

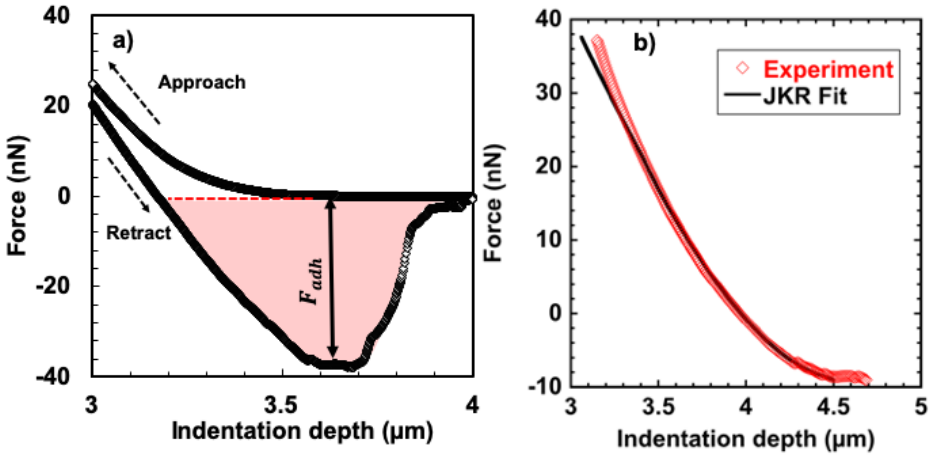

Figure A1. a) Representative indentation force vs. depth for 6% PAAm hydrogels. The pull-off force F_{adh} (black arrow) is defined as the minimum force in the retraction curve. Since the approach curve was always repulsive, the adhesion energy was calculated as the integral of the negative portion of the indentation force vs. depth curve upon retraction (red shadowed area). b) Representative fit of the JKR model to the experimental results for a 12% PAAm hydrogel at an applied load of 40 nN. Approach/retraction velocity = 2 μm/s.

Modulus, Surface energy and SEM images of hydrogels (Chapter 4)

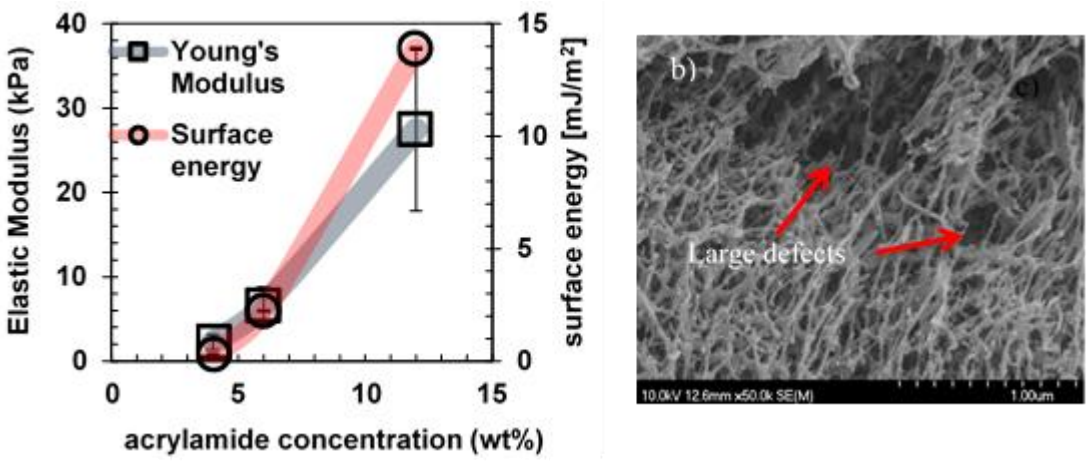

Figure A2: a) Elastic modulus (squares) and surface energy (circles) of PAAm hydrogels with a polymer concentration of 4%, 6% and 12% obtained from force-indentation curves measured by colloidal probe AFM. The Hertz model was fit to the approach force-indentation curve, while the JKR model was used to obtain the surface energy from the retraction curves. The overall adhesion energy (in Joule) is highest for the 6%-PAAm hydrogels: $(0.14\pm0.03)\cdot10^{-14}$, $(0.17\pm0.03)\cdot10^{-14}$, and $(0.13\pm0.06)\cdot10^{-14}$ J, for 4%-PAAm, 6%-PAAm and 12%-PAAm hydrogels, respectively.

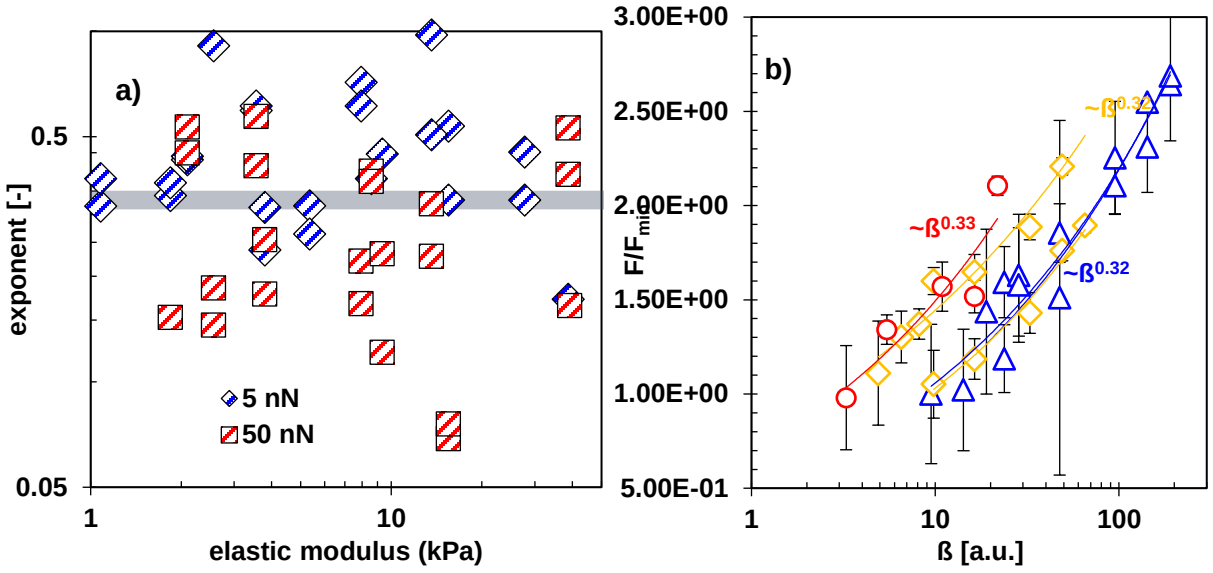

Figure A3: a) Exponent describing the relation between friction force and $\beta \sim E^{-\frac{2}{3}}V$ at two selected loads (5nN and 50 nN). An exponent equal to 0.33 (given by the grey line) would indicate a change of the friction force according to elasto-hydrodynamic lubrication. Only a few speed-dependent friction force measurements at the low load of 5 nN are consistent with this theory. An example, in which hydrodynamic lubrication might have been attained, is shown in b) for 4%PAAm- (blue triangles), 6%-PAAm (yellow diamonds), and 12%-PAAm (Red circles) hydrogels.

Table A1 Maximum Contact Stress

Maximum contact stress (in Pa) as a function of the load (no sliding conditions).

	Colloid Diameter: 20 µm			**Colloid Diameter: 5 µm**		
Load (nN)	**4wt%**	**6wt%**	**12wt%**	**4wt%**	**6wt%**	**12wt%**
5	3.79E+02	1.20E+03	2.01E+03	9.04E+02	2.22E+03	3.97E+03
10	4.59E+02	1.27E+03	2.19E+03	1.14E+03	2.54E+03	4.71E+03
15	5.20E+02	1.34E+03	2.36E+03	1.31E+03	2.81E+03	5.30E+03
20	5.70E+02	1.40E+03	2.50E+03	1.44E+03	3.04E+03	5.78E+03
25	6.13E+02	1.45E+03	2.63E+03	1.56E+03	3.24E+03	6.21E+03
30	6.51E+02	1.50E+03	2.75E+03	1.66E+03	3.42E+03	6.58E+03
40	7.17E+02	1.60E+03	2.97E+03	1.83E+03	3.74E+03	7.24E+03
50	7.74E+02	1.69E+03	3.16E+03	1.97E+03	4.01E+03	7.80E+03

Derivation of Eq. (5.2) based on ref. (104)

$$F_{adh} \sim \frac{A_v G V}{d} \int \frac{t}{\langle t \rangle_b + \tau_f} \breve{P_v}\, dt$$

Eq. A1

Where $\breve{P_v}$ is the probability of a junction to be in the bonded state, given by $\exp\left(-\frac{t}{\tau_0}\right)$, A_v is the contact area during sliding and $\langle t \rangle_b$ is the mean lifetime of junctions in the bonded state, given by:

$$\langle t_b \rangle = \tau_o \left(1 - \exp\left(-\frac{t_b}{\tau_o}\right)\right)$$

Eq. A2

where $\left(1 - \exp\left(-\frac{t_b}{\tau_o}\right)\right)$ is the probability of rupture and t_b is the time required to break the junction $t_b = \frac{l^*}{V}$. Using this, we can rewrite the elastic force in the contact area from rest till t_b as:

$$F_{adh} = \frac{A_v GV}{d(\langle t_b \rangle + \tau)} \int_0^{t_b} \mathrm{t} \cdot \exp\left(-\frac{t}{\tau_o}\right) dt$$

Eq. A3

Integrating by parts and simplifying:

$$F_{adh} = \frac{A_v GV}{d(\langle t \rangle_b + \tau)} \left[-t \cdot \tau_o \exp\left(-\frac{t}{\tau_o}\right) - \tau_o \tau_o \exp\left(-\frac{t}{\tau_o}\right)\right]_{\mathbf{0}}^{\boldsymbol{t_b}}$$

$$F_{adh} = \frac{A_v GV}{d(\langle t_b \rangle + \tau)} \left[\tau_o \exp\left(-\frac{t}{\tau_o}\right)(-t - \tau_o)\right]_0^{t_b}$$

$$F_{adh} = \frac{A_v GV}{d(\langle t_b \rangle + \tau)} \left(-\tau_o \exp\left(-\frac{t_b}{\tau_o}\right) \tau_o(-t_b - \tau_o) + {\tau_o}^2]\right)$$

$$F_{adh} = \frac{A_v GV}{d(\langle t_b \rangle + \tau)} \left(-{\tau_o}^2 \left(\exp\left(-\frac{t_b}{\tau_o}\right)\left(\frac{t_b}{\tau_o} + 1\right) - 1\right)\right)$$

Multiplying and dividing by $\langle t_b \rangle$ yields:

$$F_{adh} = \frac{\langle t_b \rangle}{\langle t_b \rangle} \frac{A_v GV}{d(\langle t_b \rangle + \tau)} \left(-{\tau_o}^2 \left(\exp\left(-\frac{t_b}{\tau_o}\right)\left(\frac{t_b}{\tau_o} + 1\right) - 1\right)\right)$$

Substituting SEq.2 in the denominator we get:

$$F_{adh} = \frac{A_v GV}{d} \frac{\langle t_b \rangle}{\langle t_b \rangle + \tau_f} \frac{-{\tau_o}^2 \left(\exp\left(-\frac{t_b}{\tau_o}\right)\left(\frac{t_b}{\tau_o} + 1\right) - 1\right)}{\tau_o \left(1 - \exp\left(-\frac{t_b}{\tau_o}\right)\right)}$$

Substituting $t_b = \frac{l^*}{V}$ gives us the final expression for the adhesive elastic friction force:

$$F_{adh} = \frac{A_v GV\tau_o}{d} \frac{\langle t_b \rangle}{\langle t_b \rangle + \tau_f} \frac{1 - \left(1 + \frac{l^*}{V\tau_o}\right) \exp\left(-\frac{l^*}{V\tau_o}\right)}{1 - \exp\left(-\frac{l^*}{V\tau_o}\right)}$$

$$F_{adh} = \frac{A_b GV\tau_o}{d} \frac{1 - \left(1 + \frac{l^*}{V\tau_o}\right) \exp\left(-\frac{l^*}{V\tau_o}\right)}{1 - \exp\left(-\frac{l^*}{V\tau_o}\right)}$$

Eq. A4

as proposed in Chapter 4.

The validity of this simplified expression relies on the assumption that the bond rupture is thermally activated, i.e. that the lateral force does not facilitate the rupture of the adhesive bonds.

Viscous Dissipation (Chapter 4)

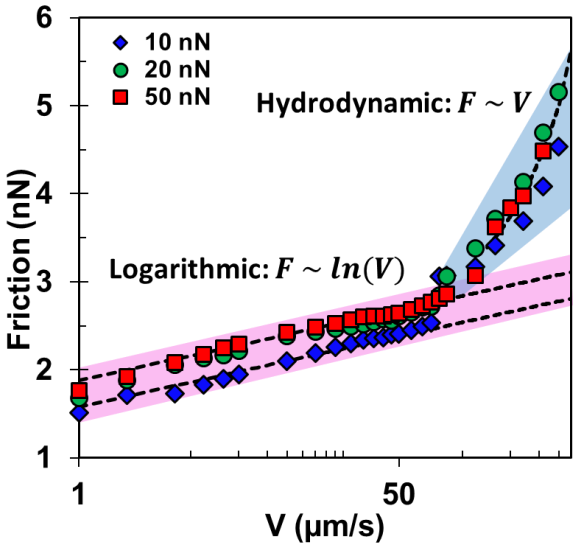

Figure A4. Friction force between a borosilicate glass surface and a silica colloid as a function of the sliding velocity at normal loads of 10 (blue diamond), 20 (green circles) and 50 (red squares) nN. The friction force shows a transition from a logarithmic dependence on velocity (fuchsia pink area at low speeds) to a linear dependence in the hydrodynamic regime at high speeds (light blue area), where $F \sim 0.005V$. This is in contrast to the reported non-Newtonian behavior of the hydrogels in this work. Colloid diameter: 20 μm, Spring Constant: 0.5 N/m.

Temperature Dependent Static Friction (Chapter 5)

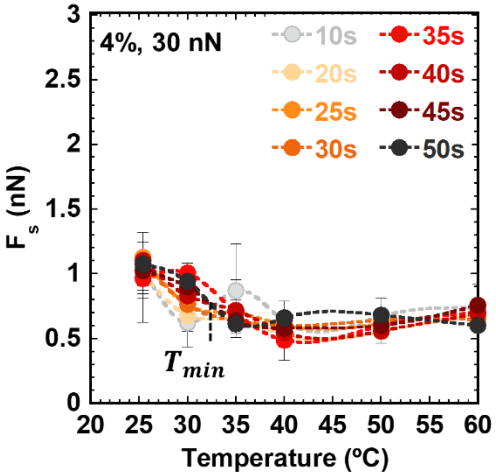

Figure A5. Static friction F_s as a function of temperature for different hold times between 5 s and 50 s (see legends) for 4% hydrogels. The lines show fits of the experimental results to spline functions to determine T_p^*, T_p and T_{min} at the extrema of the static friction. Only T_{min} is observed for 4% hydrogels at this load indicating that static friction decreases with an increase in temperature initially and transitions into a quasi-independent regime of both temperature and hold time, also refrred to as the "bulk thermodynamic limit" or liquid-like behavior. Colloid radius = 10.7 μm. Cantilever stiffness= 0.42 N/m. Lateral velocity for friction-force measurements: 1 μm/s.

Calculated poroelastic relaxation times at room temperature (Chapter 5)

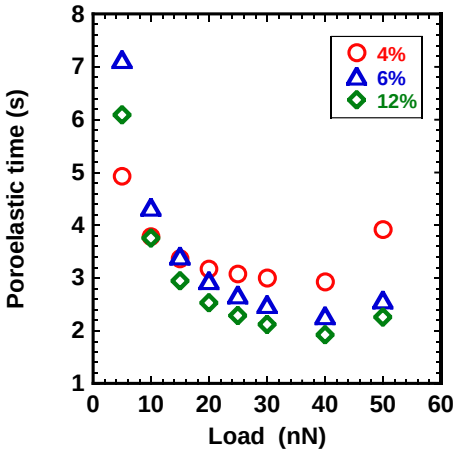

Figure A6. Estimated poroelastic relaxation times for the three hydrogels at 25 ºC according to $\tau_w = 6\pi\eta a^2/P\xi^2$, from ref.(14), where τ_w is the poroelastic time, a is the contact radius, η is the viscosity of the fluid, P is the pressure and ξ is the hydrogel mesh size. An increase in applied pressure facilitates fluid exudation, thereby causing a decrease in τ_w, until the contact area is so large that the poroelastic time increases with applied pressure, which happens here at ~50 nN. The smaller pressure on 4% hydrogels and the larger contact area lead to higher poroelastic times compared to 6% and 12% hydrogels. The smallest τ_w is estimated for 12% hydrogels at 25 ºC for loads > 10 nN.

Regression coefficients for static friction vs hold time (Chapter 6)

Table A2. Regression coefficient for the logarithmic fits to the data presented in Fig. 1 according to the $F_s = L(\alpha_s^L + \beta_s^L \ln(t_{hold}))$, where α_s^L and β_s^L are fitting parameters at each load.

Load (nN)	**4%**				**6%**				**12%**			
	0.5 µm/s	**2 µm/s**	**5 µm/s**	**10 µm/s**	**0.5 µm/s**	**2 µm/s**	**5 µm/s**	**10 µm/s**	**0.5 µm/s**	**2 µm/s**	**5 µm/s**	**10 µm/s**
5	0.98	0.78	0.93	0.85	0.81	0.88	0.87	0.98	-	0.95	0.96	0.98
10	0.92	0.98	0.99	0.93	0.93	0.97	0.91	0.99	0.98	0.96	0.87	0.91
30	0.93	0.88	0.98	0.92	0.86	0.95	0.98	0.99	0.99	0.99	0.99	0.95
50	0.92	0.99	0.93	0.91	-	0.89	0.91	0.99	0.99	0.91	0.88	0.99

Table A3 Contact Radii

Contact radii, maximum contact pressures and interfacial energy (γ) for 4%, 6%, 12%-PAAm hydrogels for loads ranging from 5 to 50 nN determined by AFM indentation according to the JKR model. The measurements were conducted with a silica colloid (radius = 10.7 μm, cantilever stiffness = 0.42 N/m) at an approach/retraction speed of 1 μm/s.

	4%-PAAm		**6%-PAAm**		**12%-PAAm**	
Interfacial Energy, γ (J/m^2)	**7.9 ± 3.1 E-5**		**3.2 ± 0.8 E-4**		**5.5 ± 1.5 E-4**	
Load (nN)	**Contact Radius (μm)**	**Max. Pressure (kPa)**	**Contact Radius (μm)**	**Max. Pressure (kPa)**	**Contact Radius (μm)**	**Max. Pressure (kPa)**
5	4.89	0.40	3.88	1.71	3.25	3.86
10	5.38	0.47	4.04	1.85	3.34	4.06
15	5.77	0.52	4.19	1.97	3.42	4.25
20	6.09	0.57	4.31	2.08	3.49	4.43
25	6.38	0.61	4.43	2.18	3.56	4.59
30	6.64	0.64	4.54	2.27	3.63	4.74
40	7.09	0.70	4.74	2.44	3.75	5.03
50	7.48	0.76	4.92	2.58	3.86	5.28

Select isotherms on PAAm hydrogel films (Chapter 7)

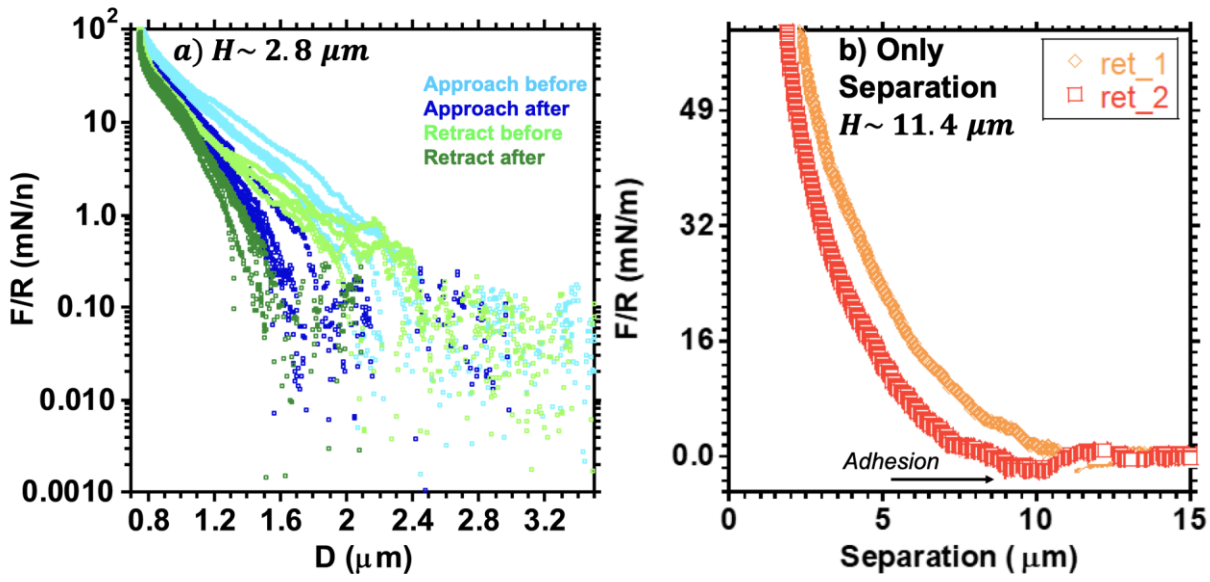

Figure A7. a) Compression and decompression isotherms performed on 6% PAAm hydrogels before and after the lateral tests show a 30% decrease in hydrogel thickness indicating damage and/ or reorganization of the hydrogel structure, here the initial thickness of the hydrogel was $H \sim 2.8\ \mu m$. b) Example separation curves where a slight adhesion was measured during retract segment (ret_2) after an initial compression (ret_1) for a 6% PAAm hydrogel.

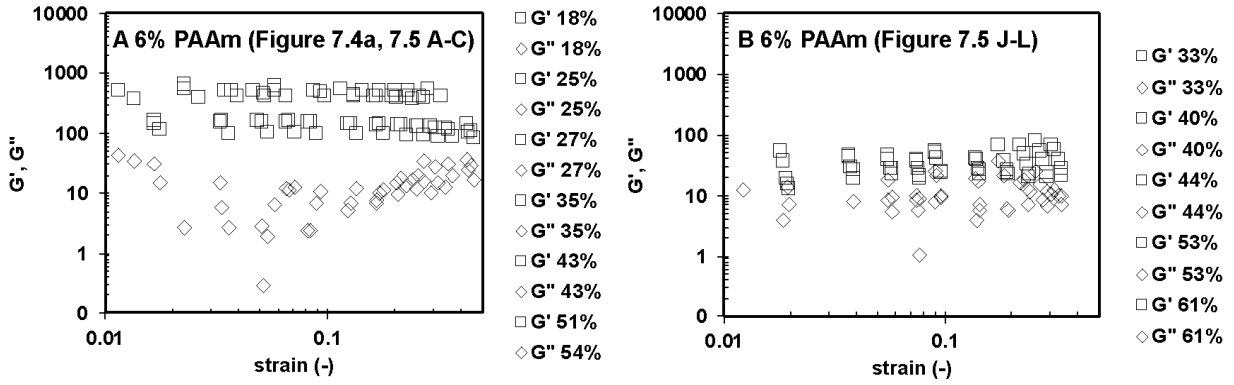

Figure A8. Storage and loss moduli measured on the two different 6% PAAm hydrogel thin films obtained as a function of the applied strain at multiple compressions. The hydrogel in B is very soft, and highly viscous, indicating a that up till 60% of its thickness, this gel had a very low crosslinking.

Table A4. Composition, thickness, experimental conditions and corresponding G^*measured from microrheology and eSFA measurements for comparison. $G^*$from the eSFA measurements was calculated at the lowest compressions applied.

PAAm	Thickness (um)	G* - eSFA(Pa)	G* - microrheology(Pa)	eSFA Load range (uN)	Compressions %
6%	4.58	231 ± 50	275 ± 30	21 to 1113	18 to 58
4%	6.27	41 ± 5	143 ± 10	4 to 3179	7 to 71
6%	13.58	154 ± 5	275 ± 30	73 to 1231	18 to 50
6%	14.00	30 ± 6	275 ± 30	71 to 570	35 to 71

QI images of 1Ag6PAAm-0.5x in Water:DMSO (Chapter 8)

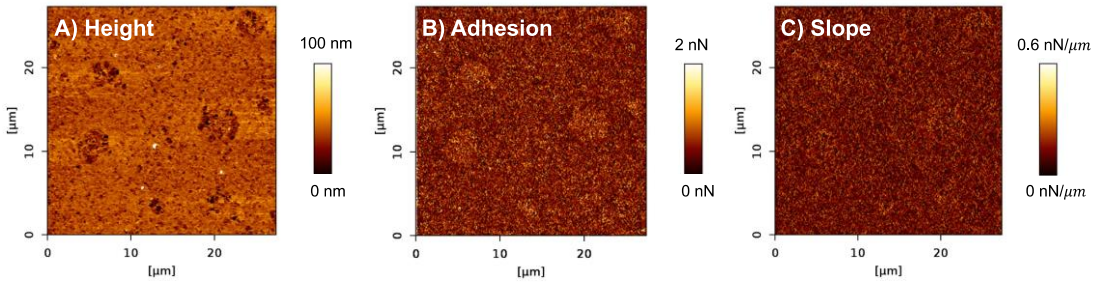

Figure A9. QI imaging of the DN hydrogel with 1Ag6PAAm-0.5x composition when the PAAm is gelated with 50% DMSO. The height profile shows circular domains ranging in size from ~1.2 to 1.2 μm in diameter in the water:DMSO mixture, where the porosity is prominently higher than the surrounding matrix. We attribute the circular domains corresponding to areas rich in PAAm. This is because 1:1 water DMSO mixtures are used in the synthesis of macroporous PAAm hydrogels where reaction induced phase separation causes a porous network to form(171, 172) due to the high affinity of water and DMSO(173, 174). Hence, the higher porosity within the circular regions seem in A) indicate the presence of PAAm. These circular domains also show up in the adhesion and slope (stiffness). The higher adhesion and stiffness occur in a dehydrated polymer network and hence indicate a collapse of the PAAm in this region.

Friction coefficients for double network hydrogels (Chapter 8)

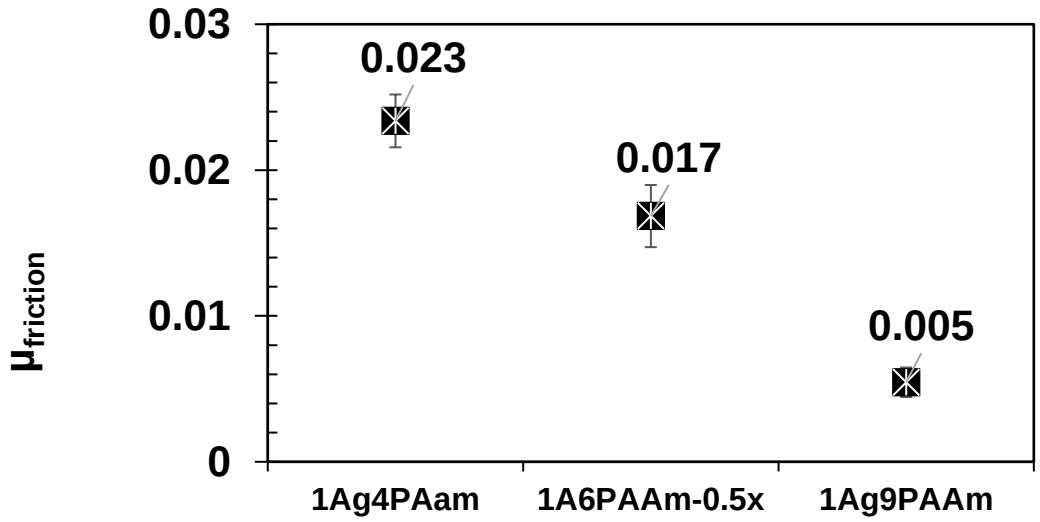

Figure A10. Friction coefficient measured in the low speed range on 1Ag4PAAm, 1Ag6PAAm-0.5x and 1Ag9PAAm DN hydrogels. A higher friction coefficient is observed on the 1Ag4PAAm, which expected due to the prominent poroelastic deformation and velocity weakening regime. Good lubricity is achieved for 1Ag6PAAm-0.5x, where a $\mu_{friction}$ is ~10^{-2} . It is noteworthy that even this hydrogel is approaching the ad hoc condition of superlubricity ($\mu_{friction}$ is ~10^{-2}). An even lower friction coefficient is measured on 1Ag9PAAm DN hydrogel. These results show a remarkable improvement in the lubrication properties of the DN hydrogels in comparison to previous works(168-170).

Consecutive isotherms showing approach and separation (Chapter 9)

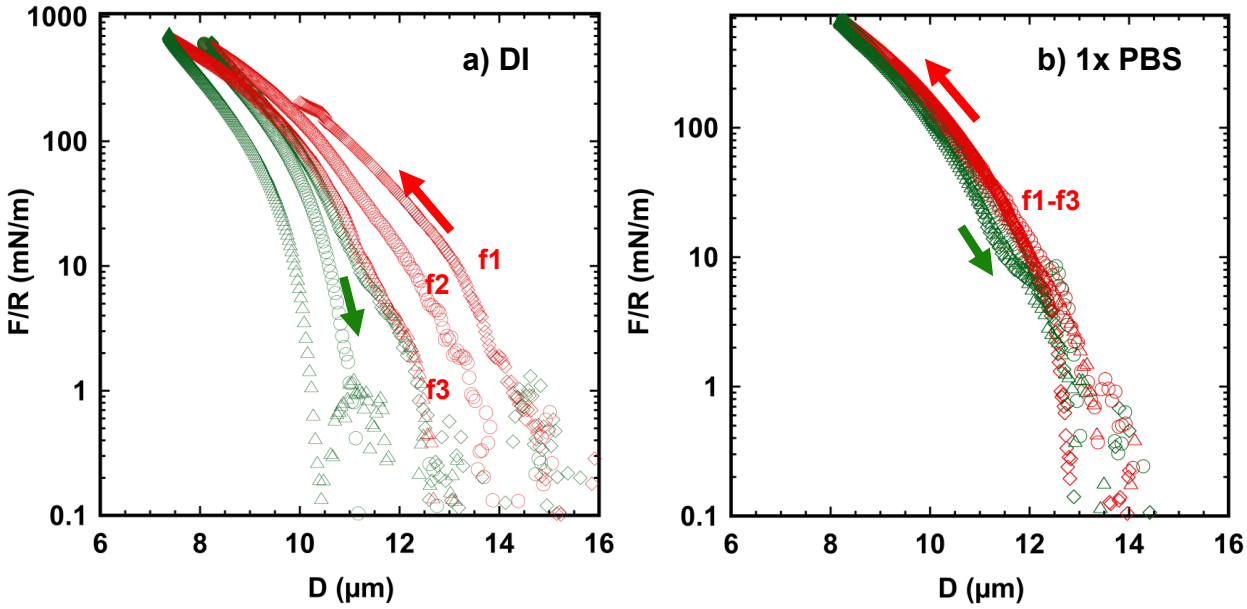

Figure A11. Reference eSFA measurements of a cartilage section with an initial thickness of 15.2 μm a) first in DI water, and then in b) 1× PBS after 12 hours of equilibration in each solution. Three compressions -red diamonds (f1), circles (f2) and triangles (f3)- and decompressions -green diamonds, circles and triangles- are shown in each diagram. The hysteresis between compression and decompression in DI water and the variation of consecutive compressions indicate that structural changes happen and the cartilage does not recover between consecutive measurements.

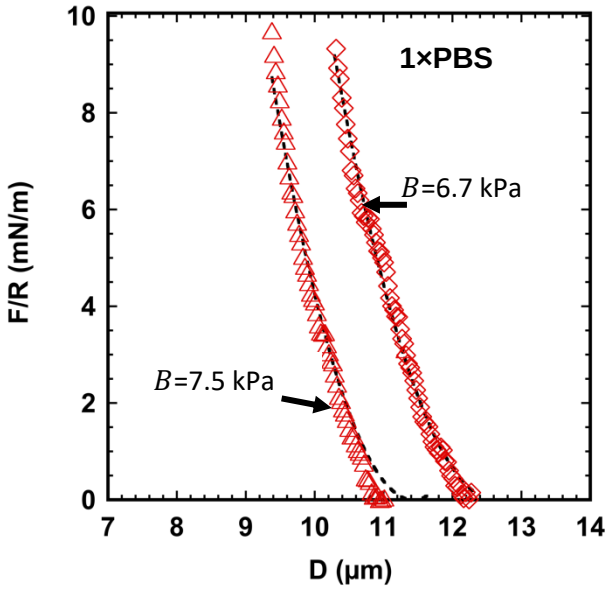

Figure A12. Fit of the compressibility model (Eqn. 9.1 in the main chapter) to measured compression isotherms in 1× PBS for the example shown in chapter 9. This yields compressive moduli (B) of 6.7 and 7.5 kPa, respectively. The fit is only possible for the first 1-1.5 μm, indicating that the modulus changes with depth.

ATR-IR spectroscopy (Chapter 8)

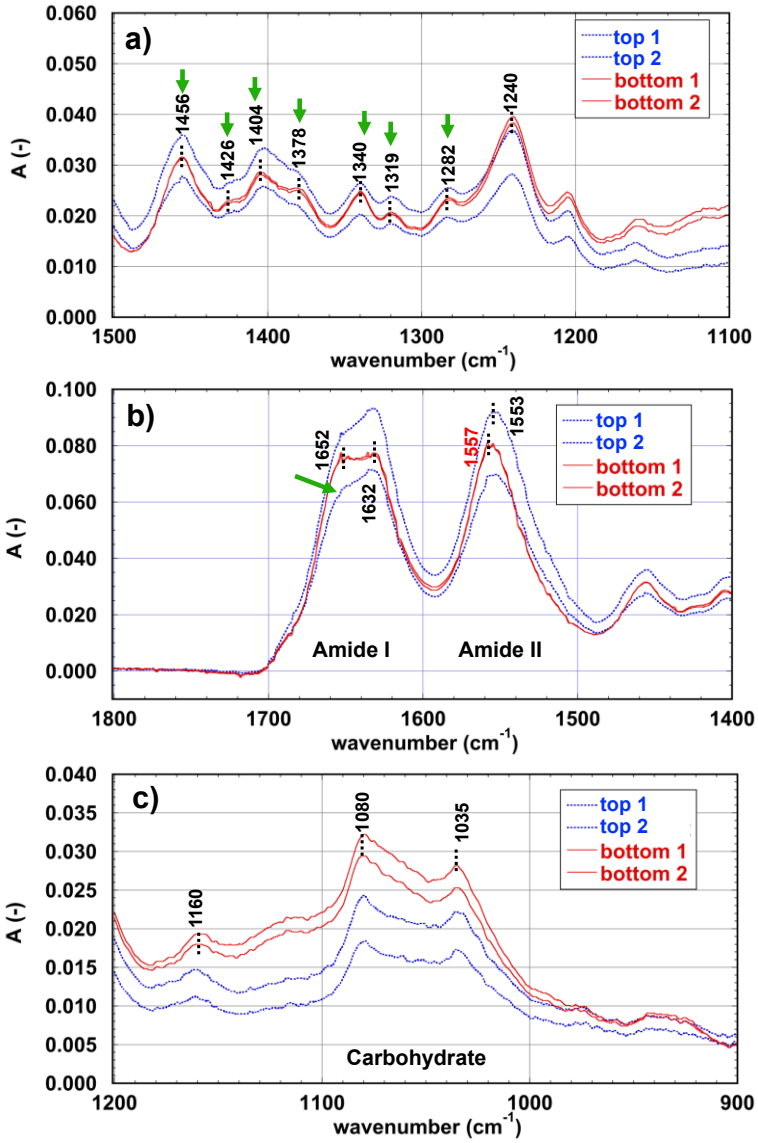

Figure A13. Representative ATR-IR spectra of hydrated cartilage sections after subtraction of the baseline of water. The penetration depth of the IR beam is 1 to 2 µm in the region of interest. The labels "top" and "bottom" indicate that upper and bottom regions are in contact with the ATR crystal, respectively.

QI Images (Chapter 10)

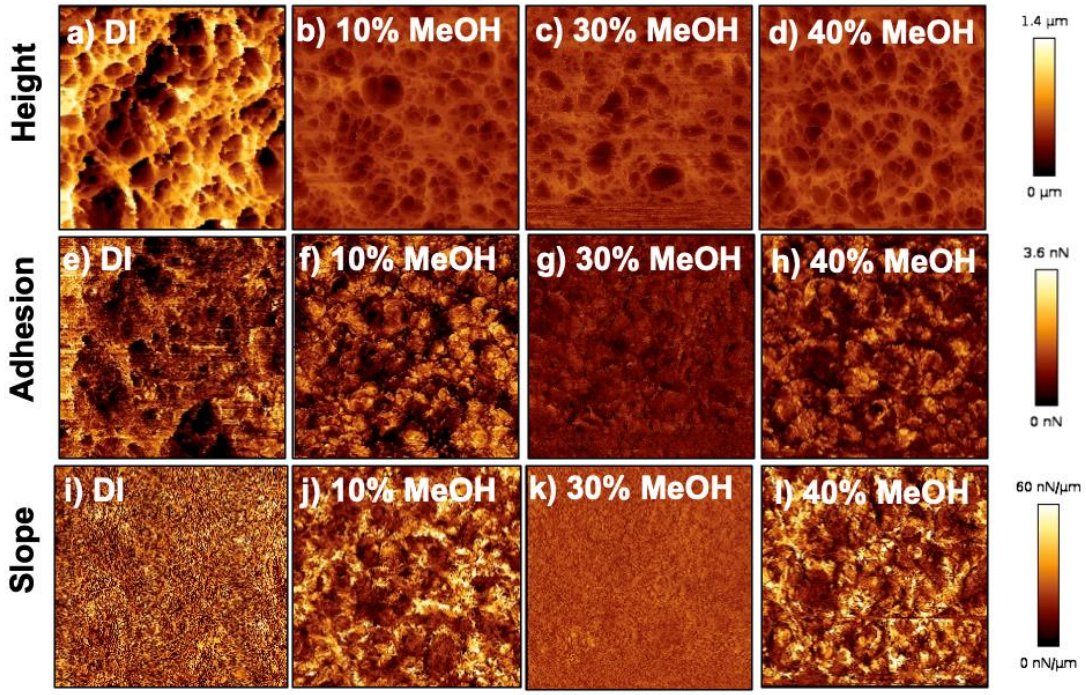

Figure A14. QI images of Agarose-PAAm DN hydrogels equilibrated in DI water, 10% MeOH, 30% MeOH and 40% MeOH, The height, adhesion and slope profiles are shown for each condition. The image size was 4 x 4 μm. . Here, we note that we are only able to image the agarose network in this hydrogel. Visible aggregation is observed in 10% and 30% MeOH. The aggregation of the surface into clusters is more evident in the adhesion and stiffness profiles in the 10% and 40% MeOH solvents. This was previously observed in the single network agarose hydrogels as well. The relatively homogenous, low stiffness and adhesion in 30% MeOH of the DN hydrogel is intriguing, however also reproducible in the AFM nanoindentation measurements. Hence, the non-monotonic trend in adhesion and stiffness of the near surface region supports the action of at least two competing determinants, perhaps related to the response of the two polymer networks.

Swelling of DN, and SN hydrogels in water-methanol mixtures (Chapter 10)

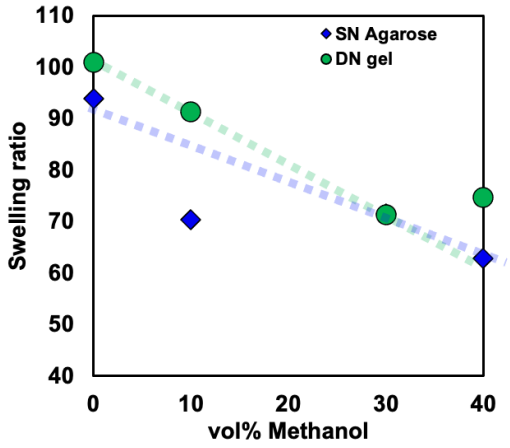

Figure A15. Swelling ratio of agarose and double network hydrogels in different water-methanol mixture. Figure 1b shows the swelling results obtained for the three hydrogels as a function of the solvent mixtures. Results for the agarose hydrogels were discussed in Chapter 10. The double network hydrogel undergoes a monotonic collapse with increasing methanol content up to 30% methanol. It is also interesting that the unexpected collapse of agarose hydrogels at 10% methanol does not happen on the DN hydrogels, which indicates the more robust microstructure or less methanol in the DN. Furthermore, the incremental collapses seizes at 40%. This nonmonotonic change in the DN swelling behavior suggests at least two competing mechanisms exist, which determine the swelling behavior, perhaps in relation to the reference single network hydrogels. We note that 40% MeOH is considered a theta solvent for the single network PAAm, and hence, it could contribute to the observed nonlinear trend as well.